REPORT No.: 699-099-513 DATE: 29 January 2001

HIGHLY LOADED AIRFRAME FITTINGS
FINAL REPORT

Revision: **Basic**
Contract No./D.O./ECP: **DAAJ02-97-C-0030**

Date: **29 January 2001**
CDRL: **A003**

DISTRIBUTION STATEMENT A
Approved for Public Release
Distribution Unlimited

Bell Helicopter TEXTRON
A Subsidiary of Textron Inc.

20010221 104

Bell Helicopter TEXTRON

A Subsidiary of Textron Inc.

TECHNICAL DATA

REPORT NO. **699-099-513** DATE: **29 January 2001**

HIGHLY LOADED AIRFRAME FITTINGS FINAL REPORT

Revision: **Basic**
Contract No./D.O./ECP: **DAAJ02-97-C-0030**
CDRL: **A003**
Work Order/EWA No: **N/A**
Page Count: **272**

Date: **29 January 2001**

Pmod No.: **N/A**
Model: **N/A**

PREPARED BY	[signature]	DATE	09 Dec 99
PREPARED BY	[signature]	DATE	28 APR 00
PREPARED BY	R H Jones	DATE	28 Apr 00
CHECKED BY		DATE	
CHECKED BY		DATE	
CHECKED BY		DATE	
APPROVED	B R Mullen Jr	DATE	4/28/00

RESTRICTED DISCLOSURE NOTICE IS ON PAGE iii

USAAMCOM TR 97-D-30

U.S. ARMY AVIATION
AND MISSILE COMMAND

HIGHLY LOADED AIRFRAME FITTINGS

Kurt E. Tessnow, J. Donn Hethcock, Rodney H. Jones

Bell Helicopter, Textron
P.O. Box 482
Fort Worth, Texas 76101

December 1999

FINAL REPORT

DISTRIBUTION STATEMENT

Approved for public release. Distribution unlimited

Prepared for

AVIATION RESEARCH, DEVELOPMENT & ENGINEERING
CENTER (AMCOM)
AVIATION APPLIED TECHNOLOGY DIRECTORATE

REPORT DOCUMENTATION PAGE

Form Approved
OMB No. 0704-0188

Public reporting burden for this collection of information is estimated to average 1 hour per response, including the time for reviewing instructions, searching existing data sources, gathering and maintaining the data needed, and completing and reviewing the collection of information. Send comments regarding this burden estimate or any other aspect of this collection of information including suggestions for reducing this burden, to Washington Headquarters Services, Directorate for Information Operationss and Reports, 1215 Jefferson Davis Highway, Suite 1204, Arlington, VA 22202-4302, and to the office of Management and Budget. Paperwork Reduction Project (0704-0188), Washington, DC 20503.

1. AGENCY USE ONLY (Leave Blank)	2. REPORT DATE	3. REPORT TYPE AND DATES COVERED
	29 January 2001	Final

4. TITLE AND SUBTITLE
Highly Loaded Airframe Fittings Final Report

5. FUNDING NUMBERS
C: DAAJ02-97-C-0030

6. AUTHOR(S)
Kurt E. Tessnow, J. Donn Hethcock, Rodney H. Jones

7. PERFORMING ORGANIZATION NAME(S) AND ADDRESS(ES)
Bell Helicopter Textron
Post Office Box 482
Fort Worth, Texas 76101

8. PERFORMING ORGANIZATION REPORT NUMBER
699-099-513

9. SPONSORING / MONITORING AGENCY NAME(S) AND ADDRESS(ES)
Aviation Applied Technology Directorate
U.S. Army Aviation and Missile Command, Research, Development, and Engineering Center (AMCOM RDEC)
Fort Eustis, VA 23604-5577

10. SPONSORING / MONITORING AGENCY REPORT NUMBER
USAAMCOM
TR 97-D-30

11. SUPPLEMENTARY NOTES

12a. DISTRIBUTION / AVAILABILITY STATEMENT
APPROVED FOR PUBLIC RELEASE. DISTRIBUTION UNLIMITED

12b. DISTRIBUTION CODE

13. ABSTRACT *(Maximum 200 words)*

The analysis and design of airframe fittings subjected to large loads applied at high strain rates has been investigated with the goals of reduced analytical inaccuracy, reduced airframe structure weight and cost, and reduced airframe structure development time. Current methodologies that account for rate sensitive material behavior and internal stress wave propagation were evaluated. A comprehensive analytical approach is proposed in which the dynamic behavior of all components in the system is accurately represented in a dynamic simulation model using an explicit nonlinear transient finite-element code.

The proposed analysis procedure was demonstrated in a redesign of the ACAP tail gear upper shock strut attachment fitting, which had failed during the original aircraft drop test. The redesigned joint compared favorably with the original in both cost and weight. The redesigned joint was drop tested to validate the design and analysis methodology. The test was unsuccessful in that a part failure away from the subject joint prevented a complete substantiation of the new design. Post-mortem analysis in which the failed part was more accurately represented in the dynamic simulation, however, achieved good qualitative agreement between the analysis and test results.

14. SUBJECT TERMS
airframe fittings, high strain rate material properties, dynamic loading, dynamic analysis, energy attenuation, landing gear, drop test, structure

15. NUMBER OF PAGES
181

16. PRICE CODE

17. SECURITY CLASSIFICATION OF REPORT	18. SECURITY CLASSIFICATION OF THIS PAGE	19. SECURITY CLASSIFICATION OF ABSTRACT	20. LIMITATION OF ABSTRACT
UNCLASSIFIED	UNCLASSIFIED	UNCLASSIFIED	UL

GENERAL INSTRUCTIONS FOR COMPLETING SF 298

The Report Documentation Page (RDP) is used in announcing and cataloging reports. It is important that this information be consistent with the rest of the report, particularly the cover and title page. Instructions for filling in each block of the form follow. It is important to ***stay within the lines*** to meet ***optical scanning requirements.***

Block 1. Agency Use Only (Leave blank).

Block 2. Report Date. Full publication date including day, month, and year, if available (e.g. 1 Jan 88). Must cite at least the year.

Block 3. Type of Report and Dates Covered. State whether report is interim, final etc. If applicable, enter inclusive report dates (e.g. 10 Jun 87 - 30 Jun 88).

Block 4. Title and Subtitle. A title is taken from the part of the report that provides the most meaningful and complete information. When a report is prepared in more than one volume, repeat the primary title, add volume number, and include subtitle for the specific volume. On classified documents enter the title classification in parentheses.

Block 5. Funding Numbers. To include contract and grant numbers; may include program element number(s), project number(s), task number(s), and work unit number(s). Use the following labels:

C -	Contract	**PR** -	Project
G -	Grant	**TA** -	Task
PE -	Program Element	**WU** -	Work Unit Accession No.

Block 6. Author(s). Name(s) of person(s) responsible for writing the report, performing the research, or credited with the content of the report. If editor or compiler, this should follow the name(s).

Block 7. Performing Organization Report Address(es). Self-explanatory.

Block 8. Performing Organization Report Number. Enter the unique alphanumeric report number(s) assigned by the organization performing the report.

Block 9. Sponsoring/Monitoring Agency Name(s) and Address(es). Self-explanatory.

Block 10. Sponsoring/Monitoring Agency Report Number. *(If known)*

Block 11. Supplementary Notes. Enter information not included elsewhere such as: Prepared in cooperation with...; Trans. of ...; To be published in.... When a report is revised, include a statement whether the new report supersedes or supplements the older report.

Block 12a. Distribution/Availability Statement. Denotes public availability or limitations. Cite any availability to the public. Enter additional limitations or special markings in all capitals (e.g. NORFORN, REL, ITAR).

- **DOD** - See DoDD 5230.24, "Distribution Statements on Technical Documents."
- **DOE** - See authorities.
- **NASA** - See Handbook NHB 2200.2.
- **NTIS** - Leave blank.

Block 12b. Distribution Code.

- **DOD** - Leave blank.
- **DOE** - Enter DOE distribution categories from the Standard Distribution for Unclassified Scientific and Technical Reports.
- **NASA** - Leave blank.
- **NTIS** - Leave blank.

Block 13. Abstract. Include a brief *(Maximum 200 words)* factual summary of the most significant information contained in the report.

Block 14. Subject Terms. Keywords or phrases identifying major subjects in the report.

Block 15. Number of Pages. Enter the total number of pages.

Block 16. Price Code. Enter appropriate price code *(NTIS only)*.

Blocks 17. - 19. Security Classifications. Self-explanatory. Enter U.S. Security Classification in accordance with U.S. Security Regulations (i.e., UNCLASSIFIED). If form contains classified information, stamp classification on the top and bottom of the page.

Block 20. Limitation of Abstract. This block must be completed to assign a limitation to the abstract. Enter either UL (unlimited) or SAR (same as report). An entry in this block is necessary if the abstract is to be limited. If blank, the abstract is assumed to be unlimited.

UNLIMITED RIGHTS NOTICE

These data are furnished with unlimited data rights to the U.S. Government in accordance with the provisions of Contract No. DAAJ02-97-C-0030.

COPYRIGHT NOTICE

Copyright© 2001
Bell® Helicopter Textron Inc.
Unpublished - all rights reserved

This material may be reproduced by the U.S. Government for Government purposes pursuant to the Copyright License under the clauses at DFARS 252.227-7013 (Nov 95).

This page intentionally left blank.

REVISION RECORD			
Rev	**Date**	**Description**	**Signatures**
			By:_____ Ck:_____ Ck:_____ Ck:_____ Ck:_____ Ck:_____ Ap:_____
			By:_____ Ck:_____ Ck:_____ Ck:_____ Ck:_____ Ck:_____ Ap:_____
			By:_____ Ck:_____ Ck:_____ Ck:_____ Ck:_____ Ck:_____ Ap:_____
			By:_____ Ck:_____ Ck:_____ Ck:_____ Ck:_____ Ck:_____ Ap:_____
			By:_____ Ck:_____ Ck:_____ Ck:_____ Ck:_____ Ck:_____ Ap:_____

This page intentionally left blank.

ABSTRACT

The analysis and design of airframe fittings subjected to large loads applied at high strain rates have been investigated with the goals of reducing analytical inaccuracy, reducing airframe structure weight and cost, and reducing airframe structure development time. Beginning with an assessment of the current state of the art in sizing highly loaded airframe fittings, analytical methodologies that account for rate-sensitive material behavior and internal stress wave propagation were evaluated. A comprehensive energy-based analytical approach is proposed in which the dynamic behavior of all the components in the system is accurately represented.

High strain rate material characterization tests were performed on various aluminum alloys commonly used in airframe fitting design. Results indicated increases in both yield strength and elongation at high strain rates. The test results indicate that, in the absence of stress concentrations, structural aluminum alloys behave in an increasingly ductile manner as strain rate increases, with no apparent change in stiffness.

The proposed energy-based analysis procedure for dynamically loaded fittings was demonstrated in a redesign of the ACAP tail gear upper shock strut attachment joint, which had failed during the original aircraft drop test. The redesigned joint compared favorably to the original in both cost and weight. Several important principles for highly loaded airframe fitting design, which had been ascertained during the analytical development task, were applied to the new joint design.

The redesigned strut attachment was drop tested to validate the developed design and analysis methodology. The drop test was unsuccessful in that a part failure away from the upper strut attachment prevented a complete substantiation of the new joint design. However, post-mortem analysis, in which the drop test model was modified to include an accurate model of the failed part, proved that the part failure could have been predicted. Good qualitative agreement between analytical predictions and the test results was achieved using the modified dynamic simulation model.

The results of this program are presented herein, along with conclusions and recommendations for continued research and development.

This page intentionally left blank.

TABLE OF CONTENTS

Paragraph **Page**

1. INTRODUCTION 1-1

2. ANALYSIS METHODOLOGY 2-1

   2.1 Static vs. Dynamic Analysis 2-1
   2.2 KRASH Hybrid FEM Analysis 2-2
   2.3 Dynamic Fitting Loads 2-3
   2.4 Dynamic Fitting Response 2-7
   2.5 MSC/DYTRAN™ Explicit FEM Analysis 2-11
   2.6 Analysis and Design Procedure 2-11
   2.7 Theoretical Impact Examples 2-14

3. APPLICATION EXAMPLE: ACAP TAIL GEAR STRUT ATTACHMENT FITTING .. 3-1

   3.1 Existing Design 3-1
   3.2 Fitting Redesign 3-1
   3.3 Fitting Analysis 3-8
   3.4 Fitting Cost and Weight Comparison 3-13

4. COUPON TESTING 4-1

   4.1 Material Characterization Tests 4-1
   4.2 Validation Coupon Tests 4-2
   4.3 Stress Concentration Coupons 4-8

5. FULL-SCALE DROP TEST 5-1

   5.1 38-ft/s Drop Test 5-1
   5.2 Postmortem Analysis 5-6

6. CONCLUSIONS 6-1

7. REFERENCES 7-1

Appendix A. High Strain Rate Materials Properties Test
Appendix B. Validation Coupon Tests
Appendix C. Validation Drop Test

LIST OF FIGURES

Page

Figure 2-1. Aluminum tube cutter dynamic test results 2-4
Figure 2-2. Lateral deflection of trailing arm and strut due to rolled landing loads 2-5
Figure 2-3. Detail of strut clevis attachment showing progressive bending and failure of the attachment fitting lug 2-6
Figure 2-4. Sample stress/time response showing effects of data filtering 2-8
Figure 2-5. Uninstalled load stroke response of tube cutter MSC/DYTRAN™ model 2-9
Figure 2-6. Installed load stroke response of tube cutter MSC/DYTRAN™ model 2-9
Figure 2-7. Bolt designed for impact loading 2-10
Figure 2-8. Impact energy required to fracture a 3 inch long, 3/8 – 16, SAE 1018, cold forged bolt of which the shank area has been reduced by turning 2-10
Figure 2-9. Overview of Building Block Approach to Dynamic System Analysis 2-12
Figure 2-10. Design and analysis procedure for highly loaded airframe fittings 2-13
Figure 2-11. Integrated Virtual Airframe Analysis Tool 2-15
Figure 2-12. Straight elastic bar subjected to impact load 2-16
Figure 2-13. Impact response of straight elastic bar 2-17
Figure 2-14. Two impacted bars with equal static strength 2-17
Figure 3-1. Bell's ACAP flight test vehicle 3-2
Figure 3-2. ACAP landing gear configuration 3-2
Figure 3-3. Isometric view of ACAP upper strut attachment fitting 3-3
Figure 3-4. ACAP tail gear upper shock strut attachment fitting installation 3-4
Figure 3-5. Failed tail gear strut upper attachment fitting after aircraft drop test 3-5
Figure 3-6. ACAP tail gear shock strut and tube cutter after aircraft drop test 3-6
Figure 3-7. Features of the new shock strut attachment design (see Figure 3-8 for orientation) 3-7
Figure 3-8. MSC/DYTRAN™ model of the tail gear drop test 3-9
Figure 3-9. Initial attempt at a representative tube cutter model 3-10
Figure 3-10. Simple tube cutter model utilized in the final analysis (shown partially stroked) 3-10
Figure 3-11. Progressive deflection of landing gear drop test model 3-11
Figure 3-12. Plastic strain fringe plot in strap fitting due to 42 ft/s crash 3-12
Figure 3-13. Minimum principal stress fringe plot from MSC/NASTRAN® analysis of original fitting for worst case ACAP design loads 3-14
Figure 4-1. Unnotched dogbone specimen geometry and gage locations 4-3
Figure 4-2. Notched impact specimen geometry and gage locations 4-3
Figure 4-3. Low and medium energy impact response of dogbone specimen 4-4
Figure 4-4. High-energy impact response of dogbone specimen 4-5
Figure 4-5. Low and medium energy impact response of notched specimen 4-6
Figure 4-6. High-energy impact response of notched specimen 4-7
Figure 4-7. Plastic strain fringe for the dogbone and notched specimens 4-8

LIST OF FIGURES (Concluded)

		Page
Figure 4-8.	Stress wave reflections in the notched impact specimen	4-8
Figure 4-9.	Constant ramp coupon (30-degree ramp shown)	4-9
Figure 4-10.	Force time history plots for various ramp angles	4-9
Figure 4-11.	Dual angle ramp coupon (15 degrees/45 degrees)	4-10
Figure 4-12.	Force time history plot for dual angle ramp coupon	4-10
Figure 5-1.	Assembled drop test fixture	5-2
Figure 5-2.	Redesigned upper shock strut attachment joint	5-3
Figure 5-3.	Simulated landing gear drop test assembly	5-4
Figure 5-4.	Failed trailing arm attachment fitting	5-5
Figure 5-5.	Failed trailing arm attachment fitting and attachment lugs	5-5
Figure 5-6.	Post-test view of stroked tube cutter	5-6
Figure 5-7.	Revised drop test model with trailing arm attachment fitting	5-7
Figure 5-8.	Trailing arm attachment fitting model showing failed elements ("colder" color indicates earlier failure)	5-8
Figure 5-9.	Deformed shape of trailing arm attachment fitting at Time = 0.014 s (initial failure at Time = 0.007 s)	5-8

LIST OF TABLES

Page

Table 3-1. Comparison of Material Properties for Candidate Alloys 3-8
Table 4-1. Summary of Split Hopkinson Bar Tension Test Results 4-1
Table 4-2. Summary of Split Hopkinson Bar Compression Test Results 4-2

1. INTRODUCTION

The design and analysis of airframe structure for modern aircraft traditionally begins with a finite-element internal load distribution analysis, followed by detail stress analysis of individual structural components and fittings using various techniques, including both finite-element modeling and more specialized computational and hand analysis. This design and analysis methodology is well developed and typically produces results that are reasonably accurate and conservative. This method is based on static force balance and material properties that are rate insensitive, which is acceptable for the operating environment of most airframe structures. There are cases, however, where highly loaded fittings such as landing gear attachments have failed during testing, indicating that this static analysis approach can be "unconservative" when applied to dynamically loaded components.

Bell Helicopter Textron Inc. (Bell) was awarded a contract in March 1997 by the United States Army Aviation Applied Technology Directorate (AATD) at Fort Eustis, Virginia, to investigate the analysis and design of airframe fittings that are subjected to large loads applied at high strain rates. The goals of this Highly Loaded Airframe Fittings (HLAF) research program are aligned with the Phase 2 (2005) Rotary Wing Vehicle TDA Goals for rotocraft structures:

- Reduction in dynamically loaded structure stress prediction inaccuracy by 30%
- Reduce airframe structure weight by 15%
- Reduce airframe structure cost by 25%
- Reduce airframe structure development time by 25%

To achieve these goals, Bell undertook the following tasks:

- Development of Analytical Methodologies – Analysis and design practices for dynamically loaded fittings and systems that account for rate sensitive material behavior and internal stress wave propagation were investigated and assimilated into a comprehensive energy-based approach.
- Design and Analysis Example – The Advanced Composite Airframe Program (ACAP) tail landing gear shock strut attachment fitting was chosen as a demonstration component for the new analysis methodology. This fitting, which failed prematurely during the aircraft full scale drop test, was redesigned applying the energy-based analytic approach and lessons learned from the methodology development phase.
- Coupon Testing – Various aircraft aluminum alloys were subjected to load rates typical of aircraft crash velocities in both tension and compression to determine the effects of high strain rates on strength and stiffness properties to be used in analysis of impact loaded fittings. Also, structural coupons were tested to validate the analysis methods and conclusions.

- Full Scale Drop Test – The ACAP tail landing gear attachment fitting was subjected to a drop test designed to validate the new design and analysis methodology.

The results of this program are presented in this document, along with conclusions and recommendations for continued research and development.

2. ANALYSIS METHODOLOGY

2.1 Static vs. Dynamic Analysis

Traditionally, the internal load distribution in an airframe structure is determined using a linear static finite-element analysis (FEA) of a coarse model. While adequate for most airframe structure, this method can produce results which are inaccurate and misleading for dynamic systems subjected to high-rate loads. Some examples of high-rate loads that aircraft structure must be designed for are landing, ditching, crash, bird strike, missile launch, airbag deployment, hail impact, and tool drop.

One source of inaccuracy in typical linear static structural analysis is the neglect of secondary loads due to structural deflections. Eccentric secondary loads are often introduced as structures deform, and these effects are not predicted by a linear finite-element analysis, in which the load distribution is determined from the initial element positions. In a dynamic system such as a wheel landing gear, eccentric secondary loads due to structural deflections can lead to premature failure if ignored, as will be shown in the ACAP tail gear strut attachment fitting.

The major source of inaccuracy in utilizing linear static FEA to distribute dynamic loads is the static force balance, in which equilibrium requires that the external and internal forces and moments on the system sum to zero. Inertial forces can be included in this balance, but only in a static manner. The time-dependent change in the state of motion of the system—the acceleration—is assumed negligible. The structural deformations are assumed to have sufficient time to reach their static values. This method is sufficiently accurate for problems in which the time between the application of a force and the setting up of effective equilibrium is short compared to the duration of the force. For problems involving high-rate loads that are applied for only short periods of time or are changing rapidly, however, dynamic time-dependent equilibrium must be considered.

In a dynamic analysis, each point in the system is allowed to move and accelerate relative to adjacent points. The pointwise static and dynamic equilibrium equations are contrasted below.

Static Equilibrium: $[M]\{a\} + [K]\{u\} = \{P\}$

where $[M]$ is the mass matrix, $\{a\}$ is the static acceleration vector, $[K]$ is the stiffness matrix, $\{u\}$ is the displacement vector, and $\{P\}$ is the applied external load vector. In this equation, all vectors are static quantities, not functions of time.

Dynamic Equilibrium: $[M]\{\ddot{u}\} + [B]\{\dot{u}\} + [K]\{u\} = \{P\}$

where $\{\ddot{u}\}$ is the acceleration vector (two dots indicate the second partial derivative with respect to time), $[B]$ is the damping matrix, and $\{\dot{u}\}$ is the velocity vector (one dot indicates the first partial derivative with respect to time). In this equation, the vector

quantities, as well as the damping and stiffness matrices, are all functions of time.

Although the two equations are similar in appearance, time-dependent inertia and damping forces are the crucial difference. When loads are applied for very short periods of time, or are changing rapidly, structures do not obey static equilibrium. As an example, consider a straight bar impacted on the one end by a mass traveling at a given velocity. At the instant of impact, the contacted end experiences a distortional impulse which causes an internal force locally in the bar. This pulse proceeds to travel down the length of the bar. The force in the bar at any point away from the impacted end remains zero until the distortional pulse reaches that point. This distortional pulse is called a stress wave. Stress waves in solids travel at a fixed velocity equal to the speed of sound in the solid, which is a function of the material density and stiffness. For the stress wave to travel the length of the bar requires time. Therefore, the force at any point in the bar due to a dynamic impact is a unique function of time.

The load history from a dynamic event such as those listed above is typically very noisy, with many short duration large amplitude spikes. In a traditional airframe analysis for conditions such as these, either the applied load is idealized as a filtered average static load and the high-energy spikes are ignored, or the peak value from the highest spike in the load time history is applied. Neither approach accurately represents the applied load condition. Using a filtered average static load can be "unconservative" because the resulting fitting, if not designed carefully, may not be robust enough to withstand the short duration spikes of load exceeding the fitting static capability, as will be shown below. This is especially true if the fitting is allowed to yield and ultimate allowables are used. Using the peak load from the highest spike is grossly conservative and will result in a heavy design because, although the load value may be very high, the energy of the spike is small due to the short duration. The recommended analysis method proposed below uses an energy-based approach that avoids the pitfalls of a static design.

2.2 KRASH Hybrid FEM Analysis

An important subcase of highly loaded airframe fittings, landing gear attachment fittings have been sized in the past using loads from a hybrid nonlinear finite-element analysis that captures some of the important dynamic effects. The most prominent hybrid finite-element model (FEM) code is KRASH (Reference 1), which was initially developed under U.S. Army sponsorship and subsequently under FAA sponsorship. The most widely used public domain version is KRASH85.

KRASH hybrid modeling has the following advantages and disadvantages:

<u>Hybrid Advantages</u>

- Relatively easy model setup
- Easily allows input of measured load-deflection data for nonlinear elements
- Fast run times
- Defines critical parameters and conditions for designer

Hybrid Disadvantages

- Approximate solutions
- Not detail element oriented
- Not stress–strain oriented
- Not local behavior oriented
- Not component design oriented

Measured data is used for the nonlinear characteristics of the crash energy-attenuating (EA) component and input directly into the KRASH code. These data are usually in the form of load-deflection data obtained from static crush tests. When a rate sensitive EA component is used, dynamic drop tests are performed to obtain the load-deflection data with approximately the proper loading rate. The assumption heretofore has been that using this hybrid test-analysis procedure improves the integrity of KRASH analyses by ensuring accurate generalization of the EA device.

Typically, even though the landing gear fitting loads were developed using a nonlinear dynamic model such as KRASH, the fittings were still sized using linear static finite-element analysis, so the effects of stress waves in the fitting were not accounted for. The demonstration component chosen for this research program, the ACAP tail gear strut support fitting, is a good example of the shortcomings of this traditional approach.

Although the landing gear assembly was included in the airframe KRASH model, the shock strut upper attachment fitting was sized to withstand the stroking load of the shock strut tube cutter, applied statically. The tube cutter dynamic test results, including load stroke curves, for the original ACAP program are shown in Figure 2-1. The fitting was shown to have adequate margins of safety for this load. Because stroking of the tube cutter only occurs in a crash condition, no ultimate load factor was applied. The premature fitting failure indicates that one or more significant effects were overlooked in the conventional stress analysis of this part, as explained in the following sections.

2.3 Dynamic Fitting Loads

An important effect that was not considered in the original analysis is secondary bending of the fitting due to lateral deflection of the landing gear. The MIL-STD-1290 requirement for a 42 ft/s crash includes 10 degrees of aircraft pitch and roll. Because the upper shock strut attachment incorporates a spherical bearing, no lateral load on the attachment fitting was considered. The 10-degree aircraft roll will cause lateral structural deflection of the trailing arm, however. Because the lower end of the shock strut attaches to the trailing arm, some lateral rotation of the shock strut is inevitable, which causes an eccentric load on the upper attachment fitting. The upper fitting is very soft laterally, so the small eccentric load can produce relatively large lateral deflection of the attachment lug. This causes additional rotation of the shock strut, which in turn magnifies the eccentric load. This progression, shown schematically in Figures 2-2 and 2-3, could have directly contributed to the premature failure of the ACAP fitting.

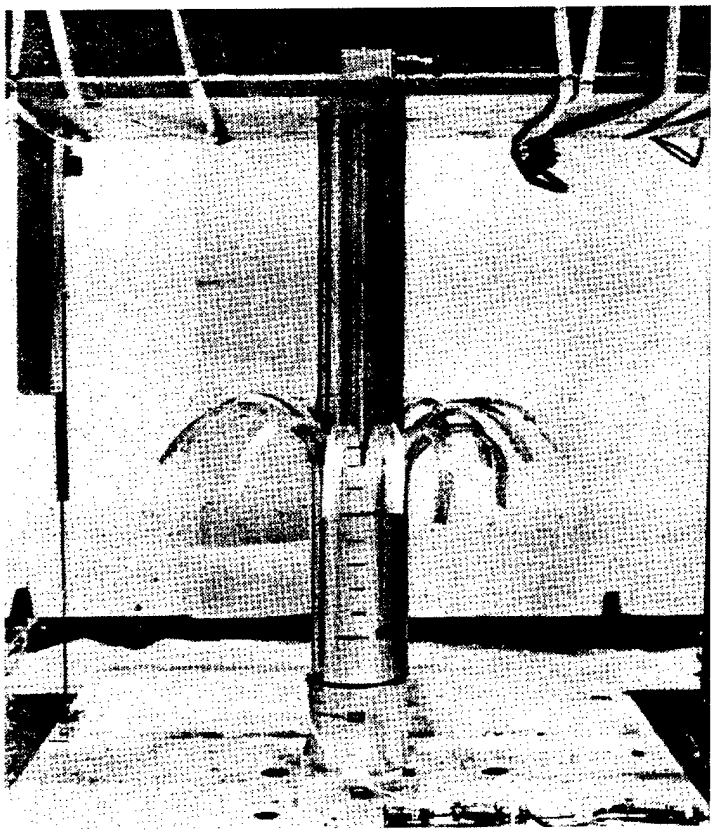

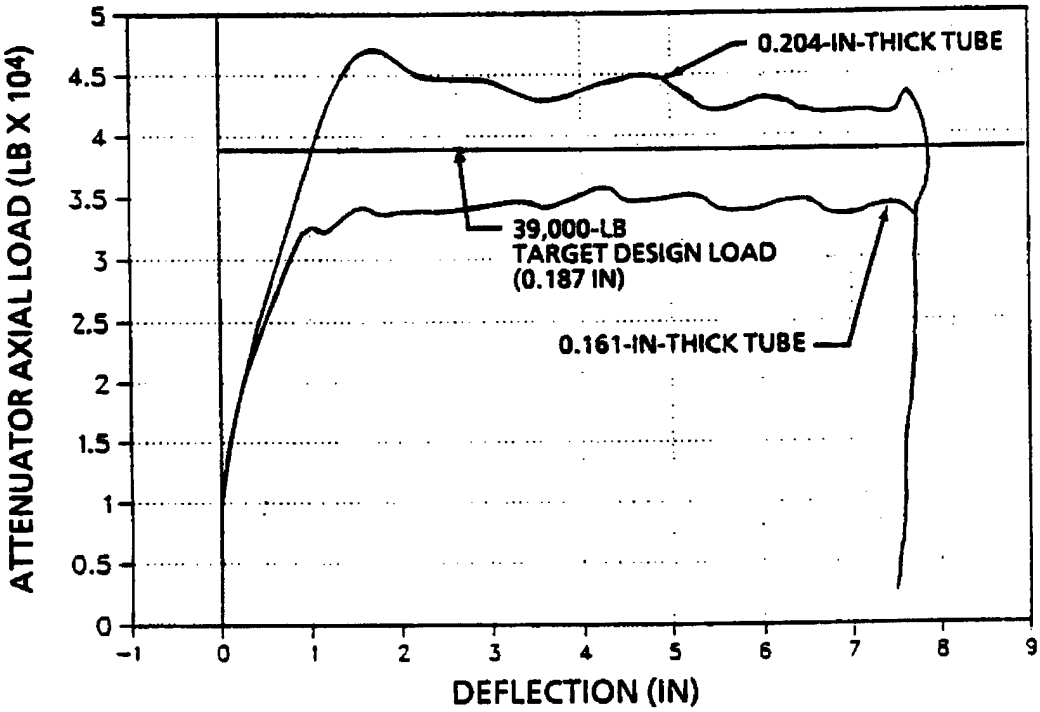

Figure 2-1. Aluminum tube cutter dynamic test results

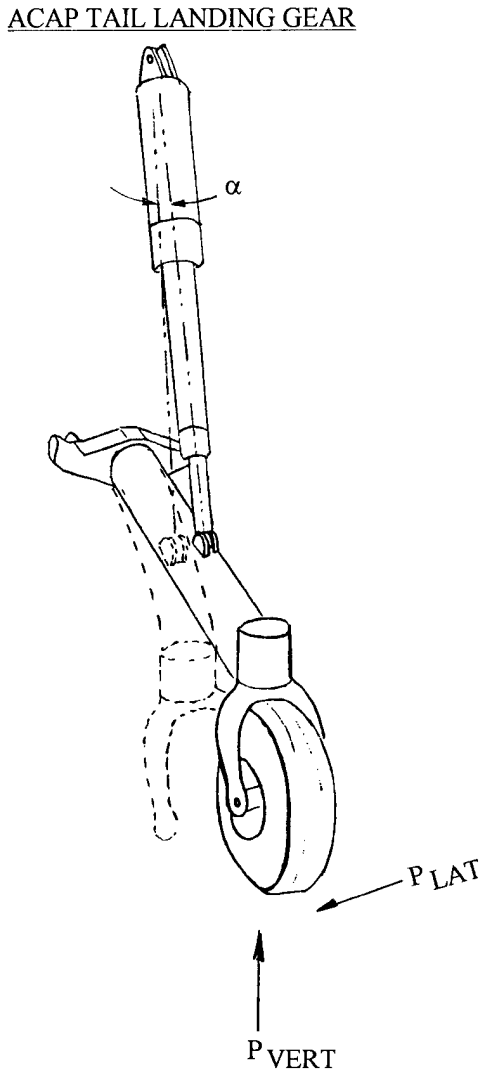

Figure 2-2. Lateral deflection of trailing arm and strut due to rolled landing loads

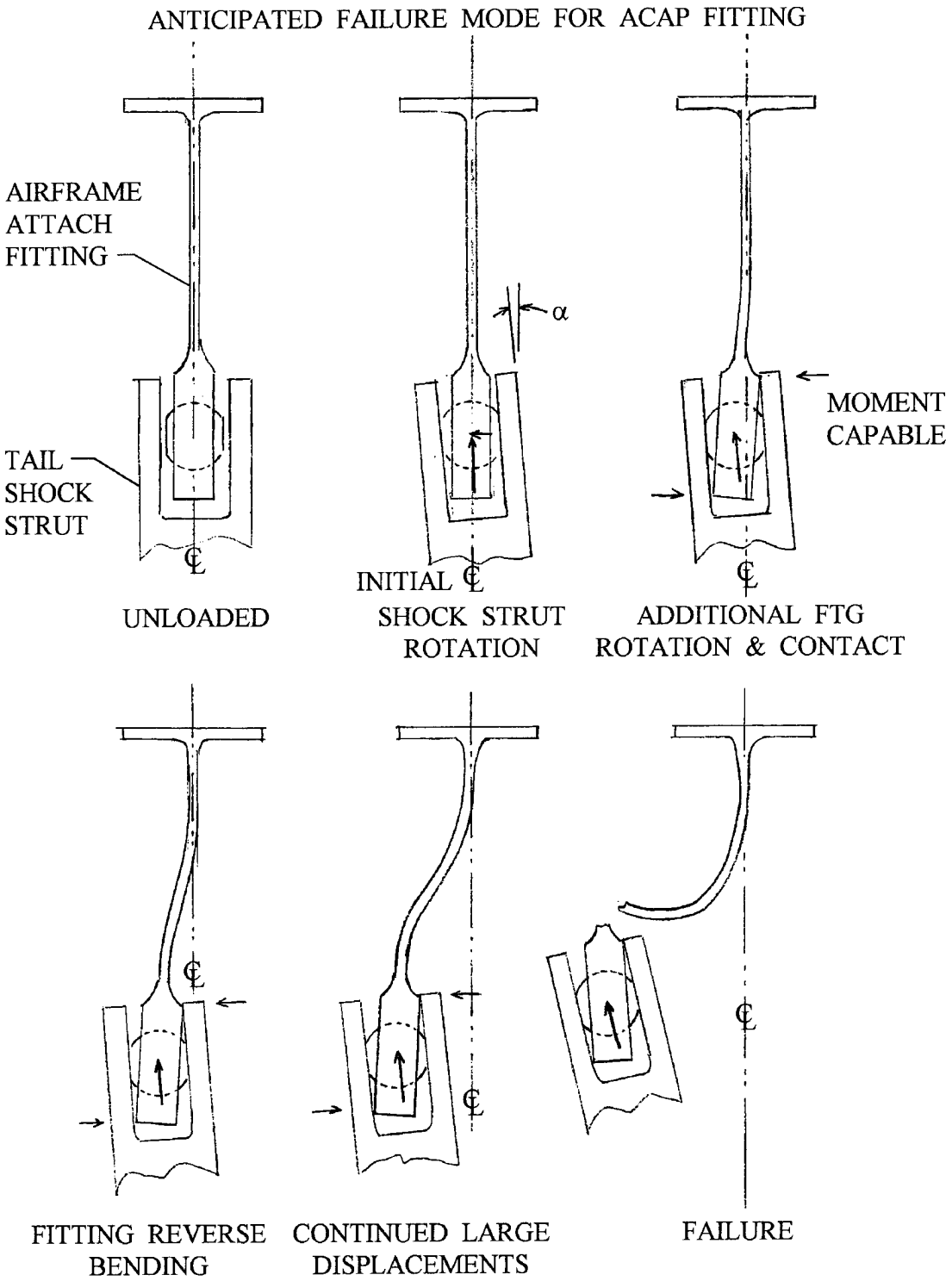

Figure 2-3. Detail of strut clevis attachment showing progressive bending and failure of the attachment fitting lug

The time-dependent nature of the applied load was also not considered in the original analysis. The tube cutter load stroke curve in Figure 2-1, used to size the fitting, is obviously filtered data. The real load stroke curve would show considerably more noise, with large short-duration spikes. This characteristic of dynamic behavior is called ringing, and is a result of the reflection and interference of distortional and dilatational stress waves in the solid. Some of these spikes can exceed the filtered maximum load by a significant amount. An example of a filtered and unfiltered stress time history is shown in Figure 2-4.

Unfortunately, the actual unfiltered response of the tube cutter device is not available, due to the strain sampling rate of the original tests. The predicted response of our simplified tube cutter numerical simulation, discussed in the following section, is probably a more realistic representation of the actual response. The predicted load stroke response of the tube cutter is shown in Figure 2-5. For comparison, both the raw data and the filtered curve are shown. A 100-Hz, 8-pole Butterworth filter that complies with the SAE J211 specification for a Class 60 Channel was used for this curve.

Another loading effect which was ignored in the original fitting design is the modification of the tube cutter load due to the dynamic behavior of the landing gear system. The installed load stroke response of the tube cutter is different from the uniaxial test response for two reasons: (1) vibration of the attached trailing arm due to the high-rate crash load is transmitted directly into the shock strut, and (2) rotation of the shock strut as it strokes is resisted by the fairly substantial inertia of the strut, which results in bending of the strut that effects the stress wave propagation through the strut. The installed load stroke response of the shock strut tube cutter is shown in Figure 2-6, along with the idealized load stroke response like the one assumed in the original KRASH analysis for the 0.161 inch thick tube.

2.4 Dynamic Fitting Response

Equally important as the simplified static representation of the applied load is the assumed static response of the support fitting. Under static or low-rate loading, elastic and plastic local deformations redistribute internal stresses and relieve local stress concentrations. For this reason, local stress concentrations are usually ignored in static ultimate stress analysis. Under high-rate dynamic loading, however, there is insufficient time for this load redistribution to occur. As a result, the applied energy tends to focus in areas of high stress concentration. If a highly loaded airframe fitting is not designed with this effect in mind, an unexpected failure is likely to occur.

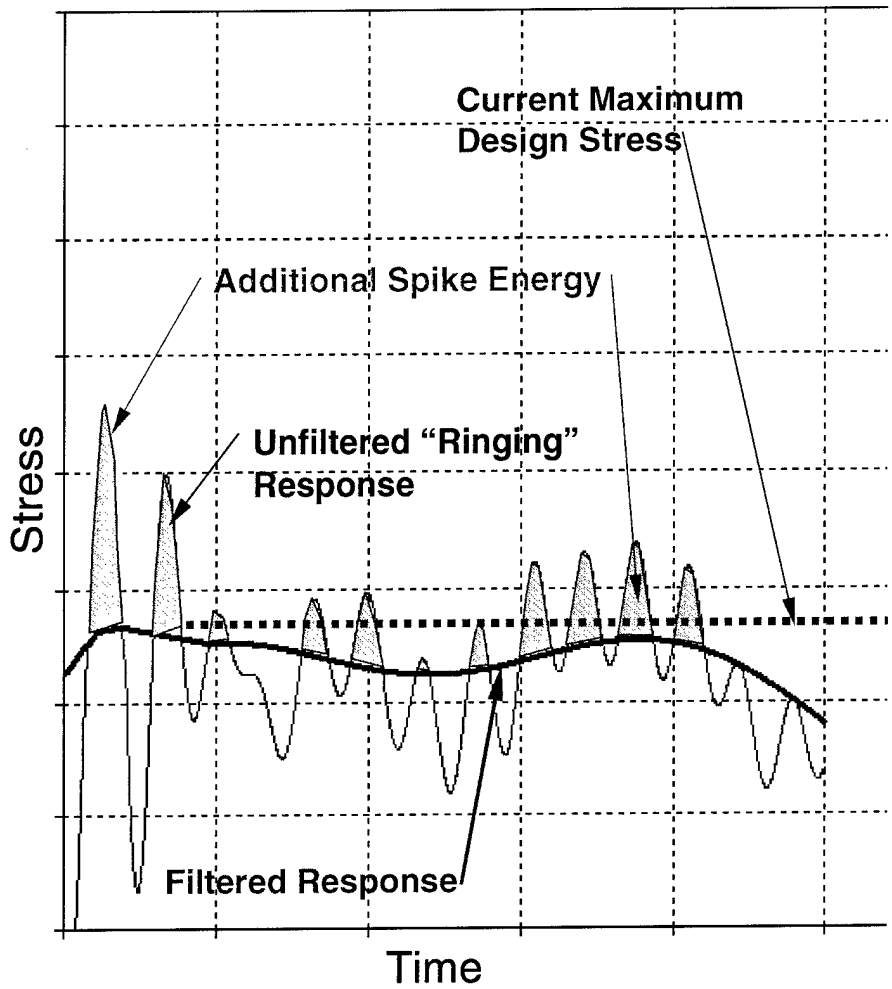

Figure 2-4. Sample stress/time response showing effects of data filtering

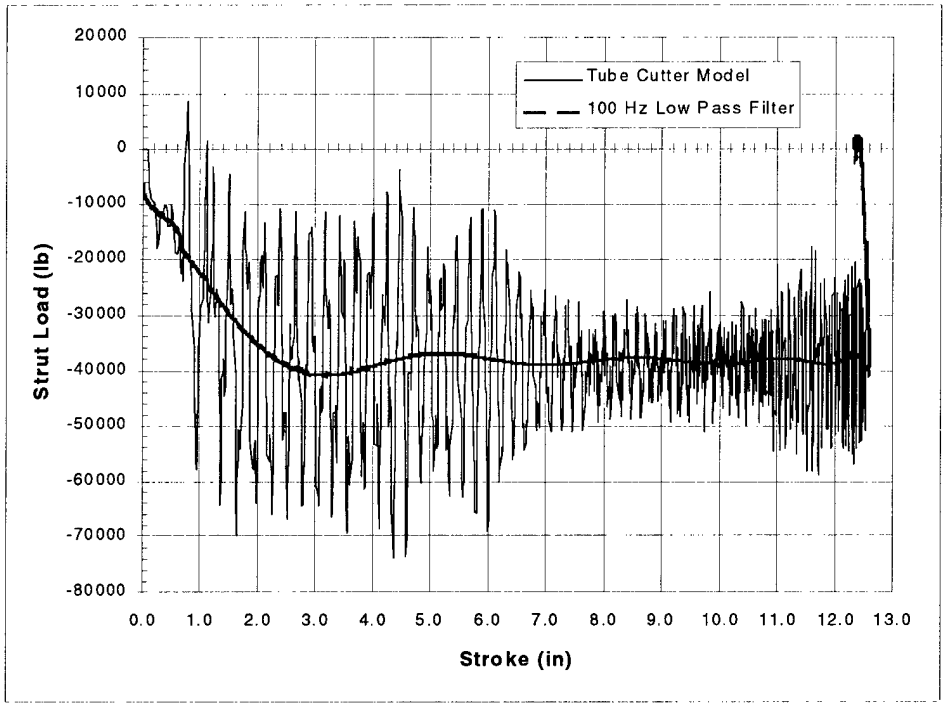

Figure 2-5. Uninstalled load stroke response of tube cutter MSC/DYTRAN™ model

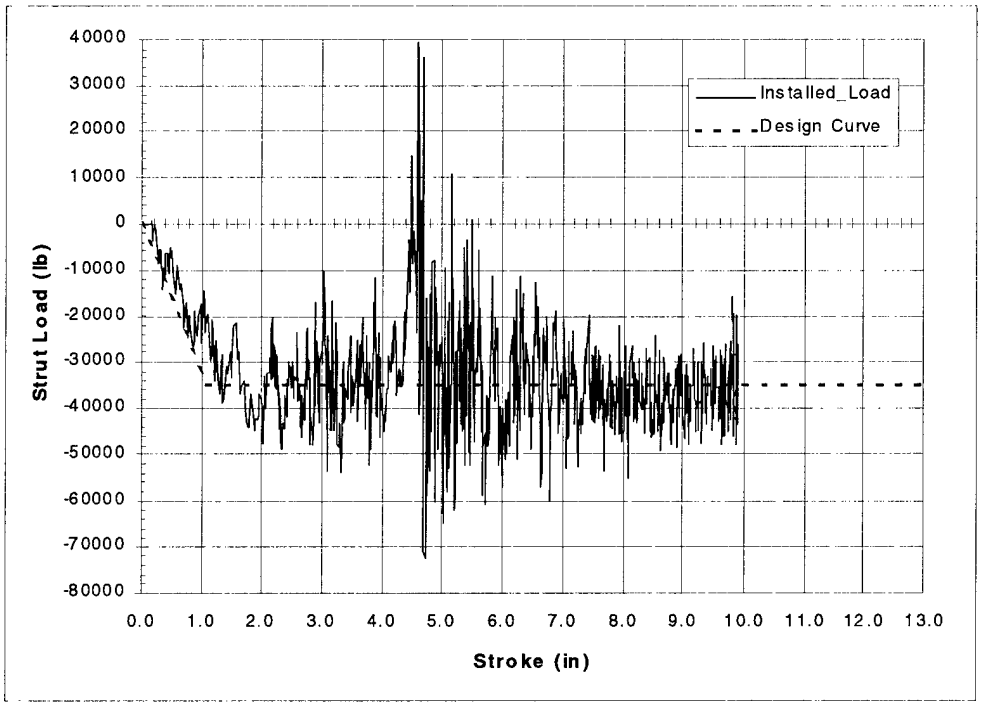

Figure 2-6. Installed load stroke response of tube cutter MSC/DYTRAN™ model

A familiar example illustrating this effect is the bolt designed for impact loading shown in Figure 2-7. In this bolt, the diameter of the shank is less than the root diameter of the threads. Statically, this bolt is weaker than a straight shanked bolt because the minimum cross section area has been reduced. The impact energy absorbing capability of this bolt has been dramatically improved, however, as shown in Figure 2-8. A traditional straight coarse thread bolt has a root area to shank area ratio of 0.64. With this ratio adjusted to 1.2 by a reduction in shank area, the impact energy absorbed by the bolt increases by 90%. The reason that the shank area reduction improves impact performance of the bolt is that the volume of material exposed to the maximum stress level is substantially increased. Under high-rate loading, energy focuses on the minimum area. Increasing the volume of material in the minimum area region of the bolt results in increased energy absorbing capability. A traditional straight bolt has only the small volume of material under the root of the first loaded thread subjected to the maximum stress, so only a small amount of energy input is required to fracture this material. This effect is critical in the design of a highly loaded aircraft fitting, and is further illustrated in the theoretical examples in Section 2.7.

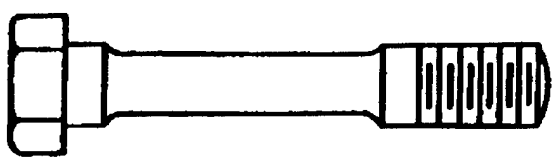

Figure 2-7. Bolt designed for impact loading

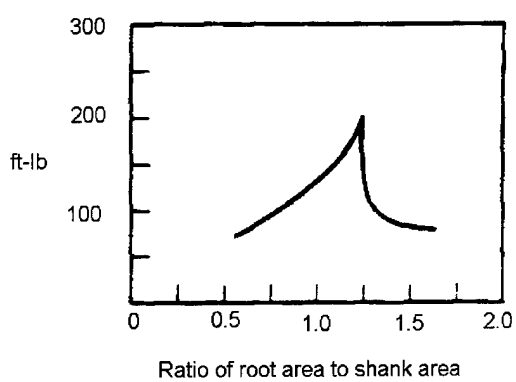

Figure 2-8. Impact energy required to fracture a 3 inch long, 3/8 – 16, SAE 1018, cold forged bolt of which the shank area has been reduced by turning

2.5 MSC/DYTRAN™ Explicit FEM Analysis

High-energy dynamic events in which stress wave phenomena are important are most efficiently solved using an explicit finite-element program such as MSC/DYTRAN™ (Reference 2) or LS/DYNA®. These commercially available codes use an explicit time step integration scheme to solve dynamic transient problems with significant geometric and material nonlinearity. Analysis time steps are sufficiently small to capture stress wave effects in the structure. These explicit codes have several advantages over traditional implicit finite-element solvers. Because no matrix inversion is required in the explicit algorithm, the solution of highly nonlinear problems is much more numerically stable than a traditional implicit scheme. For models with many degrees of freedom, the explicit solution requires less time to solve. Also, both Lagrangian (solid) and Eulerian (fluid) problems can be solved, as well as hybrid problems in which solids and fluids interact. Finally, the explicit dynamic transient finite-element codes include excellent contact solutions, including modeling of impact and friction between parts. For this research program, MSC/DYTRAN™ was selected as the primary dynamic simulation tool.

2.6 Analysis and Design Procedure

For the design and analysis of aircraft systems subjected to dynamic loading conditions, a building block approach focusing on the energy to be absorbed is recommended. An overview of this approach is shown in Figure 2-9. The first step in the design of such a system is to quantify the input energy, which is a combination of the total potential plus kinetic energy of the system. Next, the primary energy-attenuating (EA) components of the system must be identified. In the case of a landing gear assembly subjected to crash loads, the primary EA device would typically be a tube cutter or composite crush tube shock strut.

The characteristic behavior of each primary EA device must be determined through component testing and correlated with a representative component finite-element model. The EA component test results and representative finite-element models should be maintained, so that for future designs with similar requirements the amount of development testing and analysis may be reduced. The component testing of EA devices should be performed with simple calibrated boundary conditions, so that the amount of energy that is not absorbed by the device itself but is instead transmitted to the surrounding fittings can be measured. In order to withstand the high magnitude short duration load spikes that are typical of any high-energy structural response, system components other than the primary EA devices should also be capable of some energy absorbtion. The calibrated boundary conditions should provide a means to estimate the magnitude of this overshoot energy. Highly loaded airframe fittings that support landing gear shock struts are examples of components that are subjected to dynamic overshoot energy.

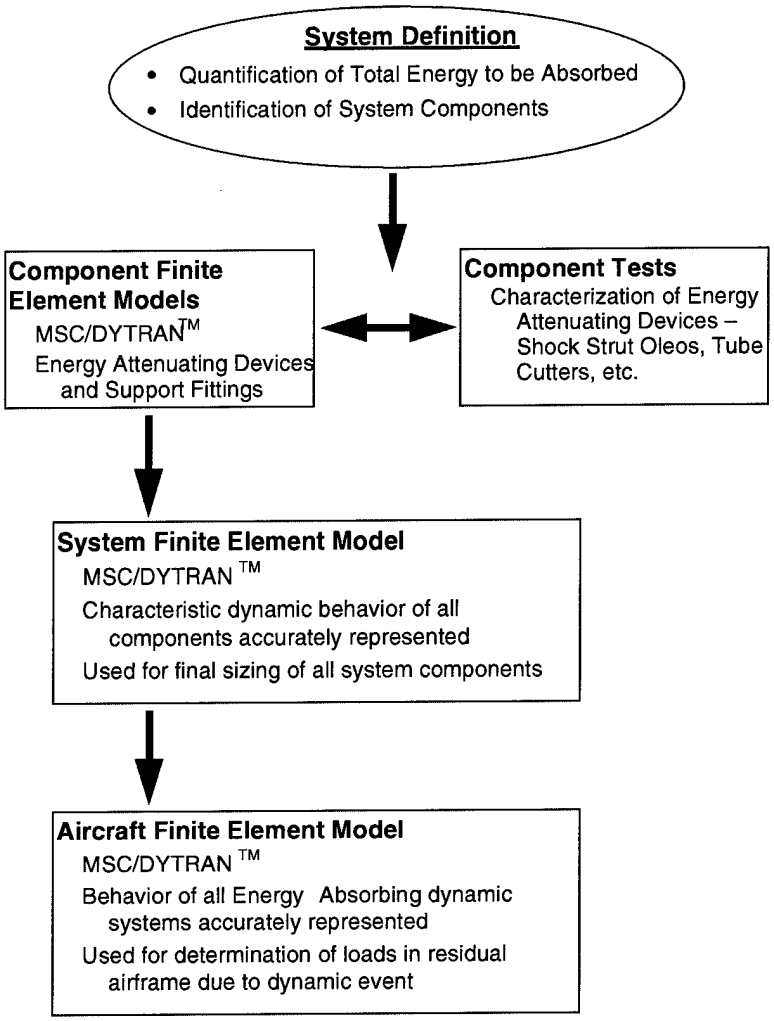

Figure 2-9. Overview of Building Block Approach to Dynamic System Analysis

The representative component models are assembled into a global system model, in which the energy absorbing characteristics of each system component are represented. This system model contains a finite-element representation of each system component, and is used for the final sizing of all components, including those which primarily store energy elastically. Highly loaded attachment fittings usually remain elastic throughout most of their volume, only dissipating energy at discrete zones of plastic flow. The success of the EA devices and other system components at absorbing the applied energy and surviving the dynamic event can be evaluated using the global system model. A simplified representative finite-element model of the system can then be integrated into the dynamic model of the entire airframe for analysis of the residual aircraft structure for loads imparted during the dynamic event.

Figure 2-10 shows a more detailed flow chart of the recommended analysis and design procedure for dynamic energy-absorbing systems.

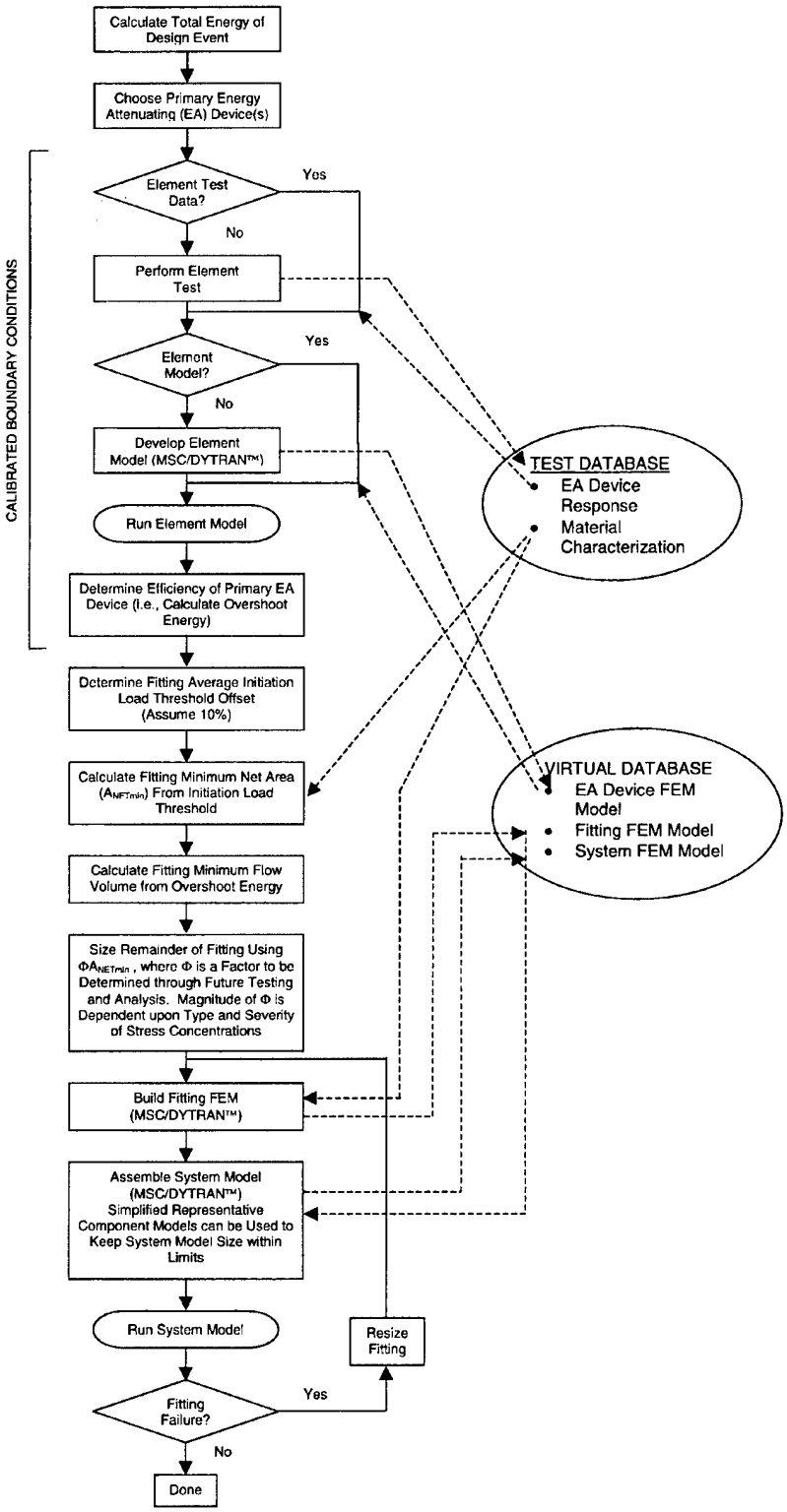

Figure 2-10. Design and analysis procedure for highly loaded airframe fittings

In the future, analysis of dynamically loaded components could be integrated into a larger plan for a comprehensive airframe analysis model. This global airframe simulation tool would unify the airframe loads, dynamics, and stress analysis models into a global database that allows isolation of components for detail analysis, but retains the proper boundary conditions of the residual airframe using generalized elements. This comprehensive solution, which would dramatically increase the accuracy and decrease the conservatism of detail part stress and dynamic analysis, is possible using the commercial tools already in use by the analysis community. This integrated approach, shown schematically in Figure 2-11, would require the development of an automated framework to integrate models from various simulation tools into a single database, here called the Finite-element Aircraft Mockup, or FEAMU.

2.7 Theoretical Impact Examples

To gain confidence in the MSC/DYTRAN™ solution, the response of a simple elastic bar subjected to an impact load on one end and supported on the other end was studied. The bar, shown schematically in Figure 2-12, has the following properties:

Cross Sectional Area	$A = 0.200\ \text{in}^2$
Elastic Modulus	$E = 10.5$ Msi
Yield Stress	$F_{cy} = 70$ ksi
Material Density	$\rho = 0.101\ \text{lb/in}^3 = 0.000262\ \text{lb}\cdot\text{s}^2/\text{in}^4$
Bar Length	$L = 6.00$ in

The impactor is assumed rigid, and has the following properties:

Impactor Weight	$W = 1.2$ lb
Impactor Mass	$m = 0.00311\ \text{lb}\cdot\text{s}^2/\text{in}$
Impact Velocity	$v_0 = 20\ \text{ft/s} = 240\ \text{in/s}$
Impact Energy	$E = \frac{1}{2}\, m\, v_0^2 = 89.6\ \text{in}\cdot\text{lb}$

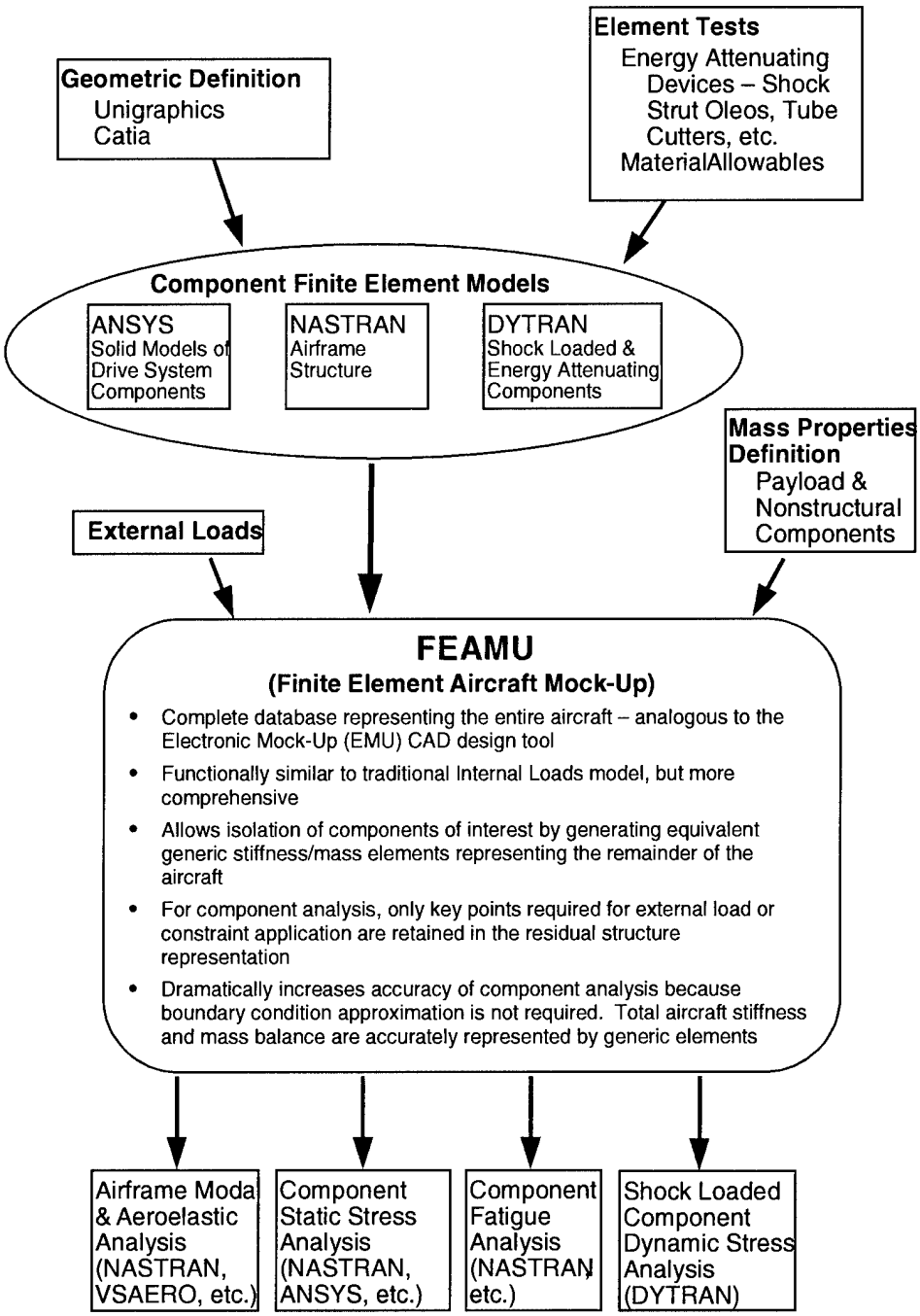

Figure 2-11. Integrated Virtual Airframe Analysis Tool

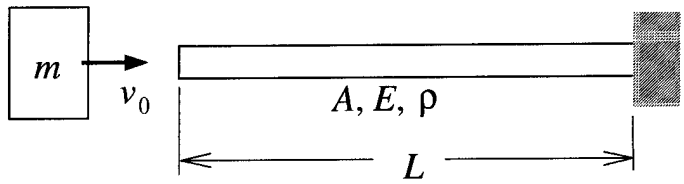

Figure 2-12. Straight elastic bar subjected to impact load

When the bar is first impacted, the initial stress wave begins to travel along the length from the impacted end to the support. From simple one dimensional elasticity, the magnitude of the initial pulse is given by

$$P_{\text{pulse}} = A\,v_0\sqrt{E\rho} = 2{,}500 \text{ lb}$$

The initial pulse travels along the length of the bar with a fixed velocity equal to the speed of sound in the solid, which is in this case

$$c = \sqrt{E/\rho} = 200{,}322 \text{ in/s}$$

Therefore, the time required for the pulse to traverse the bar is

$$t = \frac{L}{c} = 0.03 \text{ ms}$$

When the stress wave pulse reaches the fixed boundary, it is reflected as a compressive stress wave traveling back towards the impactor. Because the initial pulse did not impart the entire impact energy to the bar, the impactor is still moving forward. Therefore, a secondary compressive pulse is initiated with a slightly lower magnitude than the initial pulse because the velocity of the impactor is slightly reduced. This secondary pulse adds directly to the reflected initial pulse. This process continues with the addition of ever-diminishing pulse magnitudes until all the impact energy has been absorbed. From conservation of energy, the magnitude of the peak load in the bar is

$$P_{\text{MAX}} = \sqrt{\frac{E\,A\,m}{L}} \times v_0 = 7{,}900 \text{ lb}$$

Figure 2-13 shows the predicted response of the elastic straight bar using a simple MSC/DYTRAN™ model. As shown in the figure, the correlation of theoretical calculations with the MSC/DYTRAN™ predictions is very good.

Another simple illustrative example is a study of the effects of bar shape on impact energy absorbing capability. The capability of the straight bar from the above example is contrasted with the capability of a "dogbone" shaped bar, with equivalent throat area but thicker on each end. The two bars are shown in Figure 2-14. Because the minimum areas of each bar are equal, the static strengths are equivalent.

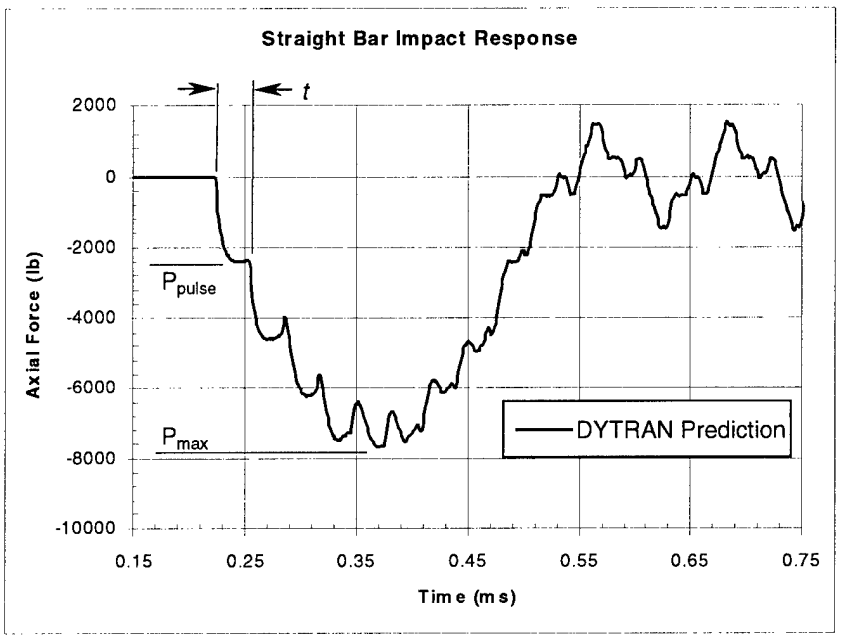

Figure 2-13. Impact response of straight elastic bar

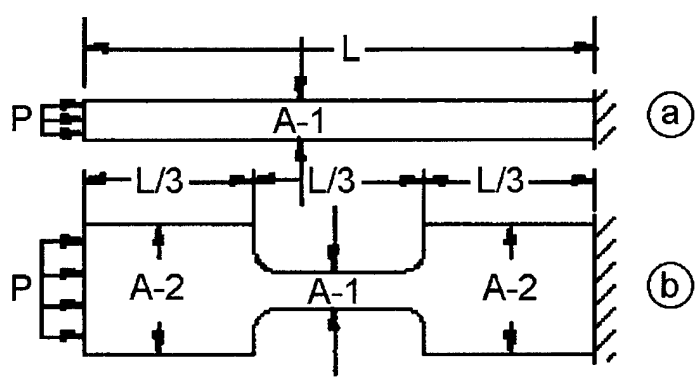

Figure 2-14. Two impacted bars with equal static strength

For this simple example, stress concentration effects and material damping are neglected. Therefore, the maximum static load that each bar can carry elastically is

$$P = A_1 \cdot F_{cy}$$

The impact energy required to yield the two bars is calculated using conservation of energy. The kinetic impact energy, T, is stored in the bar as potential energy, U. If K is the spring rate of the bar, χ is the elongation, ε is the strain, and E_c is the compressive modulus of the material, then

$$T = U$$

$$T = \frac{1}{2} \cdot K \cdot \chi^2$$

For bar "a":

$$T_a = \frac{1}{2}\left(\frac{A_1 E_c}{L}\right)(\varepsilon \cdot L)^2$$

$$T_a = \frac{A_1 E_c L}{2} \cdot \left(\frac{F_{cy}}{E_c}\right)^2$$

$$\boxed{T_a = \frac{A_1 L}{2E_c} \cdot F_{cy}^2}$$

For bar "b":

$$\varepsilon_1 = \frac{3 \cdot \chi_1}{L}$$

$$\varepsilon_2 = \frac{3 \cdot \chi_2}{2L}$$

$$\sigma_1 = E_c \cdot \varepsilon_1 = E_c\left(\frac{3 \cdot \chi_1}{L}\right)$$

$$\sigma_2 = E_c \cdot \varepsilon_2 = E_c\left(\frac{3 \cdot \chi_2}{L}\right)$$

$$\chi_1 = \frac{\sigma_1 L}{3E_c}$$

$$\chi_2 = \frac{\sigma_2 L}{3E_c}$$

$$T_b = \frac{1}{2} K_1 \cdot \chi_1^2 + 2\left(\frac{1}{2} K_2 \cdot \chi_2^2\right)$$

$$T_b = \frac{3A_1 E_c}{2L} \cdot \left(\frac{\sigma_1 L}{3E_c}\right)^2 + \frac{3A_2 E_c}{L} \cdot \left(\frac{\sigma_2 L}{3E_c}\right)^2$$

At the point of yielding:

$$\sigma_1 = F_{cy} = \frac{P}{A_1} => P = A_1 \cdot F_{cy}$$

and

$$\sigma_2 = \frac{P}{A_2} = \frac{A_1}{A_2} \cdot F_{cy}$$

thus

$$T_b = \frac{A_1 L}{6E} \cdot F_{cy}^2 + \frac{A_2 L}{3E}\left(\frac{A_1}{A_2} \cdot F_{cy}\right)^2$$

$$T_b = \left(\frac{1}{3} \cdot \frac{2}{3} \cdot \frac{A_1}{A_2}\right)\frac{A_1 L}{2E_c} \cdot F_{cy}^2$$

If $$\frac{A_1}{A_2} = \frac{0.4375 \cdot 0.375}{1.500 \cdot 0.375} = 0.292$$

then

$$\boxed{\frac{T_a}{T_b} = \frac{\left(\frac{0.164 \times 6.00}{2 \times 10.6 \times 10^6}\right)\left(70 \times 10^3\right)^2}{\left(\frac{1}{3} + \frac{2}{3} \times 0.292\right)\left(\frac{0.164 \times 6.00}{2 \times 10.6 \times 10^6}\right)\left(70 \times 10^3\right)^2} = 1.894}$$

Therefore, bar "a" can absorb 89.4% more energy than bar "b" can absorb prior to yielding.

After the necked-down region of the dogbone bar yields, the stiffness of this region decreases dramatically and plastic deformation locally accelerates. This softening prevents the material in the larger area zones at either end of the bar from ever reaching yield. In contrast, the constant section bar is a much more effective energy absorber because the entire bar yields at once, and plastic flow occurs uniformly. This example illustrates how impact energy tends to focus on the minimum cross section zoned of a fitting, limiting the effectiveness of material outside this zone for absorbing impact energy.

This page intentionally left blank.

3. APPLICATION EXAMPLE: ACAP TAIL GEAR STRUT ATTACHMENT FITTING

3.1 Existing Design

The ACAP tail landing gear shock strut upper attachment fitting was selected as an ideal component to demonstrate the energy-based analysis approach proposed in Section 2. The ACAP flight test vehicle is shown in Figure 3-1. The ACAP main and tail landing gear, shown in Figure 3-2, along with elements of the seat support and fuselage structure, are designed to absorb the energy from a MIL-STD-1290 42 ft/s crash. The tail gear consists of a trunnion mounted trailing arm and an oleo shock strut with a tube cutter energy attenuator. The upper end of the tail gear shock strut is supported by an aluminum fitting attached to the fuselage aft bulkhead. This fitting, shown in Figure 3-3 and shown as installed in Figure 3-4, failed prematurely during the aircraft drop test. The failed fitting is shown in Figure 3-5. Pretest analysis indicated that the tail gear shock strut tube cutter would stroke 11.9 inches, absorbing 50% of the crash energy. Due to the premature fitting failure, the tube cutter did not stroke at all, as shown in Figure 3-6.

3.2 Fitting Redesign

The premature failure of the original fitting during the aircraft drop test proved the inadequacy of the existing design. For this research project, a new strut upper attachment was designed utilizing the lessons learned during the analytical development phase of the project, listed below.

- Under dynamic loading conditions, the applied energy is focused on the weakest part of a structure, typically the minimum cross sectional area, until that part fails.
- Stress concentrations outside of the minimum area region have little effect on the energy absorbing capability of a fitting.
- Increasing the volume of material in the minimum area region of a fitting dramatically improves its energy absorbing capability.
- Simplification of load paths is important so that the weakest link in a structure can be more easily identified.
- Robust fittings should be capable of withstanding repeated short duration load spikes beyond their static capability.

Figure 3-1. Bell's ACAP flight test vehicle

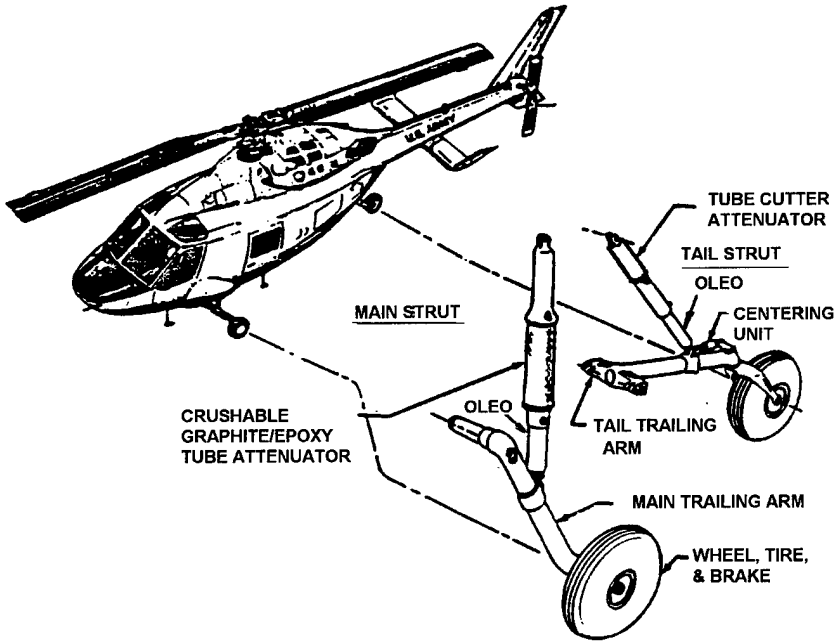

Figure 3-2. ACAP landing gear configuration

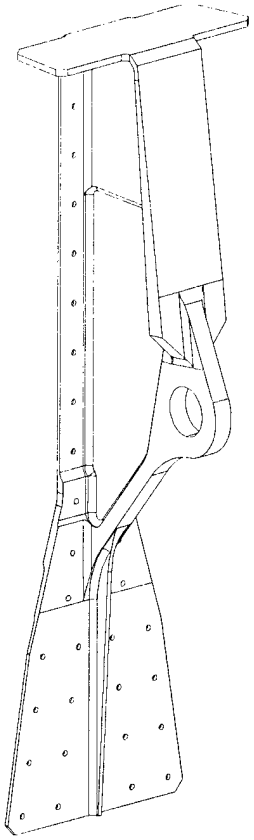

Figure 3-3. Isometric view of ACAP upper strut attachment fitting

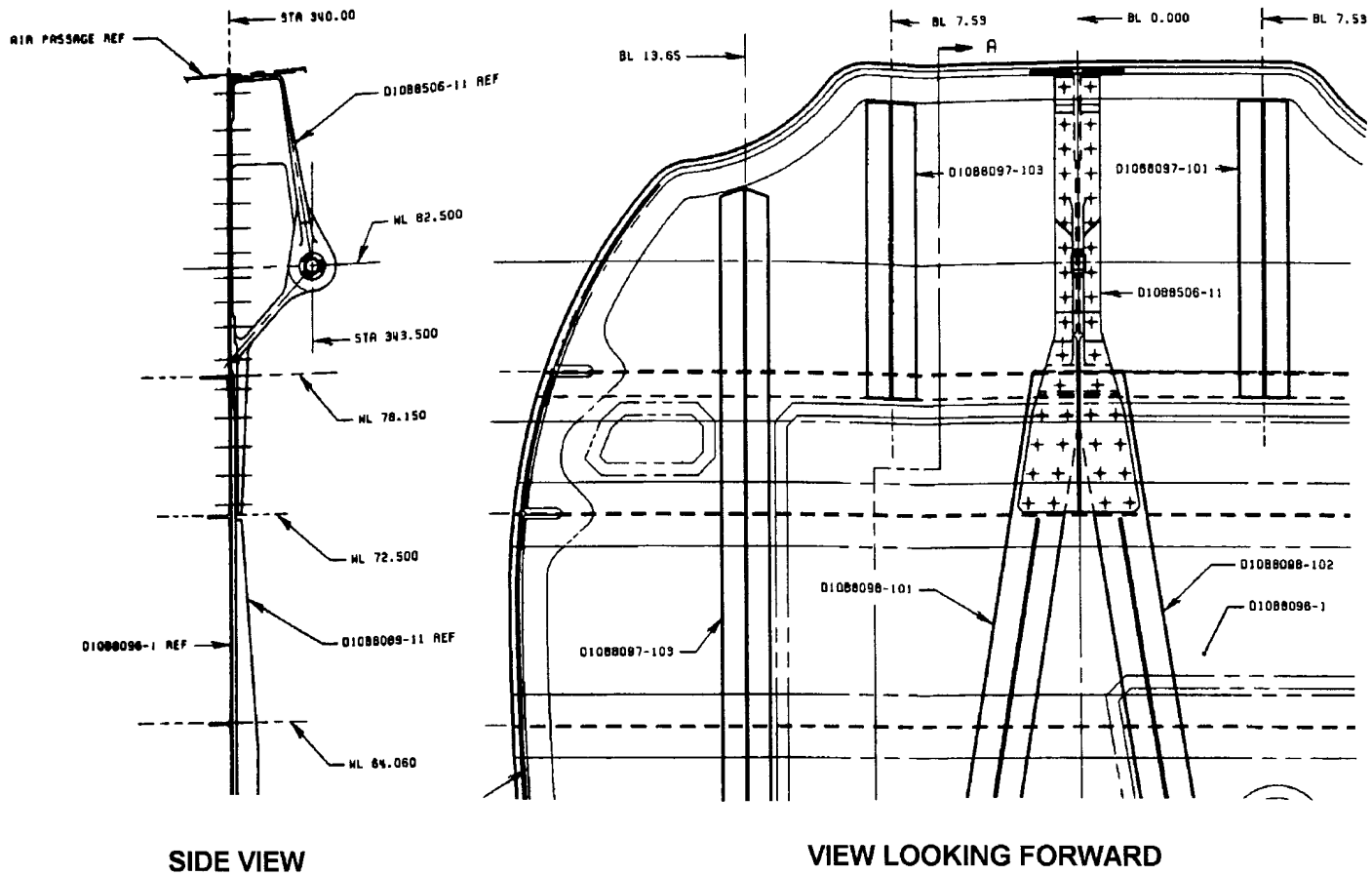

Figure 3-4. ACAP tail gear upper shock strut attachment fitting installation

Figure 3-5. Failed tail gear strut upper attachment fitting after aircraft drop test

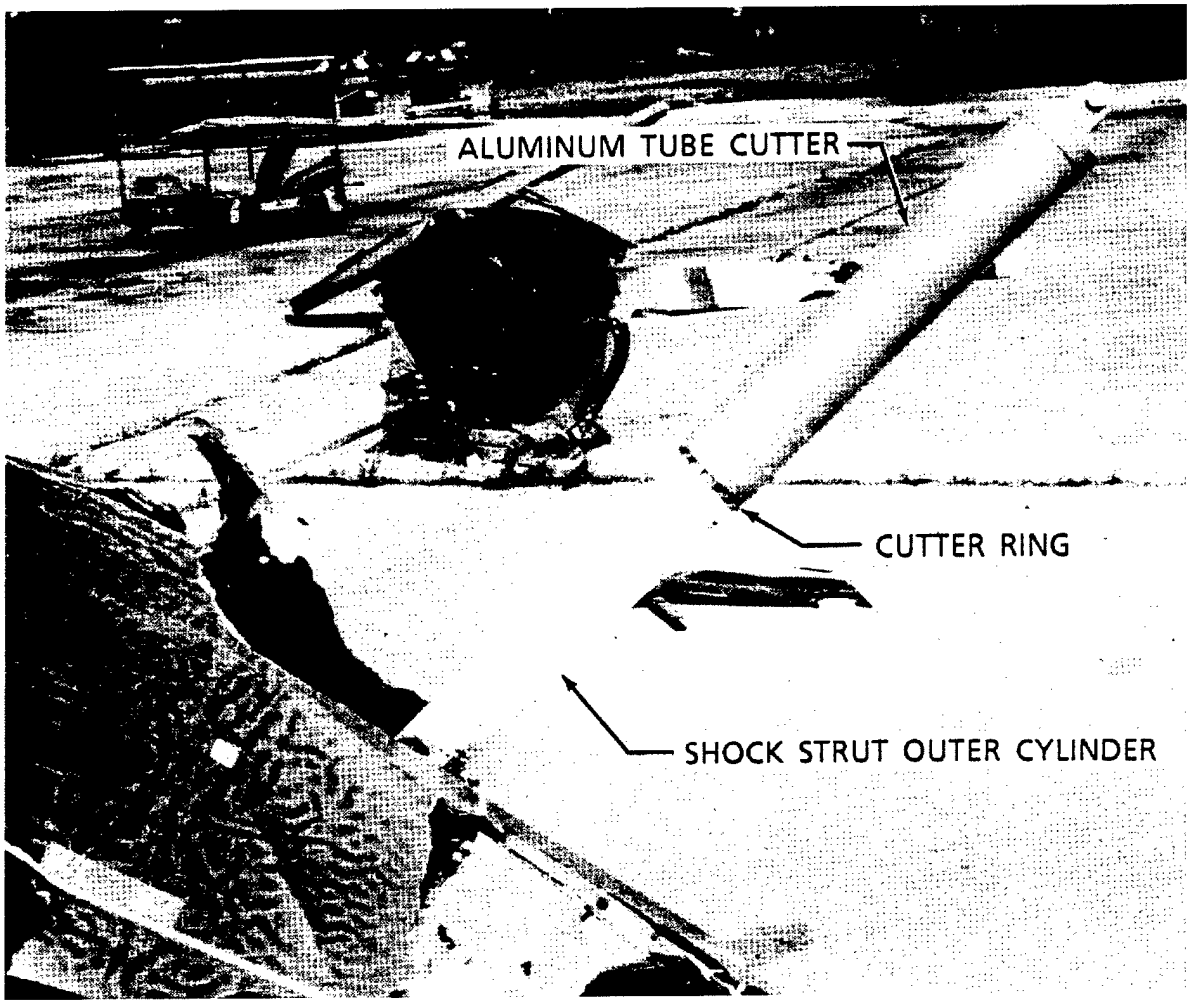

Figure 3-6. ACAP tail gear shock strut and tube cutter after aircraft drop test

The redesigned joint, shown in Figure 3-7, is a radical departure from the existing design. The clevis on the end of the shock strut is replaced by a large radius bearing pad, which seats into the bend of a laminated 7075-T6 strap composed of three sheets, each 0.100 inch thick. This strap carries the primary landing and crash loads from the shock strut as tension. The laminated design prevents large bending stresses due to structural deflections, because the three sheets are not attached to each other except at the ends, where they are bolted to the aircraft bulkheads. The interfaces between straps are lubricated, to ensure the laminated strap effectively acts as a leaf spring due to the lack of shear continuity through the thickness. When a single-layer strap design was attempted, analysis predicted premature failure due to bending around the strut head as the strap stretched. Thickening the strap made the bending problem worse, so a laminated "leaf spring" approach was a design improvement. The imbalance in the strap load due to strut angles other than 45 degrees is reacted by a separate machined 7050-T7451 compression link. Bending in the joint due to eccentricity of the applied load is effectively eliminated by separating the tensile and compressive load paths, resulting in increased fitting efficiency in reacting dynamic loads.

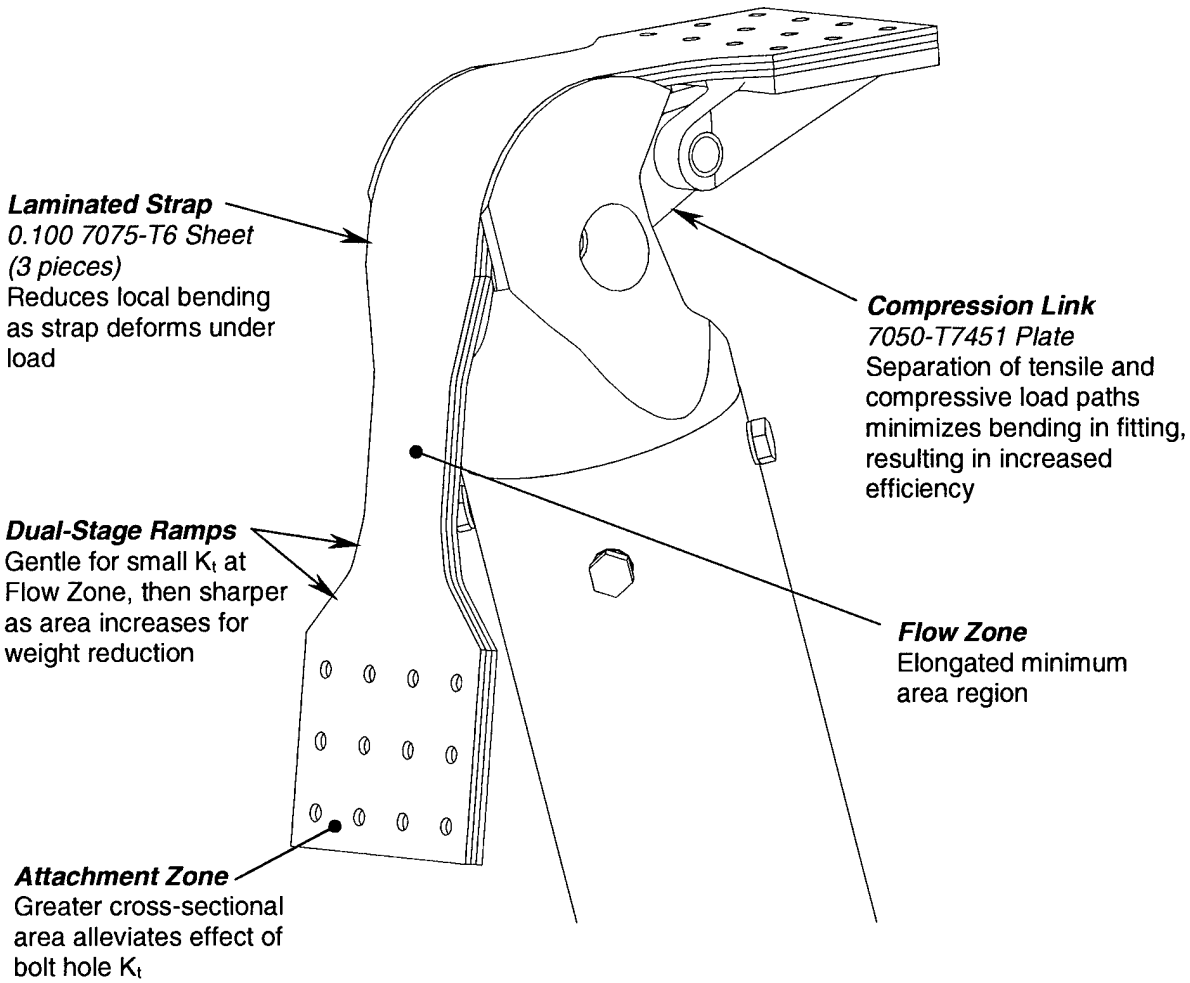

Figure 3-7. Features of the new shock strut attachment design (see Figure 3-8 for orientation)

The laminated strap incorporates a necked-down flow zone, an elongated minimum area region to absorb the excess energy from transient load spikes above the static capability of the fitting. The strap width transitions from the minimum width region to the wider attachment zone using a dual stage ramp. The initial ramp angle from the narrow region is 15 degrees, to minimize the stress concentration in the minimum area region. The ramp transitions to 45 degrees as the strap width increases to minimize the length of the transition region and thereby save weight. This design is validated through an analytical coupon study described in Section 4. The attachment zone on each end of the strap through which all in-plane loads are sheared into the adjacent bulkheads is much wider than the flow zone. The greater cross sectional area alleviates the effects of the bolt hole stress concentrations.

Material selection for the new strap fitting was critical. Various aluminum alloys were investigated, including 7050-T7451, 7055-T7751, and 7075T6/T651 (depending on thickness). Important material characteristics for a highly loaded fitting are high yield and ultimate strengths, high elongation, and high hardening modulus. These properties are compared in Table 3-1. The properties shown are static values rather than high-rate test results as shown in Section 4, because the predicted strain rate of the installed strap fitting is an order of magnitude less than that of the Hopkinson Bar tests. Also, the high-rate tests indicated that the use of static properties in a dynamic analysis for these alloys is conservative.

High yield and ultimate strengths are important to prevent plastic flow or material failure from initiating too early during a dynamic event. High elongation provides increased capability for absorbing transient energy spikes prior to failure. A higher hardening modulus allows a plastic flow zone to converge and stabilize once flow has initiated. If a material does not significantly harden, there is little resistance to increased plastic flow as the dynamic loading event continues and the material rapidly reaches the elongation limit. The 7055-T7751 alloy initially appeared superior due to the high yield and ultimate strengths, but the drop test analytical model proved that a 7055-T7751 fitting does not sufficiently harden to provide a stable plastic flow zone. 7050-T7451 plate was eliminated for the primary strap fitting because the design called for formed sheet. Therefore, 7075-T6 was selected for the strap fitting.

Table 3-1. Comparison of Material Properties for Candidate Alloys

Alloy	Yield Strength, F_{Ty} (ksi)	Yield Strength, Fc_y (ksi)	Ultimate Strength, F_{Tu} (ksi)	Elongation to Failure, e (%)	Hardening Modulus, E_H (avg) (ksi)
7050-T7451	67	64	76	10	92
7055-T7751	88	87	91	7	44
7075-T6	72	71	80	8	103

Source: MIL-HDBK-5G, B-Basis

3.3 Fitting Analysis

The new landing gear strut attachment was analyzed for the 38 ft/s and 42 ft/s crash landing conditions using the global MSC/DYTRAN™ landing gear model shown in Figure 3-8. The dynamic characteristics of all components of the tail landing gear system upstream of the redesigned joint were represented in the model, including the energy-attenuating shock strut tube cutter. All other upstream components in the model were assumed to behave elastically. The traditional method for representing an energy-attenuating device such as the tube cutter is to model it using a nonlinear spring element with an idealized response, like the design curve shown in Figure 2-6. As discussed in Section 2, one of the premises of this research project is that this simple representation is inadequate. Therefore, a special tube cutter model was required.

Various approaches were attempted, including a brute force explicit model of the tube cutting mechanism, as shown in Figure 3-9. This approach proved to be too computationally intensive

and too difficult to tune due to the complex geometry and an unstable elastic material failure representation. Hence, the simple tube cutter representation shown in Figure 3-10 was developed. In this model, lateral rods are stretched by a rigid ramped "cutter."

Because all the mechanisms in the tube cutter model are represented with one-dimensional elements, tuning the model to achieve the desired response is simple. The air/oil oleo and tube elements have axial properties to match the real parts, while the area of the stretch links is tuned to achieve the desired stroking load. This tuning does not effect the harmonic behavior of the strut because the stretching mechanism is perpendicular to the strut line of action. The spacing of the stretch links and the ramp angle on the cutter can also be tuned. The geometry shown here was arbitrarily chosen for the validation drop test model because the unfiltered response of the actual tube cutter was not available. This model produced the load/stroke response shown in Figures 2-5 and 2-6.

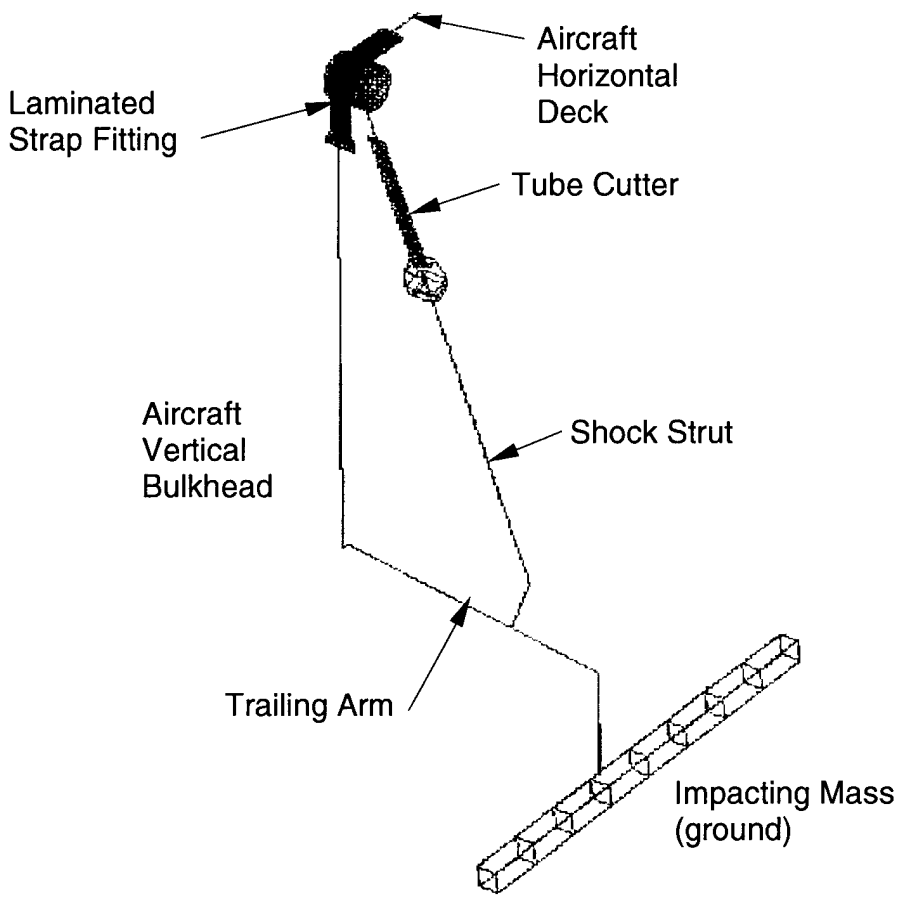

Figure 3-8. MSC/DYTRAN™ model of the tail gear drop test

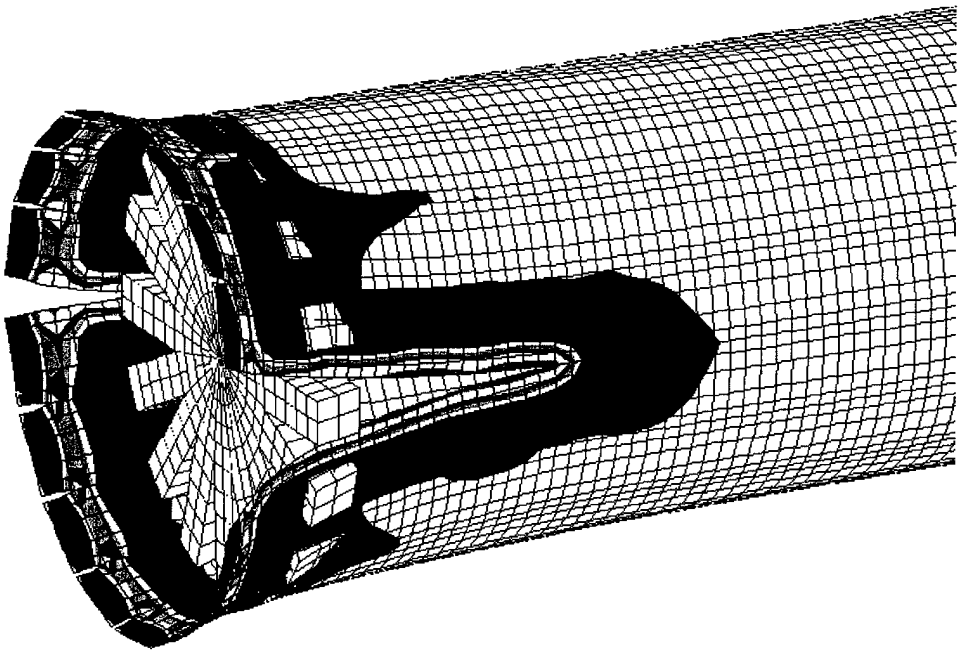

Figure 3-9. Initial attempt at a representative tube cutter model

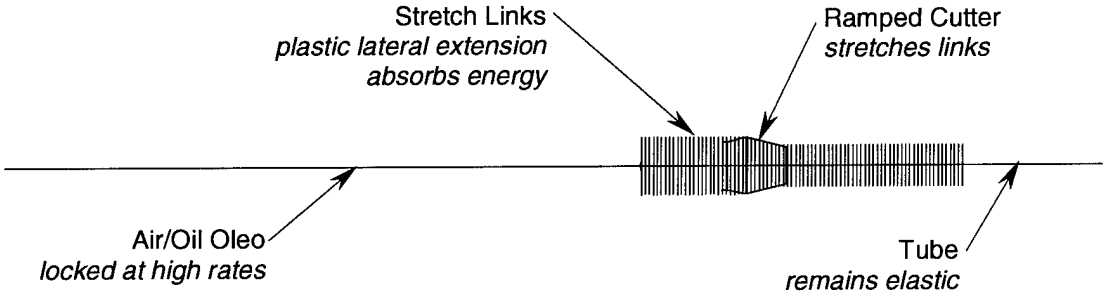

Figure 3-10. Simple tube cutter model utilized in the final analysis (shown partially stroked)

The upper strut attachment joint was represented in the global model as shown in Figure 3-8. The strap fitting model consists of three layers of overlayed plate elements with unattached coincident nodes to represent the laminated construction in which the three pieces are not attached to each other. The cylindrical interface between the shock strut and strap was modeled using rigid solid elements that loaded the strap fitting through contact. The compression strut was modeled using bar elements because the pinned end joints ensure that it will only be subjected to one-dimensional loading. The small plate elements around the bend in the strap fitting controlled the solution time step, which was about 0.3 microseconds. The total impact event spans approximately 0.1 seconds.

For the final design, the landing gear drop test model progressively deflected as the tube cutter stroked, as shown in Figure 3-11, until the entire drop energy was absorbed.

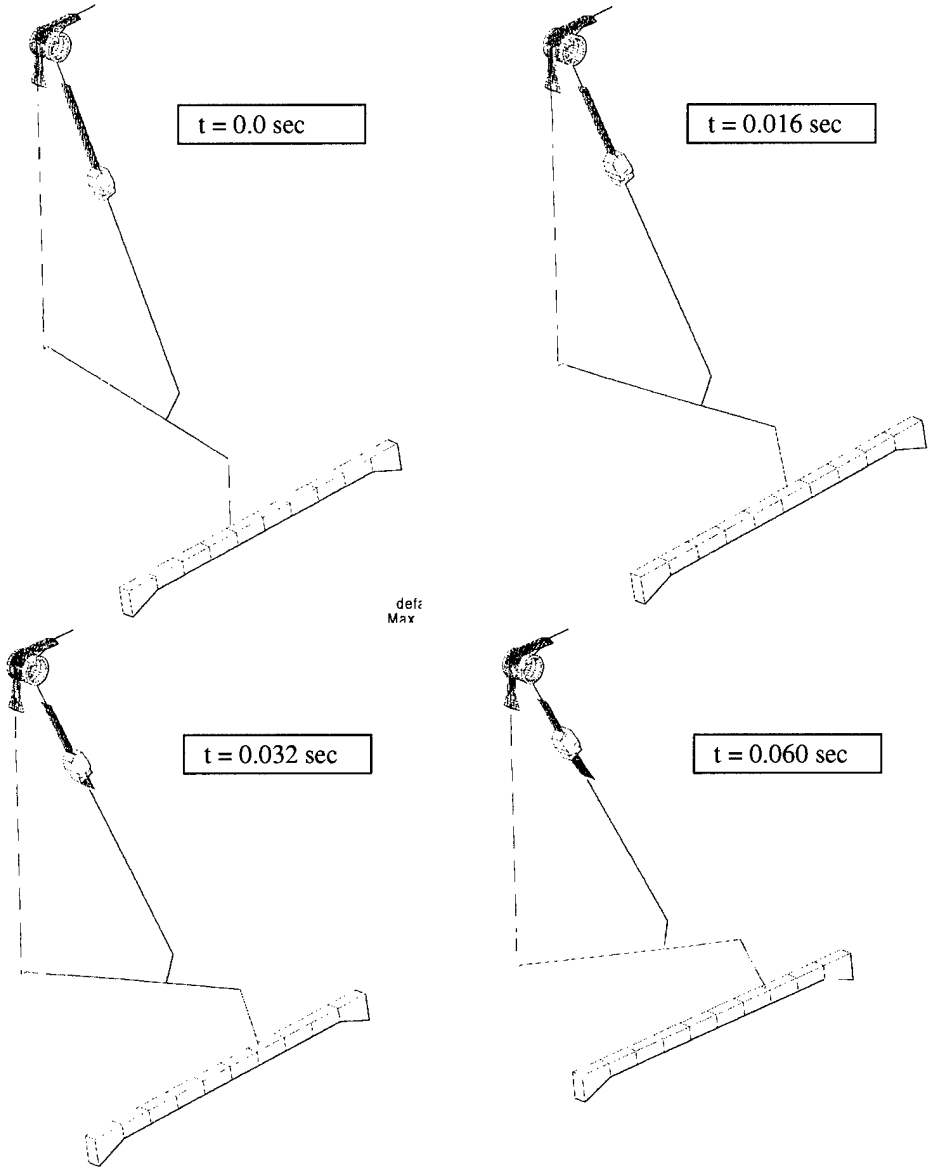

Figure 3-11. Progressive deflection of landing gear drop test model

The model predicted no failure of the upper strut attachment joint. Predicted plastic strains in one layer of the laminated strap fitting are shown in Figure 3-12 for the 42 ft/s crash with 10-degree pitch and roll. Predicted strains in all three strap layers were approximately equal. It is apparent from the fringe plot in Figure 3-12 that the strap fitting performed as designed. Some local yielding occurred at the corner due to bending of the strap around the strut end, but this region did not diverge and initiate failure because the elongated flow zone began to stroke first.

The peak predicted plastic strain is 0.060, or 6.0% elongation. Conservatively using the static elongation allowable of 8.0% for 7075-T6 from Table 3-1, the margin of safety for this strap is

$$\text{M.S. (elongation)} = \frac{e}{\varepsilon_{P\max}} - 1.0 = \frac{0.08}{0.06} - 1.0 = \underline{\underline{+0.33}}$$

Using a traditional static sizing approach, the fitting would be sized for the tube cutter filtered stroking load. A tube with wall thickness of 0.161 inch was used for the drop test, so the design static stroking load using the peak from Figure 2-1 is 35,000 lb. This matches the idealized design curve shown in Figure 2-6. The elongated flow zone in the strap is 1.75 inch wide and each strap is 0.100 inch thick, for a minimum cross sectional area A = 0.525 in^2. The initial strut angle of 22 degrees from vertical results in the maximum strap load, P_{strap}, calculated below.

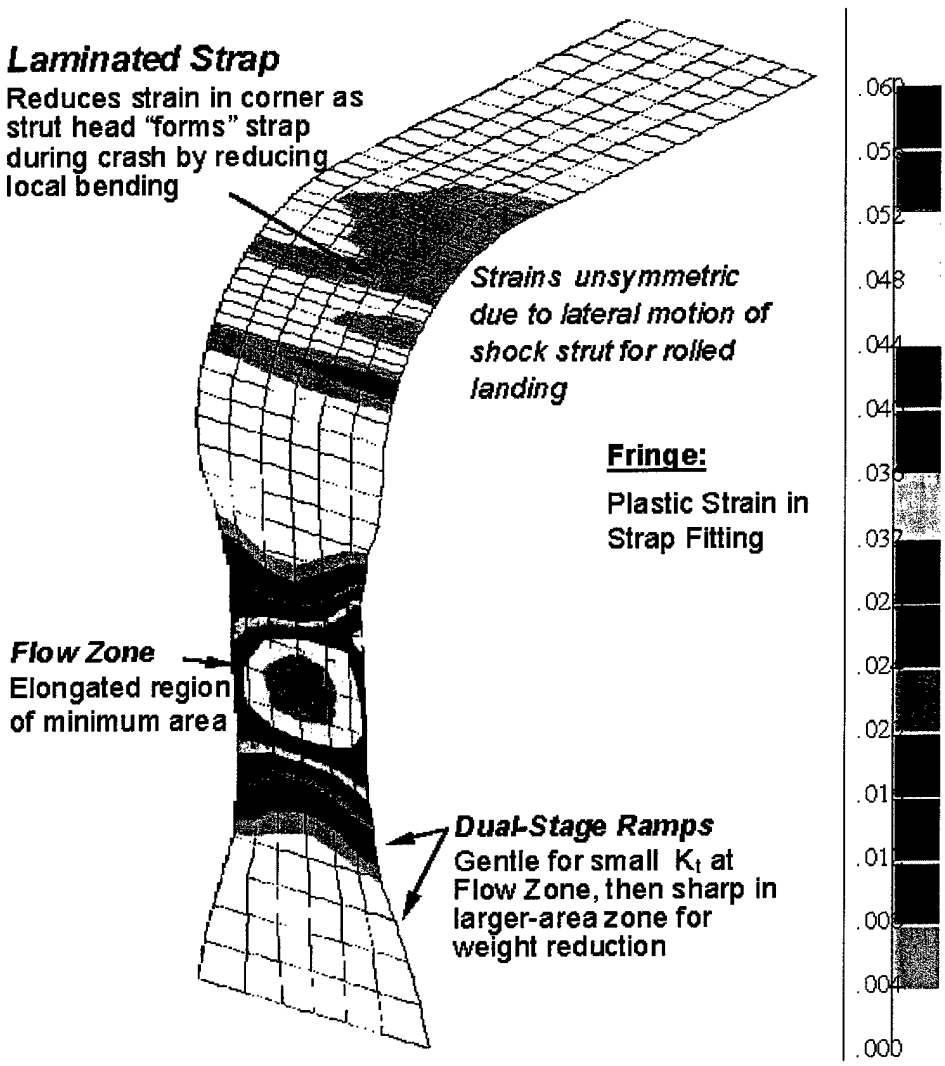

Figure 3-12. Plastic strain fringe plot in strap fitting due to 42 ft/s crash

P_{strap} = (35,000 lb) (cos 22 deg) = 32,451 lb

From Table 3-1, the yield strength of the material F_{Ty} is 72 ksi, and the ultimate strength F_{Tu} is 80 ksi. Therefore, the static margins of safety are

$$\text{M.S. (yield)} = \frac{F_{Ty} \cdot A}{P_{strap}} - 1.0 = \frac{72{,}000 \times 0.525}{32{,}451} - 1.0 = \underline{\underline{+0.16}}$$

$$\text{M.S. (ult. tension)} = \frac{F_{Tu} \cdot A}{P_{strap}} - 1.0 = \frac{80{,}000 \times 0.525}{32{,}451} - 1.0 = \underline{\underline{+0.29}}$$

Note that no ultimate factor is used because the tube cutter stroking is a crash condition. The original ACAP fitting was sized using this type of loading assumption. The interesting conclusion to note from this analysis is that the traditional static calculation using the idealized loading assumption indicates that the strap fitting will not yield during a crash. The dynamic analysis results shown in Figure 3-12, however, clearly indicate that significant plastic flow has occurred. Obviously, using a traditional static analysis and ignoring the dynamic overshoot spikes from the tube cutter stroke is unconservative. For the original ACAP fitting, a more traditional lug design, the minimum margin of safety was +0.00 against compression stability, with the compressive yield strength F_{Cy} used as an allowable (Reference 6). A dynamic analysis with a more realistic representation of the tube cutter load characteristic would have indicated yielding in the part, and therefore most likely have predicted a stability failure of the fitting.

3.4 Fitting Cost and Weight Comparison

The new joint design consists of multiple inexpensive parts with simplified load paths, while the original ACAP joint shown in Figure 2-7 was a single complex forged fitting. Due to budget and schedule constraints, the new joint components produced for the demonstration drop test were not optimized for cost and weight. With a few simple modifications, significant weight and cost savings is possible with the new design. The compression link for the test was somewhat overdesigned, for example. The fairly complex machining could be replaced by a simple uniform thickness routed plate link with no loss of capability. Also, the clevis attaching the compression link to the strap upper deck attachment could be substantially reduced in size using a simple extruded shape with a smaller bolt pattern footprint. The smaller bolt pattern footprint results in a strap width reduction at the upper attachment, too. These modifications result in a total joint weight, including attachment hardware, of 2.26 lb. The projected joint cost per unit assuming 100 units is $1,175, which includes fabrication and installation. Note that these cost and weight figures do not include the modified upper end of the shock strut, which was crudely designed to meet the drop test requirements, but no resources were expended for any optimization.

The existing ACAP fitting failed during the aircraft drop test, so it is obviously not adequate as designed. For an impartial weight comparison some growth must be assumed to increase the capability of the existing fitting. At an early stage of this program, an MSC/NASTRAN® static finite-element analysis of the original fitting was performed using loads from the KRASH analysis. The stresses resulting from the worst case loads are shown in Figure 3-13. The

predicted peak stress value is –115 ksi. To survive the impact, plastic flow in this fitting should be minimized due to the numerous stress concentrations and complex redundant load paths. The original fitting was 7050-T73652 hand forging, with yield strength F_{Cy} = 60 ksi. The assumption used here is that in order to prevent massive plastic flow and instability, the fitting must grow by 50% of the stress ratio. The original fitting weight was 1.65 lb, so the assumed fitting weight for comparison is

$$\text{Weight} = 1.65\left[1 + 0.50\left(\frac{f_{\text{peak}}}{F_{Cy}} - 1\right)\right] = 1.65\left[1 + 0.50\left(\frac{115}{60} - 1\right)\right] = 2.41\,\text{lb}$$

Adding installation hardware, the total joint weight is 2.89 lb. Therefore, the projected weight savings for the new design is 22%. The original fitting cost per unit for 100 units in current dollars is $1,437, which includes fabrication and installation. Therefore, the projected cost savings for the new design is 18%.

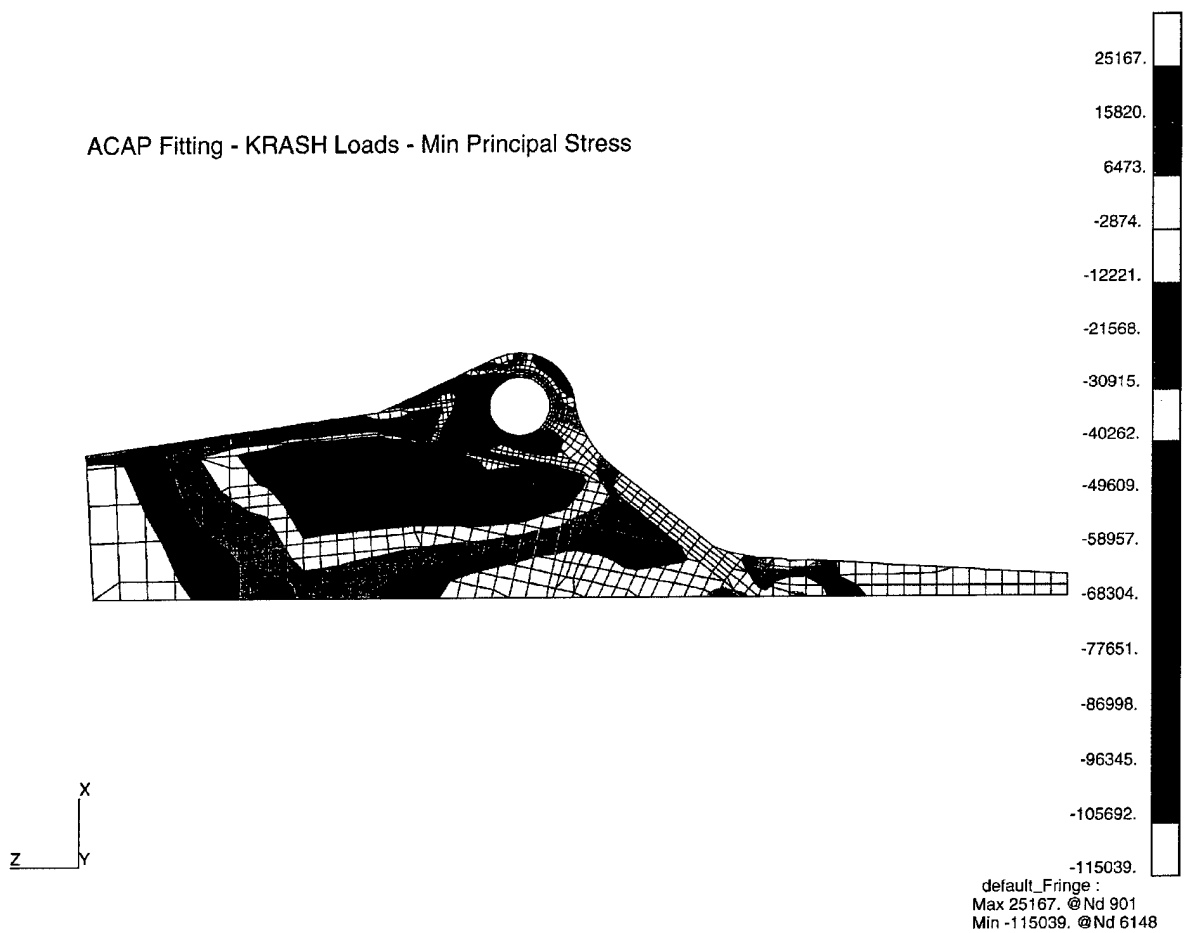

Figure 3-13. Minimum principal stress fringe plot from MSC/NASTRAN® analysis of original fitting for worst case ACAP design loads

4. COUPON TESTING

4.1 Material Characterization Tests

The Southwest Research Institute in San Antonio, TX was contracted to perform high strain rate material characterization tests on selected aluminum alloys. Comparisons of the static and dynamic response of various steels were readily available. However, data providing a similar comparison for aluminum alloys that are commonly used in airframe structures could not be found in the literature.

Three aluminum alloys were selected for the test: 7050-T7451, 7055-T7751 and 7075-T7351. The 7050 and 7075 alloys are commonly used in airframe fitting applications. The 7055 alloy was recently developed by ALCOA for fitting applications, offering improved fracture toughness and yield strength. The laminated strap design was not conceived until after these tests, so the alloy used for the new fitting, 7075-T6, was unfortunately not included. No data were found to correlate grain direction to strain rate sensitivity. Specimens were, therefore, prepared and tested from the longitudinal, long transverse, and short transverse grain directions for all three alloys. Tension and compression tests were performed using the Split Hopkinson Pressure Bar technique. This test is described in detail in Appendix A.

The tensile test results are summarized in Table 4-1 below. In general, the tensile stress/strain plots shown in Appendix A show yielding followed by rapidly increasing strain with oscillating stresses that exhibited a slight declining trend. For all three alloys, the short transverse direction displayed both the lowest elongation and lowest maximum stress. The long direction displayed the highest elongation and maximum stress, and the long transverse properties fell somewhere in between. The 7075 and 7050 specimens showed the best long direction elongation, and 7075 showed the best long transverse elongation. In general, all observed elongation values were significantly larger than the static allowables reported in MIL-HDBD-5. The 7055 specimens showed the highest peak stress values.

Table 4-1. Summary of Split Hopkinson Bar Tension Test Results

Alloy	Direction	Average strain rate (sec^{-1})	Average elongation (%)	Average peak stress (ksi)
7050-T7451	Long	1,581	15.7	101
	Long Transverse	1,609	12.1	91
	Short Transverse	1,643	9.4	88
7055-T7751	Long	1.443	13.3	112
	Long Transverse	1,516	12.4	104
	Short Transverse	1,532	6.4	94
7075-T7351	Long	1,581	15.7	96
	Long Transverse	1,627	13.9	88
	Short Transverse	1,633	9.2	84

The compression test results are summarized in Table 4-2 below. The compressive stress/strain curves shown in Appendix A displayed less oscillation than the tensile plots, so were more easily interpreted. In general, the specimens displayed a well-defined yield point followed by a region of rapidly increasing strain and slowly increasing stresses. The compressive data were sufficient quality to define an elastic modulus, yield stress, and hardening modulus in addition to the maximum stress and elongation. The elastic modulus results reveal nothing unexpected except for the large measurement for the long direction 7050 low-rate specimen. The strain rate for this specimen, 735 sec^{-1}, is on the low end for this test method, so this measurement is suspect. Yield stresses for all specimens were significantly higher than the static allowables from MIL-HDBK-5, with the 7055 alloy exhibiting the highest values. Observed elongations were also substantially higher than published static allowables, particularly in the transverse directions.

Table 4-2. Summary of Split Hopkinson Bar Compression Test Results

Alloy	Direction	Strain rate (sec^{-1})	Elastic modulus (Msi)	Yield stress (ksi)	Maximum stress (ksi)	Elongation (%)	Hardening modulus (Msi)
7050-T7451	Long	735	13.3	89	110	5.0	0.42
		1,66	9.9	89	112	11.5	0.20
		3,343	9.7	92	123	24.0	0.13
	Long trans	1,699	10.1	90	115	11.9	0.21
		2,126	10.2	92	121	15.0	0.19
		2,678	10.2	94	122	19.0	0.15
	Short trans	1,637	9.7	92	117	9.7	0.26
7055-T7751	Long	1,553	10.6	109	126	10.5	0.16
	Long trans	1,521	10.3	113	132	10.3	0.18
	Short trans	1,517	10.4	114	135	10.2	0.21
7075-T7351	Long	1,632	10.1	84	108	11.2	0.21
	Long trans	1,605	10.0	89	113	11.0	0.22
	Short trans	1,608	10.2	89	112	11.0	0.21

Both the tensile and compressive results dispel the widely held belief that metallic materials behave in an increasingly brittle manner as strain rate increases due to their inherent interatomic inertia. These tests prove that, in the absence of stress concentrations, just the opposite is true. The reason apparently brittle failures have been observed in parts subjected to high-rate loads is poor design details allowing the applied energy to focus on a small volume of material, not the microstructure of the material.

4.2 Validation Coupon Tests

Two subelement coupon tests were devised in order to verify the analytical methods and conclusions concerning stress wave propagation and plastic flow localization—an unnotched dogbone coupon, shown in Figure 4-1, and a notched coupon shown representative of typical fitting design details, shown in Figure 4-2. The subelement coupon tests were performed at

Integrated Technologies, Inc. (Intec) of Bothell, Washington. All coupons were machined from 7075-T651 plate, and were subjected to impact tup velocities ranging from 7.5 to 42 ft/s. The test procedure, coupon geometry, and results are documented in Appendix B. Comparisons of test results and MSC/DYTRAN™ analytical predictions are shown below.

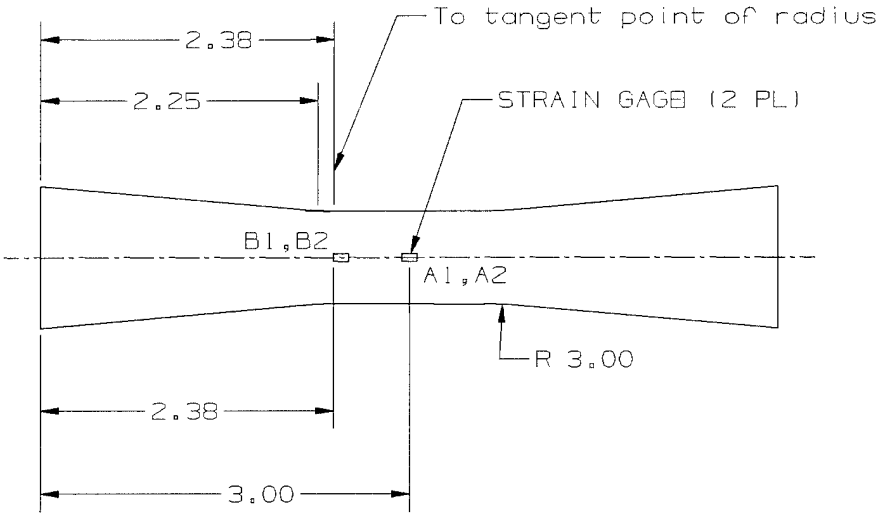

Figure 4-1. Unnotched dogbone specimen geometry and gage locations

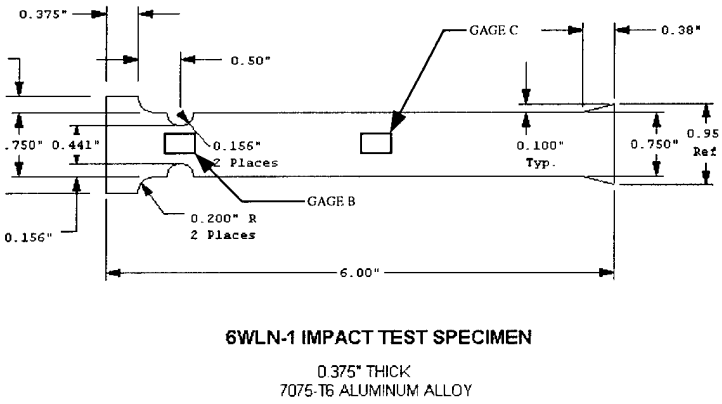

Figure 4-2. Notched impact specimen geometry and gage locations

Coupon testing under high-rate impact loading conditions is difficult, with complications associated with high-frequency data acquisition, very large strains, and undesirable secondary effects that cause impact energy to be absorbed by elements other than the coupon itself. The unnotched dogbone coupon tests provided an opportunity to work through some of the testing difficulties and tune the analysis model to more closely match the test setup. In order to obtain unfiltered strain data at a sufficient sampling rate to observe the stress wave behavior in the specimens, special circuitry had to be devised which bypassed the standard strain conditioner typically used. Also, high strain capacity "EP" gages had to be employed in high plastic flow

zones to capture strain readings potentially as high as 10%. Finally, the shape of the impact tup was modified and all interfaces in the test setup were machined to very close tolerances to prevent any local yielding of material away from the specimen gage section. It was important to channel as much of the impact energy as possible to the specimen and not the surroundings, because the analytical model assumed the test setup was a perfect system with no energy loss.

After considerable trial and error, good correlation between test and analytical results was achieved for low and medium energy impacts, as shown in Figure 4-3. For higher energy impacts, there was still an undetermined energy absorbing mechanism in the test setup that prevented the specimen from being subjected to the entire target energy, as shown in Figure 4-4. One potential explanation is local yielding or crushing of a test fixture part. The issue was not resolved due to insufficient schedule and budget.

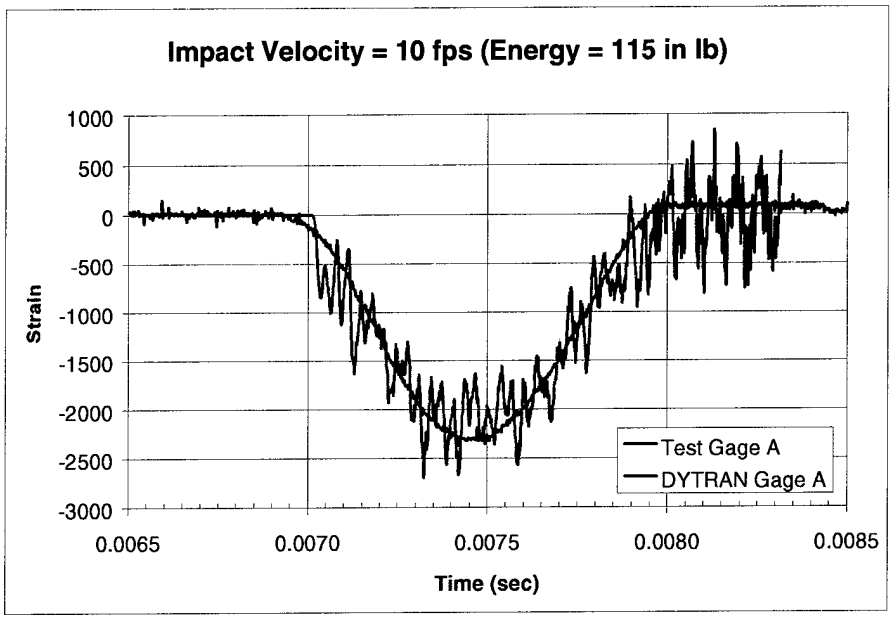

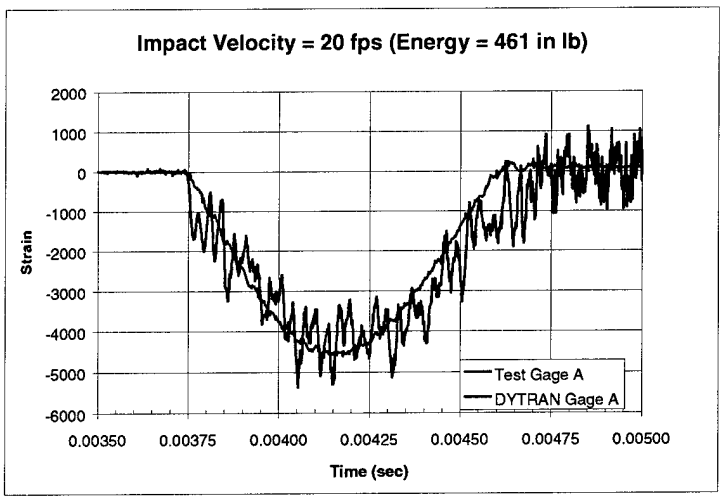

Figure 4-3. Low and medium energy impact response of dogbone specimen

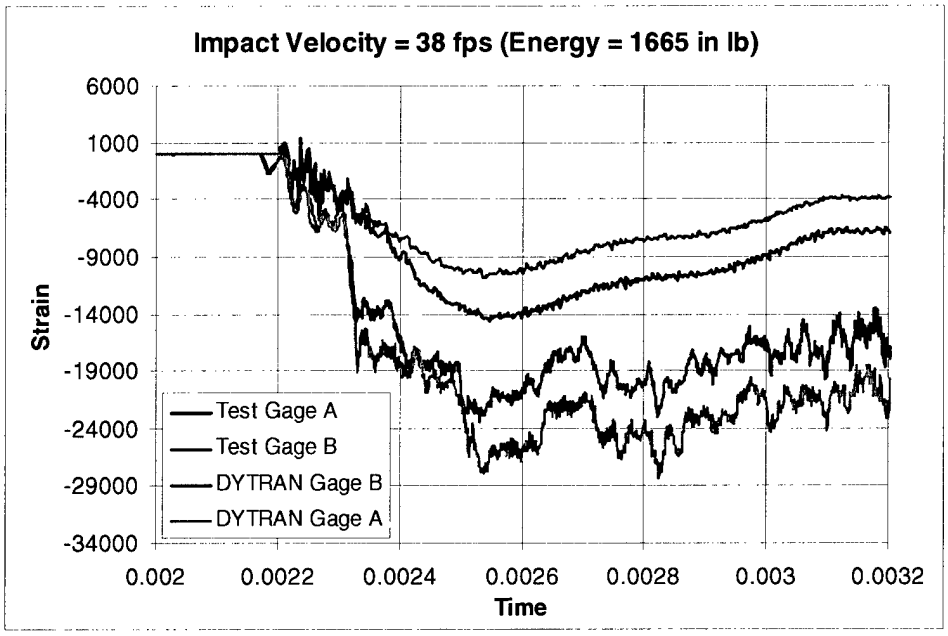

Figure 4-4. High-energy impact response of dogbone specimen

Correlation of the notched coupon tests involved more risk because the energy-absorbing plastic flow zone was much smaller, which results in considerably larger plastic strains. The notched specimen was tested near the limit of its energy-absorbing capability, whereas the dogbone had considerably more reserve. Like the dogbone specimen results, good correlation was achieved at the lower and medium impact energy levels, as shown in Figure 4-5. This was encouraging because, for this specimen, even the medium energy impact resulted in strains well beyond material yield. Also like the dogbone specimen, the higher impact energy response did not correlate very well with analysis, as shown in Figure 4-6.

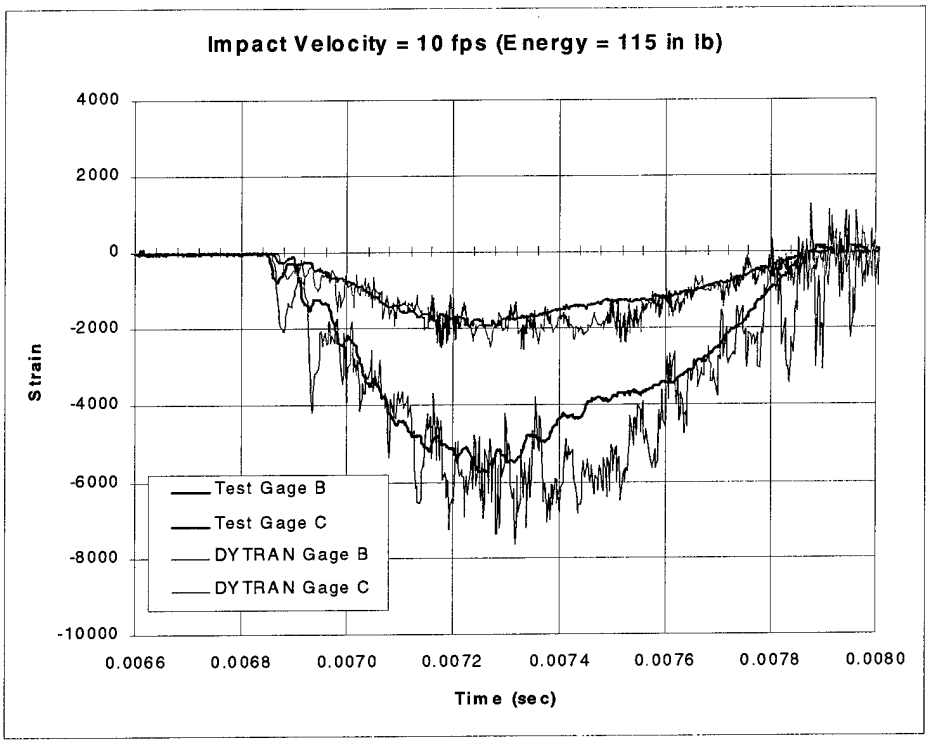

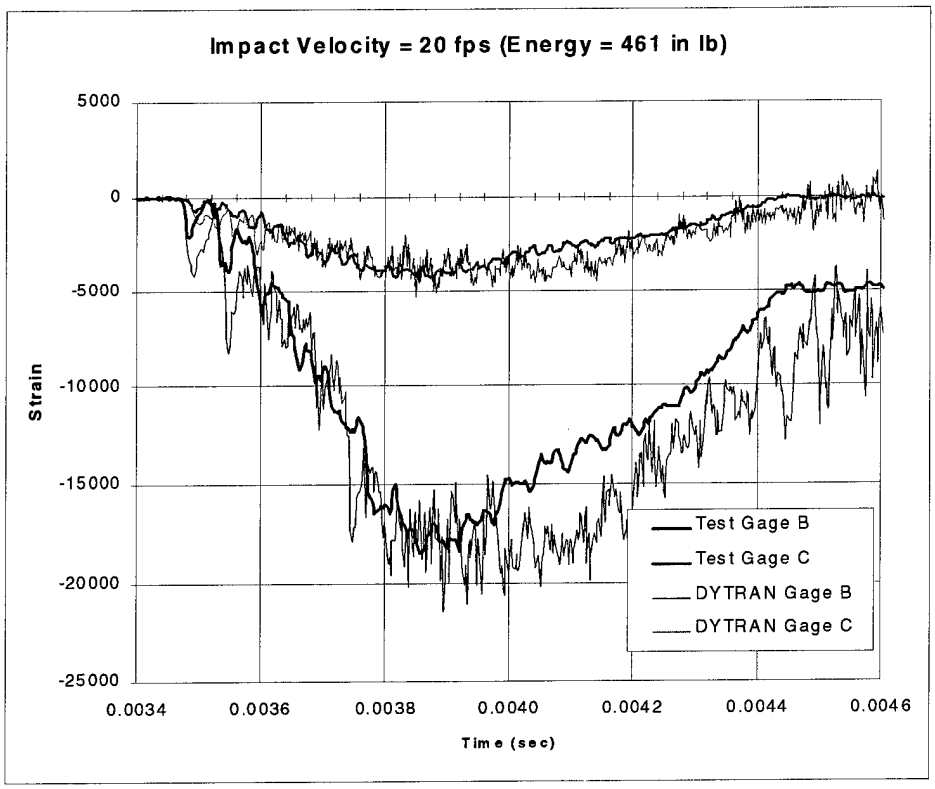

Figure 4-5. Low and medium energy impact response of notched specimen

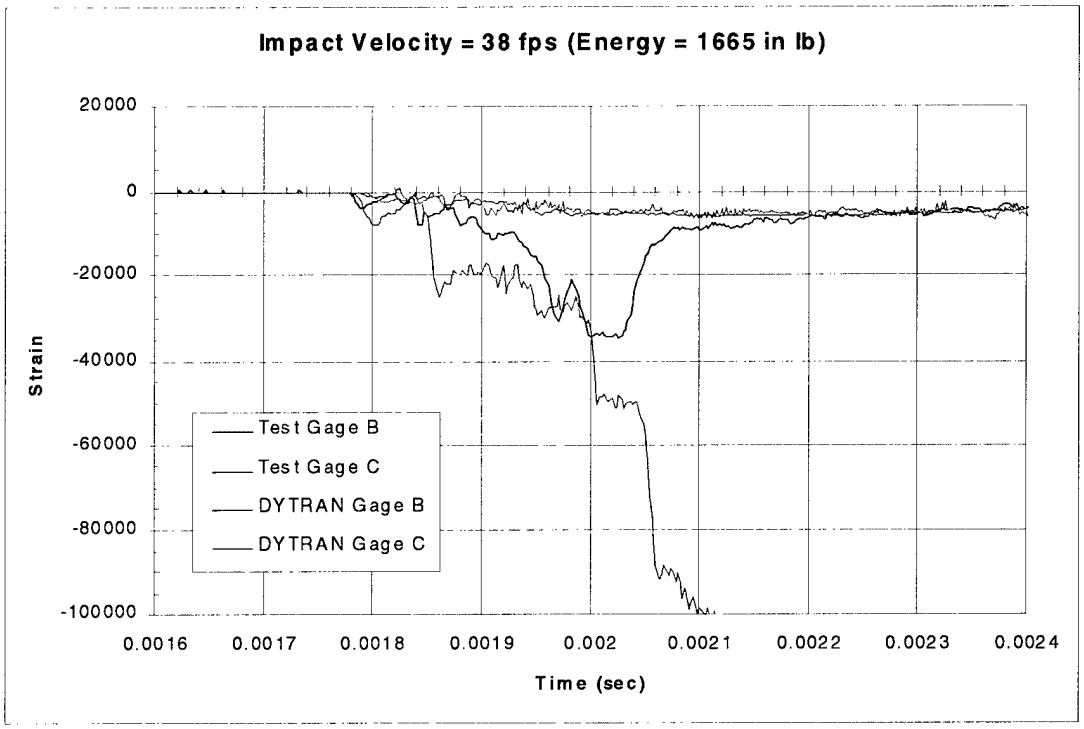

Figure 4-6. High-energy impact response of notched specimen

The subelement coupon tests provided confidence in the use of the MSC/DYTRAN™ finite-element simulation tool to predict the high-rate response of highly loaded airframe fittings. Test strain gage readings showed similar characteristics to the analytical results. The test results confirm the localization of plastic flow in the minimum cross section region. Similarly, the results indicate that plastic flow occurs in the entire volume of minimum area material, because the energy-absorbing capability of the dogbone type specimen was much greater than that of the notched specimen, as evidenced by the strain levels at equivalent energies. The predicted plastic strain distribution in the two specimens, which shows the extent of yielded material, is shown in Figure 4-7. A stress fringe plot of the notched specimen during the impact event prior to complete energy absorption is shown in Figure 4-8. The stress wave pattern due to reflections from various boundaries is clearly visible in the figure.

Unnotched Coupon (Dogbone): Plastic Strain

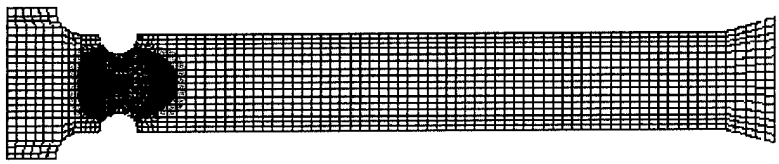

Notched Coupon: Plastic Strain

Figure 4-7. Plastic strain fringe for the dogbone and notched specimens

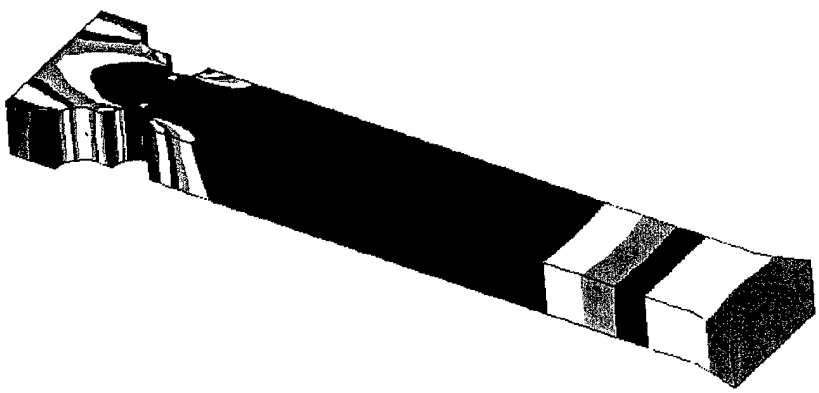

Figure 4-8. Stress wave reflections in the notched impact specimen

4.3 Stress Concentration Coupons

One of the more interesting conclusions to be drawn from this research program is that under high-energy, high-rate loading conditions, high stress concentrations outside the minimum cross sectional area of a fitting have little effect on the fitting capability. The bolt designed for impact loads shown in Figure 2-7 is a clear example. The stress concentration at the root of the threads, K_T = 3.85, is much greater than the optimal area reduction factor, 1.2. The 20% reduction in shank area is sufficient, however, to induce plastic flow and subsequent failure away from the sharp K_T and into the smooth necked-down region. In contrast, if the maximum stress concentration occurs at the minimum area section of the part, plastic flow will initiate more

rapidly, causing premature failure. The relationship between stress concentration and minimum cross sectional area requires more investigation to achieve truly optimal fitting designs.

This effect was considered as it applies to the redesigned ACAP tail gear strut attachment fitting, described in Section 3. The fitting incorporates a necked-down dogbone region designed to increase the energy-absorbing capacity of the fitting. In order to minimize the size of the fitting, a steeper ramp angle was desirable. A steeper ramp creates a worse stress concentration, however. A simple MSC/DYTRAN™ study was undertaken to examine the effects of changing the ramp angle on the energy absorbing capability of a fitting. Aluminum dogbone coupons with various ramp angles were modeled, and subjected to a tensile impact of sufficient energy to fracture all the coupons. An example coupon model is shown in Figure 4-9. The area under the axial force time history curve, analogous to the energy absorbed prior to fracture, was compared for each coupon, as shown in Figure 4-10. The ramp angle effect is significant, with a change from a 45-degree ramp to a 15-degree ramp, resulting in a 10% increase in energy absorbed.

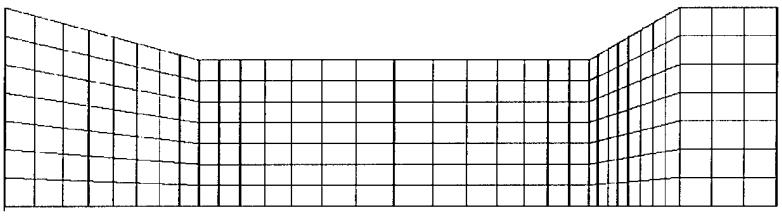

Figure 4-9. Constant ramp coupon (30-degree ramp shown)

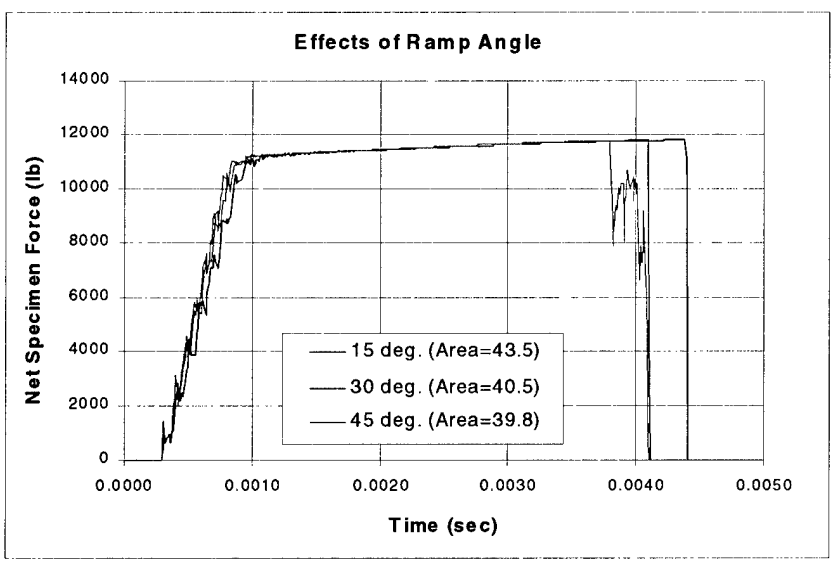

Figure 4-10. Force time history plots for various ramp angles

In an attempt to minimize fitting size and weight yet still take advantage of a shallow ramp angle, a dual-angle ramp was devised, in which the ramp angle adjacent to the minimum area necked-down region is 15 degrees, but a short distance away transitions to a 45-degree ramp. The coupon model used to test the effectiveness this approach is shown in Figure 4-11, with the results shown in Figure 4-12. The difference between energy absorbed by the dual ramp coupon and the 15-degree constant ramp coupon was minimal, less than 1%. Therefore, this approach was adopted for the ACAP fitting redesign. With further study of this and other stress concentration effects, weight savings could be achieved. Ultimately, a set of general design guidelines concerning various stress concentrations such as ramps, bosses and fastener holes could be established to aid in minimizing the weight and cost of highly loaded airframe fittings.

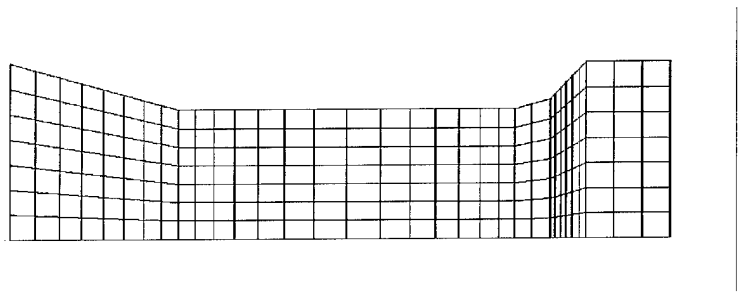

Figure 4-11. Dual angle ramp coupon (15 degrees/45 degrees)

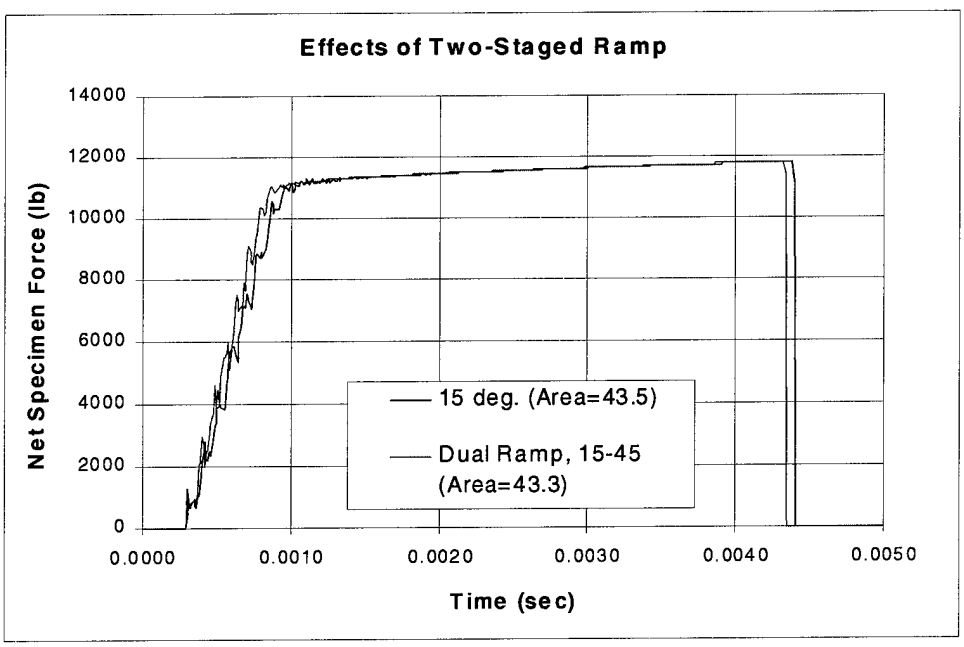

Figure 4-12. Force time history plot for dual angle ramp coupon

5. FULL-SCALE DROP TEST

The original proposal for this program contemplated validation tests that represented the ACAP tail landing gear loading at vertical impact velocities of 17, 38, and 42 ft/s (5.2, 11.6, and 12.8 m/s). The impact attitude was to represent 12 degrees of aircraft pitch and roll for the 17 ft/s test and 10 degrees of pitch and roll for the remaining tests.

The 17 ft/s test was deleted from the program with the Government's approval, in order to utilize additional funds for more extensive instrumentation and data collection during the high-velocity impacts. Little was expected to be learned from this particular test. While 17 ft/s represents a very hard landing, it is in the range of shocks absorbed solely by the oleo system and below the tube cutter initiation threshold. Full-scale drop testing was conducted at Simula Technologies, Inc. of Phoenix, AZ.

5.1 38-ft/s Drop Test

The redesigned upper shock strut attachment was assembled to a steel support fixture, as shown in Figure 5-1. A closeup view of the redesigned joint is shown in Figure 5-2. A simulated ACAP tail landing gear shock strut was attached to the test fitting to provide the load input path. This shock strut had the same energy absorbing tube cutter and overall length as the ACAP strut, but without the oleo portion. The upper end of the shock strut was redesigned to interface with the new fitting. The oleo portion of the ACAP strut design that provides energy absorption and cushioning under normal landing conditions was replaced by a solid tube to reduce costs.

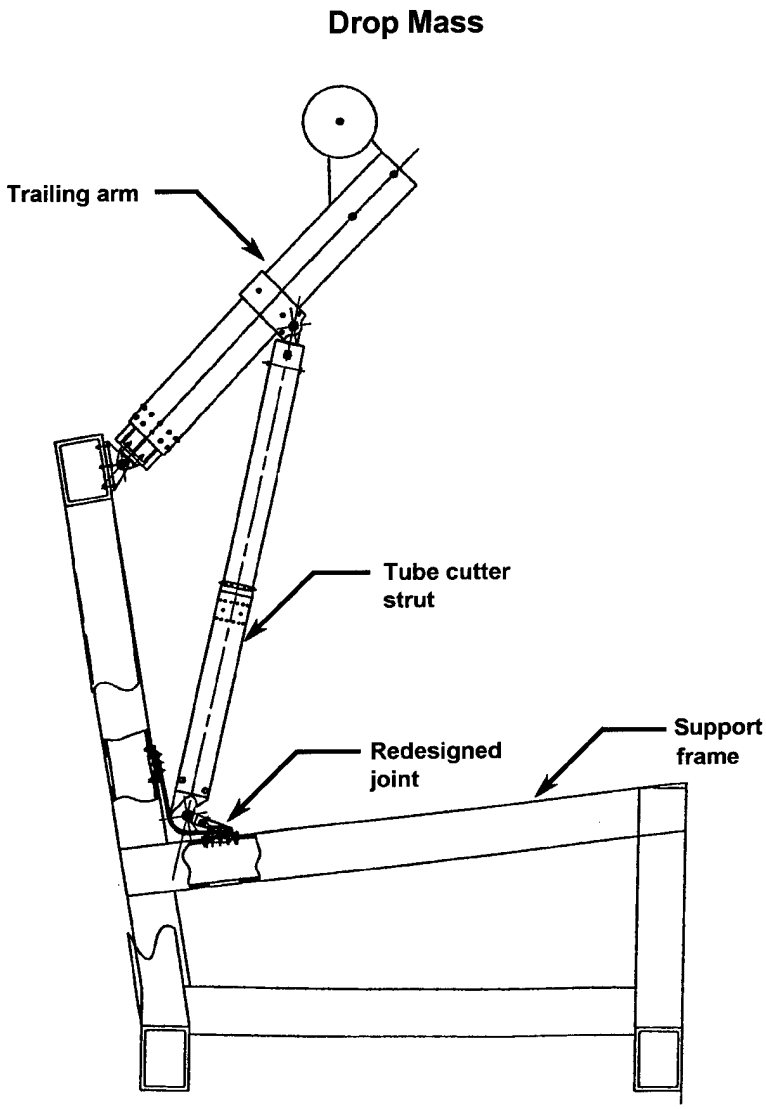

Figure 5-1. Assembled drop test fixture

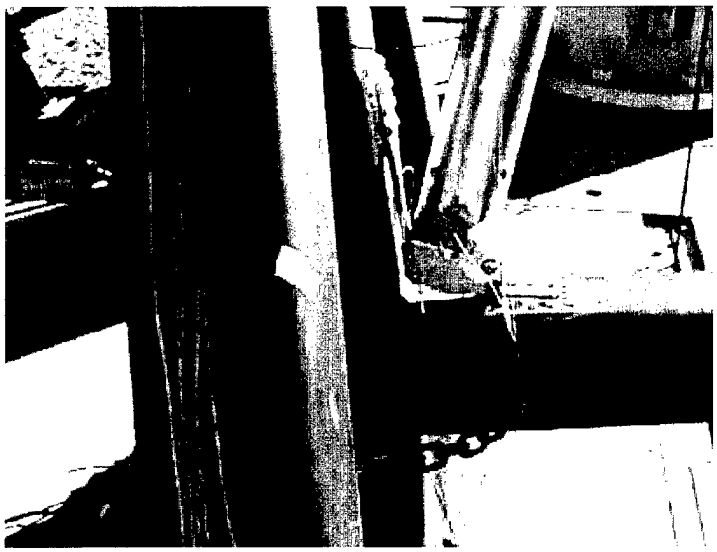

Figure 5-2. Redesigned upper shock strut attachment joint

The ACAP trailing arm assembly had successfully passed the landing gear qualification drop tests and the full-scale aircraft drop tests. This aluminum forging was replicated by an aluminum tube to which machined fittings were bolted that provided the attach points to the steel support fixture and for the shock strut and wheel assemblies. The actual wheel was represented by machined aluminum disks and spacers.

The steel support fixture was designed to support the simulated landing gear assembly in an inverted position and orient it to represent an aircraft attitude of 10 degrees pitch and 10 degrees roll. Two aluminum lug fittings, sized to represent the trailing arm attachment lugs in the ACAP air vehicle, were bolted to the fixture, as was the test fitting.

The fixture, with the simulated landing gear attached, was mounted to the base of Simula's 75 ft outdoor drop tower. A guide cage was weighted to 1,685 lb, and provided with a shock-absorbing pad on the lower surface to simulate the landing gear tire. The drop weight was adjusted from the nominal 1,800 lb to account for an effective rotor lift of 1,200 lb. The weighted cage was raised to a height of 22.4 ft and dropped onto the inverted landing gear assembly, as shown in Figure 5-3.

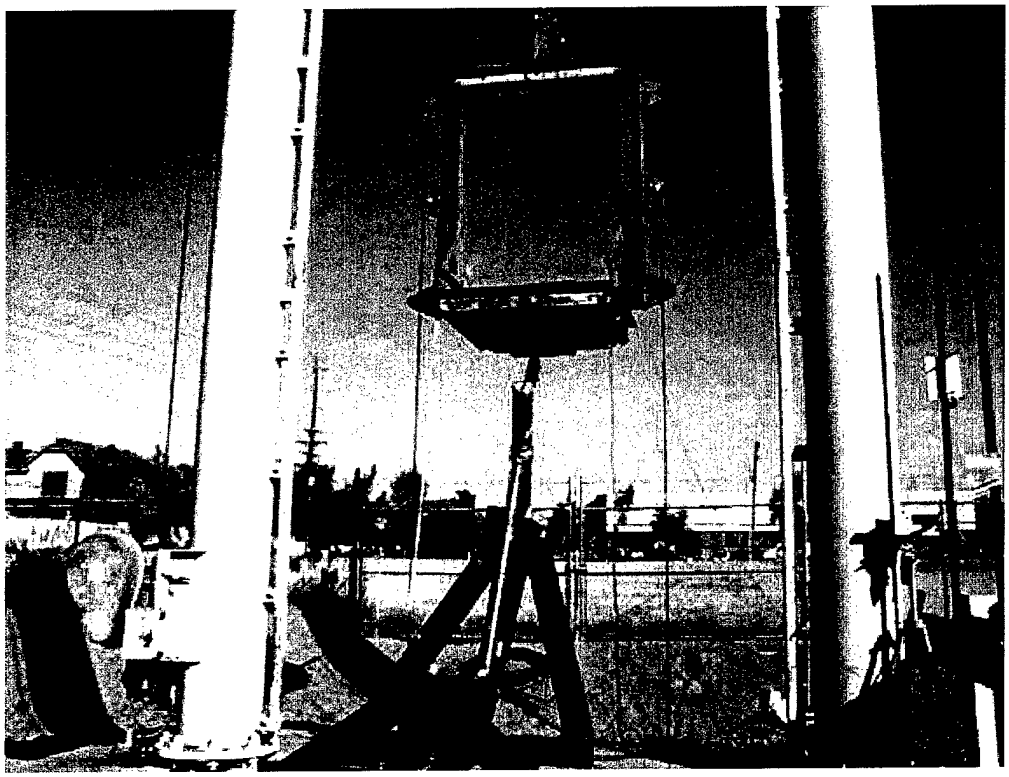

Figure 5-3. Simulated landing gear drop test assembly

The impact sheared the tube cutter retaining rivets and initiated tube cutting action. The tube cutter acts as a load limiting device. The initiation of tube cutting is, therefore, the point of maximum load on the test fitting.

The machined part that represented the fuselage attachment end of the trailing arm failed during the test, as shown in Figure 5-4. The resulting twisting of the trailing arm destroyed one of the fixture-mounted support lugs and failed the attachment on both ends of the shock strut, as shown in Figure 5-5. The drop test setup provided no catcher for the drop mass, and the ensuing uncontrolled impact resulted in additional secondary damage to virtually all parts. Due to the premature failure, the tube cutter only stroked a small amount, less than 2.00 inches, as shown in Figure 5-6.

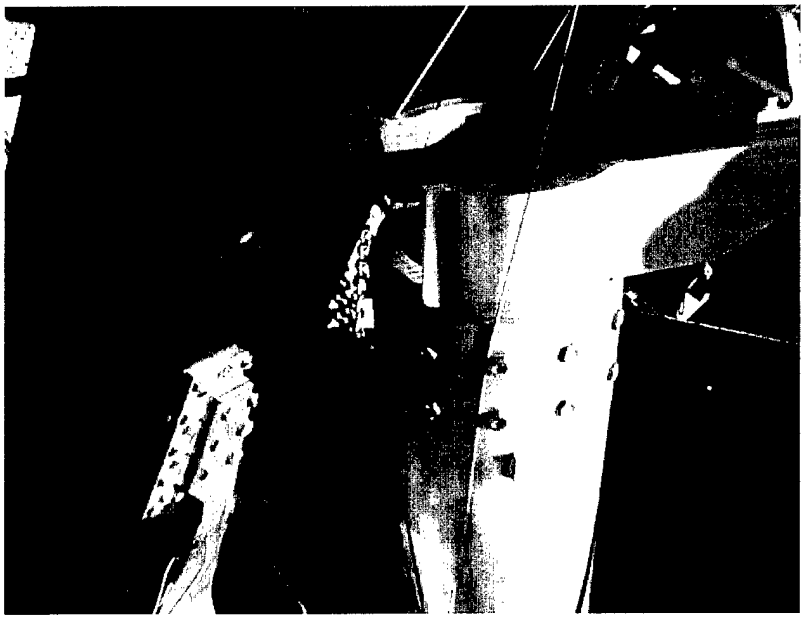

Figure 5-4. Failed trailing arm attachment fitting

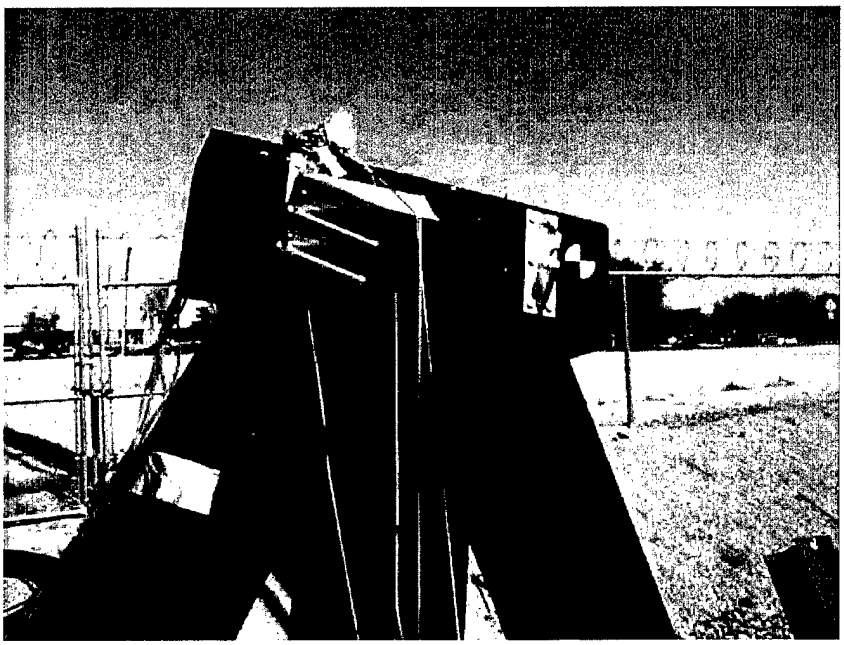

Figure 5-5. Failed trailing arm attachment fitting and attachment lugs

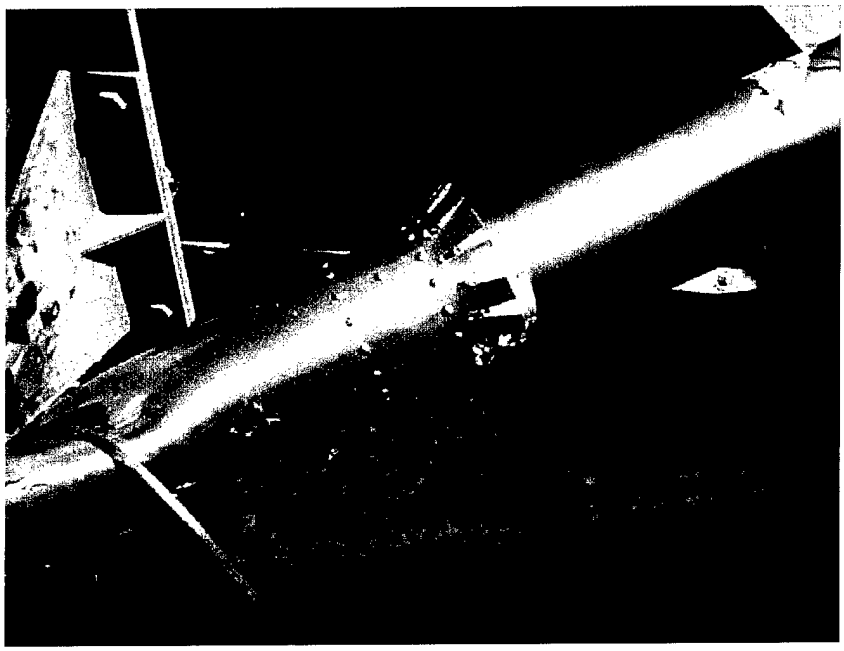

Figure 5-6. Post-test view of stroked tube cutter

Since no spare parts were available for many of the damaged components, the test program had to be terminated at this point. The fixture and test fitting drawings, drop mass calculations, and the Simula Test Report are contained in Appendix C.

5.2 Postmortem Analysis

The failure of the simulated trailing arm assembly was not expected. This part was patterned after an ACAP part that had not failed in previous tests. Therefore, little analysis effort was expended on this part and it was not detailed in the MSC/DYTRAN™ model.

Subsequent investigation points to the change from a one-piece forging to an assembled machined part, and uncertainty over the actual dimensions of the original ACAP part as contributing factors to the eventual test failure. The original ACAP trailing arm was designed by a vendor to a subcontractor, and detail drawings are not on file at Bell.

The failed part was detailed in the MSC/DYTRAN™ model after the test in an effort to understand the test result. No other modifications were made to the drop test model. The revised model is shown in Figure 5-7. The MSC/DYTRAN™ analysis predicted failure of the trailing arm attachment fitting about 5 milliseconds after the initial impact. A detail view of the trailing arm attachment fitting model with the failed elements highlighted is shown in Figure 5-8. The predicted post-failure deformed shape of the trailing arm attachment fitting is shown in Figure 5-9. A comparison of Figures 5-8 and 5-9 with the post test photos Figures 5-4 and 5-5 above indicate that the MSC/DYTRAN™ analytical results qualitatively correlate very well with the test results. No quantitative comparison can be made because the trailing arm fitting was not

instrumented during the test. The total tube cutter stroke predicted in the analysis was 1.4 inches, which also correlates well with the actual test.

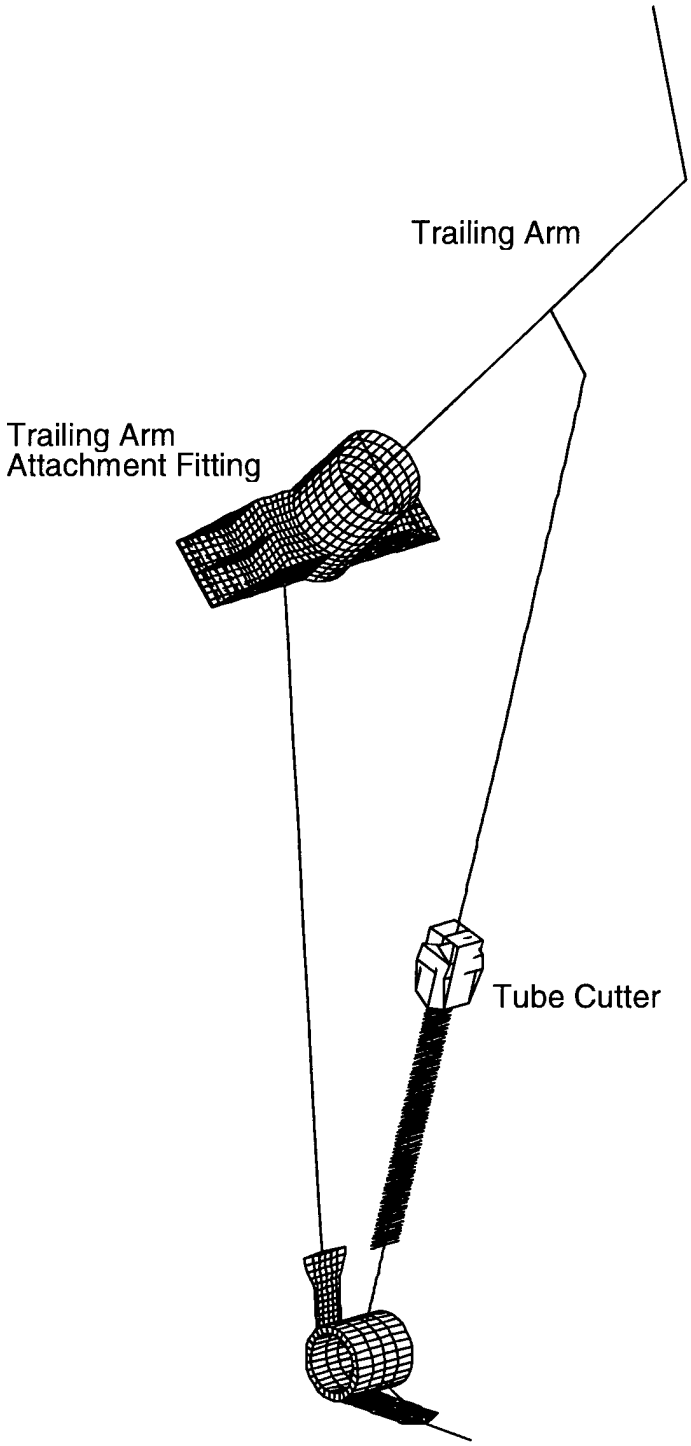

Figure 5-7. Revised drop test model with trailing arm attachment fitting

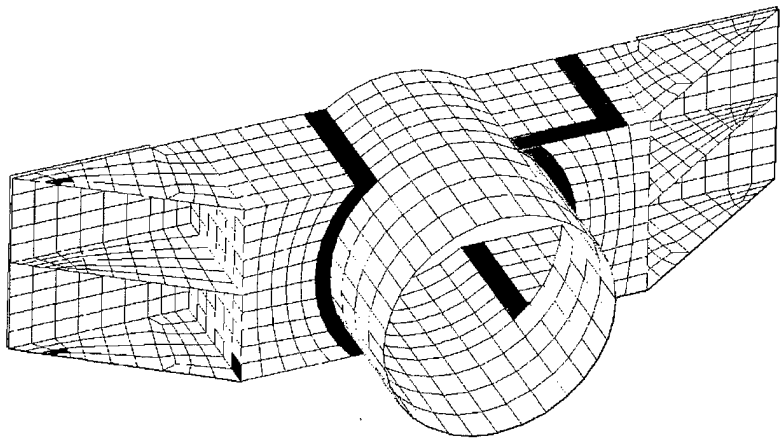

Figure 5-8. Trailing arm attachment fitting model showing failed elements ("colder" color indicates earlier failure)

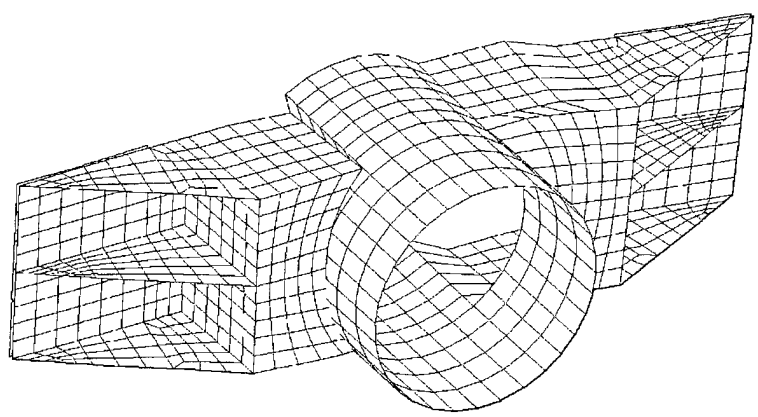

Figure 5-9. Deformed shape of trailing arm attachment fitting at Time = 0.014 s (initial failure at Time = 0.007 s)

The upper shock strut attachment joint that was the primary focus of the drop test suffered only surface damage in the final collapse of the test setup. A compression link that fixed the position of the shock strut head in relation to the strap fitting was sheared off when the failure of the trailing arm twisted the shock strut out of plane. There was no apparent damage that was

associated with the design loading of the fitting. The upper joint seemed to perform as expected prior to the trailing arm failure.

The test did validate the analysis technique including MSC/DYTRAN™ modeling that formed the basis of this effort. The part that was designed using this method performed as expected. A part that was initially not subjected to MSC/DYTRAN™ modeling failed during the drop sequence in a manner that post-mortem analysis proved would have been predicted by MSC/DYTRAN™. The test only reaffirmed the conclusion that during a dynamic impact event the applied energy will focus on the weakest component in the system and if that component is not designed properly, it will fail. The redesign of the upper strut attachment fitting eliminated the weakest component of the original system, with the unfortunate result of exposing the next weakest component in the tail gear system—the trailing arm attachment.

This page intentionally left blank.

6. CONCLUSIONS

A systematic investigation of the design and analysis of airframe fittings that are subjected to large loads applied at high rates proved very enlightening. Beginning with an assessment of the current state of the art in sizing highly loaded airframe fittings, analytical methodologies that account for rate-sensitive material behavior and internal stress wave propagation were evaluated. A comprehensive analytical approach using MSC/DYTRAN™ is proposed in which the dynamic behavior of all the components in the system is accurately represented.

The recommended analysis procedure was demonstrated in a redesign of the ACAP tail gear upper shock strut attachment joint, which had failed during the original aircraft drop test. The redesigned joint compared favorably with the original in both cost and weight. Several important principles for highly loaded airframe fitting design ascertained during the analytical development task were applied to the new joint design. These lessons learned are repeated below for emphasis.

- Under dynamic loading conditions, the applied energy is focused on the weakest part of a structure, typically the minimum cross sectional area, until that part fails.

- Stress concentrations outside of the minimum area region have little effect on the energy absorbing capability of a fitting. Further analysis and testing is required to more completely understand the relationship between area and stress concentration for dynamically loaded components.

- Increasing the volume of material in the minimum area region of a fitting dramatically improves its energy absorbing capability.

- Simplification of load paths is important, so that the weakest link in a structure can be more easily identified.

- Robust fittings should be capable of withstanding repeated short duration load spikes beyond their static capability.

High strain rate material characterization tests were performed on various aluminum alloys commonly used in airframe fitting design. Results indicated increases in both yield strength and elongation at high strain rates. The use of static allowables is therefore conservative. This conclusion cannot be expanded to include steels and titanium alloys, however. The test results seem to indicate that, in the absence of stress concentrations, structural aluminum alloys behave in an increasingly ductile manner as strain rate increases, with no apparent change in stiffness. This conclusion dispels the widely held belief that these materials behave in an increasingly brittle manner as strain rate increases due to their inherent interatomic inertia. In the past, fittings subjected to high-rate loads have failed due to poor design details allowing the applied energy to focus on a small volume of material, not because of the microstructure of the material.

The redesigned strut attachment was drop tested to validate the developed design and analysis methodology. The drop test was unsuccessful in that a part failure away from the upper strut

attachment prevented a complete substantiation of the new joint design. Post-mortem analysis in which the drop test model was modified to include an accurate model of the failed part, however, proved that the part failure could have been predicted. Good qualitative agreement between analytical predictions and the test results was achieved using the modified dynamic simulation model.

Funding constraints prevented the replacement of damaged test components and successful completion of the test program. The test fixture is still at the test site, however, awaiting potential follow-on testing. A logical future program would encompass the following:

1. Expanding the MSC/DYTRAN™ dynamic simulation model to accurately represent all parts that are loaded during the drop test impact.

2. Using the modified model to investigate all joints not directly linked to the shock strut upper attachment, and redesigning them, if necessary, to ensure no failure occurs away from the shock strut upper attachment.

3. Modification of the test facility to provide a device that arrests the weighted drop cage at a position corresponding to a fully stroked tube cutter, to prevent additional secondary damage of test articles in the event of a failure.

4. Repeating the 38 ft/s drop test and, with a reinforced trailing arm attachment fitting, if successful, proceeding with the originally planned 42 ft/s test. This would allow quantitative assessment of the analysis procedure and validation of the new upper shock strut attachment.

5. Performing a separate 38 ft/s impact test on the simulated tube cutter assembly to obtain unfiltered load-stroke data and validate the tube cutter model used in the joint analysis.

An additional recommendation is to develop a global airframe simulation tool that would unify the airframe loads, dynamics, and stress analysis models into a comprehensive database. This database would allow isolation of components for detail analysis, but retain the proper boundary conditions of the residual airframe using generalized elements. This comprehensive solution, which would dramatically increase the accuracy and decrease the conservatism of detail part stress and dynamic analysis, is possible using the commercial tools already in use by the analysis community.

7. REFERENCES

1. Wittlin, G. and Gamon, M.A., "Experimental Program for the Development of Improved Helicopter Structural Crashworthiness Analytical and Design Techniques," USAAMRDL TR 72072, May 1973

2. MacNeal-Schwendler Corporation, *MSC/DYTRAN Version 4.0 Users Manual*, November 1997

3. MIL-HDBK-5G, *Metallic Materials and Elements for Aerospace Vehicle Structures*, 1 November 1994

4. Vigness, Irwin and Welch, W.P., "Shock and Impact Considerations in Design," *ASME Handbook, Metals Engineering – Design*, Second Edition, 1965, pp. 365-377

5. Kolsky, H., *Stress Waves in Solids*, Dover Publications, Inc., 1963

6. Grumman Aerospace Corporation, "Drawing No. D10B8506 ACAP Strut Support Fitting, Sta. 340 at WL 80 Structural Analysis," 17 November 1981

This page intentionally left blank.

APPENDIX A

HIGH STRAIN RATE MATERIAL PROPERTIES TEST

Characterization of Aluminum Alloys at High Strain Rates

FINAL REPORT

Project No. 18-1898-001

Prepared for:

Bell Helicopter TEXTRON Inc.
Fort Worth, Texas

Prepared by:

Andrew Nagy and Arthur E. Nicholls
Southwest Research Institute

April 1999

SOUTHWEST RESEARCH INSTITUTE
SAN ANTONIO HOUSTON
DETROIT WASHINGTON

TABLE OF CONTENTS

INTRODUCTION A-1
THEORY OF MEASUREMENT A-1
DESCRIPTION OF SPLIT HOPKINSON PRESSURE BAR (SHPB) SYSTEM A-4
DATA ACQUISITION SYSTEM A-7
(a) Strain Gage Signal Conditioner A-7
(b) Velocity Measurement A-8
(c) High Speed Data Recording System A-8
DYNAMIC CALIBRATION OF SHPB SYSTEM A-8
TEST PROCEDURE A-9
DATA ANALYSIS PROCEDURE A-10
TEST MATRIX A-11
SUMMARY A-12
Addendum A: Compression Engineering Stress/Strain Plots A-13
Addendum B: Tension Engineering Stress/Strain Plots A-21

LIST OF FIGURES

Figure 1. Traditional Compression of SHPB Configuration with Strain Pulses A-2
Figure 2. Overall View of the Split Hopkinson Pressure Bar System A-5
Figure 3. Dimension of the SHPB Tensile Specimen A-6
Figure 4. Pressure Bar Configuration for Tensile Specimen A-6
Figure 5. Dimension of the SHPB Compression Specimen A-7
Figure 6. Shape of the Calibration Pulse A-9

INTRODUCTION

In recent years, the Hopkinson pressure bar has become an increasingly popular and useful test equipment in the study of the dynamic response of materials. The device dates back to 1914, when B. Hopkinson devised it as perhaps the first method of measuring transient impulsive stresses. In essence, the Hopkinson pressure bar is simply an elastic bar of appreciable length into which an unknown pressure-time loading applied at one end is propagated. It is assumed that this pressure pulse propagates without appreciable distortion or attenuation. By suitable measurement technique, either at the end of the bar or at a point along the radial surface, and by the application of elastic wave theory, the details of the applied pulse can be reconstructed. Since the bar remains elastic, it can be used to measure either loads or displacements.

Maximum use of the Hopkinson pressure bar for material testing is made in the arrangement first devised by H. Kolsky, where a short compression specimen is sandwiched between two bars, and it is loaded by a single pulse traveling through the system. The pressure bars in this arrangement are used both to apply the load to the specimen, and as transducers to measure the displacements and applied loads at the faces of the specimen in contact with the bars. This Split Hopkinson Pressure Bar (SHPB) technique has been applied to material testing by numerous investigators over the years.

THEORY OF MEASUREMENT

When the compressive loading pulse in the incident pressure bar reaches the specimen, a portion of the pulse is reflected from the interface, while part of the pulse is transmitted through the specimen to the transmitter bar. The relative amplitudes of the incident, reflected, and transmitted pulse will depend on the physical properties of the specimen.

If the continuous strain-time histories of the three pulses, incident, reflected and transmitted, are recorded from the pressure bars, one is then able to determine the force and displacement boundary conditions at both faces of the specimen. Having records of the incident, reflected and transmitted strain pulses, denoted as ε_I, ε_R, and ε_T, respectively, one can establish conditions at the specimen-bar interfaces as shown in Figure 1.

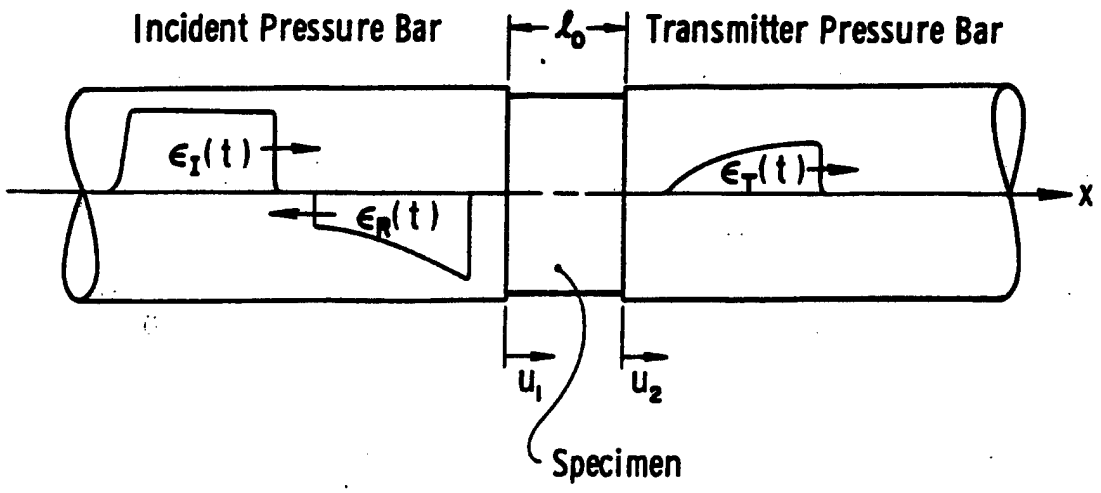

Figure 1. Traditional Compression of SHPB Configuration with Strain Pulses.

From the one-dimensional theory of elastic wave propagation,

$$u = C_0 \int_0^t \varepsilon dt \qquad \textit{Equation 1}$$

where u= displacement at time t

C_0 = elastic wave velocity of the bar material

ε = strain.

The displacement u_1 of the face of the incident bar is the result of both the incident pulse ε_I traveling in the positive x direction, and the reflected pulse ε_R traveling in the negative x direction.

Thus

$$u_1 = C_0 \int_0^t \varepsilon_I dt + (-C_0) \int_0^t, \varepsilon_R dt = C_0 \int_0^t (\varepsilon_I - \varepsilon_R) dt \qquad \textit{Equation 2}$$

Similarly, the displacement u_2 of the face of the transmitter bar is obtained from the transmitted strain pulse ε_T as

$$u_2 = C_0 \int_0^t \varepsilon_T dt \qquad \textit{Equation 3}$$

The nominal strain in the specimen ε_s is then

$$\varepsilon_s = \frac{(u_1 - u_2)}{l_0} = \frac{C_0}{l_0} \int_0^t (\varepsilon_I - \varepsilon_R - \varepsilon_T) dt \qquad \textit{Equation 4}$$

where l_0 = the initial length of the specimen.

This expression can be simplified somewhat if we assume the stress across the short specimen to be constant, which becomes exact as l_0 approaches zero. With this assumption

$$\varepsilon_R = \varepsilon_T - \varepsilon_I \qquad \textit{Equation 5}$$

After substitution into equation [4]

$$\varepsilon_s = \frac{-2C_0}{l_0} \int_0^t \varepsilon_R dt \qquad \textit{Equation 6}$$

The applied loads P_1 and P_2 on the respective faces of the specimen are

$$P_1 = EA(\varepsilon_I + \varepsilon_R)$$

and

$$P_2 = EA\varepsilon_T$$

where

E = Modulus of elasticity of the bars

A = Cross-sectional area of the pressure bars

Thus, the average stress in the specimen Φ_s is

$$\sigma_s = \frac{(P_1 + P_2)}{2A_s} = \frac{E}{2}\left(\frac{A}{A_s}\right)(\varepsilon_I + \varepsilon_R + \varepsilon_T) \qquad \textit{Equation 7}$$

where

A_s = Cross-sectional area of the specimen.

Again using equation [5], this simplifies to

$$\sigma_s = E\left(\frac{A}{A_s}\right)\varepsilon_T \qquad \textit{Equation 8}$$

In the above derivations, the recorded signals ε_I, ε_R, and ε_T are always assumed to be shifted along the time axis so as to be coincident at the specimen. In addition, the pulses are assumed unattenuated by the pressure bars.

Using equations [6] and [8], only the pulses ε_R and ε_T are required to define the strain and stress in the specimen.

DESCRIPTION OF SPLIT HOPKINSON PRESSURE BAR (SHPB) SYSTEM

The strain rate range of 1 x 10^2 sec^{-1} and 1.3 x 10^3 sec^{-1} exceeds the capabilities of the standard hydraulic test systems and, therefore, the performance of tensile or compression tests in this regime requires the use of a Split Hopkinson Pressure Bar.

An overall view of the SHPB system is shown in Figure 2. The specimen is located between the incident and transmitter pressure bars. The bars are made of high strength alloy steel. The faces in contact with the specimen are ground flat and maintained parallel. Teflon bearings are used to support the incident and transmitter bars without restricting the passage of the pressure pulse. A momentum trap at the far end of the transmitter bar is used to absorb the axial impulse.

The loading pulse is produced by an axial impact of the strike bar. It is accelerated to the desired impact velocity by a "sling-shot" type mechanism whose driving force is supplied by a torsion bar spring.

The striker bar is of the same material and has the same diameter as the pressure bars. It is released from the sling and is in free flight prior to impacting the incident bar. This method of loading produces a pressure pulse of constant amplitude and finite duration. The striker bar unloads the incident bar after the initial compression wave returns to the impact face as a tensile pulse. The tensile wave is the result of the compression wave being reflected from the free end of the striker bar as a tensile pulse. The pulse in the incident bar is, therefore, twice the length of the striker bar. The amplitude of the pulse is directly proportional to the impact velocity, which is controllable by setting the release position of the "sling-shot" mechanism.

When the compressive loading pulse in the incident pressure bar reaches the specimen, a portion of the pulse is reflected from the interface, while part of the pulse is transmitted through the specimen to the transmitter bar. The relative amplitudes of the incident, reflected, and transmitted pulse will depend on the physical properties of the specimen.

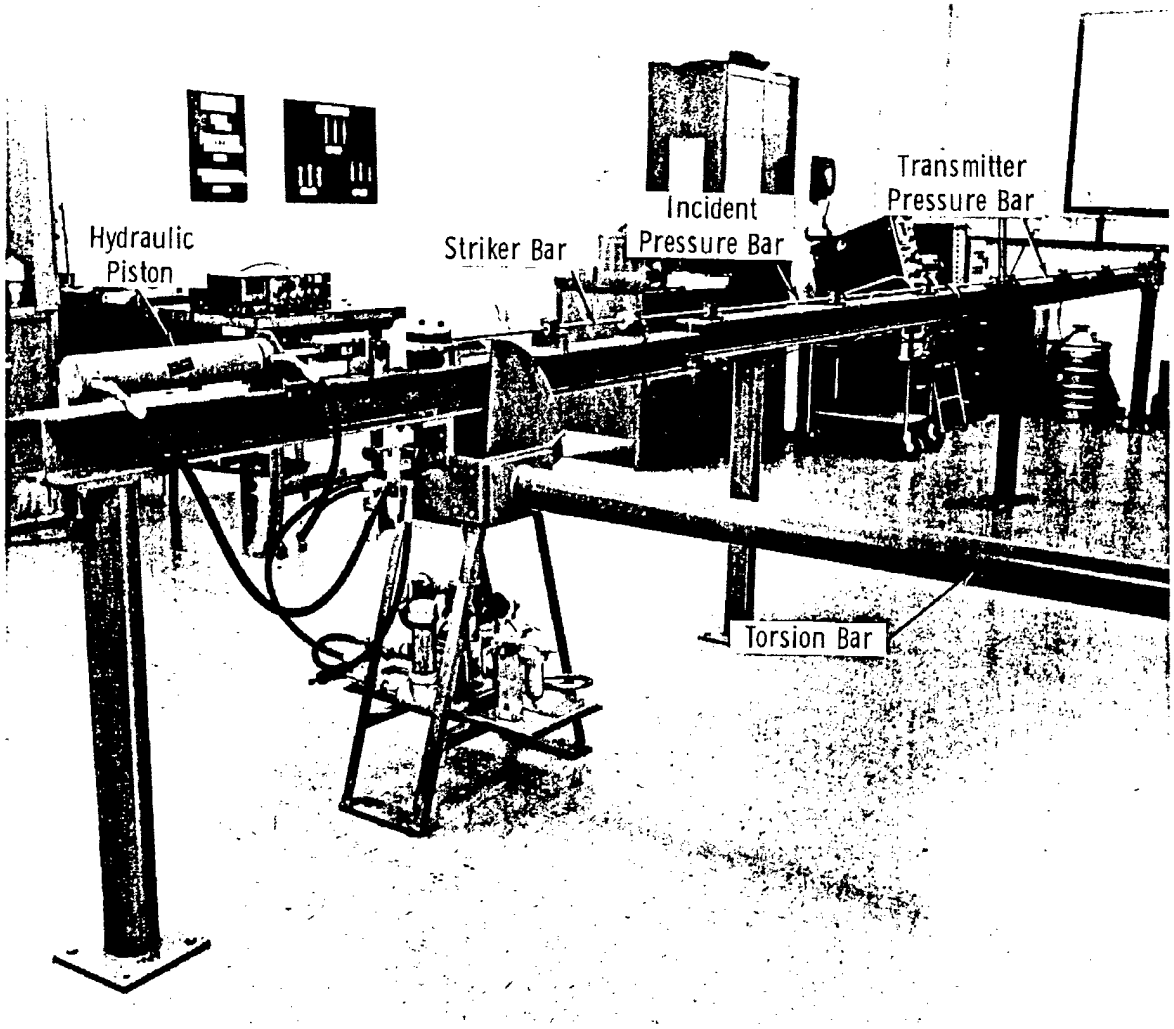

Figure 2. Overall View of the Split Hopkinson Pressure Bar System.

If the continuous strain-time histories of the incident, reflected and transmitted pulses are recorded from the pressure bars, one is then able, as noted earlier, to construct a stress-strain curve for the test specimen sandwiched between the bars using equations [6] and [8] derived above.

The pulses are recorded by means of resistive strain gages mounted on the radial surfaces of the pressure bars. The location of the gages is important in order that continuous records of each pulse may be obtained without interference from reflections. For this reason, the gages are positioned so that the distance between each gage and the ends of their respective pressure bars is greater than the length of the striker bar. On the incident pressure bar, this allows the complete incident pulse to be recorded before the arrival of the reflected pulse.

To conduct tensile testing in the SHPB, a substandard size, threaded tensile specimen (Figure 3), proportional to the standard tensile specimens specified by ASTM E-8, is employed. These specimens are attached to the incident and transmitter bars by directly threading the specimen into both bars. A split sleeve is placed around the specimen (Figure 4) to support the initial compressive pulse and to protect the specimen until the arrival of the tensile loading pulse of interest. Since the tensile loading pulse is generated by the reflection of the compressive pulse from the free distal end of the transmitter bar, the roles of the incident and transmitter bars are effectively reversed. However, the equations derived in the previous section are applicable and the measuring methodology is otherwise unchanged for both the tension and compression configurations.

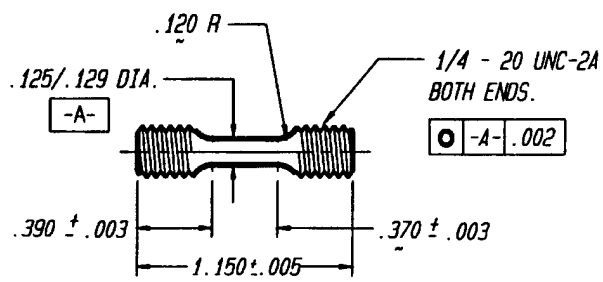

Figure 3. Threaded SHPB tensile specimen.

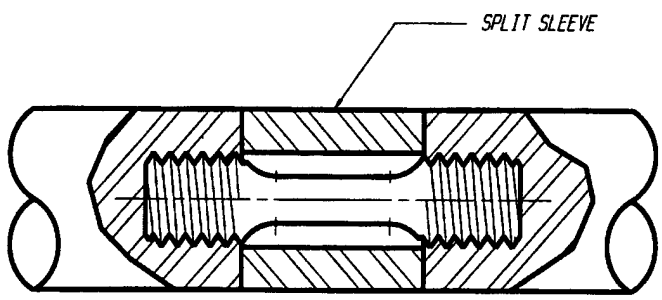

Figure 4. Protective split sleeve.

Compression testing is much more straightforward. Specimens (Figure 5) are placed between the incident and transmitter bar, centered, and held in place by a very slight compressive force from the bar system. Strain/time histories from the system (Figure 1) are analyzed as outlined in the preceding section.

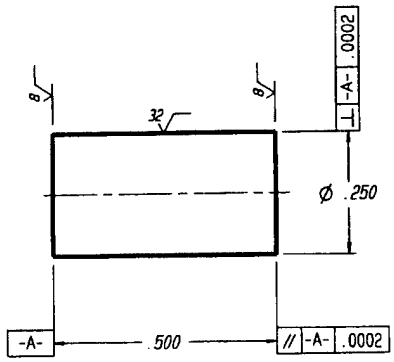

Figure 5. SHPB compression specimen.

DATA ACQUISITION SYSTEM

The most critical component of the SHPB system is, unquestionably, its instrumentation package. Precise and detailed recording of the events taking place during the loading of the test specimen is absolutely essential to allow the most accurate determination of the dynamic properties of the test material.

The instrumentation package consists of

(a) Strain gage signal conditioners,

(b) Velocity measurement device, and

High speed data recording system.

7.1 (a) Strain Gage Signal Conditioner

Approximately 20 years ago, SwRI staff designed a modular strain gage signal conditioner that has been a principal part of SwRI's dynamic material testing instrumentation. The original performance characteristics of the conditioner were rather impressive:

Bandwidth without filter	>2 MHZ
Bandwidth with built-in filter	DC to 1 MHz
Output noise (wide band)	<0.6 mVpp
Common mode rejection at 9.0 Vpp and 100 kHz	70db min.

The conditioner demonstrated excellent and trouble free performance during the past 20 years. This amplifier is still an active part of the instrumentation package and it is used to process the strain gage signals generated in the incident and transmitter bar by the impact pulse.

7.2 (b) Velocity Measurement

Accurate measurement of the impact velocity is an essential data point required for the proper operation of the SHPB system. A photo emitter/photo diode based measuring system is an accurate method for determining projectile speed prior to impact. Two pairs of emitter/diode combination are mounted in a common housing, where the pairs are accurately spaced at 0.500-inch apart. The assembly is positioned such that the impact bar velocity in free flight is measured immediately prior to impacting the incident pressure bar. The time interval between the signals of the two-diode systems is accurately measured with an HP 5315A Universal Counter. Impact velocity is calculated from the known travel distance and the time interval measured.

7.3 (c) High Speed Data Recording System

The data recording system occupies an equally important position with the strain gage conditioners in the overall instrumentation package. Currently, a NICOLET Model 4094B is used to capture the high speed signals processed by the strain gage signal conditioners described above.

DYNAMIC CALIBRATION OF THE SHPB SYSTEM

Dynamic calibration of the SHPB system for compression testing is performed with the incident and transmitter bars in contact without a specimen. The calibration is based on a loading pulse generated by an impact from the striker bar. Since the striker bar has a known length, and is of the same material and diameter as the pressure bars, the basically rectangular pulse duration is

$$\Delta t = \frac{2l_s}{C_0} \qquad \textit{Equation 9}$$

and the average strain amplitude is

$$\bar{\varepsilon} = \frac{V_0}{2C_0} \qquad \textit{Equation 10}$$

as shown schematically in Figure 6, where V_0 is the striker bar impact velocity and l_S is the length of the striker bar. If the impact velocity is accurately measured, it can be used to calibrate the output from the strain gage stations on the bars, and thus define the stress and strain in the specimen by using the following relationships:

1. The nominal strain in the specimen is

$$\varepsilon_s = \frac{-2C_o}{l_o}\int_0^t \varepsilon_R dt \qquad \textit{Equation 11}$$

and

2. The average stress in the specimen is

$$\sigma_s = E\left(\frac{A}{A_s}\right)\varepsilon_T \qquad \textbf{Equation 12}$$

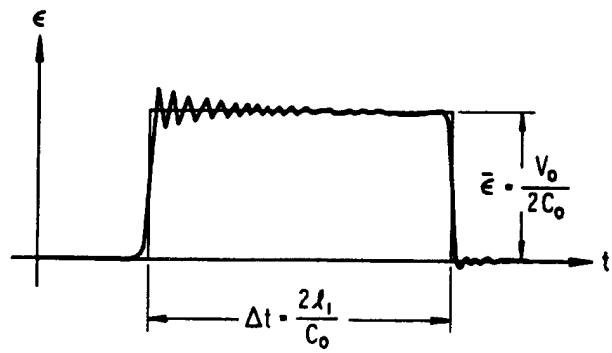

Figure 6. Shape Of The Calibration Pulse.

In the above relations, the recorded signals ε_R and ε_T are always assumed to be time coincident at the specimen.

Due to the configuration of the SHPB for tensile testing, no independent calibration shot is required. As the initial compressive pulse travels to the free end of the transmitter bar via the split sleeve around the specimen, both incident and transmitter strain gage stations can be calibrated during each test.

TEST PROCEDURE

To conduct the high strain rate tests in the SHPB system, the specimen is sandwiched between the incident and transmitter bars. A positive contact is maintained between the specimen and the bars at all times.

The loading pulse is initiated by an axial impact from the striker bar, which is accelerated to the desired impact velocity by the "sling-shot" type torsion bar mechanism, as shown in

Figure 2, for tensile testing or a gas-operated breach mechanism for compression. This method of loading produces a pressure pulse of constant amplitude and of finite duration as defined by Equations [10] and [9], respectively.

The compression wave is reflected as a tensile wave from the free end of the striker bar, returning to the impact face and thus unloading the incident bar after the initial compression wave. The pulse duration in the incident bar is therefore a function of the length of the striker bar, as defined by equation [9]. The amplitude of the pulse, as defined by equation [10], is directly proportional to the impact velocity of the striker bar. For compression testing, when the compressive loading pulse in the incident pressure bar reaches the specimen, a portion of the pulse is reflected from the interface, while part of it is transmitted through the specimen into the transmitter bar. The relative amplitudes of the incident, reflected and transmitted pulses will depend on the physical properties of the specimen material. If the continuous strain-time histories of the incident, reflected and transmitted pulses are recorded from the pressure bars, the force and displacement boundary conditions at both faces of the specimen can be determined. Again, for tensile testing, due to the configuration of the system, the strain/time histories recorded from the incident and transmitter bars are interchanged during data analysis. The pulses are recorded by means of resistance strain gages mounted on the radial surfaces of the pressure bars.

DATA ANALYSIS PROCEDURE

Stress waves generated in the incident and transmitter bars are measured by resistive strain gages mounted on the radial surfaces of the pressure bars. Each bar has two diametrically opposed gages oriented to measure strain in the long axis of the bar. These gage pairs are wired into SwRI-developed high-speed strain gage signal conditioners in a half bridge configuration. A Nicolet 4094B high-speed digital oscilloscope,* operating at a rate of 2 MS/s for tensile tests and 10 MS/s for compression tests, is used to record the amplified strain signals versus time to disk. Recorded signals are then downloaded into a PC with Vu-Point©, a data analysis software package from S-Cubed, a division of Maxwell Laboratories, Inc. Vu-Point© is used to scale and integrate the signals to determine strain rate and generate engineering stress and strain curves utilizing formulae outlined elsewhere in this report. These values are then output in ASCII-formatted columnar files, which are subsequently input into an Excel spreadsheet for the generation of engineering stress/strain plots and printing.

When required, specimens would have two strain gages applied. Located in the center of the gage section, the diametrically opposed gages were amplified and recorded individually. During analysis with Vu-Point©, the strain signals were scaled, averaged and made time coincident with the stress/strain data from the bars. Subsequently, these data would be incorporated into the ASCII-formatted output, as mentioned above.

* Nicolet Instrument Corporation, Madison, WI.

TEST MATRIX

Compression and tensile specimens were supplied to SwRI by Bell Helicopter TEXTRON Inc. in finished form. Samples were taken from each of three aluminum alloys, 7050, 7055, and 7075, and are identified in this report as Series 50, 55, and 75, respectively. In addition, specimens from each series were machined from each of three orientations, longitudinal, long transverse, and short transverse (L, LT, and ST, respectively). The complete test matrices for both tension and compression are summarized in Tables 1 and 2. All specimens were tested at a single strain rate range of 1200 to 1500 sec^{-1}.

Table 1. Tension Test Matrix

Series	Orientation	Strain Gage*	Number of Tests
50	L	H	3
	LT	NR	3
	ST	A	3
55	L	H	3
	LT	NR	3
	ST	A	3
75	L	H	3
	LT	NR	3
	ST	A	3

*A=Axial, H=Hoop, NR=Not Required

Table 2. Compression Test Matrix

Series	Orientation	Strain Gage*	Number of Tests
50	L	NR	1
	LT	NR	1
	ST	NR	1
55	L	NR	1
	LT	NR	1
	ST	NR	1
75	L	NR	1
	LT	NR	1
	ST	NR	1

*A=Axial, H=Hoop, NR=Not Required

SUMMARY

High strain rate tension and compression tests were run at a single high strain rate within the range of 1200 to 1500 s^{-1}. Three specimen orientations, longitudinal, long transverse, and short transverse, from each of the aluminum alloys, 7050, 7055, and 7075, were tested. Selected samples were strain gauged in either the axial or hoop direction.

Test results are presented in the form of engineering stress/strain plots and are included in the appendices. Several additional compression tests were run on the 50 series samples while defining the appropriate striker impact velocity to produce the desired strain rates.

The specimen identification strategy employed can be used to determine material, specimen orientation, and type of loading. The first two digits refer to material (as identified by series) and the next letter(s) denote orientation. The suffix of the test ID indicates sample number and a "C" if compressive loading was employed.

Compression Engineering Stress/Strain Plots

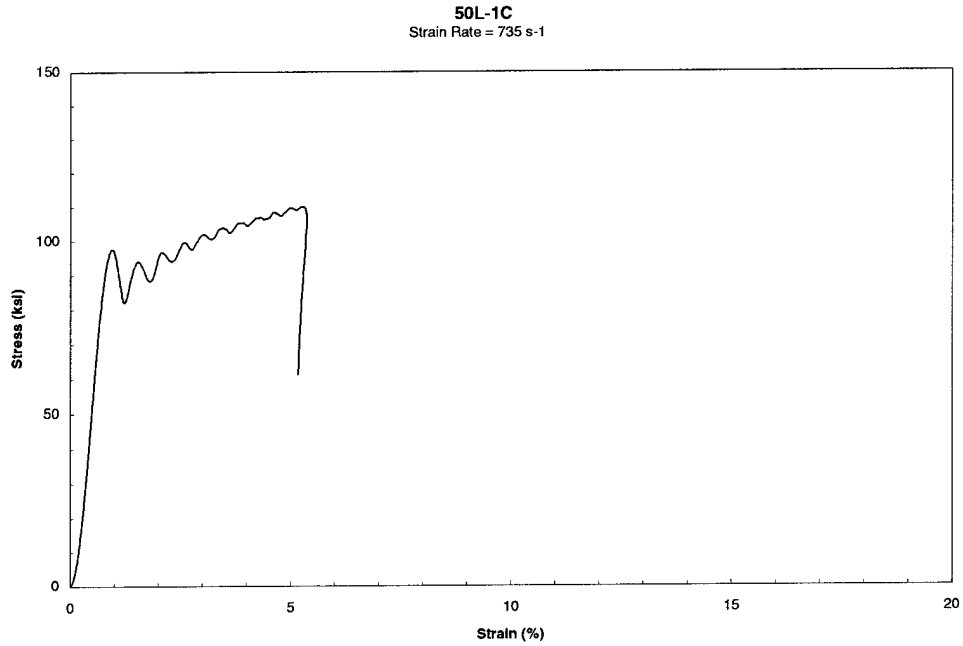
50L-1C
Strain Rate = 735 s-1
150
100
50
0
Stress (ksi)
0
5
10
15
20
Strain (%)

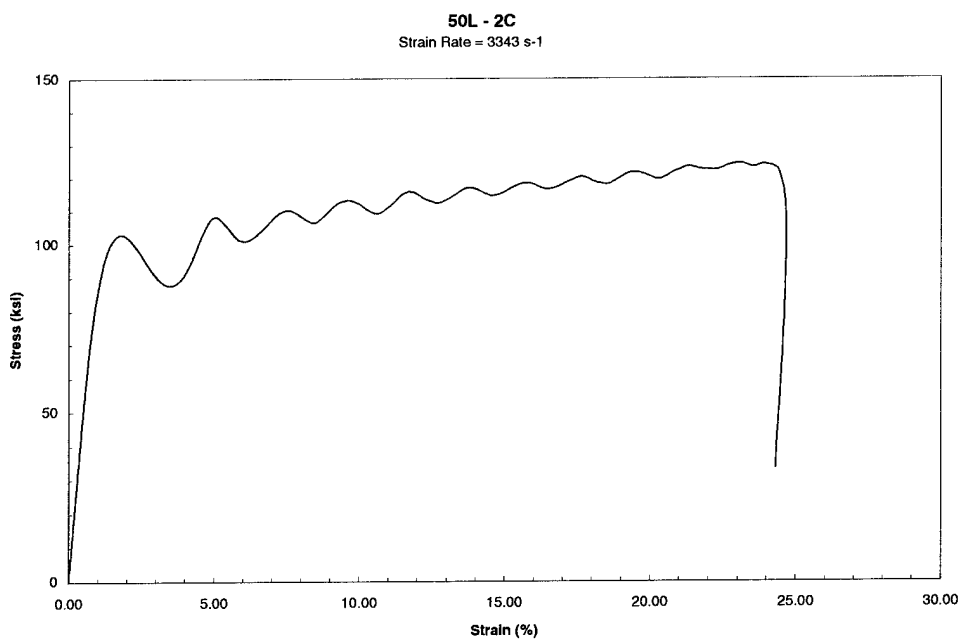
50L - 2C
Strain Rate = 3343 s-1
150
100
50
0
Stress (ksi)
0.00
5.00
10.00
15.00
20.00
25.00
30.00
Strain (%)

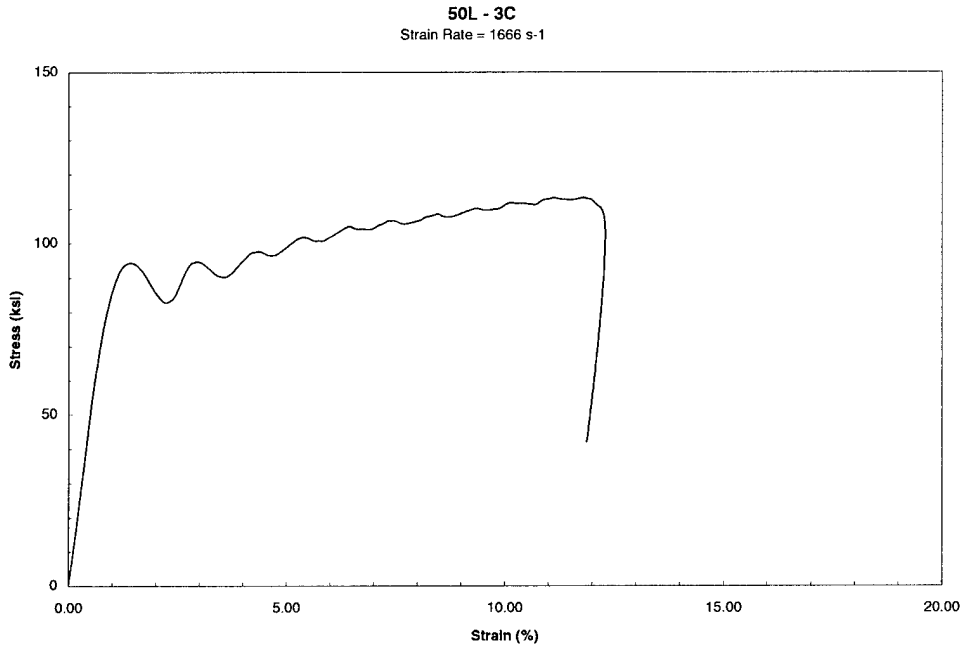
50L - 3C
Strain Rate = 1666 s-1
150
100
50
0
Stress (ksi)
0.00
5.00
10.00
15.00
20.00
Strain (%)

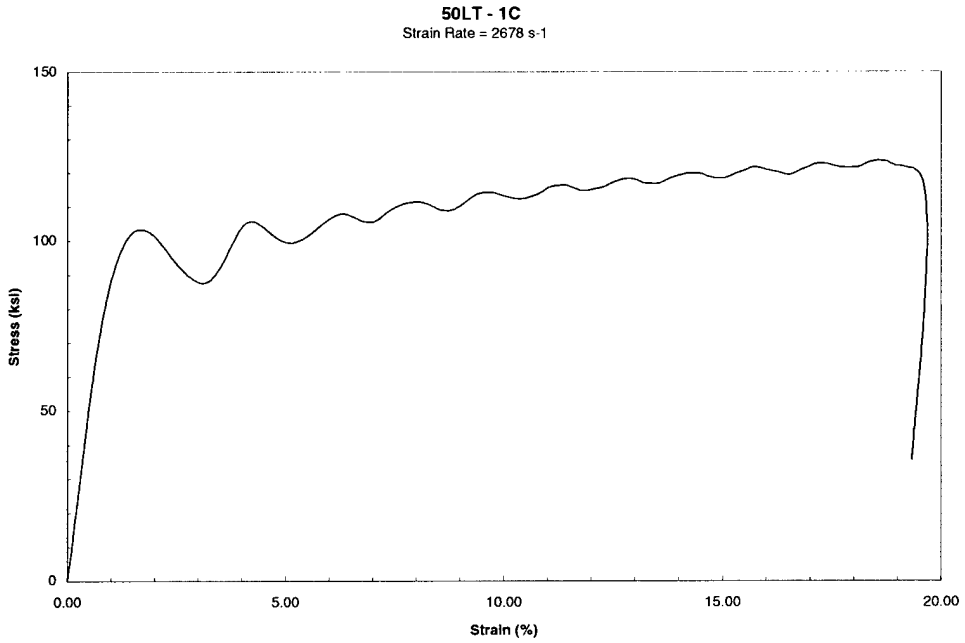
50LT - 1C
Strain Rate = 2678 s-1
150
100
50
0
Stress (ksi)
0.00
5.00
10.00
15.00
20.00
Strain (%)

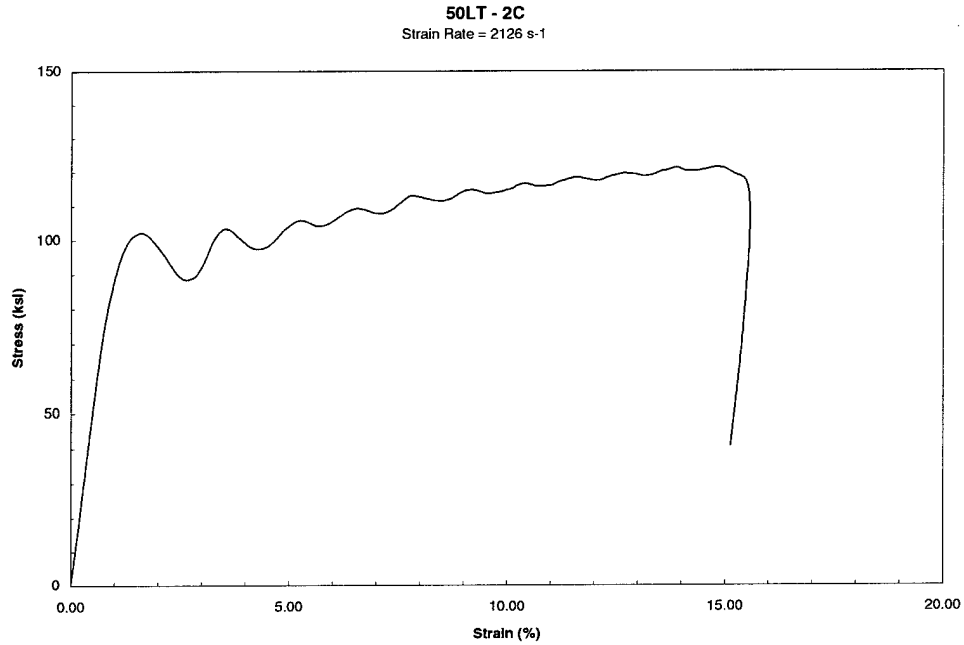
50LT - 2C
Strain Rate = 2126 s-1
150
100
50
0
Stress (ksi)
0.00
5.00
10.00
15.00
20.00
Strain (%)

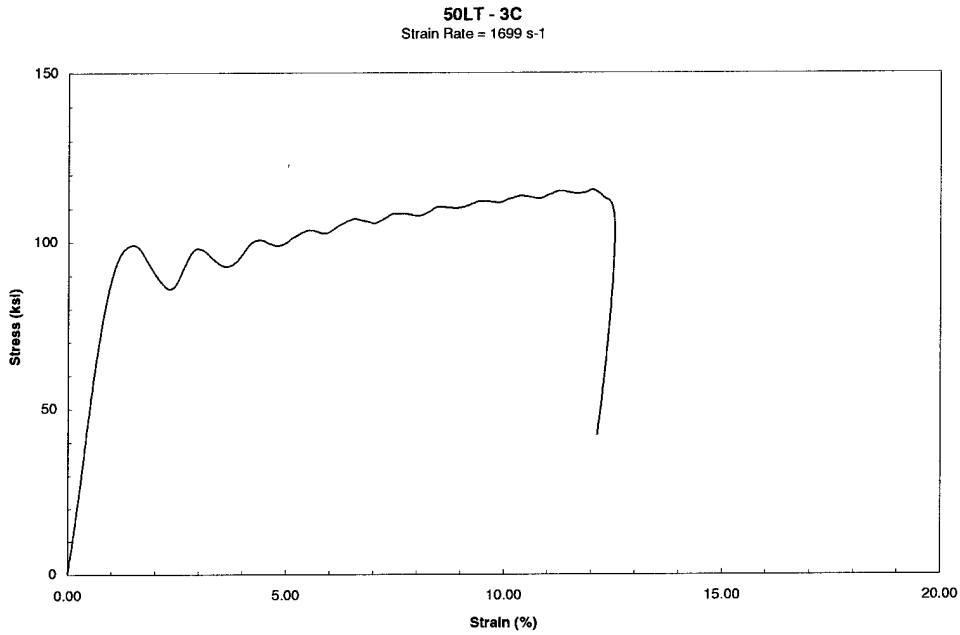
50LT - 3C
Strain Rate = 1699 s-1
150
100
50
0
Stress (ksi)
0.00
5.00
10.00
15.00
20.00
Strain (%)

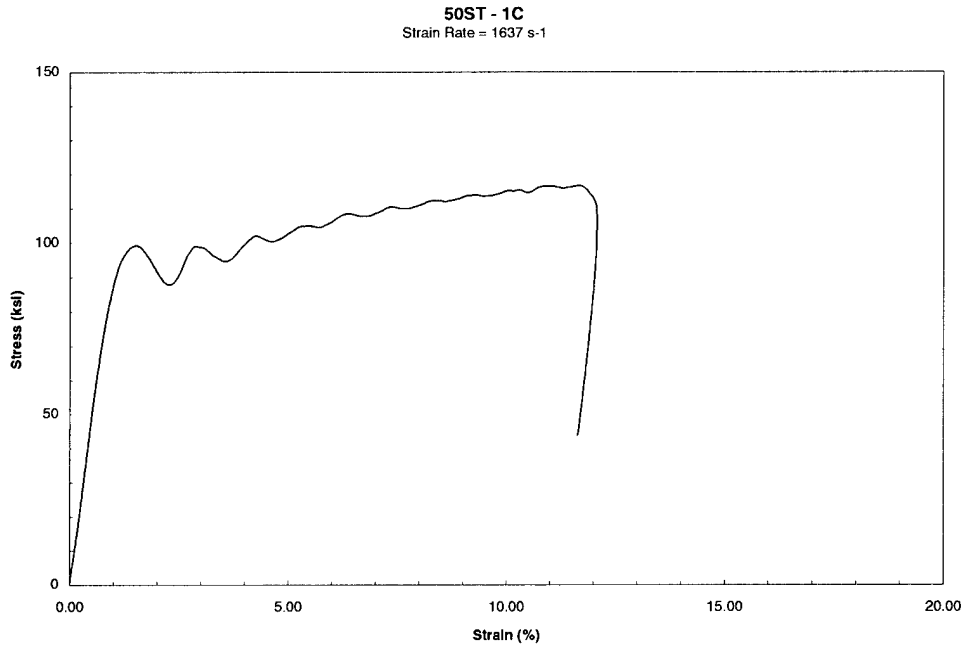
50ST - 1C
Strain Rate = 1637 s-1
150
100
50
0
Stress (ksi)
0.00
5.00
10.00
15.00
20.00
Strain (%)

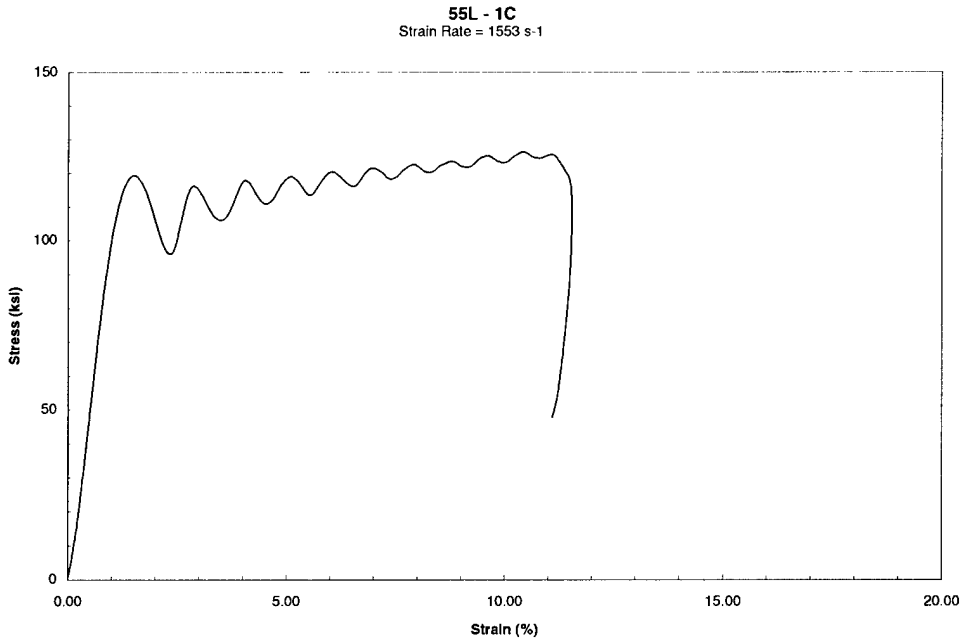
55L - 1C
Strain Rate = 1553 s-1
150
100
50
0
Stress (ksi)
0.00
5.00
10.00
15.00
20.00
Strain (%)

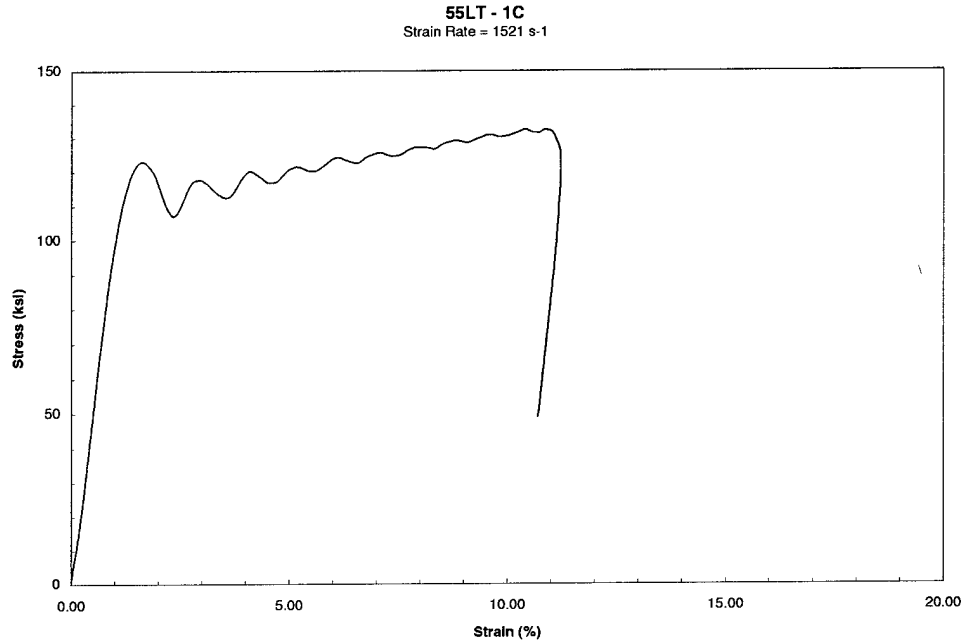
55LT - 1C
Strain Rate = 1521 s-1
150
100
50
0
Stress (ksi)
0.00
5.00
10.00
15.00
20.00
Strain (%)

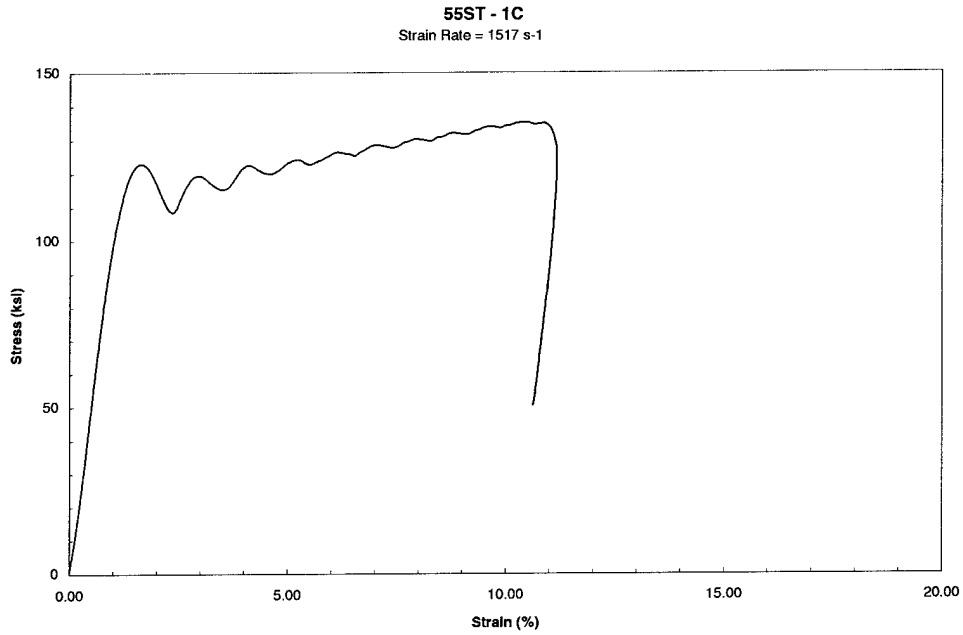
55ST - 1C
Strain Rate = 1517 s-1
150
100
50
0
Stress (ksi)
0.00
5.00
10.00
15.00
20.00
Strain (%)

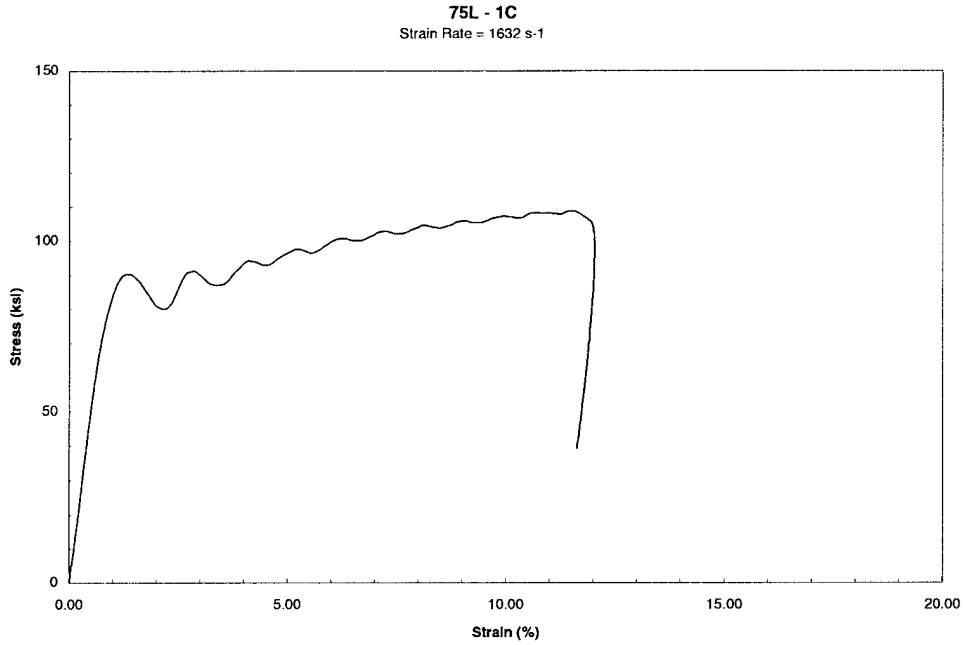
75L - 1C
Strain Rate = 1632 s-1
150
100
50
0
Stress (ksi)
0.00
5.00
10.00
15.00
20.00
Strain (%)

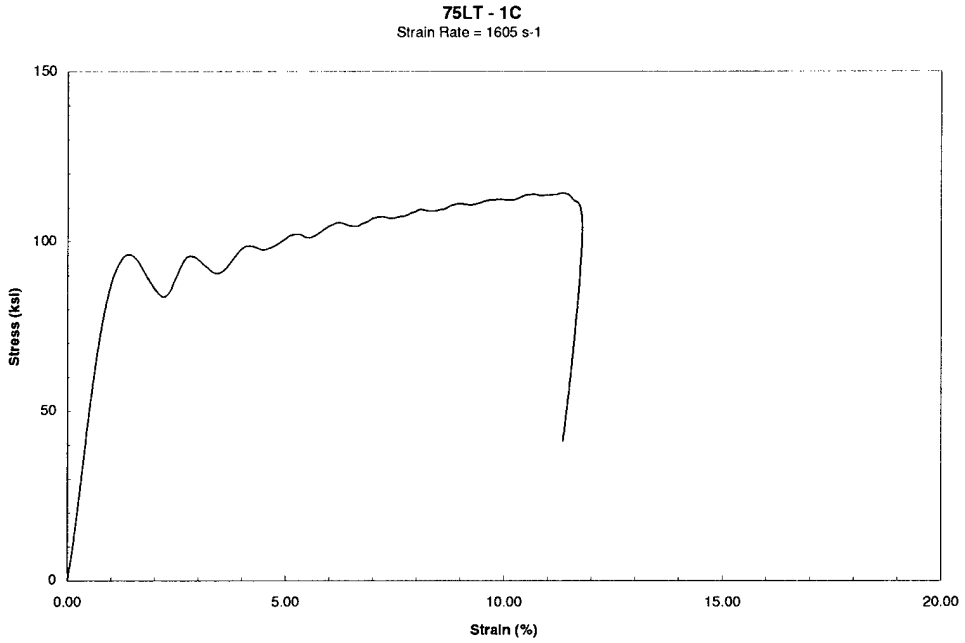
75LT - 1C
Strain Rate = 1605 s-1
150
100
50
0
Stress (ksi)
0.00
5.00
10.00
15.00
20.00
Strain (%)

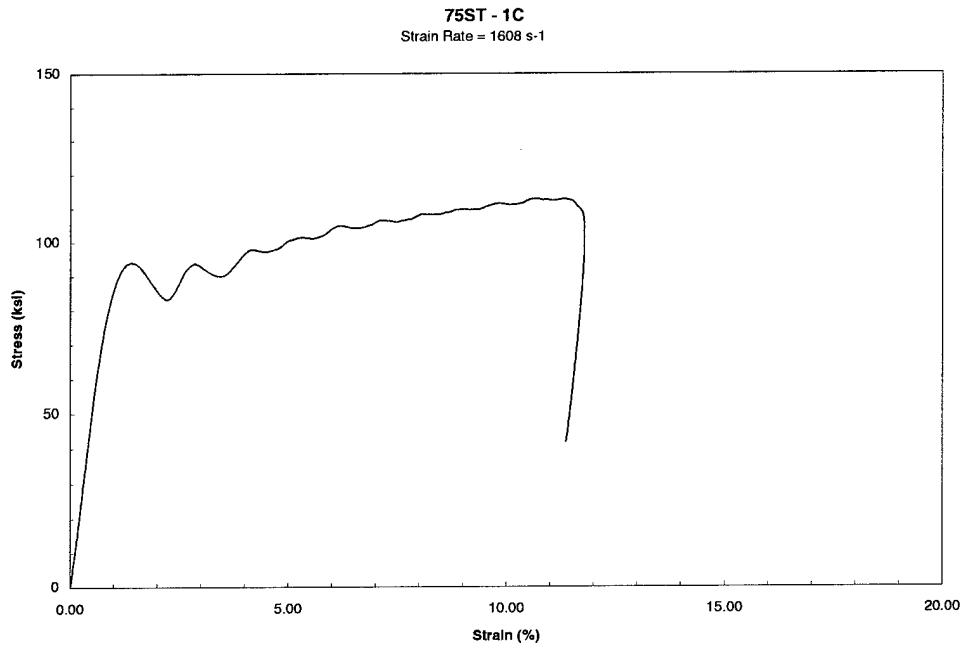
75ST - 1C
Strain Rate = 1608 s-1
150
100
50
0
Stress (ksi)
0.00
5.00
10.00
15.00
20.00
Strain (%)

Addendum B to Appendix A

Tension Engineering Stress/Strain Plots

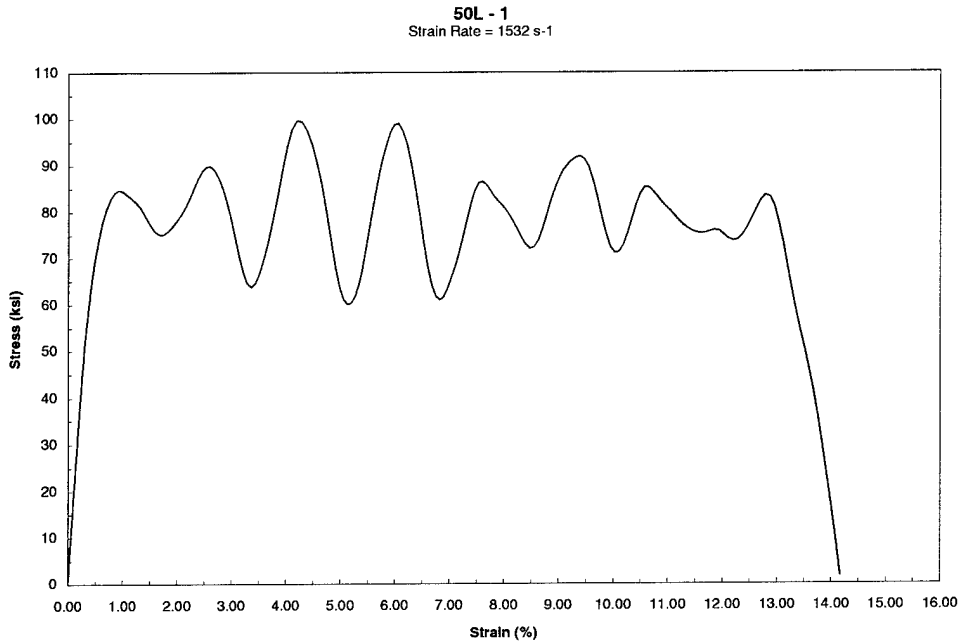
50L - 1
Strain Rate = 1532 s-1
Stress (ksi)
Strain (%)
0
10
20
30
40
50
60
70
80
90
100
110
0.00
1.00
2.00
3.00
4.00
5.00
6.00
7.00
8.00
9.00
10.00
11.00
12.00
13.00
14.00
15.00
16.00

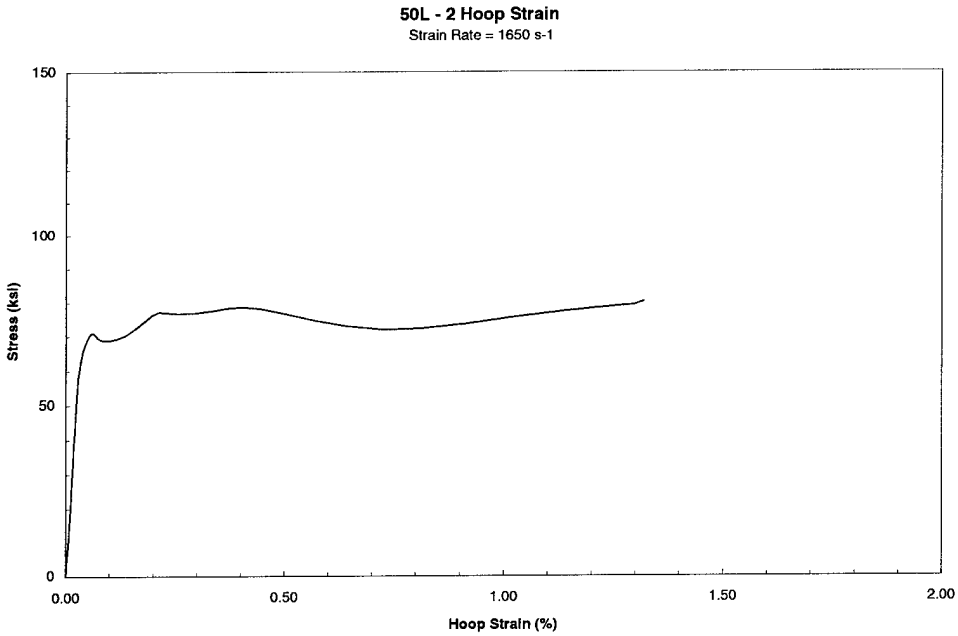
50L - 2 Hoop Strain
Strain Rate = 1650 s-1
Stress (ksi)
Hoop Strain (%)
0
50
100
150
0.00
0.50
1.00
1.50
2.00

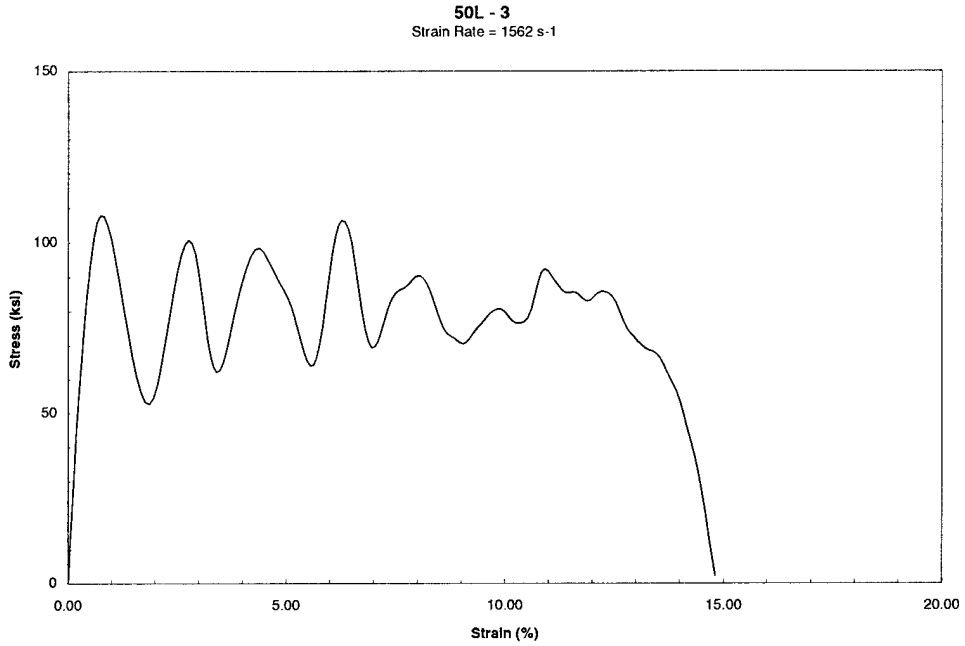
50L - 3
Strain Rate = 1562 s-1
150
100
50
0
Stress (ksi)
0.00
5.00
10.00
15.00
20.00
Strain (%)

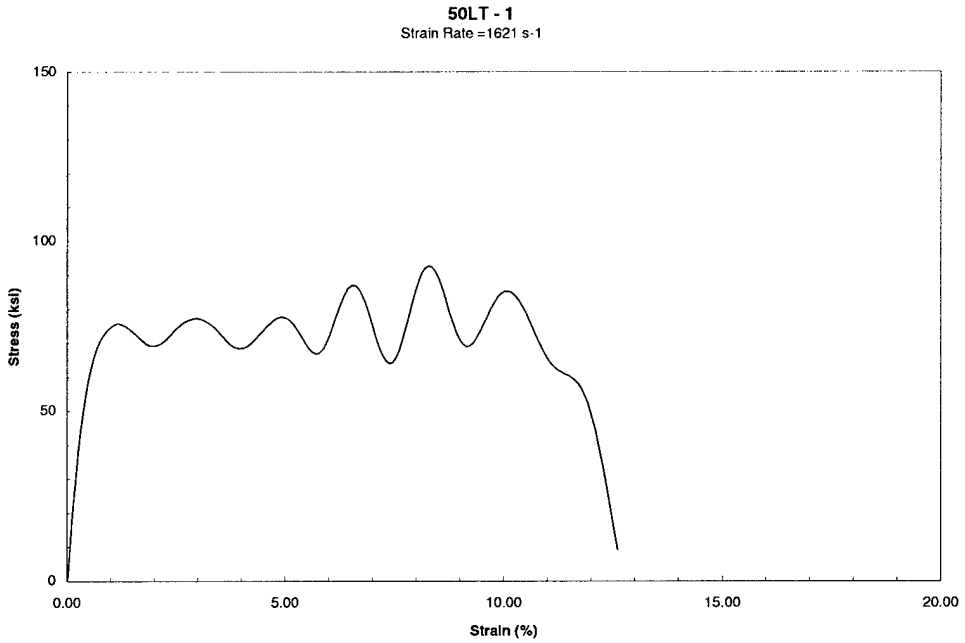
50LT - 1
Strain Rate =1621 s-1
150
100
50
0
Stress (ksi)
0.00
5.00
10.00
15.00
20.00
Strain (%)

50LT - 2
Strain Rate = 1591 s-1

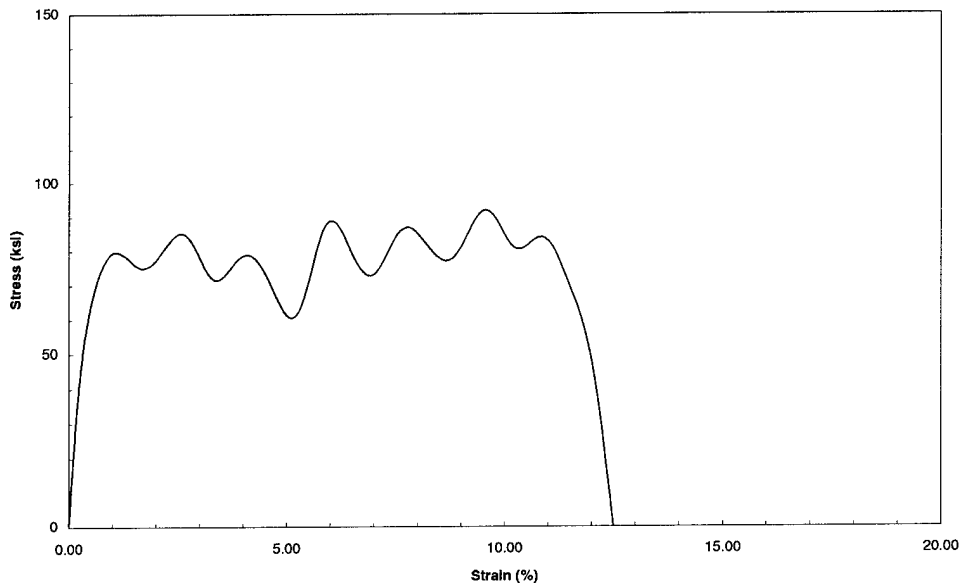

50LT - 3
Strain Rate = 1616 s-1

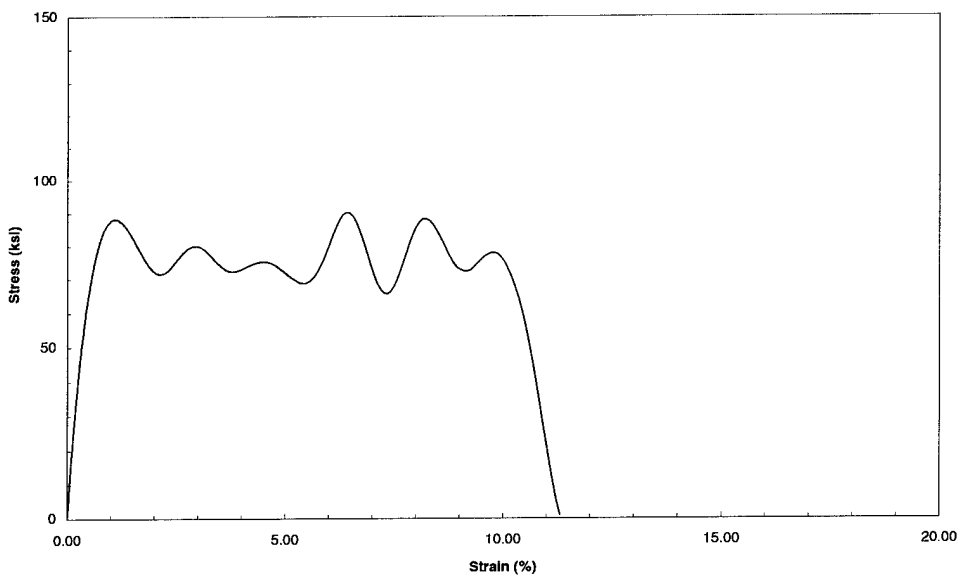

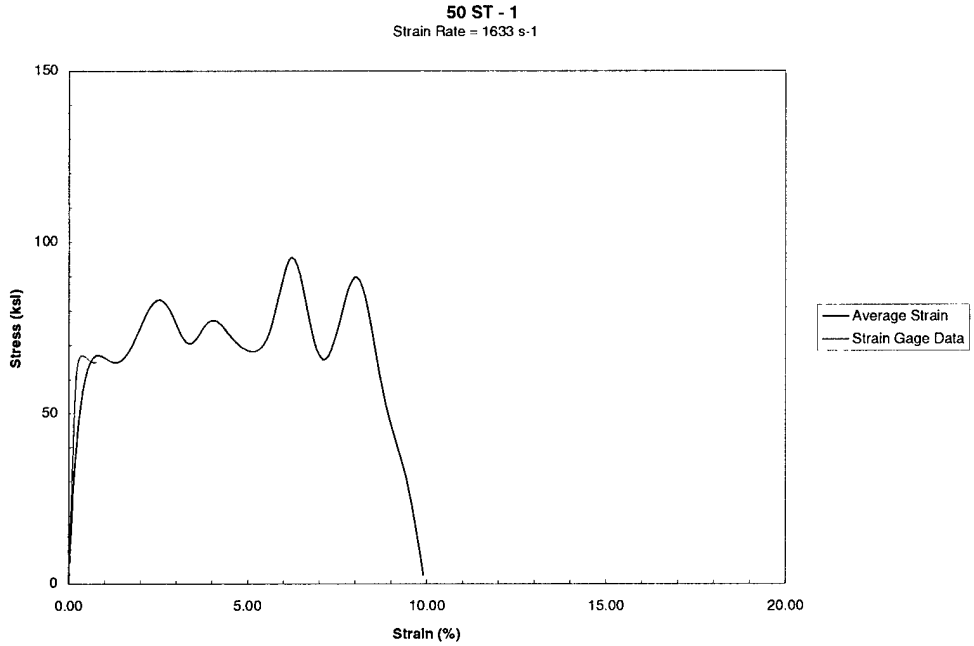
50 ST - 1
Strain Rate = 1633 s-1
150
100
50
0
Stress (ksi)
0.00
5.00
10.00
15.00
20.00
Strain (%)
Average Strain
Strain Gage Data

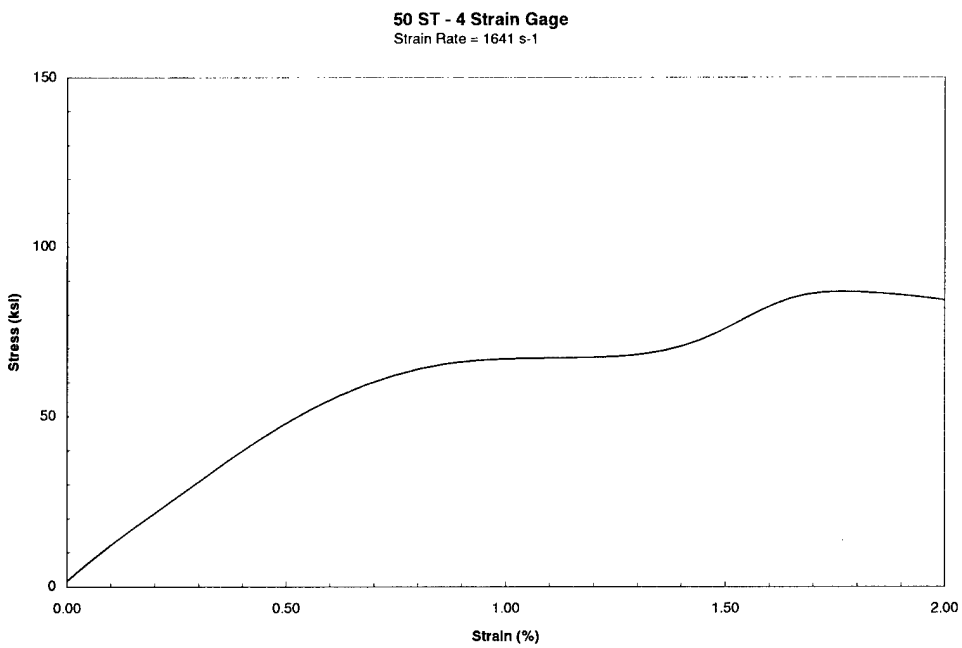
50 ST - 4 Strain Gage
Strain Rate = 1641 s-1
150
100
50
0
Stress (ksi)
0.00
0.50
1.00
1.50
2.00
Strain (%)

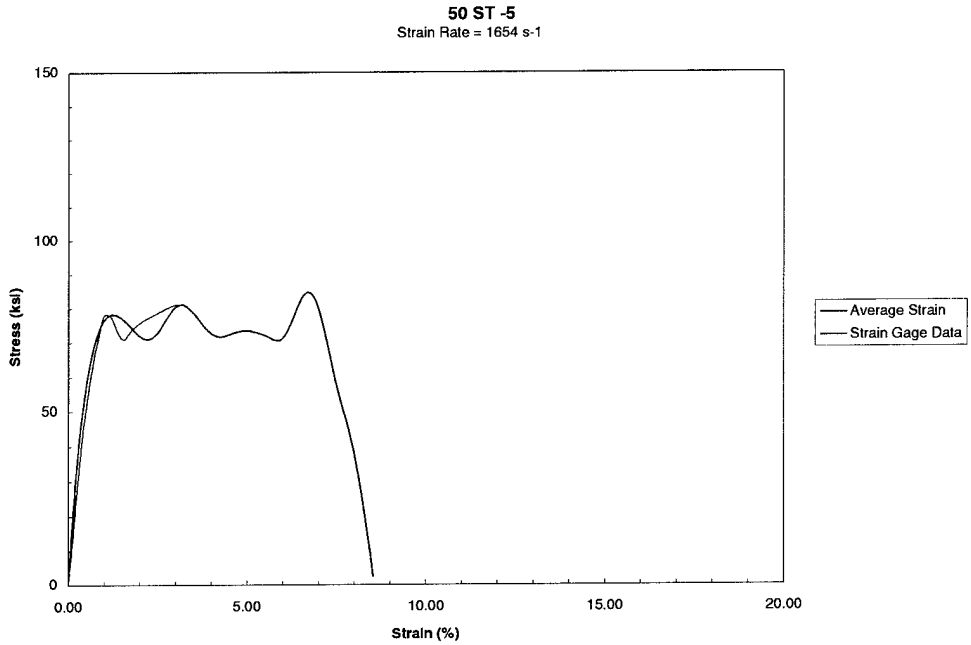
50 ST -5
Strain Rate = 1654 s-1
150
100
50
0
Stress (ksi)
0.00
5.00
10.00
15.00
20.00
Strain (%)
Average Strain
Strain Gage Data

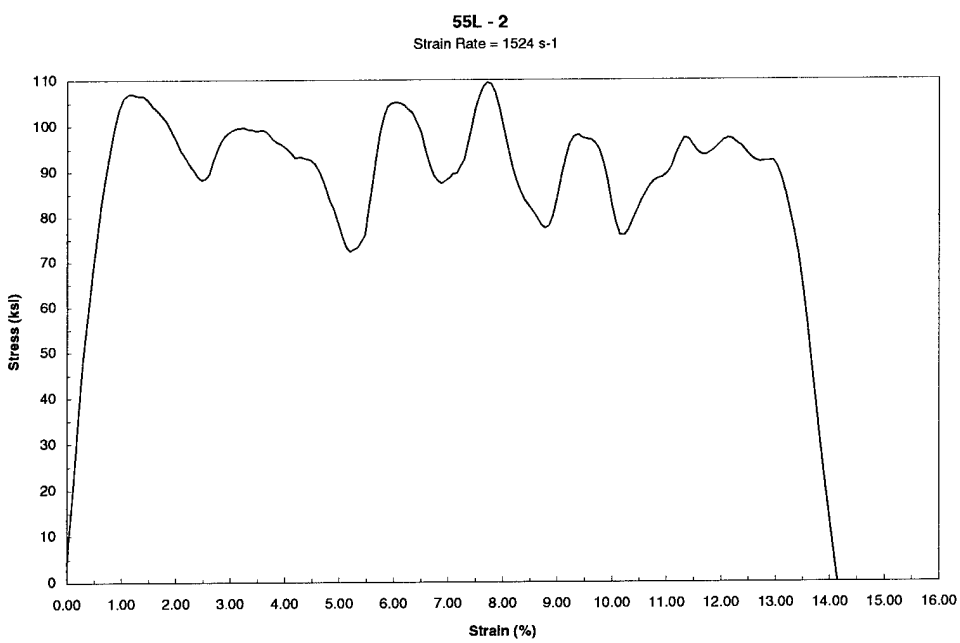
55L - 2
Strain Rate = 1524 s-1
110
100
90
80
70
60
50
40
30
20
10
0
Stress (ksi)
0.00
1.00
2.00
3.00
4.00
5.00
6.00
7.00
8.00
9.00
10.00
11.00
12.00
13.00
14.00
15.00
16.00
Strain (%)

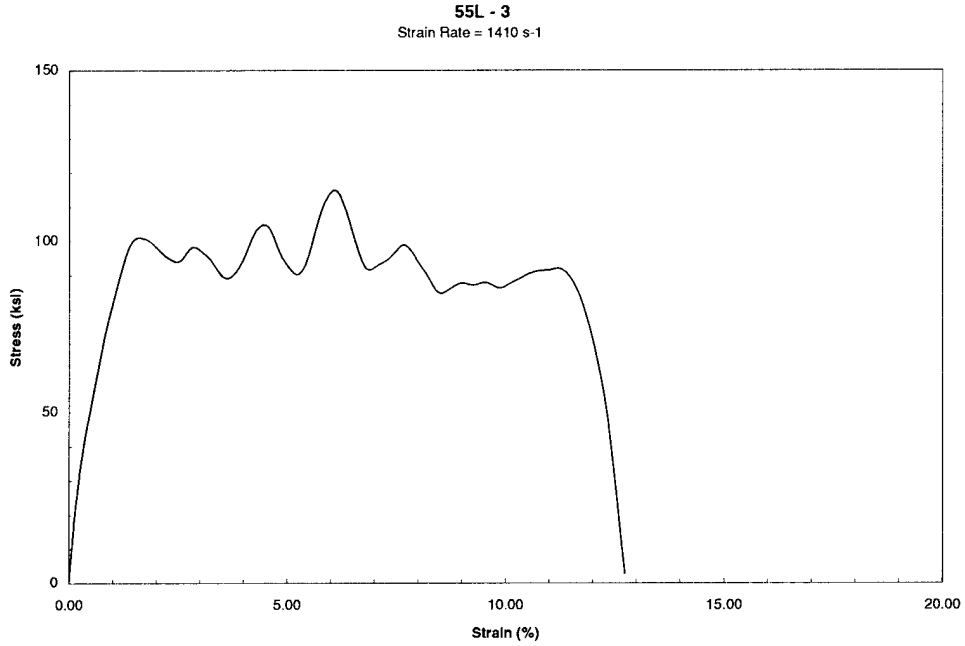
55L - 3
Strain Rate = 1410 s-1
150
100
50
0
Stress (ksi)
0.00
5.00
10.00
15.00
20.00
Strain (%)

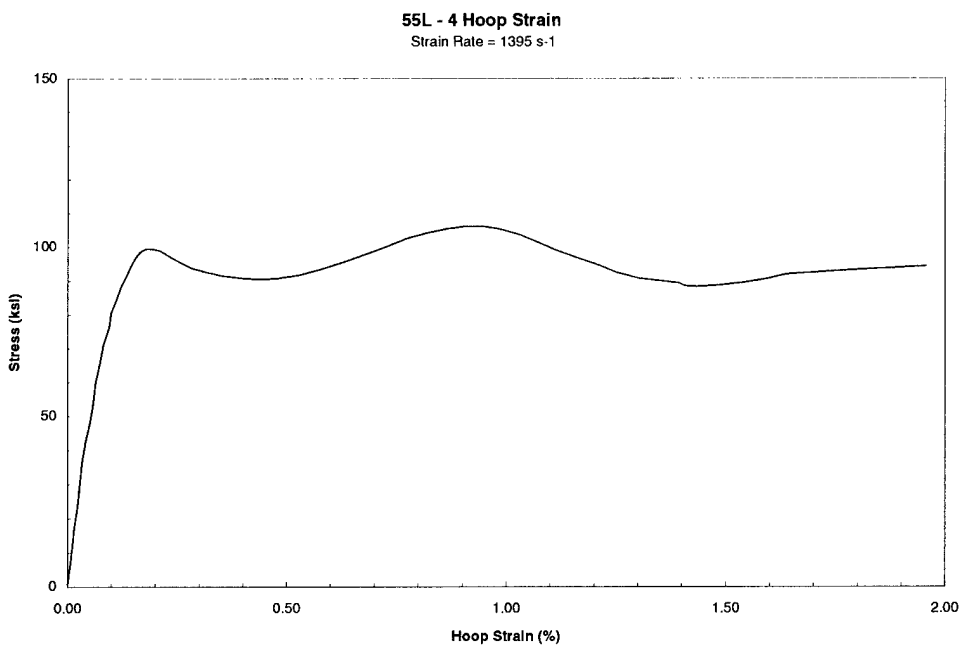
55L - 4 Hoop Strain
Strain Rate = 1395 s-1
150
100
50
0
Stress (ksi)
0.00
0.50
1.00
1.50
2.00
Hoop Strain (%)

55LT - 1
Strain Rate = 1479 s-1

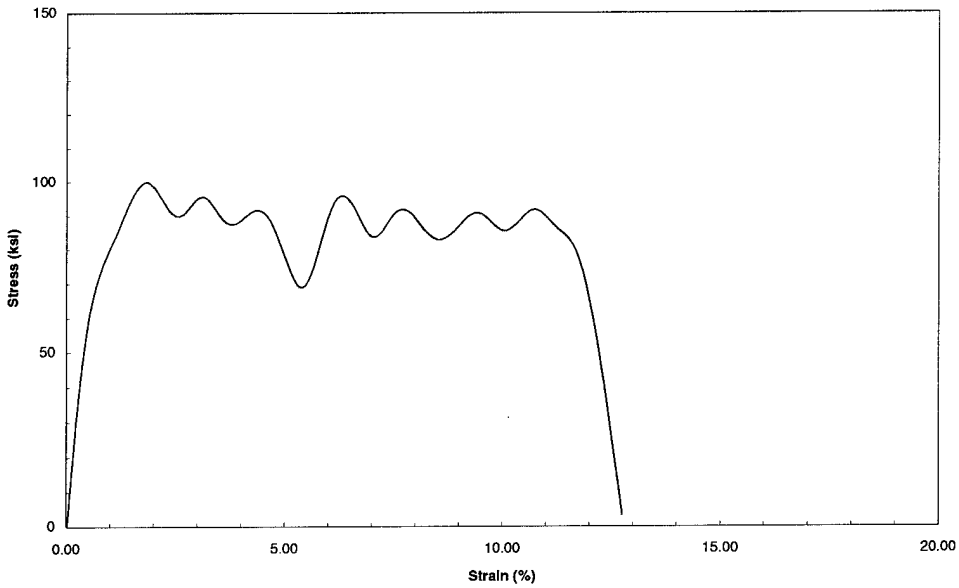

55LT - 2
Strain Rate = 1561 s-1

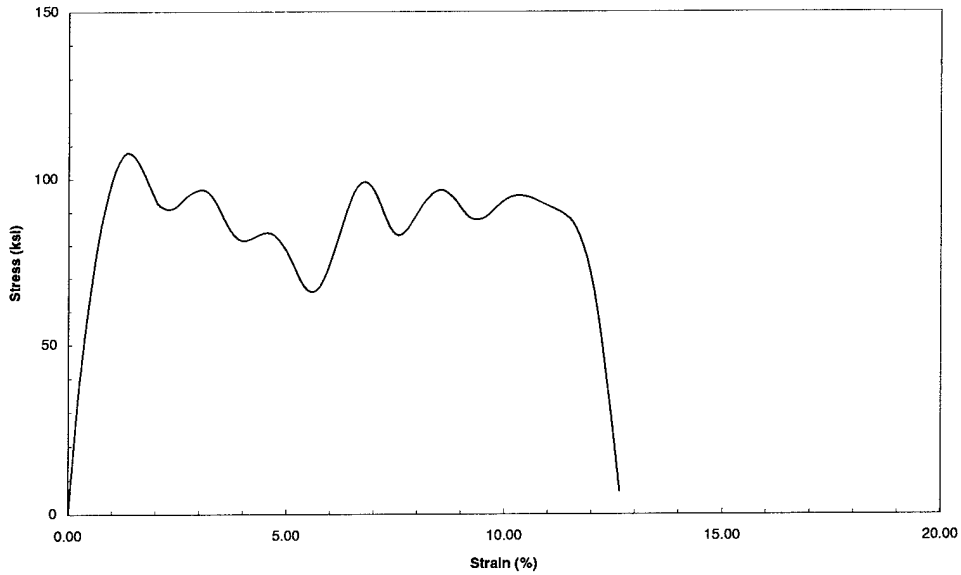

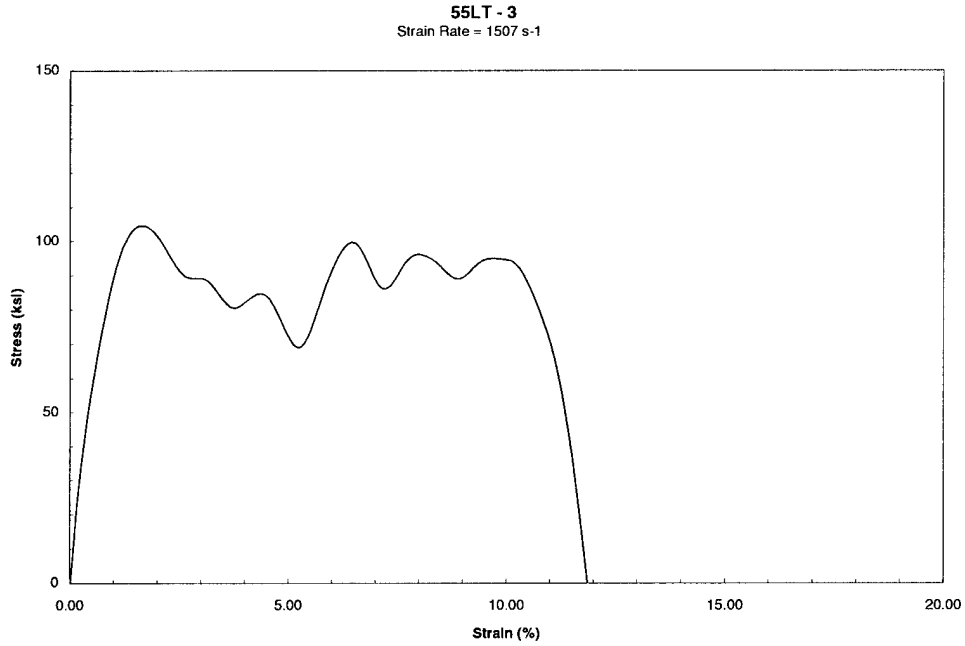
55LT - 3
Strain Rate = 1507 s-1
150
100
50
0
Stress (ksi)
0.00
5.00
10.00
15.00
20.00
Strain (%)

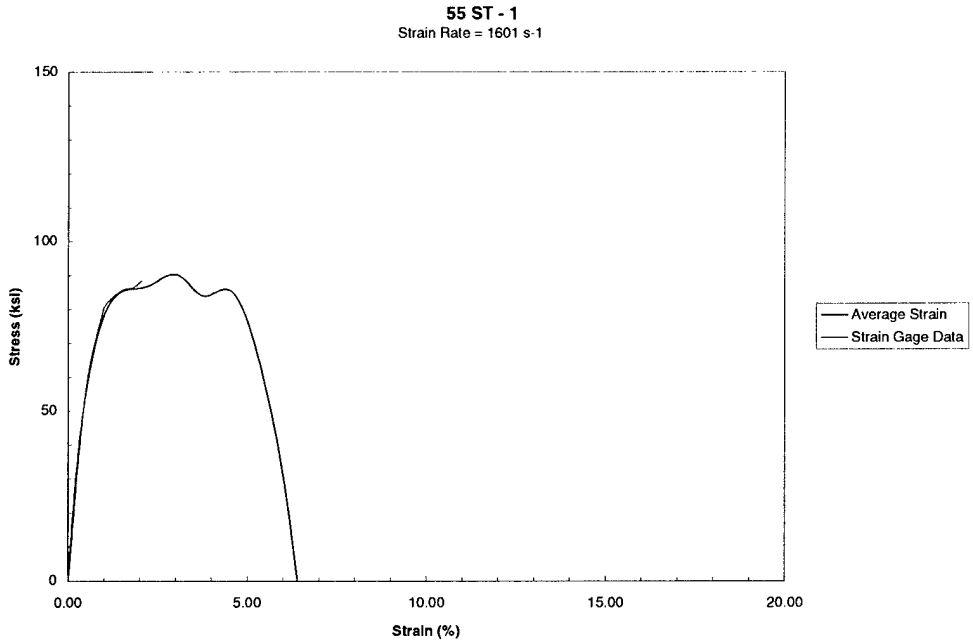
55 ST - 1
Strain Rate = 1601 s-1
150
100
50
0
Stress (ksi)
0.00
5.00
10.00
15.00
20.00
Strain (%)
Average Strain
Strain Gage Data

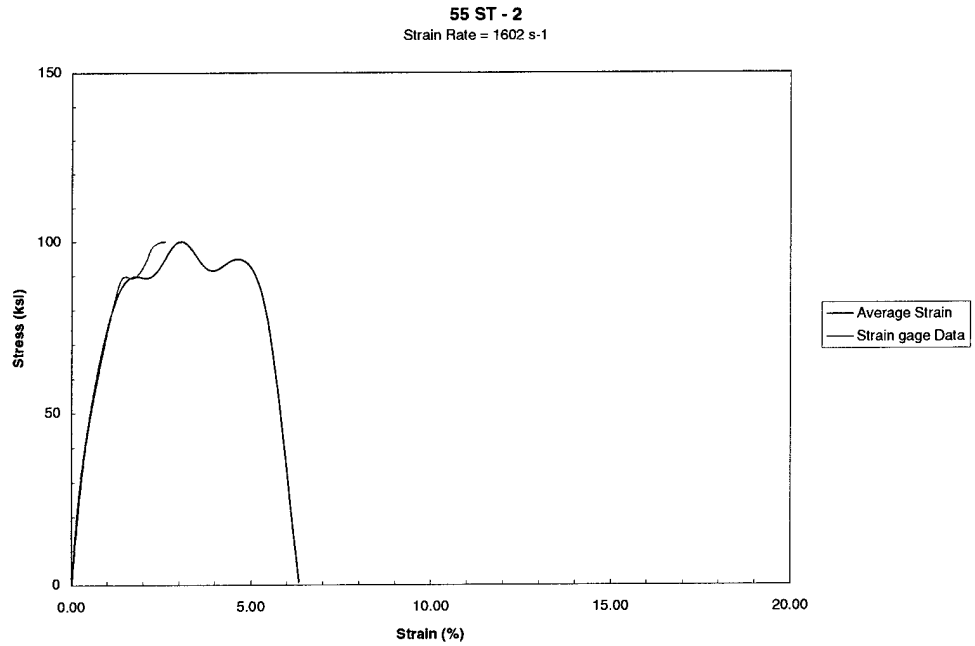
55 ST - 2
Strain Rate = 1602 s-1
150
100
50
0
Stress (ksi)
0.00
5.00
10.00
15.00
20.00
Strain (%)
Average Strain
Strain gage Data

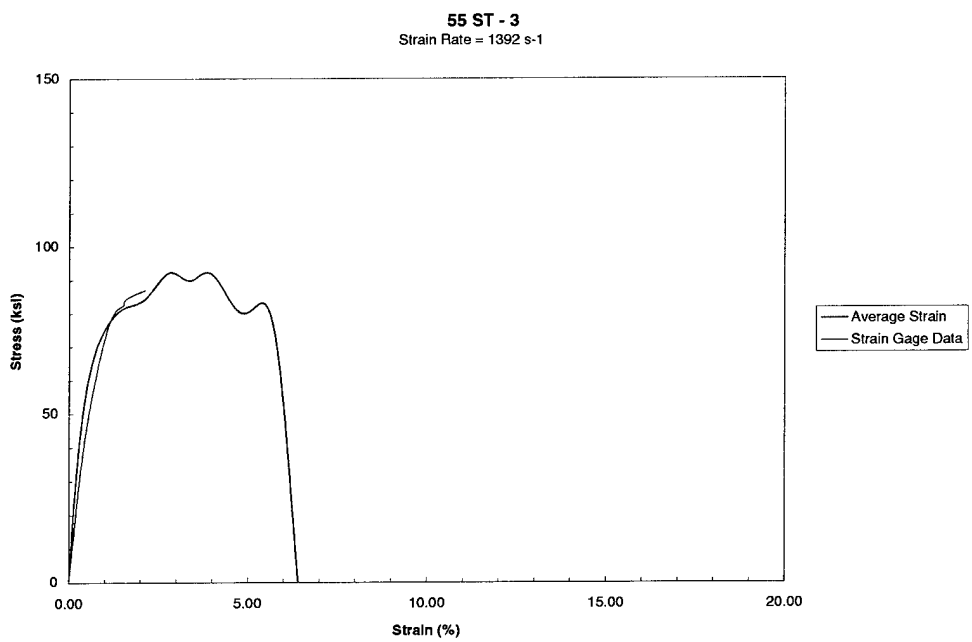
55 ST - 3
Strain Rate = 1392 s-1
150
100
50
0
Stress (ksi)
0.00
5.00
10.00
15.00
20.00
Strain (%)
Average Strain
Strain Gage Data

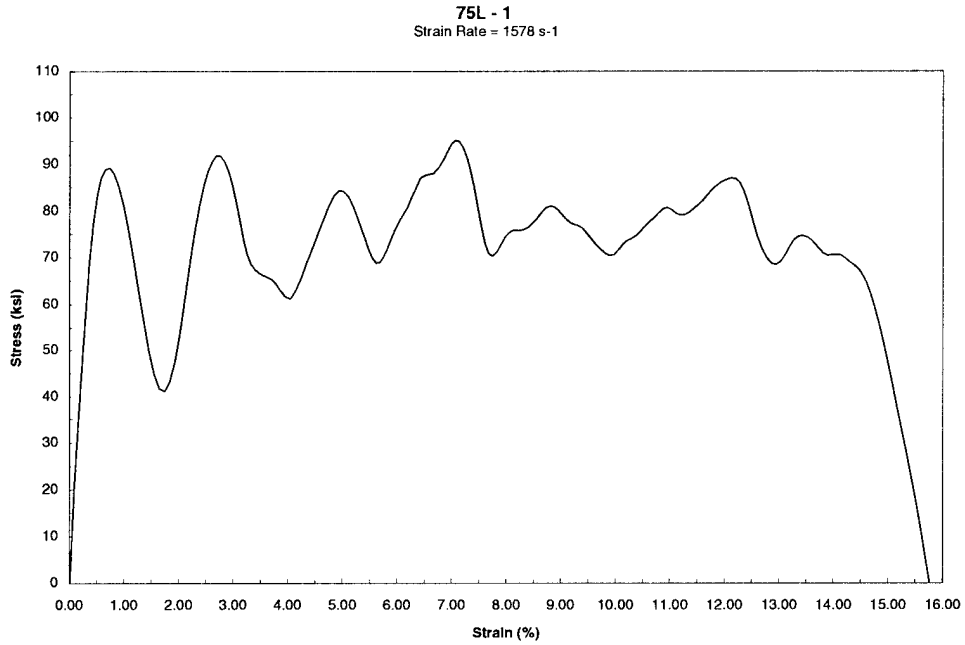
75L - 1
Strain Rate = 1578 s-1
Stress (ksi)
Strain (%)
0
10
20
30
40
50
60
70
80
90
100
110
0.00
1.00
2.00
3.00
4.00
5.00
6.00
7.00
8.00
9.00
10.00
11.00
12.00
13.00
14.00
15.00
16.00

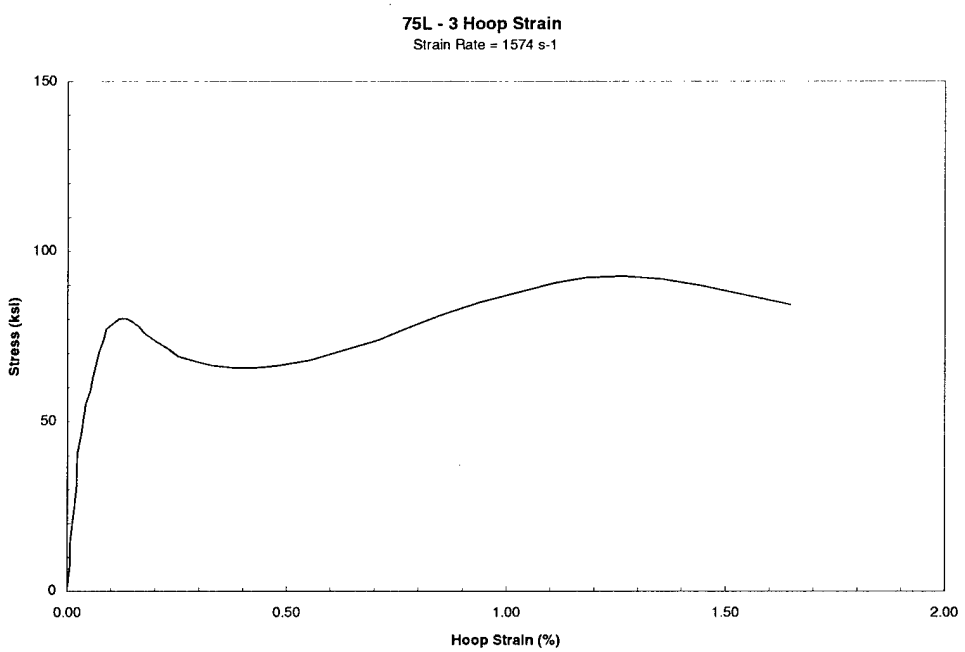
75L - 3 Hoop Strain
Strain Rate = 1574 s-1
Stress (ksi)
Hoop Strain (%)
0
50
100
150
0.00
0.50
1.00
1.50
2.00

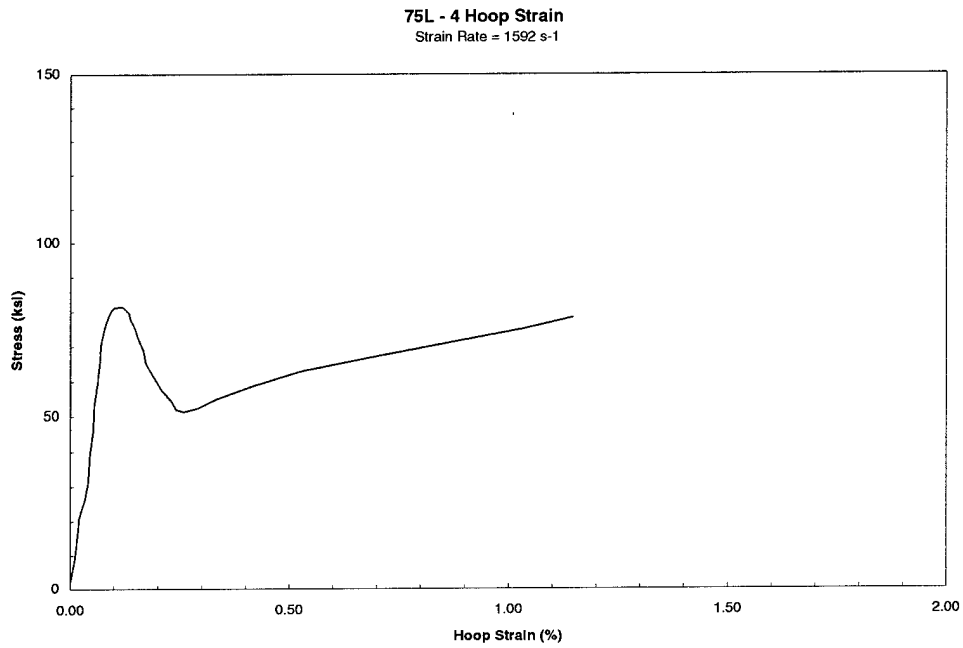
75L - 4 Hoop Strain
Strain Rate = 1592 s-1
150
100
50
0
Stress (ksi)
0.00
0.50
1.00
1.50
2.00
Hoop Strain (%)

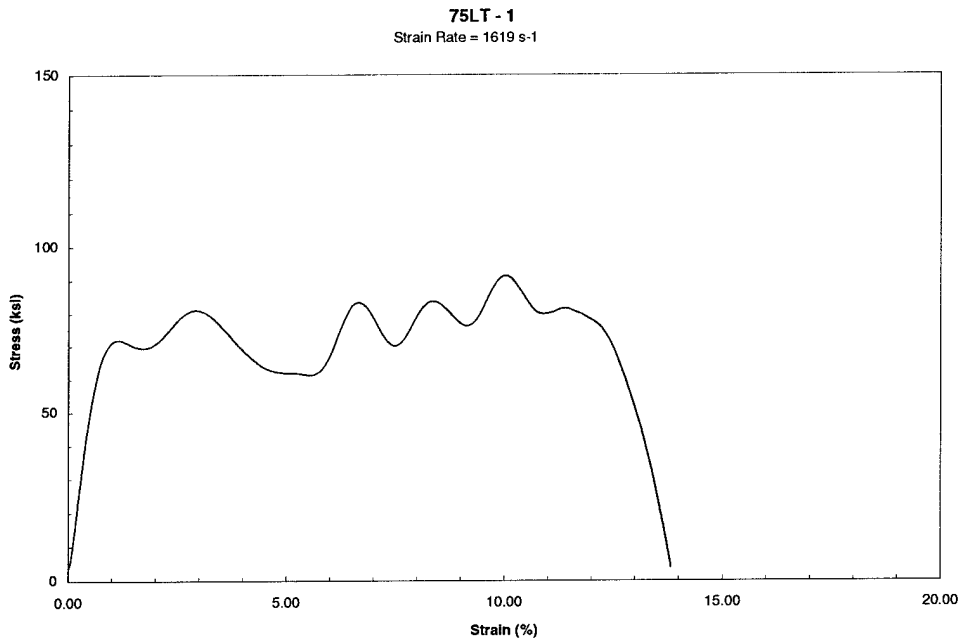
75LT - 1
Strain Rate = 1619 s-1
150
100
50
0
Stress (ksi)
0.00
5.00
10.00
15.00
20.00
Strain (%)

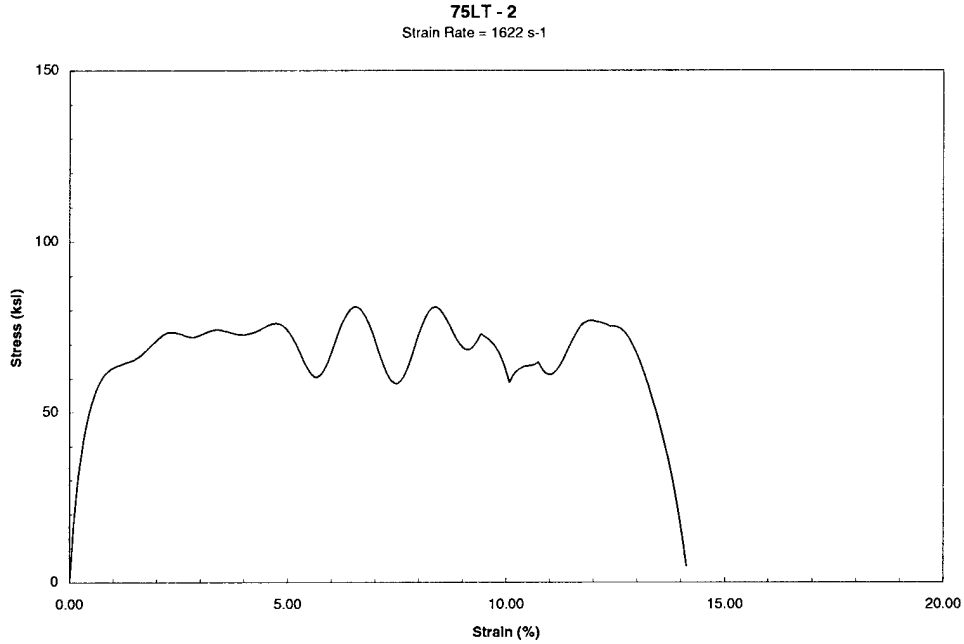
75LT - 2
Strain Rate = 1622 s-1
150
100
50
0
Stress (ksi)
0.00
5.00
10.00
15.00
20.00
Strain (%)

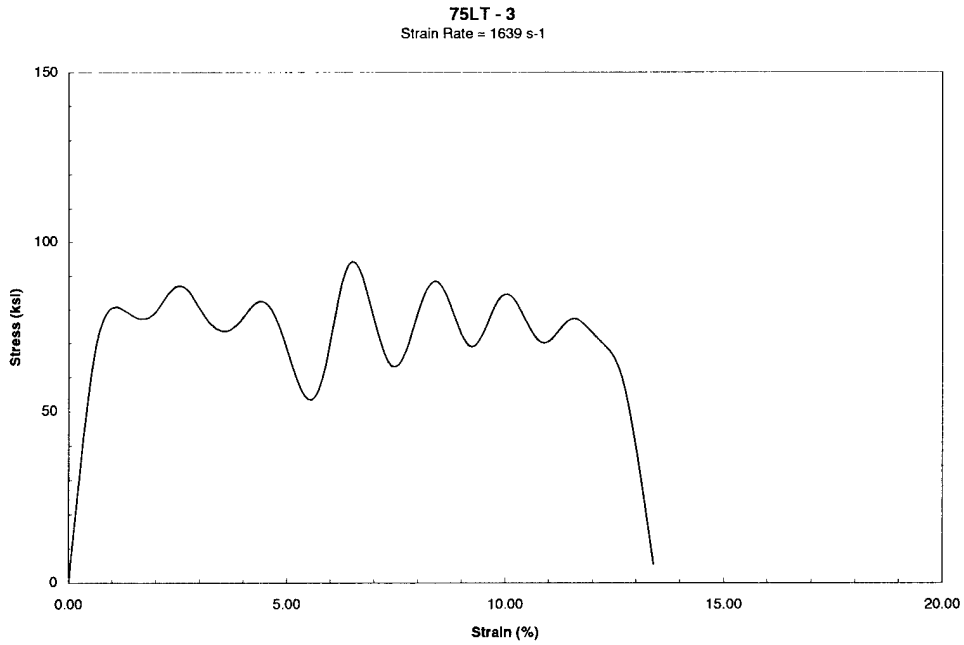
75LT - 3
Strain Rate = 1639 s-1
150
100
50
0
Stress (ksi)
0.00
5.00
10.00
15.00
20.00
Strain (%)

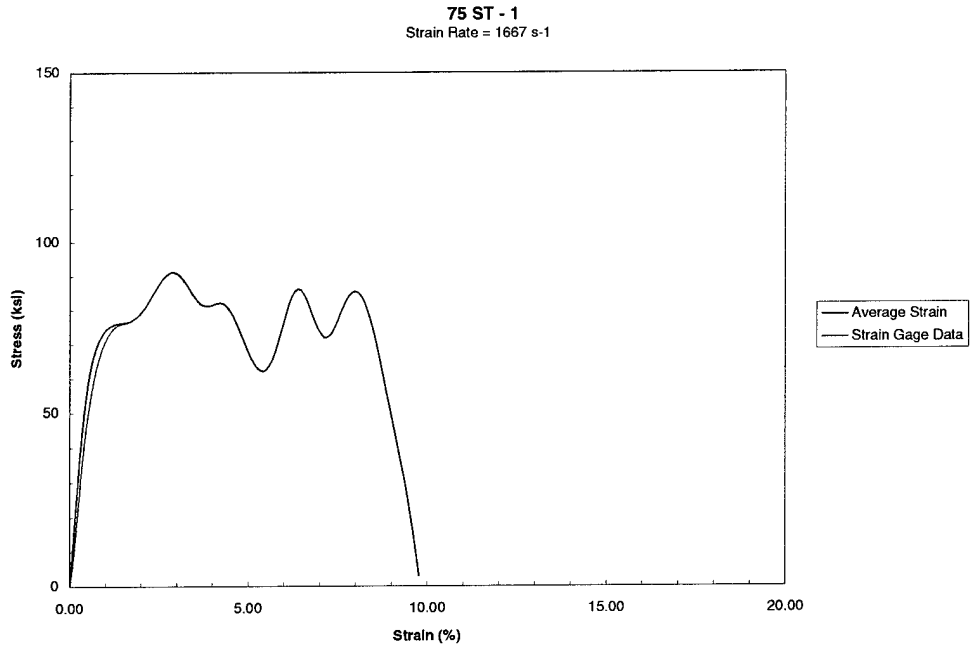
75 ST - 1
Strain Rate = 1667 s-1
150
100
50
0
Stress (ksi)
0.00
5.00
10.00
15.00
20.00
Strain (%)
Average Strain
Strain Gage Data

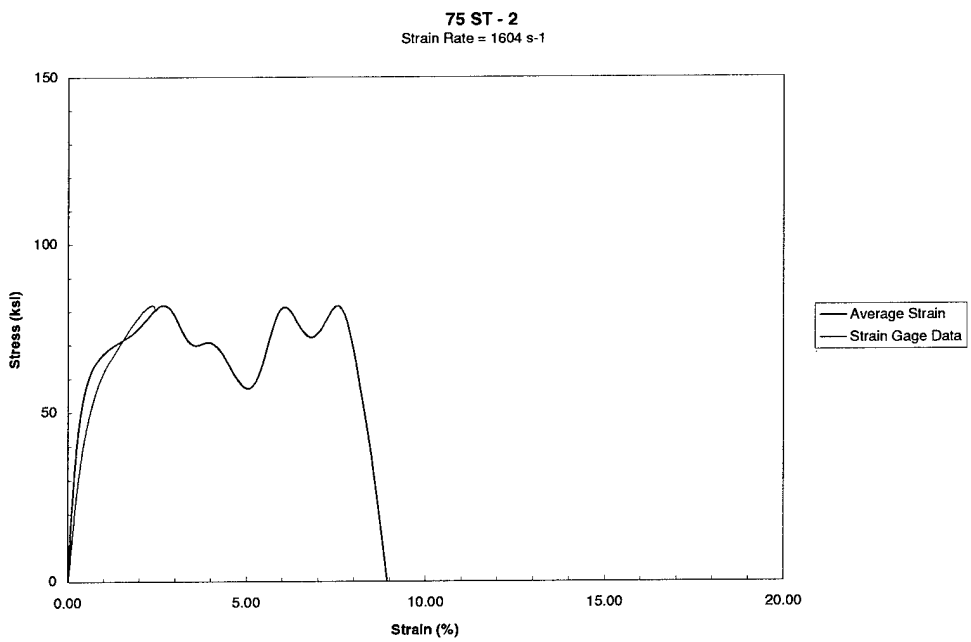
75 ST - 2
Strain Rate = 1604 s-1
150
100
50
0
Stress (ksi)
0.00
5.00
10.00
15.00
20.00
Strain (%)
Average Strain
Strain Gage Data

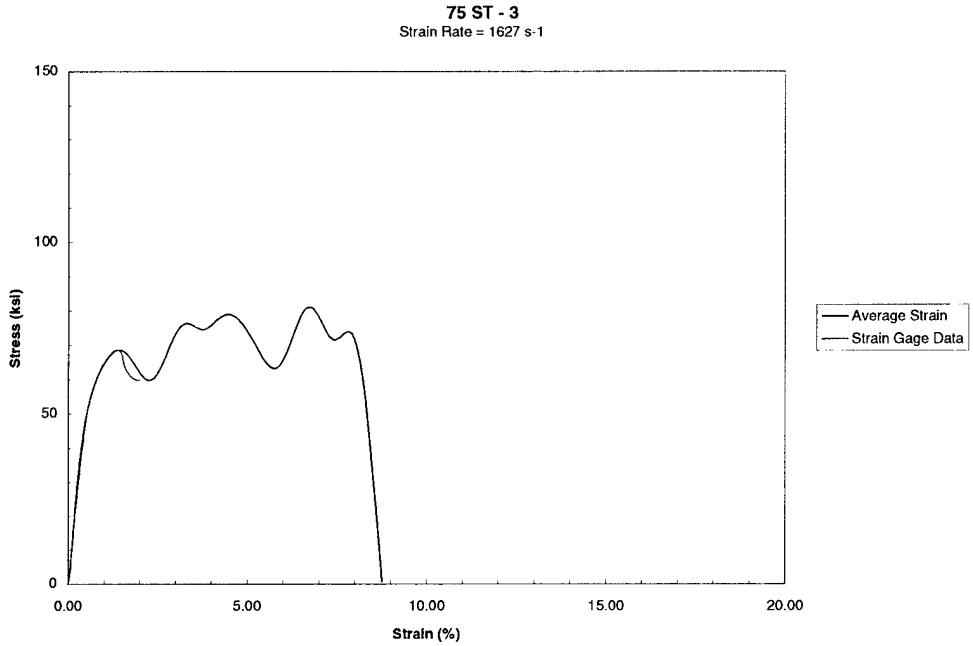
75 ST - 3
Strain Rate = 1627 s-1
150
100
50
0
Stress (ksi)
0.00
5.00
10.00
15.00
20.00
Strain (%)
Average Strain
Strain Gage Data

This page intentionally left blank.

APPENDIX B

VALIDATION COUPON TESTS

TEST REQUEST IRAD	SERIAL NO. IRAD-rhj-0698		PAGE 1 OF 5
	DATE: 06/05/98	REV LTR -	

MODEL: IRAD W.O. # 6WLN	TEST TYPE __STATIC __VIBRATION __FATIGUE IMPACT_____(OTHER)

TITLE:

Highly Loaded Airframe Fittings Program
Characterization of the Impact Response of Aluminum Structural Components

_X_MATERIAL QUALIFICATION ___DESIGN VERIFICATION TEST	CONFORMITY REQUIRED: __YES _X_NO

DESCRIPTION AND OBJECTIVES:

1. Introduction

The response of structural materials subjected to high-rate impulse loads is important in applications such as landing gear attachment fittings. The effect of stress concentrations on the high-rate response of structures is of particular interest. The purpose of this test is to provide some basic information characterizing the response of an aluminum coupon with large stress concentrations subjected to an impact load. There are three material behavior regimes targeted in this test: complete linear elastic response of the specimen, elastic response with plastic flow across the entire notched cross section, and failure of the material at the notched cross section. The data obtained in this test will be correlated with an MSC DYTRAN analysis of the specimen response in order to gain confidence in the analytical technique for future sizing applications.

ORIGINATED BY: R. Jones 5 June, 1998	DESIGN:	STRUCTURES:	PROJECT:	STRUCT DER:

B-1 Test Methods and Procedures

The specimen geometry is shown in Figure 1. All specimens are fabricated from 0.375 thick 7075T651 Aluminum plate. The specimens shall be supported and instrumented with strain gages as shown in Figures 2 and 3. Prior to testing, the mass and volume of each specimen shall be measured. The mass shall be determined to within ± 0.001 lb. The volume shall be determined to within ± 0.001 in^3. Also, a dimensional inspection of each specimen shall be conducted. The width and thickness of each specimen shall be measured at each of the three strain gage locations (A, B, and C) indicated in Figure 2. The length of each specimen and the axial locations of each set of strain gages shall also be recorded. All dimensional measurements shall be accurate to within ± 0.005 inches.

The specimens shall be impacted using an instrumented DynaTup according to the test condition matrix defined in Section B-2. Strain data from all gages must be recorded at a sampling frequency of 10^5 Hz in order to capture the longitudinal stress waves traversing the specimen during the impact event.

The dimensional measurements indicated above shall be repeated after each impact event, with any changes from pre-test measurements being noted. Re-measurement of the specimen mass and volume is not required.

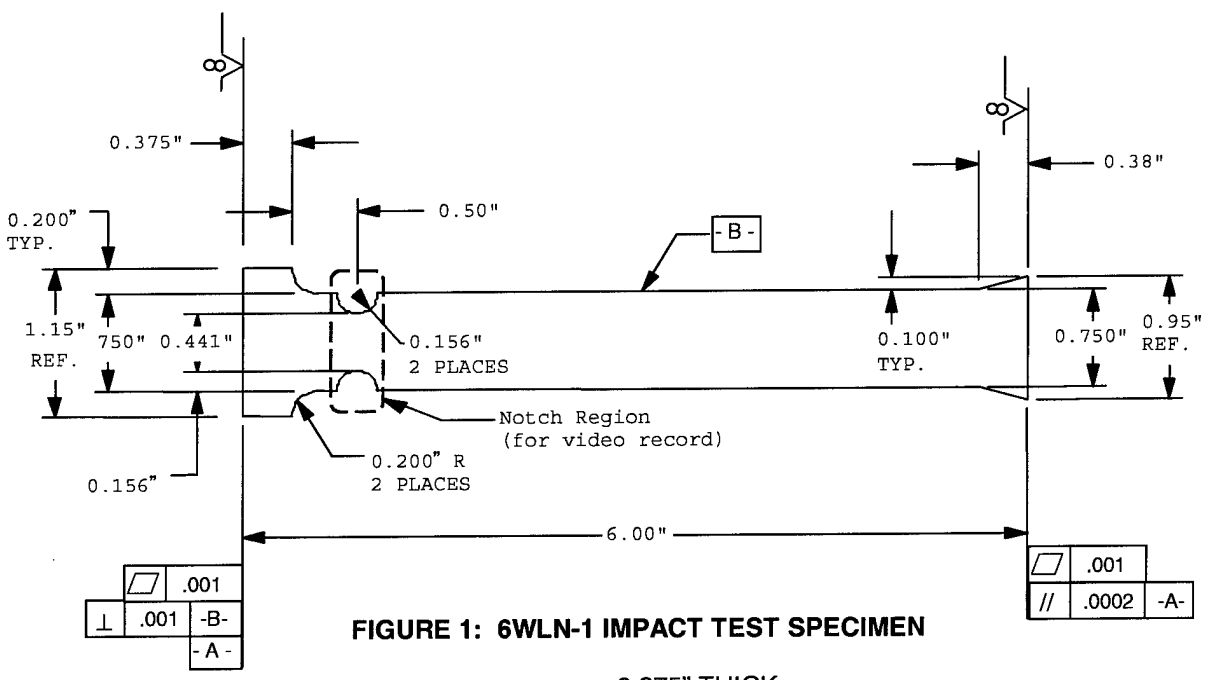

FIGURE 1: 6WLN-1 IMPACT TEST SPECIMEN

0.375" THICK
7075T651 ALUMINUM ALLOY

NOTE: ALL EDGES MUST BE SMOOTH AND FREE FROM NICKS AND BURRS

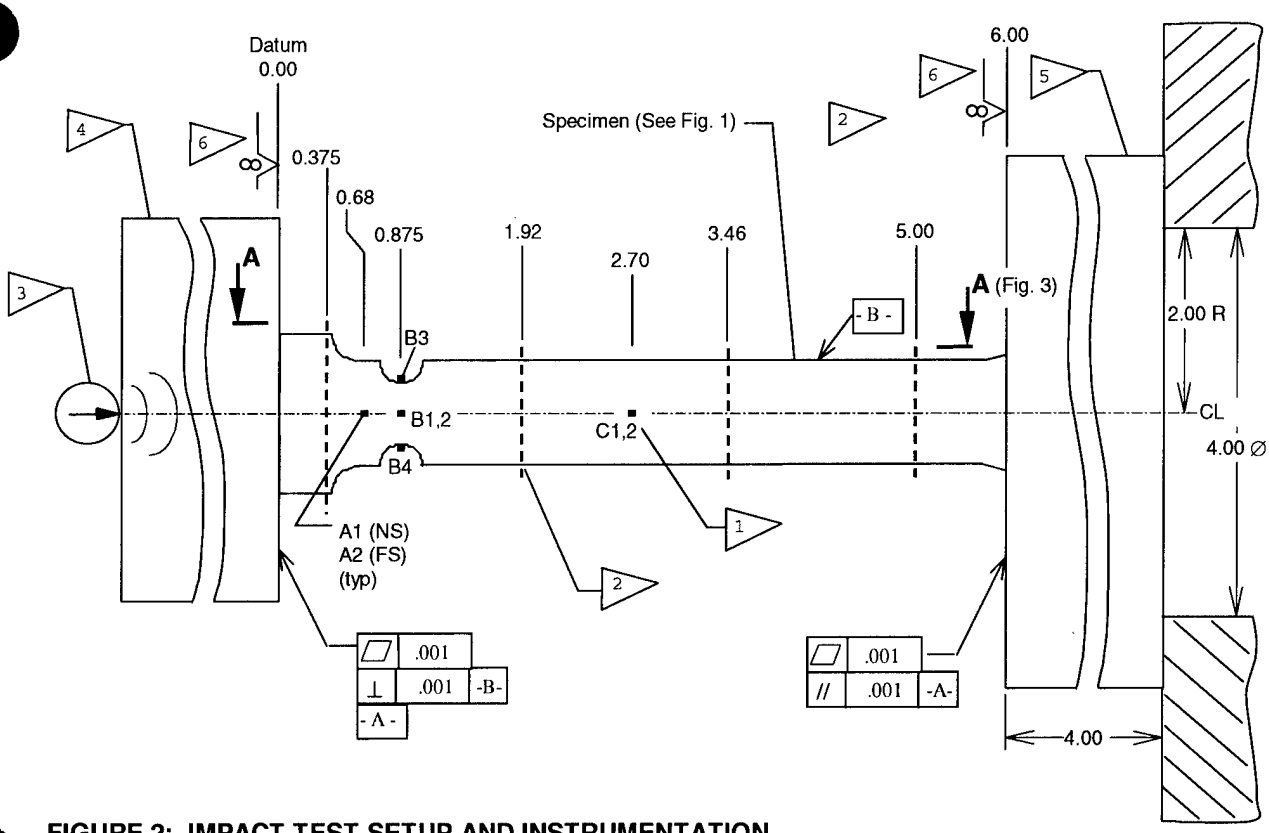

FIGURE 2: IMPACT TEST SETUP AND INSTRUMENTATION

NOTES:

1. Axial Strain Gage (Typ – 8 places)
   a. Data from the following gage pairs should be recorded using a single channel so that the indicated response is an average of the two: A1-A2, B1-B2, B3-B4 & C1-C2.
   b. Gages A1 – A2 & C1 – C2 should be capable of measuring ±(10000±50) με
   c. Gages B1 – B4 should be capable of measuring from +1000 to –200000 ± 100 με

2. Out-of-Plane Support, 4 places (see Figure 3, View A-A for typical detail)

3. Impactor (DynaTup)

4. Impact Bearing Block: 1.50" X 1.50" X 1.50"

5. Support Bearing Block: 6.0" X 6.0" X 4.0" Steel

6. Surface Finish requirement applies only to portion of surface in contact with specimen + 0.1 inch.

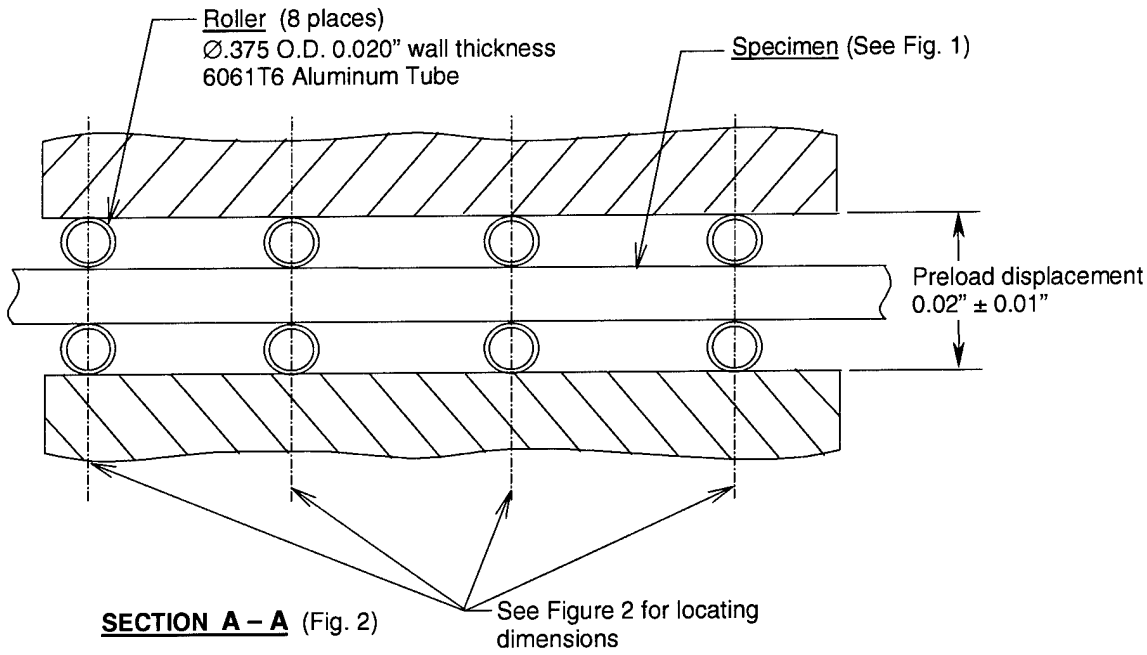

FIGURE 3: OUT-OF-PLANE SUPPORT CONFIGURATION FOR IMPACT TEST

B-2 Impact Test Conditions

The six (6) specimens shall be subjected to the impact conditions specified in Table 1 below. All specimens will be impacted at both 17 ft/s and 38 ft/s with the small masses indicated in order to measure the specimen elastic response. Four of the specimens will then be impacted with a larger mass at 38 ft/s to measure the specimen response with sufficient energy input to force material plastic flow at the notch. Two of the specimens will not be subjected to this condition. Finally, all six specimens will be impacted with a larger mass at 38 ft/s in order to produce a material failure at the notch. Because the initial calculations were based on idealized boundary conditions, which will not necessarily represent the test conditions, the impactor masses indicated in Table 1 should be considered preliminary. Final values will be provided after the test boundary conditions are more clearly identified.

Table 1: Impact Test Conditions

Response	Impact Condtion		Number of Specimens
	Mass (lb)	Velocity (in/sec)	
Elastic	0.55 ± 0.05	204 ± 12	6
	0.07 ± 0.05	456 ± 12	6
Plastic (Notch)	1.00 ± 0.05	456 ± 12	4
Failure	10.00 ± 0.05	456 ± 12	6

B-3. Data Requirements

The complete dimensional record including all measurements indicated in Section 2.1 shall be provided for each specimen.

A complete time history of all recorded specimen strains indicated in Figure 2 for a period not to exceed 1.00 second encompassing the duration of the impact event shall be provided for each impact in digital format (either ASCII or MS Excel file). Also, a complete time history of the velocity and acceleration of the impactor and the impact force for the duration of the impact event shall be provided for each impact in digital format (either ASCII or MS Excel file). All data should be recorded at a frequency of at least 10^5 Hz.

Photographs of a typical test setup shall be provided, as well as a video record of each of the six "Failure" tests (see Section 2.2). The video camera should be focused on the notched region of each specimen (see Figure 1).

B-4 Test Results

Test results are provided in Table 2.

Table 2. Test Results

Specimen No.	Spec. Type	Notch Response	Impact Condition: Tup Mass (lb)	Velocity: Target ft/s	Velocity: Actual ft/s	Impact Bearing Block: Mass (lb)	Dimensions (in.)
437-001	notch		6.05	7.5	7.50	15 lb.	
437-001	notch		6.05	7.5	7.51	15 lb.	
437-001	notch		6.05	7.5	7.51	15 lb.	
437-001	notch		6.05	7.5	7.51	15 lb.	
437-001	notch		6.05	7.5	7.52	15 lb.	
437-001	notch		6.05	7.5	7.53	15 lb.	
437-001	notch		6.05	10.0	10.03	15 lb.	
437-001	notch		6.05	14.0	14.03	15 lb.	
437-001	notch		6.05	7.5	7.51	15 lb.	
437-001	notch		6.05	20.0	19.91	15 lb.	
437-001	notch		6.05	20.0	19.91	15 lb.	
437-001	notch		6.05	42.0	41.63	19 lb.	
437-002	notch	All Elastic	6.18 ± 0.05	7.5 ± 0.5	7.55	15.28 ± 0.05	4 x 1.5 x 9.0
437-002	notch	Peaks Past Yield (Filtered Curve Elastic)	6.18 ± 0.05	10 ± 0.5	10.03	15.28 ± 0.05	4 x 1.5 x 9.0
437-002	notch	Filtered Curve Yields	6.18 ± 0.05	14 ± 0.5	13.99	15.28 ± 0.05	4 x 1.5 x 9.0
437-002	notch	Initial Full Wave Yields	6.18 ± 0.05	20 ± 0.5	20.35	15.28 ± 0.05	4 x 1.5 x 9.0
437-002	notch	Large Strain >20%	6.18 ± 0.05	38 ± 0.5	37.99	4.58 ± 0.05	1.2 x 1.5 x 9.0
437-003	notch		6.05	42.0	42.28	15 lb.	

Specimen No.	Spec. Type	Notch Response	Impact Condition Tup Mass (lb)	Velocity Target ft/s	Actual ft/s	Impact Bearing Block Mass (lb)	Dimensions (in.)
437-003	notch		6.24	42.0	43.40	15 lb.	
437-004	notch	Elastic trial impact	6.18 ± 0.05	10.0	9.89	4.58 ± 0.05	1.2 x 1.5 x 9.0
437-004	notch	Elastic trial impact	6.18 ± 0.05	20.0	19.78	4.58 ± 0.05	1.2 x 1.5 x 9.0
437-004	notch	Elastic trial impact	6.18 ± 0.05	10.0	9.89	4.58 ± 0.05	1.2 x 1.5 x 9.0
437-004	notch	Large Strain >20%	6.18 ± 0.05	38 ± 0.5	37.89	4.58 ± 0.05	1.2 x 1.5 x 9.0
437-005	notch	Elastic trial impact	6.18 ± 0.05	10.0	10.39	4.58 ± 0.05	1.2 x 1.5 x 9.0
437-005	notch	Large Strain >20%	6.18 ± 0.05	38 ± 0.5	37.85	4.58 ± 0.05	1.2 x 1.5 x 9.0
437-006	notch	Elastic trial impact	6.18 ± 0.05	10.0	9.97	4.58 ± 0.05	1.2 x 1.5 x 9.0
437-006	notch	Large Strain >20%	6.18 ± 0.05	38 ± 0.5	38.43	4.58 ± 0.05	1.2 x 1.5 x 9.0
655-001	dogbone		7.329	42.0	44.10	15 lb.	
655-002	dogbone	Large Strain >20%	13.43	10.0		15.28 ± 0.05	4 x 1.5 x 9.0
655-002	dogbone	Large Strain >20%	13.43	20.0		15.28 ± 0.05	4 x 1.5 x 9.0
655-002	dogbone	All Elastic	6.18 ± 0.05	20.0		15.28 ± 0.05	4 x 1.5 x 9.0
655-002	dogbone	All Elastic	6.18 ± 0.05	10.0		15.28 ± 0.05	4 x 1.5 x 9.0
655-002	dogbone	Uniform Plastic Flow in Necked Down Portion of Dogbone	6.18 ± 0.05	38.0		4.58 ± 0.05	1.2 x 1.5 x 9.0
655-003	dogbone	All Elastic	6.18 ± 0.05	10 ± 0.5	9.95	15.28 ± 0.05	4 x 1.5 x 9.0
655-003	dogbone	All Elastic	6.18 ± 0.05	20 ± 0.5	20.30	15.28 ± 0.05	4 x 1.5 x 9.0

Specimen No.	Spec. Type	Notch Response	Impact Condition: Tup Mass (lb)	Velocity: Target ft/s	Velocity: Actual ft/s	Impact Bearing Block: Mass (lb)	Dimensions (in.)
655-003	dogbone	Uniform Plastic Flow in Necked Down Portion of Dogbone	6.19 ± 0.05	42 ± 0.5	42.23	4.58 ± 0.05	1.2 x 1.5 x 9.0
655-004	dogbone	All Elastic	6.18 ± 0.05	20 ± 0.5	20.01	15.28 ± 0.05	4 x 1.5 x 9.0

APPENDIX C

VALIDATION DROP TEST

Simula Technologies Inc.

TEST REPORT NO. **TR-99098**

REVISION **"NEW"**

DYNAMIC TEST REPORT

LANDING GEAR SHOCK STRUT DESIGN METHODOLOGY

PREPARED FOR

Bell Helicopter Textron, Inc
P.O. Box 482
Fort Worth, TX 76101

PREPARED BY

Simula Technologies, Inc
10016 South 51st Street
Phoenix, AZ 85044

INITIAL RELEASE PREPARED BY: Michele Burdick DATE: 11.19.99
Michele Burdick, Test Engineer

INITIAL RELEASE APPROVED BY: Christopher A. Bradney DATE: 11-22-99
Christopher Bradney, Manager, Test Labs

LIST OF ACTIVE PAGES

PAGE NO.	REV	PAGE NO.	REV	PAGE NO.	REV
i	new	A1	new	B6	new
ii	new	A2	new	B7	new
iii	new	A3	new	B8	new
iv	new	A4	new	B9	new
v	new	A5	new	B10	new
		A6	new	B11	new
1	new	A7	new	B12	new
2	new	A8	new	B13	new
3	new	A9	new	B14	new
4	new			B15	new
5	new	B1	new	B16	new
6	new	B2	new	B17	new
7	new	B3	new	B18	new
8	new	B4	new	B19	new
9	new	B5	new	B20	new

RECORD OF REVISIONS

REVISIONS							
REVISION	CHANGED BY	REVISED PAGE(S)	ADDED PAGE(S)	DELETED PAGE(S)	DESCRIPTION	DATE	APPROVAL
NEW	N/A	N/A	N/A	N/A	INITIAL RELEASE	11/22/99	[illegible]

TABLE OF CONTENTS

LIST OF ACTIVE PAGES i
RECORD OF REVISIONS ii
TABLE OF CONTENTS iii
REFERENCES v
1.0 Introduction: 1
2.0 Dynamic Testing: 1
2.1 Test Article Description: 1
2.2 Test Facility Description: 1
2.3 Test Witness: 1
2.4 Test Objective: 3
2.5 Test Description: 3
2.6 Test Summary: 6
2.7 Test Equipment: 6
2.8 Test Procedure: 8
3.0 Conclusion: 9
APPENDIX A: CALIBRATION RECORDS A1
APPENDIX B: TEST DATA PLOTS B1
ATTACHMENT I: TEST PHOTOGRAPHS 1

LIST OF FIGURES

Figure 1: Test Article and Fixture 2
Figure 2: Test Set-Up 3
Figure 3: Trailing Arm Assembly Gages 4
Figure 4: Strut Assembly Gages 5
Figure 5: Joint Assembly Gages 5

LIST OF TABLES

Table 1: Test Parameters 6
Table 2: Dynamic Test Instrumentation 7
Table 3: Dynamic Test Results 9

REFERENCES

1. BHTI Drawing R99-001-001, Revision New, *Drop Test Instl. - Highly Loaded A/F Fitting*

2. SAE J211 Part 1, Aerospace Standard, *Instrumentation for Impact Tests – Part I, - Electronic Instrumentation Recommended Practice,* Society of Automotive Engineers, revised March 1995.

3. MIL-C-45662A, *Calibration System Requirements*

4. TR-98022, Revision B, *Test Facility Document,* Simula Technologies, Inc., Phoenix, AZ, dated July 15, 1998.

1.0 Introduction:

This report provides the test parameters and set-ups for development of Bell Helicopter Textron, Inc. (BHTI) design methodology for airframe fittings that are subjected to impact loadings. The landing gear shock strut was designed and developed by BHTI for utilization on Bell's Advanced Composite Airframe Program (ACAP). To demonstrate the strut performance and validate the design parameters established from DYTRAN computer simulation and coupon level impact testing, dynamic drop tests were required.

Two tests were scheduled, however due to an unfortunate failure, only one test was conducted. This report contains the results of the drop test conducted and summarizes those results in one convenient location.

2.0 Dynamic Testing:

2.1 Test Article Description:

BHTI landing gear shock strut consisted of a trailing arm assembly with wheel, upper shock strut assembly, and upper joint assembly. Figure 1, which is from BHTI drawing R99-001-001, provides dimensions for the test article and test fixture.

2.2 Test Facility Description:

The dynamic test described in this report was conducted at Simula Technologies, Inc. (STI) in Phoenix, Arizona. STI is a Federal Aviation Administration (FAA) excepted test lab and contains both indoor and outdoor test facilities. The indoor facility that is environmentally controlled consists of a 120-foot deceleration sled and a 30-foot guided drop tower. The outdoor facility consists of a 70-foot guided drop tower system. STI has provisions for high-speed (HS) video filming and motion analysis of testing. The facility also contains state-of-the-art signal conditioning and data recording equipment conforming to the requirements of US Government agencies and industrial customers. For any facility questions, please contact Chris Bradney at phone: (480) 753-2093.

2.3 Test Witness:

A representative from BHTI, Kurt Tessnow, was present for the test conducted.

2.0 Dynamic Testing: (continued)

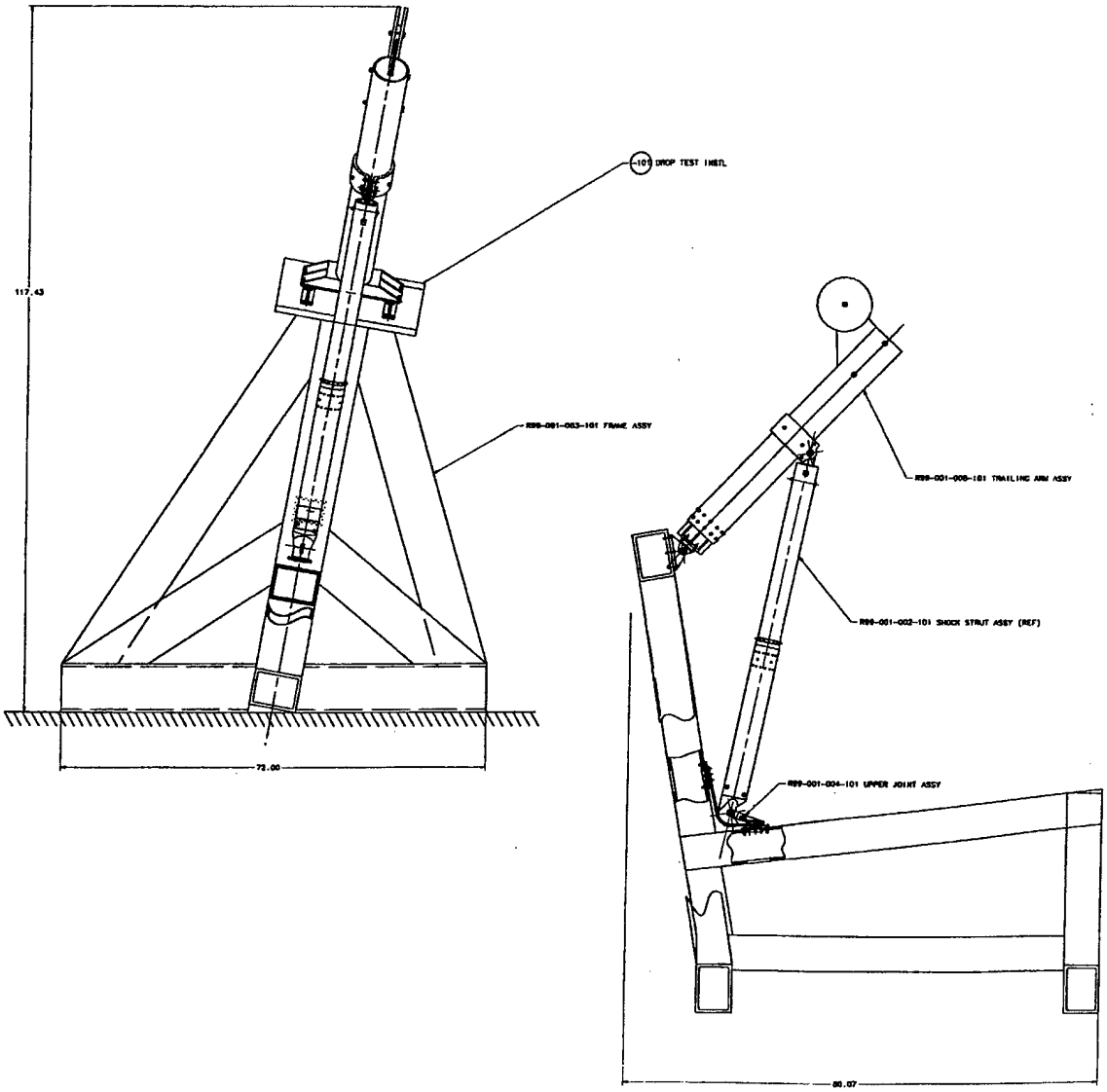

Figure 1: Test Article and Fixture

2.0 Dynamic Testing: (continued)

2.4 Test Objective:

The objective of the dynamic drop test was to validate the development of a design methodology for airframe fittings that are subjected to impact loading. The dynamic test was conducted to verify the design parameters obtained from DYTRAN computer simulations and coupon level impact tests.

2.5 Test Description:

To validate the design methodology, the dynamic test was conducted on a drop tower to simulate / represent vertical impact pulse. Figure 2 shows the set-up used for the test. The test was conducted with 10° airframe pitch and roll. The test pulse requirement was a 38 feet/second (fps) impact velocity with a 1685 pound drop mass.

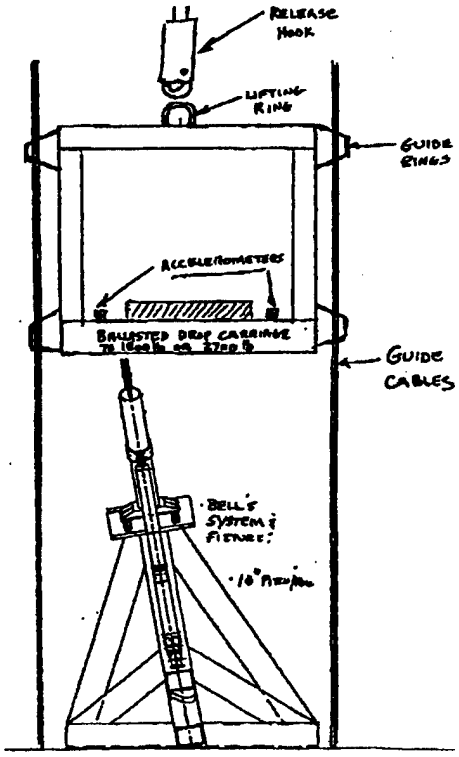

Figure 2: Test Set-Up

2.0 Dynamic Testing: (continued)

2.5 Test Description: (continued)

BHTI test articles were instrumented with strain gages for collection of loads, moments, and torsion of the trailing arm assembly. The strain gage locations, and directions are shown in Figure 3. The strut assembly was instrumented with strain gages for collection of load data as shown in Figure 4. The joint assembly was instrumented with strain gages for collection of load data as shown in Figure 5.

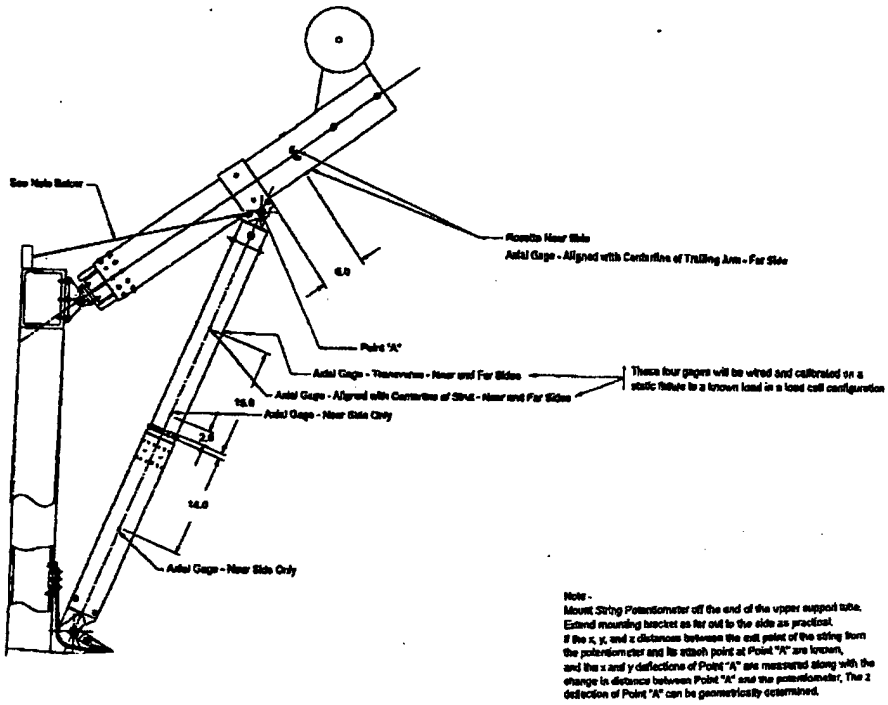

Figure 3: Trailing Arm Assembly Gages

2.0 Dynamic Testing: (continued)

2.5 Test Description: (continued)

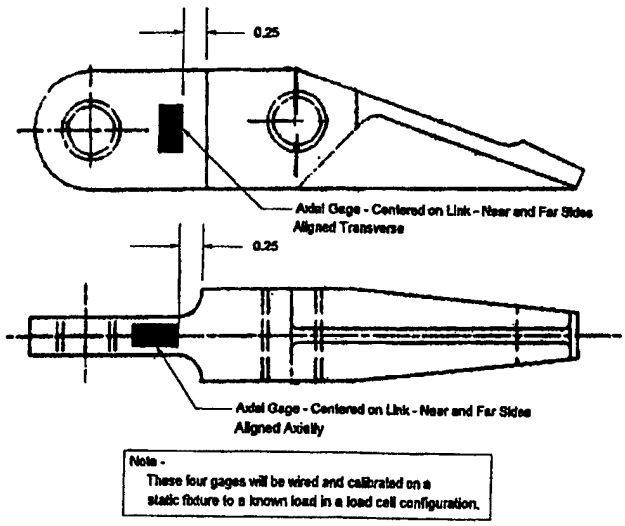

Figure 4: Hinge Gages

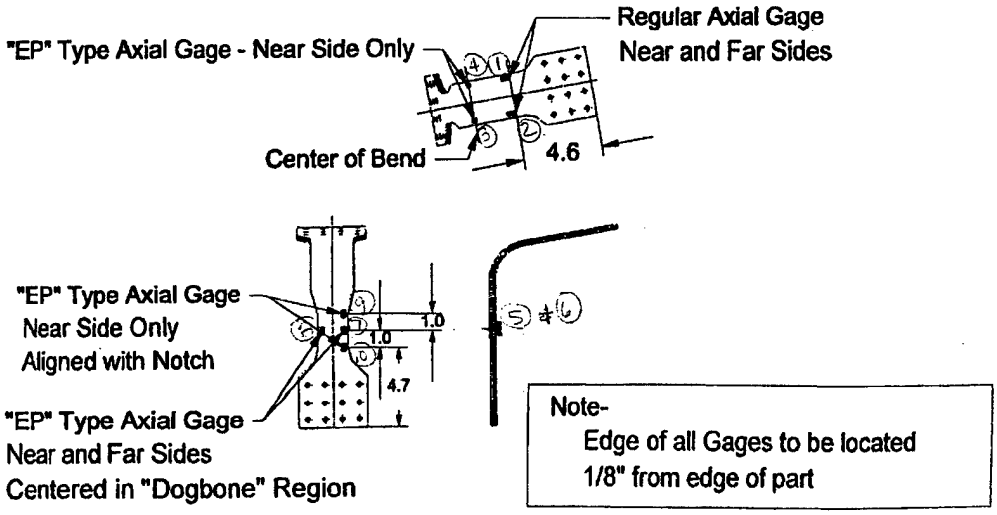

Figure 5: Joint Assembly Gages

2.0 Dynamic Testing: (continued)

2.6 Test Summary:

Table 1 provides the test conditions and parameters that were established by the computer simulations and coupon tests for the dynamic drop tests to validate.

Table 1: Test Parameters

Test #	Impact Velocity (feet/second)	Drop Weight (lbs)	Drop Height (feet)
1	38	1685	22.4
2*	42	2549	27.4

* Test was not accomplished due to failures that occurred during Test #1.

2.7 Test Equipment:

Instrumentation used was in accordance with SAE J211 and calibrated in accordance with MIL-C-45662A. Copies of the calibration records are in Appendix A. Raw acceleration, load, moments, and displacements was sensed by accelerometer, strain gages, and displacement transducers, amplified through signal conditioners, and recorded digitally. All instrumentation was installed on the test article, except for the accelerometers. Two accelerometers were installed on the drop mass to obtain impact velocity. One accelerometer was identified as primary, and the other as redundant. A personal computer (PC) -based computer program accomplished subsequent processing of the data from digital format. "Quick-look" data was provided after each test for review. The final test data is located in Appendix B.

Photographic documentation of the tests was accomplished by two HS film cameras set at 500 frames per second and one HS video camera set at 1000 frames per second. See Appendix C for exact camera locations, distances, and settings. Still photographs from a 35-mm camera also documented the pre-test and post-test conditions. A set of all photographs is presented in Attachment I.

Table 2 provides a list of instrumentation used for the dynamic drop tests.

2.0 Dynamic Testing: (continued)

2.7 Test Equipment: (continued)

Table 2: Dynamic Test Instrumentation

Item	Instrument	Type	Range	Location	Class	Cal Date
1	C15117	accelerometer	250g	Drop cage - primary	60	12/02/99
2	C15871	Accelerometer	250g	Drop cage – secondary	60	04/23/00
3	Load cell	Strain gage	5000	Shock strut	60	11/05/00
4	Load cell	Strain gage	5000	Link	1000	11/05/00
5	Load cell	Strain gage	5000	Trailing arm	1000	11/05/00
6	Moment X	Strain gage	5000	Trailing arm	1000	11/05/00
7	Moment Y	Strain gage	5000	Trailing arm	1000	11/05/00
8	Torsion	Strain gage	5000	Trailing arm	1000	11/05/00
9	Gage 1	Strain gage	5000	Strap	1000	11/05/00
10	Gage 2	Strain gage	5000	Strap	1000	11/05/00
11	Gage 3	Strain gage	5000	Strap	60	11/05/00
12	Gage 4	Strain gage	5000	Strap	60	11/05/00
13	Gage 5	Strain gage	5000	Strap	60	11/05/00
14	Gage 6	Strain gage	5000	Strap	60	11/05/00
15	Gage 7	Strain gage	5000	Strap	60	11/05/00
16	Gage 8	Strain gage	5000	Strap	60	11/05/00
17	Gage 9	Strain gage	5000	Strap	60	11/05/00
18	Gage 10	Strain gage	5000	Strap	60	11/05/00
19	Gage 11	Strain gage	5000	Shock strut	60	11/05/00
20	Gage 12	Strain gage	5000	Shock strut	60	11/05/00

2.0 Dynamic Testing: (continued)

2.8 Test Procedure:

This section provides the detailed test procedures for each dynamic test performed.

TEST #1: Impact Velocity of 38 fps

Step	Description
1	ballasted drop cage to 1800 lbs using additional weights
2	raised drop cage to orient test article under the honeycomb plies
3	installed instrumentation cables, final checks performed on system
4	pre-test photos taken (minimum 4 sides)
5	loaded film into HS film cameras
6	positioned cameras and lights
7	performed camera run-out
8	verified lighting (if required)
9	installed and function checked all data triggers
10	confirmed test readiness of all personnel and witness(es)
11	raised drop cage to 22.4 feet above the test article wheel
12	performed test
13	post-test photos taken, removed film for processing, downloaded video
14	downloaded data for "quick look"
15	removed test article for further inspection

3.0 Conclusion:

The final test data plots, photographs, and calibration records for the test is in the appendices of this report. Table 3 provides a summary of the test results.

Table 3: Dynamic Test Results

Test #	**1**
Run #	990597
Test Date	11/11/99
Weight (lbs)	1685
Height (ft)	22.4
Acceleration (g)	26.32
Trailing Arm Loads	
P_x (lbs)	4503.24
M_x (in-lbs)	5750.54
M_y (in-lbs)	6074.51
M_z (in-lbs)	118.79
Shock Strut Loads	
P_x (lbs)	356.37
Joint Loads	
P_x (lbs)	226.78
Point "A" Deflection	
X (in)	na
Y (in)	na
Z (in)	na

APPENDIX A

CALIBRATION RECORDS

VIBRACON/BOUCHE LABS: 621 Via Alondra #604, Camarillo, CA 93012
(805) 445-7654, FAX (805) 482-7530

Report No.	7488
Purchase Order No.	10400
Calibration Date:	December 2, 1998
Submitted By:	Simula Technologies, Inc. 10016 S. 51st Street Phoenix, AZ 85044

CERTIFICATE OF CALIBRATION

Endevco Model 7231C-750 Accelerometer, SN C15117, 10 Vdc Input

Frequency, Hz	Sensitivity, mV/g
10	.2857
20	.2823
50	.2825
100	.2826
200	.2812
500	.2847
800	.2797
1,000	.2782
1,500	.2731
2,000	.2680

Input Resistance: 474 ohms
Output Resistance: 456 ohms

Standard Used: Bouche Labs Model 1000AD Primary Vibration Standard Shaker,SN 134
Temperature 72° F, Relative Humidity 54%
Calibration Performed By: B. Bouche
Due Date: December 2, 1999

The calibration was performed by the comparison method in accordance with S2.11-1969 and S2.2-1959, American National Standards Institute and in accordance with the monograph Calibration of Shock and Vibration Measuring Transducers, and other papers published by the Shock and Vibration Information Center, Washington D.C. All instruments and methods used in the calibration are in compliance with MIL-STD-45662A / ANSI/NCSL Z540-1-1994. This calibration is traceable to the National Institute of Standards and Technology reference NIST Test Report No. 732/246308 and 732/245605.

R.R. Bouche, Ph. D., P. E.
Technical Director

VIBRACON/BOUCHE LABS: 621 Via Alondra #604, Camarillo, CA 93012
(805) 445-7654, FAX (805) 482-7530 www.bouchelabs.com

Report No.	7883
Purchase Order No.	10551
Calibration Date:	April 23, 1999
Submitted By:	Simula Technologies, Inc. 10016 S. 51st Street Phoenix, AZ 85044

CERTIFICATE OF CALIBRATION

Endevco Model 7231C-750 Accelerometer, SN C15871, 10 Vdc Input

Frequency, Hz	Sensitivity, mV/g
10	.2090
20	.2093
50	.2039
100	.2031
200	.2043
500	.2081
800	.2122
1,000	.2131
1,500	.2182
2,000	.2242

Input Resistance: 552 ohms
Output Resistance: 558 ohms

Standard Used: Bouche Labs Model 1000AD Primary Vibration Standard Shaker,SN 136
Temperature 72° F, Relative Humidity 48%
Calibration Performed By: B. Bouche
Due Date: April 23, 2000

The calibration was performed by the comparison method in accordance with S2.11-1969 and S2.2-1959, American National Standards Institute and in accordance with the monograph Calibration of Shock and Vibration Measuring Transducers, and other papers published by the Shock and Vibration Information Center, Washington D.C. All instruments and methods used in the calibration are in compliance with MIL-STD-45662A / ANSI/NCSL Z540-1-1994. This calibration is traceable to the National Institute of Standards and Technology reference NIST Test Report No. 732/246308 and 732/245605.

R.R. Bouche, Ph. D., P. E.
Technical Director

EA Strut

48.63947	77.82813	-0.0039063	0	0
505.8704	525.3461	-0.0039063	0	0
1011.791	1011.791	-0.0078125	-0.003906	-0.009652
1556.563	1537.087	-0.015625	-0.011719	-0.01906
2013.818	202.3531	-0.019531	-0.015625	-0.193038
2500.213	2548.877	-0.025391	-0.021485	-0.021485
				-0.048647

2548.8 lb is equal to -.0486 Volts. Excitation voltage is 10 and bridge resistance 352 ohms.

Sensitivity
-0.001984

0.015625
0.10547
0.20313
0.30859
0.040625
0.51172

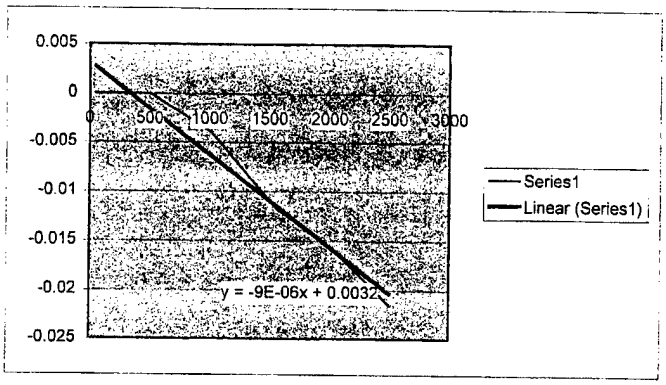

EA Strut

48.63947	87.55602	-0.0039063	0	0
505.8704	710.191	-0.0039063	0	0
1011.791	1011.791	-0.0078125	-0.003906	-0.009652
1556.563	1527.374	-0.015625	-0.011719	-0.019181
2013.818	2013.818	-0.019531	-0.015625	-0.019397
2500.213	2548.877	-0.025391	-0.021485	-0.021073
				-0.01386

2548.8 lb is equal to -.0138 Volts. Excitation voltage is 10 and bridge resistance 352 ohms.

Sensitivity
-0.000544

0.017578
0.14258
0.20313
0.30664
0.4043
0.51172

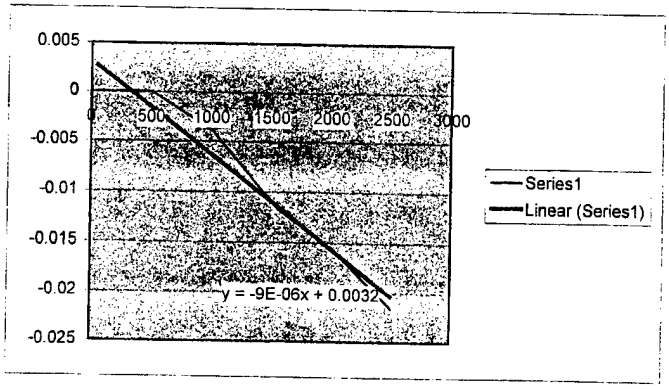

Moment X

48.63947	77.82813	0.019531	0	0
505.8704	525.3461	-0.021484	-0.041015	-0.195181
1011.791	992.3148	-0.068359	-0.08789	-0.221427
1556.563	1527.374	-0.11328	-0.132811	-0.217385
2013.818	2013.818	-0.1543	-0.173831	-0.215798
2500.213	2529.402	-0.20313	-0.222661	-0.222661
				-0.214490

2529. lb is equal to -.0214 Volts. Excitation voltage is 10 and bridge resistance 352 ohms.

Sensitivity
-0.008749

0.015625
0.10547
0.19922
0.30664
0.4043
0.50781

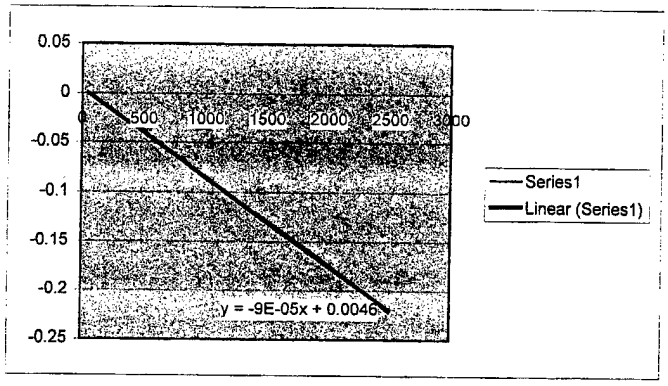

Moment X

48.63947	68.10023	0.021484	0	0
505.8704	525.3461	-0.047578	-0.069062	-0.32865
1011.791	1002.028	-0.064453	-0.085937	-0.214408
1556.563	1507.898	-0.10937	-0.130854	-0.216948
2013.818	2023.531	-0.1543	-0.175784	-0.217175
2500.213	2509.976	-0.19727	-0.218754	-0.217885
				-0.239013

2509.9 lb is equal to -.239 Volts. Excitation voltage is 10 and bridge resistance 352 ohms.

Sensitivity
-0.009523

0.013672
0.10547
0.20117
0.30273
0.40625
0.50391

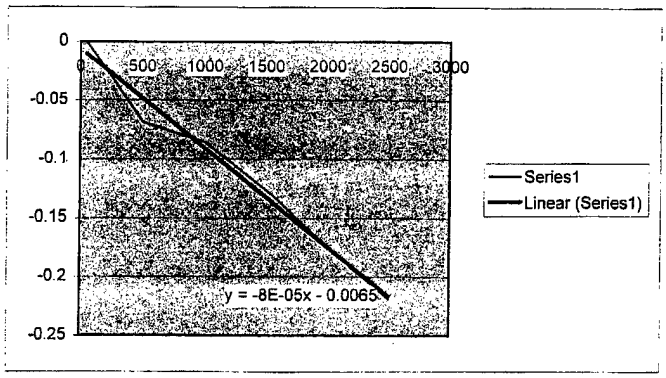

				Moment Y
48.63947	1318.533	0.01367	0	0
505.8704	11663.95	-0.099609	-0.113279	-0.02428
1011.791	22670.88	-0.2168	-0.23047	-0.025415
1556.563	34116.2	-0.33984	-0.35351	-0.025905
2013.818	45562.64	-0.45898	-0.47265	-0.025934
2500.213	57007.96	-0.58203	-0.5957	-0.5957
				-0.139447

57007.96 in-lb is equal to -.139 Volts. Excitation voltage is 10 and bridge resistance 352 ohms.

Sensitivity(mV/V/in-lb)
-0.000245

0.0117
0.1035
0.20117
0.30273
0.4043
0.50586

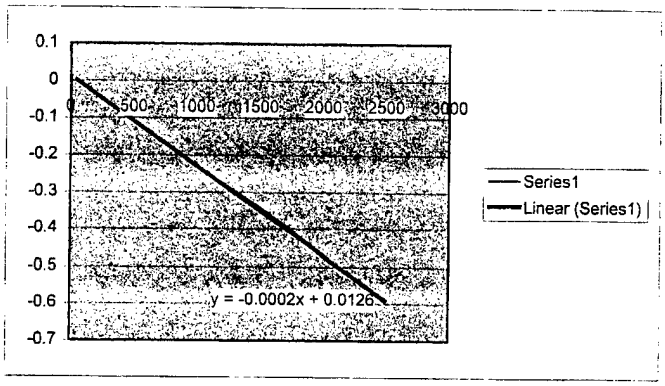

				Moment Y
48.63947	1100.468	-0.003906	0	0
505.8704	11445.32	-0.10547	-0.101564	-0.022185
1011.791	22891.76	-0.22266	-0.218754	-0.02389
1556.563	35217.23	-0.35352	-0.349614	-0.024818
2013.818	45562.64	-0.46484	-0.460934	-0.025291
2500.213	56567.32	-0.58789	-0.583984	-0.583984
				-0.136034

56567.3 in-lb is equal to .136 Volts. Excitation voltage is 10 and bridge resistance 352 ohms.

Sensitivity(mV/V/in-lb)
-0.00024

0

0.009765
0.10156
0.20313
0.3125
0.4043
0.50195

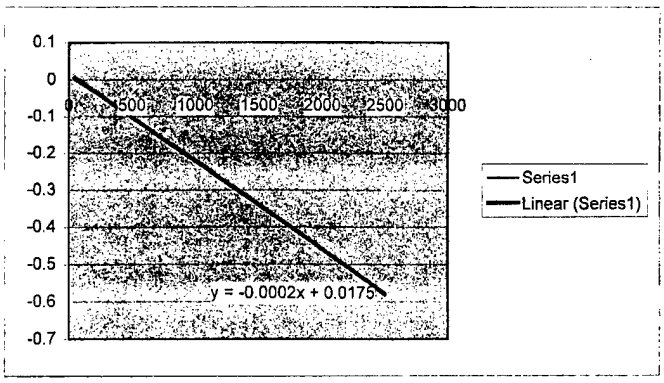

Load Z

48.639465	38.91406	0.011719	0	0
505.87036	525.3461	0.019531	0.007812	0.037175
1011.79053	1011.791	0.029297	0.017578	0.043433
1556.5625	1488.472	0.033203	0.021484	0.036084
2013.8183	1974.867	0.042969	0.03125	0.03956
2500.21295	2451.598	0.050781	0.039062	0.039062
				0.039063

2451.5 lb is equal to .039063 Volts. Excitation voltage is 10 and bridge resistance 351 ohms.

Sensitivity
0.001593

0.007813
0.10547
0.20313
0.29883
0.39648
0.49219

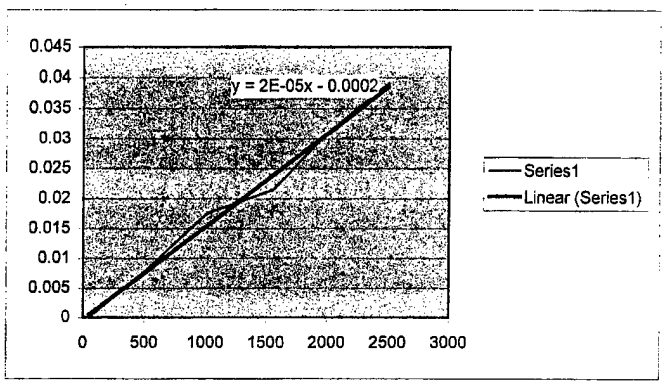

Load Z

48.63947	85.62339	0.007813	0	0
505.8704	525.3461	0.019531	0.011719	0.055766
1011.791	992.3148	0.025391	0.017579	0.044287
1556.563	1488.472	0.033203	0.025391	0.042645
2013.818	1974.867	0.042969	0.035157	0.044505
2500.213	2471.024	0.050781	0.042969	0.043472
				0.046135

2471.0 lb is equal to .0461 Volts. Excitation voltage is 10 and bridge resistance 351 ohms.

Sensitivity
0.001867

0

0.01719
0.10547
0.19922
0.29883
0.39648
0.49609

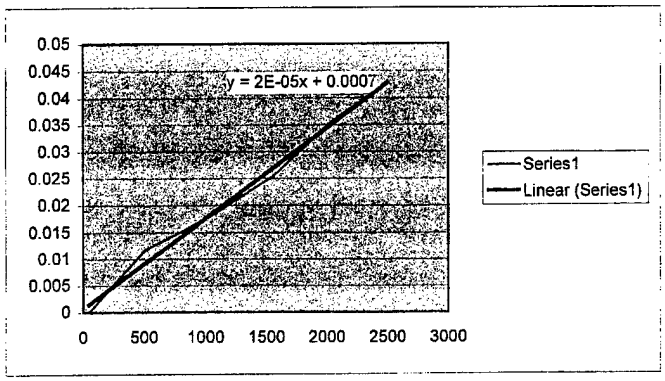

Torsion

48.63947	97.28391	0.029297	0	0
505.8704	535.059	0.070313	0.041016	0.191642
1011.791	1021.503	0.11914	0.089843	0.219879
1556.563	1546.85	0.17188	0.142583	0.230441
2013.818	2043.007	0.2168	0.187503	0.229445
2500.213	2539.164	0.26758	0.238283	0.234608
				0.221203

2539 lb is equal to .221 Volts. Excitation voltage is 10 and bridge resistance 352 ohms.

Sensitivity
0.008712

0.019531
0.10742
0.20508
0.31055
0.41016
0.50977

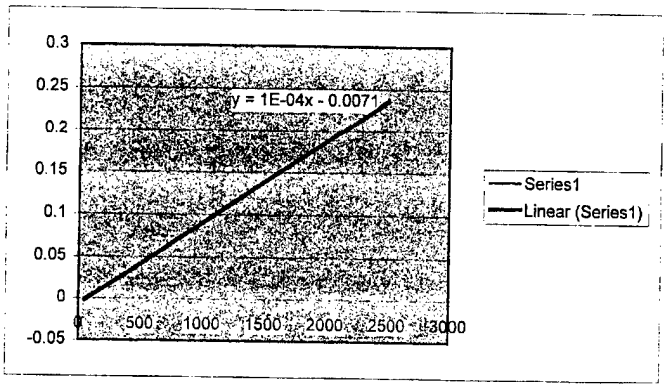

Torsion

48.63947	29.18567	0.017578	0	0
505.8704	525.3461	0.068359	0.050781	0.241655
1011.791	1320.363	0.11523	0.097652	0.184896
1556.563	1527.374	0.16602	0.148442	0.242969
2013.818	2043.007	0.2168	0.199222	0.243785
2500.213	2558.59	0.26953	0.251952	0.251952
				0.233052

2558.5 lb is equal to .233 Volts. Excitation voltage is 10 and bridge resistance 351 ohms.

Sensitivity
0.009506

0.005859
0.10547
0.26508
0.30664
0.41016
0.51367

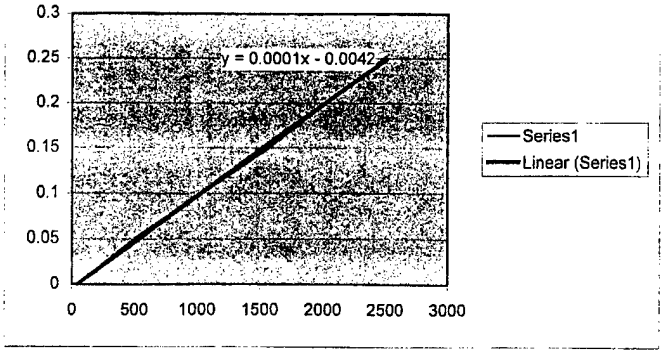

Link 1

0	55.2411	0.001066	0	0
500	502.367	0.369093	0.368027	1.831465
1000	1005.68	0.820761	0.819695	2.037664
1500	1525.96	1.34492	1.343854	2.201653
2000	2028.39	1.85793	1.856864	2.288593
2500	2535.21	2.36536	2.364294	2.331458
3000	3027.69	2.88394	2.882874	2.380424
3500	3544.17	3.39137	3.390304	2.391465
4000	4031.38	3.88765	3.886584	2.410207
4500	4532.94	4.36162	4.360554	2.404926
5000	5028.93	4.86348	4.862414	2.417221
				2.269508

Sensitivity
0.08952

5028.93 lb is equal to 2.27 Volts. Excitation voltage is 10 and bridge resistance 352 ohms.

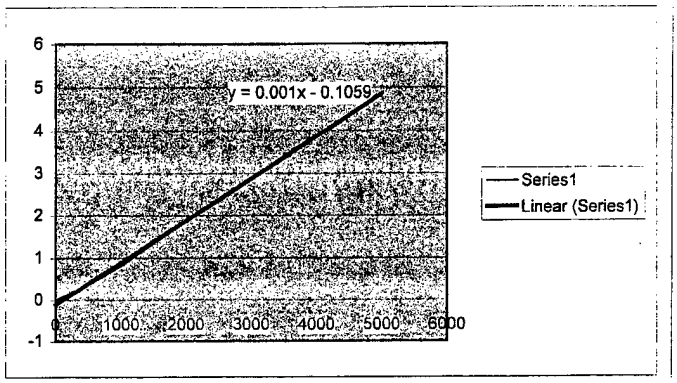

Link 2

0	36.8059	0.006642	0	0
500	502.952	0.036909	0.030267	0.150448
1000	1015.63	0.848642	0.842	2.072605
1500	1503.72	1.34492	1.338278	2.224945
2000	2001.47	1.83562	1.828978	2.284543
2500	2510.04	2.35978	2.353138	2.343726
3000	3038.52	2.88952	2.882878	2.371943
3500	3546.22	3.39137	3.384728	2.386152
4000	4044.55	3.90438	3.897738	2.409253
4500	4541.42	4.37277	4.366128	2.403504
5000	5000.84	4.84117	4.834528	2.416858
				2.106398

Sensitivity
0.083919

5000.84 lb is equal to 2.106 Volts. Excitation voltage is 10 and bridge resistance 352 ohms.

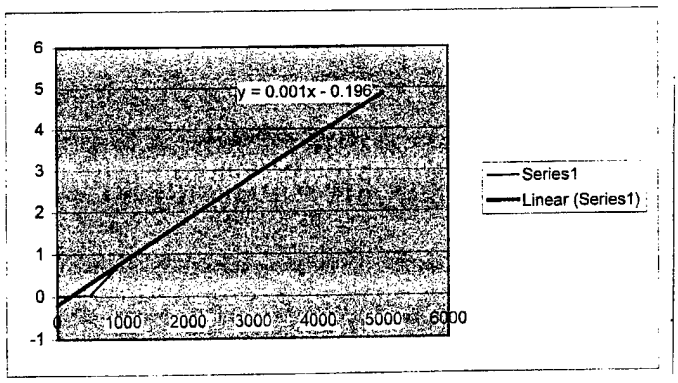

APPENDIX B

TEST DATA PLOTS

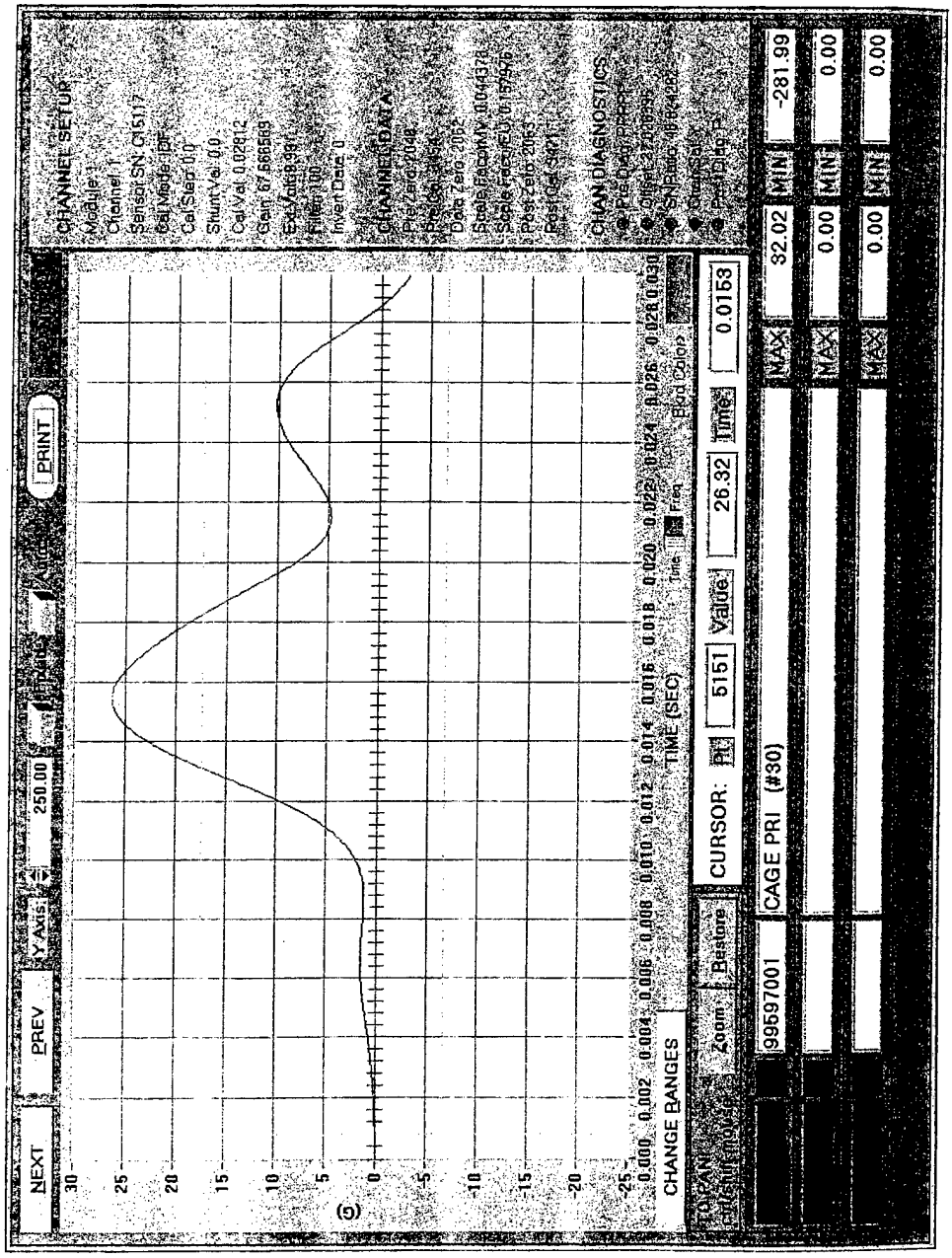
NEXT
PREV
Y Axis:
250.00
PRINT
CHANNEL SETUP
CHANNEL DATA
CHAN DIAGNOSTICS
(G)
TIME (SEC)
CHANGE RANGES
Zoom
Restore
CURSOR:
5151
Value
26.32
Time
0.0153
99597001
CAGE PRI (#30)
MAX
32.02
MIN
-281.99
MAX
0.00
MIN
0.00
MAX
0.00
MIN
0.00

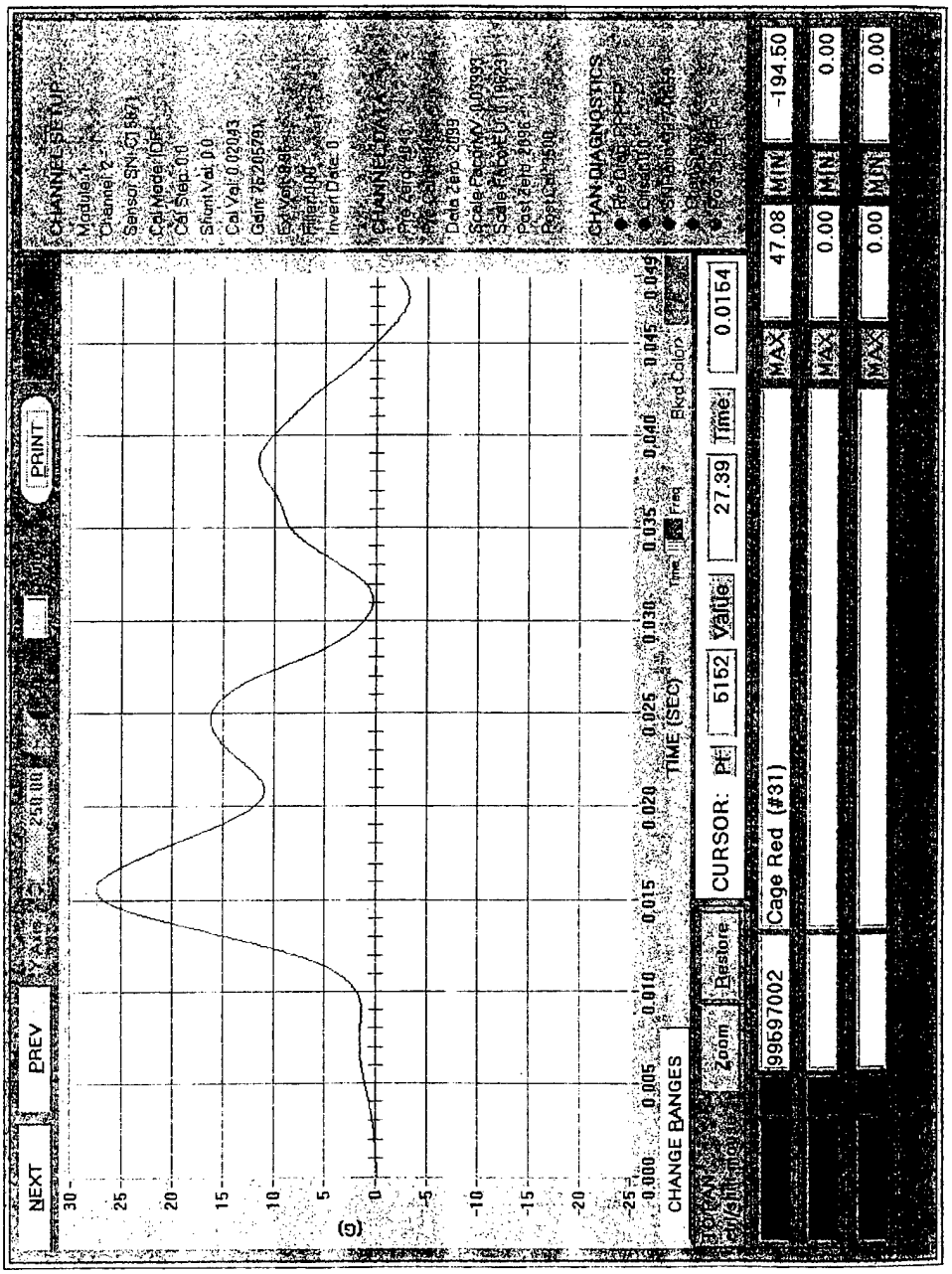
NEXT
PREV
PRINT
CHANNEL SETUP
CHANNEL DATA
CHAN DIAGNOSTICS
(G)
TIME (SEC)
CHANGE RANGES
Zoom
Restore
CURSOR: Pt 5152 Value 27.39 Time 0.0154
99597002
Cage Red (#31)
MAX 47.08 MIN -194.50
MAX 0.00 MIN 0.00
MAX 0.00 MIN 0.00

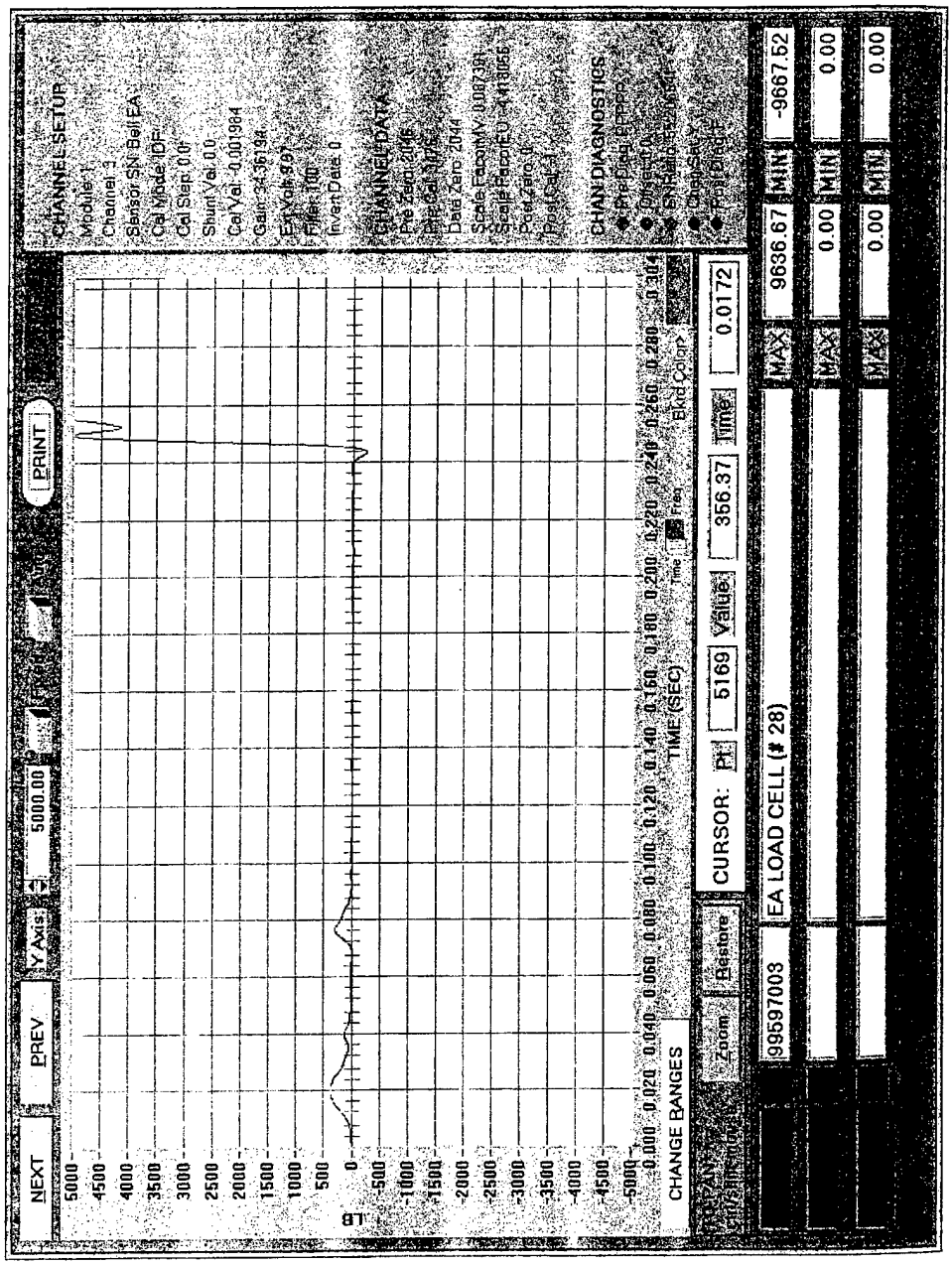
NEXT
PREV
Y Axis:
5000.00
PRINT
CHANNEL SETUP
Module: 1
Channel: 3
Sensor SN: Bell EA
Cal Mode: IDF
Cal Step: 0.0
Shunt Val: 0.0
Cal Val: 0.001984
Gain: 34.3194
Ext Volt: 9.91
Filter: 100
Invert Data: 0
CHANNEL DATA
Pre Zero: 2016
Data Zero: 2044
Post Zero: 0
Post Cal: 1
CHAN DIAGNOSTICS
LB
TIME (SEC)
CHANGE RANGES
Zoom
Restore
CURSOR:
Pt
5169
Value
356.37
Time
0.0172
99597003
EA LOAD CELL (# 28)
MAX
9636.67
MIN
-9667.52
0.00
0.00

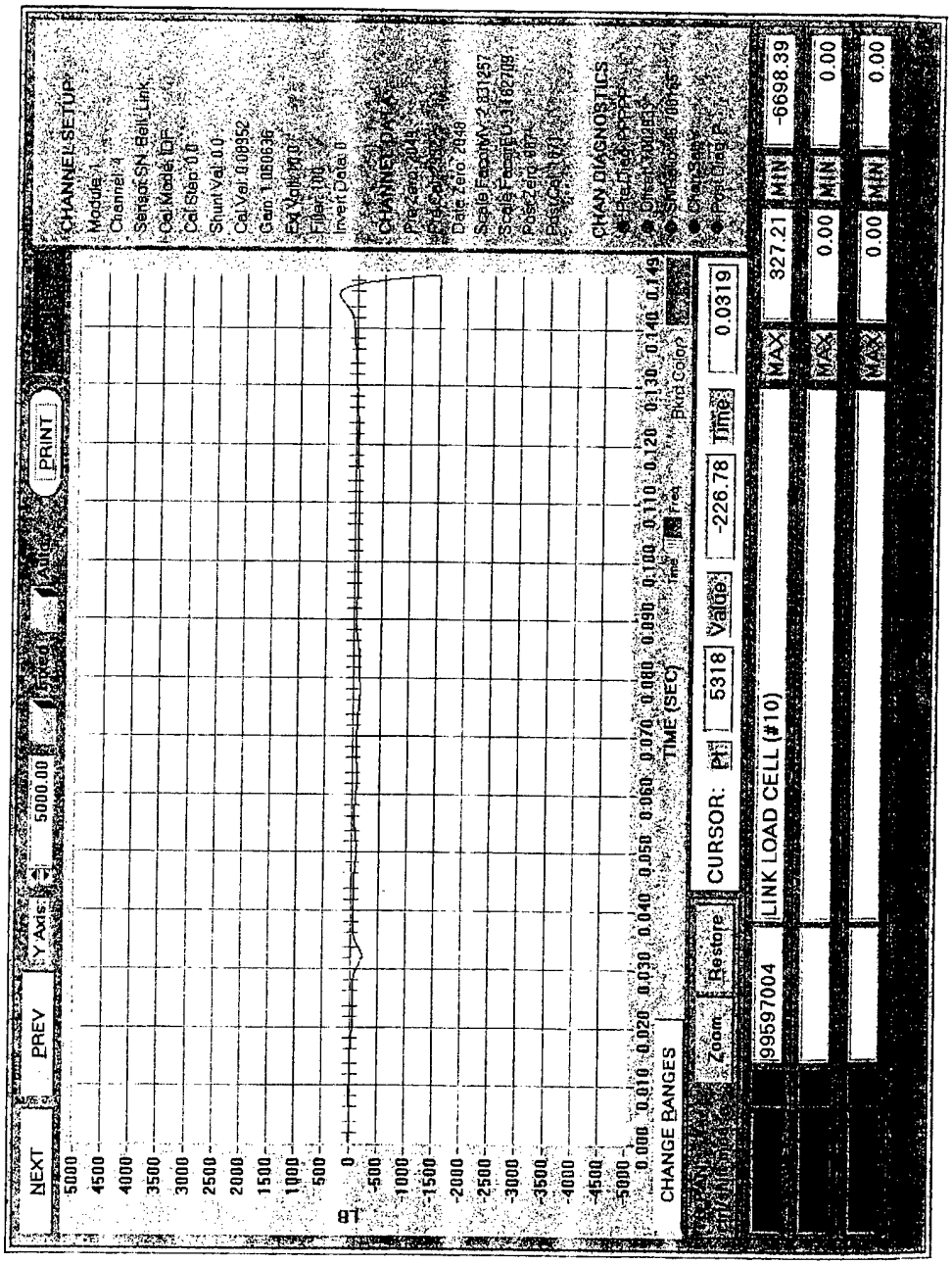
NEXT
PREV
Y Axis
5000.00
PRINT
CHANNEL SETUP
CHAN DIAGNOSTICS
LB
TIME (SEC)
CHANGE RANGES
Zoom
Restore
CURSOR:
5318
Value
-226.78
Time
0.0319
99597004
LINK LOAD CELL (#10)
MAX
327.21
MIN
-6698.39
0.00
0.00

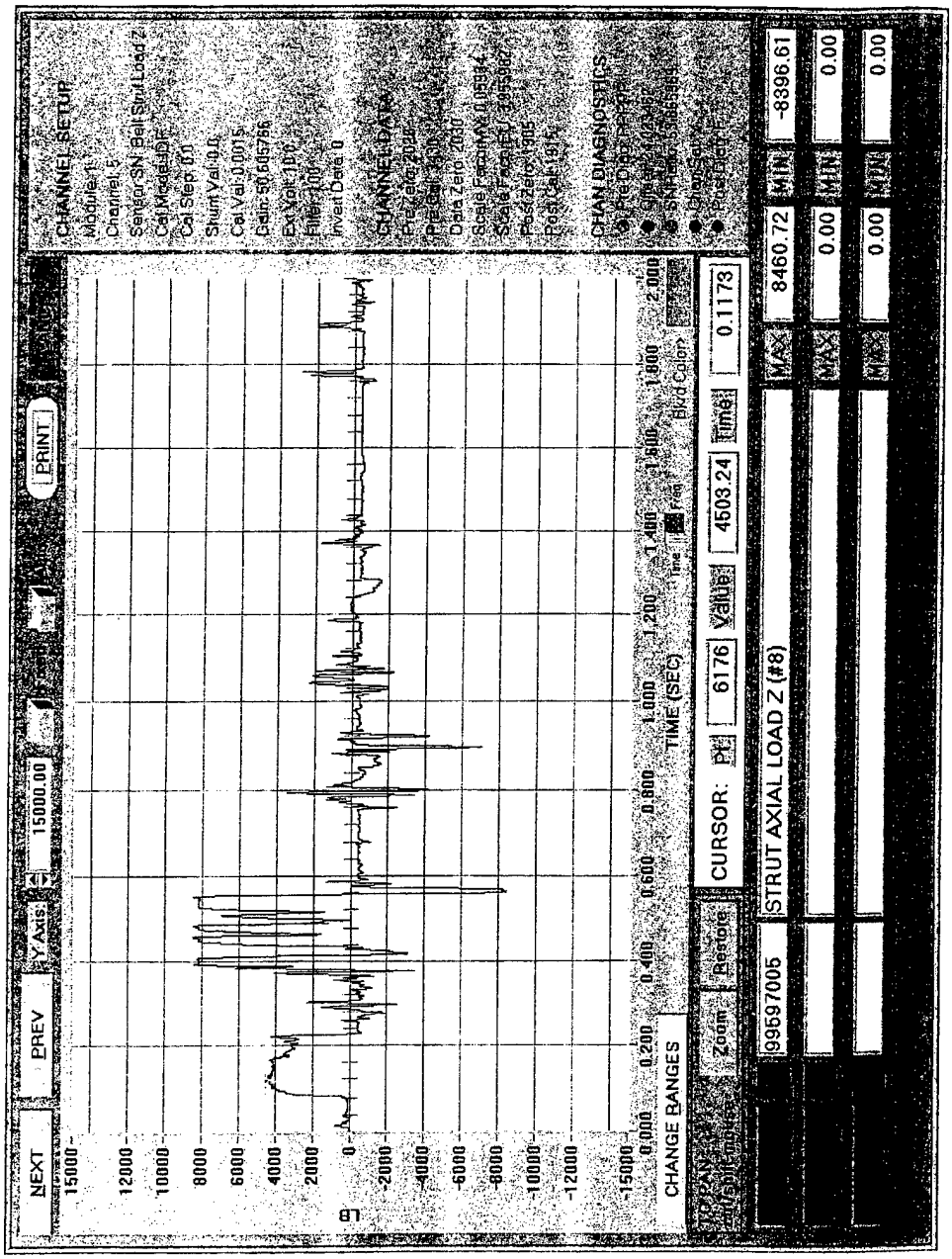
NEXT
PREV
Y Axis
15000.00
PRINT
CHANNEL SETUP
CHANNEL DATA
CHAN DIAGNOSTICS
LB
TIME (SEC)
CHANGE RANGES
Zoom
Restore
CURSOR:
Pt
6176
Value
4503.24
Time
0.1173
99697005
STRUT AXIAL LOAD Z (#8)
MAX
8460.72
MIN
-8396.61
0.00
0.00
0.00
0.00

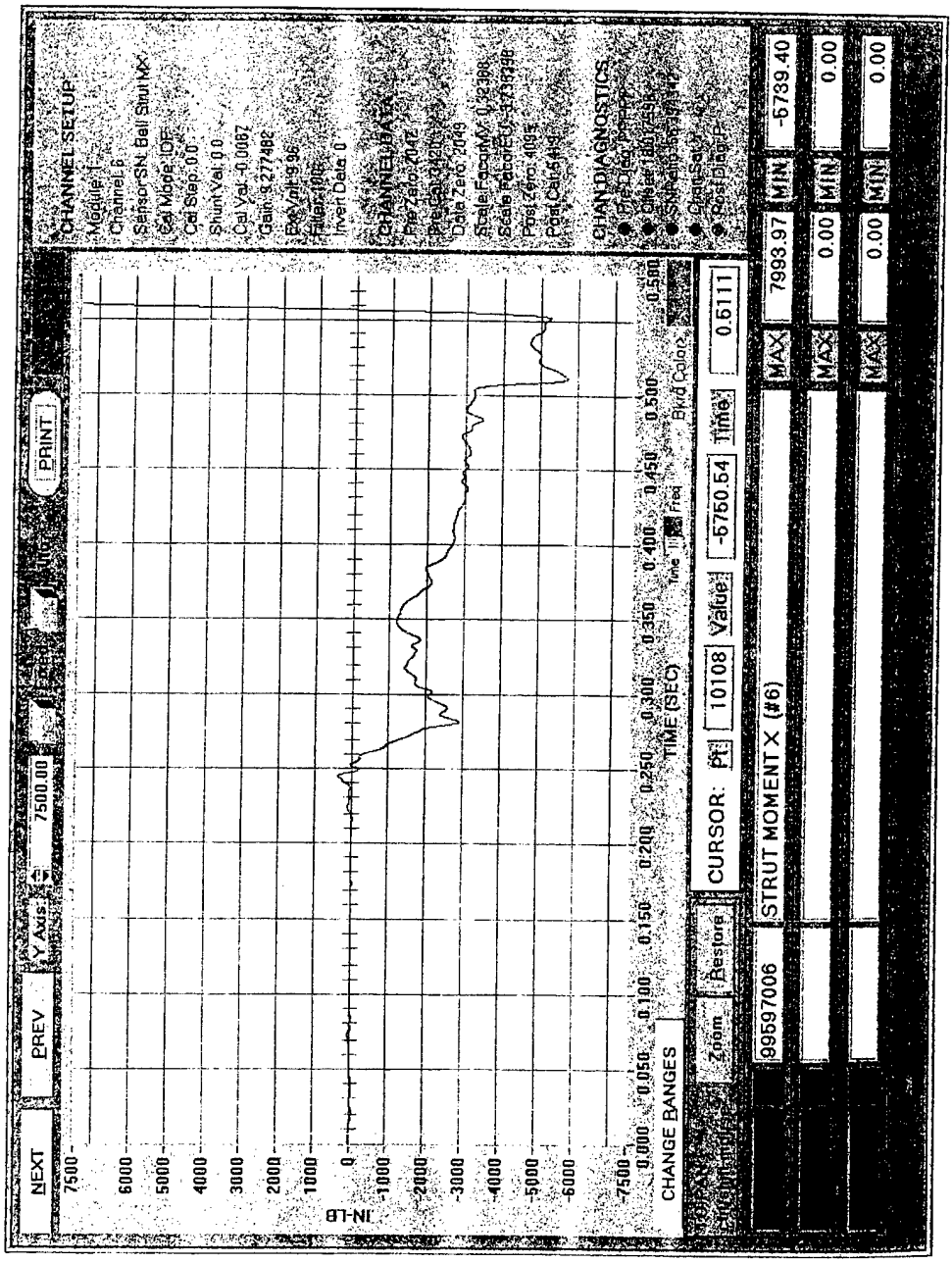
NEXT
PREV
Y Axis
7500.00
PRINT
CHANNEL SETUP
CHANNEL DATA
CHAN DIAGNOSTICS
IN-LB
TIME (SEC)
CHANGE RANGES
Zoom
Restore
CURSOR:
10108
Value
-6750.54
Time
0.6111
MAX
7993.97
MIN
-6739.40
MAX
0.00
MIN
0.00
MAX
0.00
MIN
0.00
99597006
STRUT MOMENT X (#6)

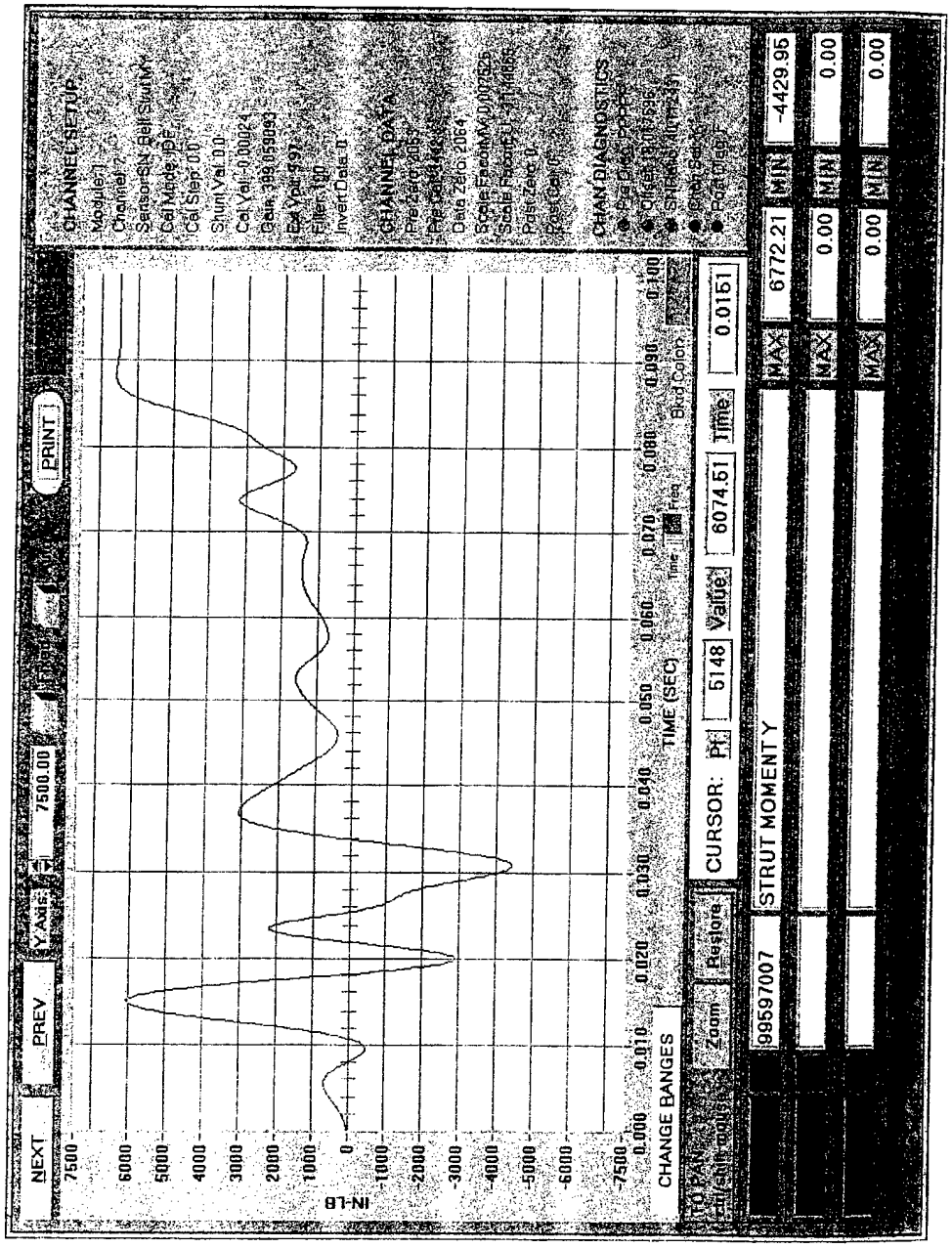
NEXT
PREV
Y Axis
7500.00
PRINT
CHANNEL SETUP
CHANNEL DATA
CHAN DIAGNOSTICS
IN-LB
TIME (SEC)
CHANGE RANGES
Zoom
Restore
CURSOR:
Pt
5148
Value
6074.51
Time
0.0151
MAX
6772.21
MIN
-4429.95
0.00
0.00
0.00
0.00
99597007
STRUT MOMENT Y

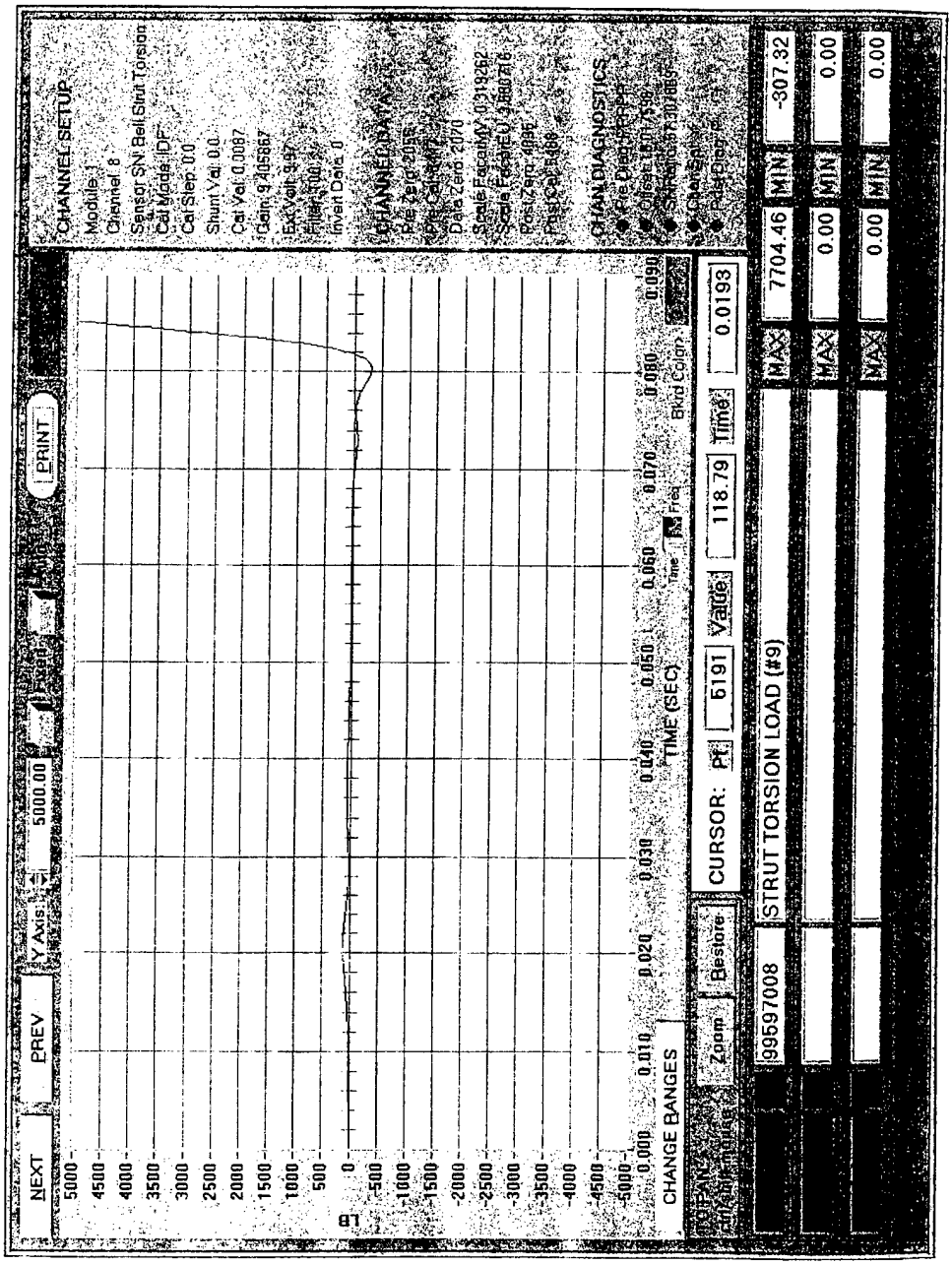
NEXT
PREV
Y Axis
5000.00
PRINT
CHANNEL SETUP
Module: 1
Channel: 8
Sensor: SN Bell Strut Torsion
Cal Mode: IDF
Cal Step: 0.0
Shunt Val: 0.0
Cal Val: 0.0087
Gain: 9.405867
Ext Volt: 9.97
Filter: 100
Invert Data: 0
CHANNEL DATA
Pre Zero: 2055
Data Zero: 2070
Scale Factor: 0.319262
Post Zero: 4095
CHAN DIAGNOSTICS
LB
5000
4500
4000
3500
3000
2500
2000
1500
1000
500
0
-500
-1000
-1500
-2000
-2500
-3000
-3500
-4000
-4500
-5000
0.000
0.010
0.020
0.030
0.040
0.050
0.060
0.070
0.080
0.090
TIME (SEC)
CHANGE RANGES
Zoom
Restore
CURSOR: Pt
6191
Value
118.79
Time
0.0193
99597008
STRUT TORSION LOAD (#9)
MAX
7704.46
MIN
-307.32
MAX
0.00
MIN
0.00
MAX
0.00
MIN
0.00

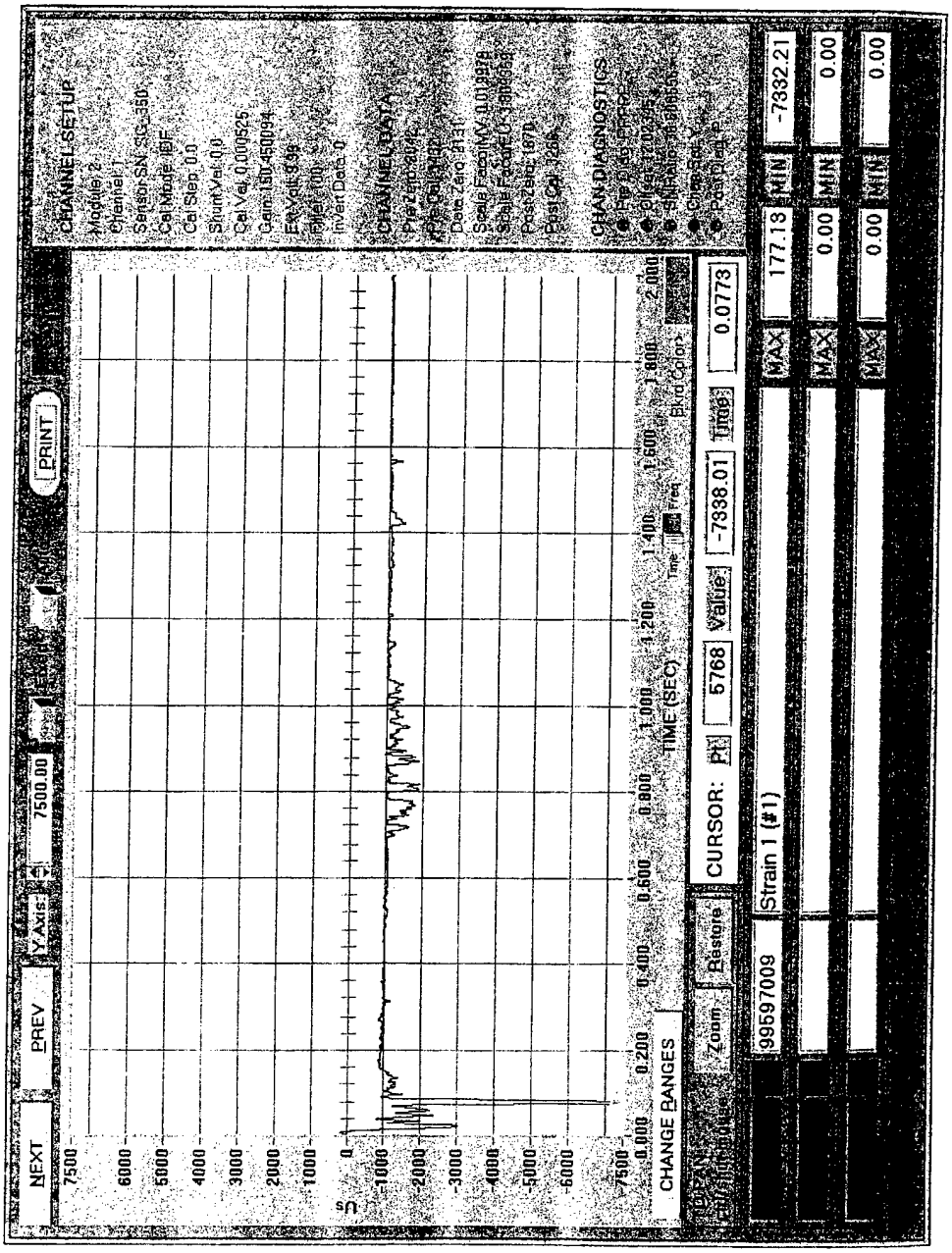
NEXT
PREV
Y Axis
7500.00
PRINT
CHANNEL SETUP
CHANNEL DATA
CHAN DIAGNOSTICS
CHANGE RANGES
Zoom
Restore
CURSOR:
Pt
5768
Value
-7338.01
Time
0.0773
TIME (SEC)
99597009
Strain 1 (#1)
MAX
177.13
MIN
-7332.21
MAX
0.00
MIN
0.00
MAX
0.00
MIN
0.00

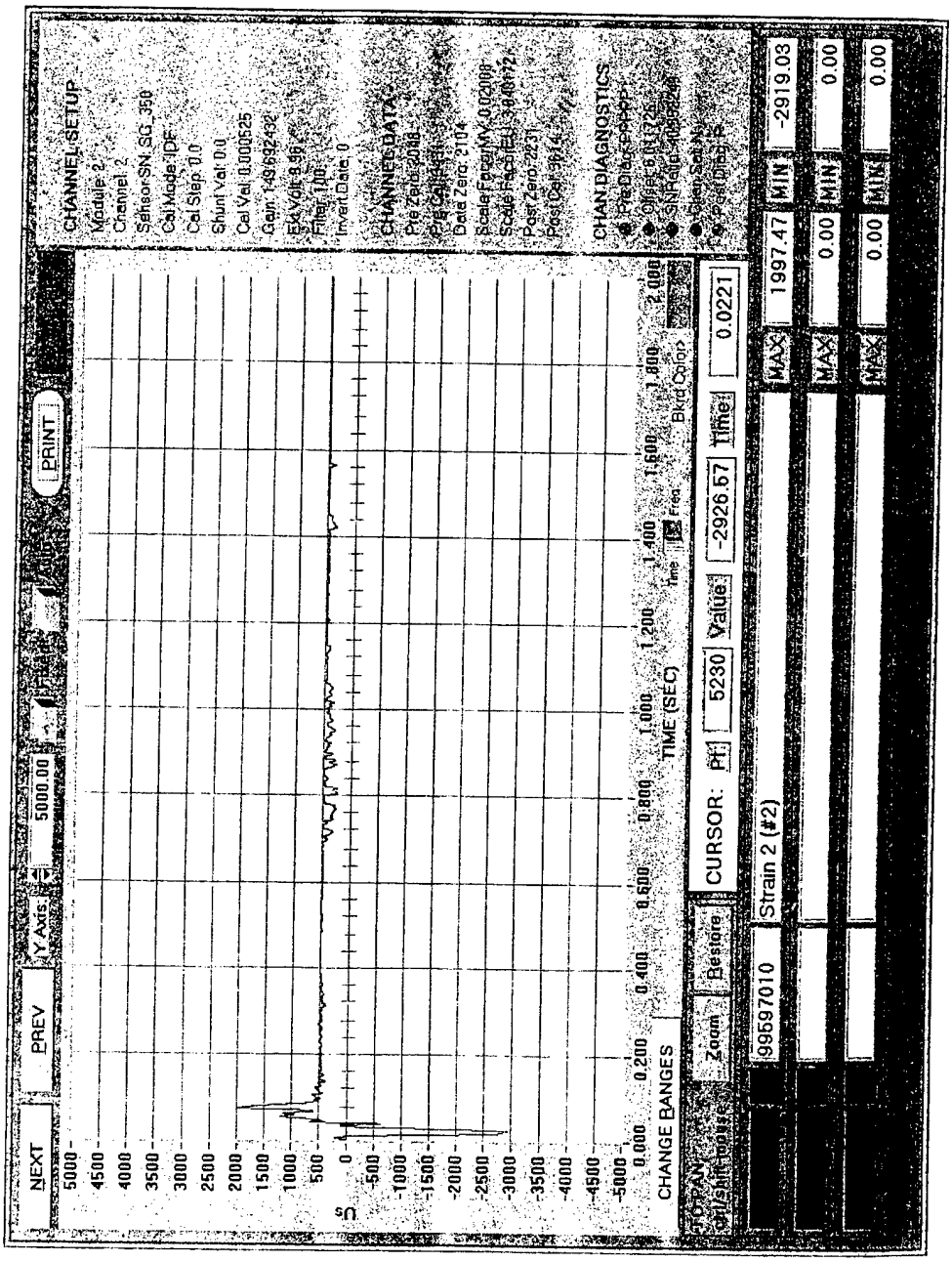
NEXT
PREV
Y Axis:
5000.00
PRINT
CHANNEL SETUP
Module: 2
Channel: 2
Sensor SN: SG_350
Cal Mode: IDF
Cal Step: 0.0
Shunt Val: 0.0
Cal Val: 0.000525
Gain: 149.692432
Filter: 100
Invert Data: 0
CHANNEL DATA
Data Zero: 2104
CHAN DIAGNOSTICS
Us
TIME (SEC)
CHANGE RANGES
Zoom
Restore
CURSOR: Pt: 5230 Value: -2926.57 Time: 0.0221
99597010
Strain 2 (#2)
MAX 1997.47 MIN -2919.03
MAX 0.00 MIN 0.00
MAX 0.00 MIN 0.00

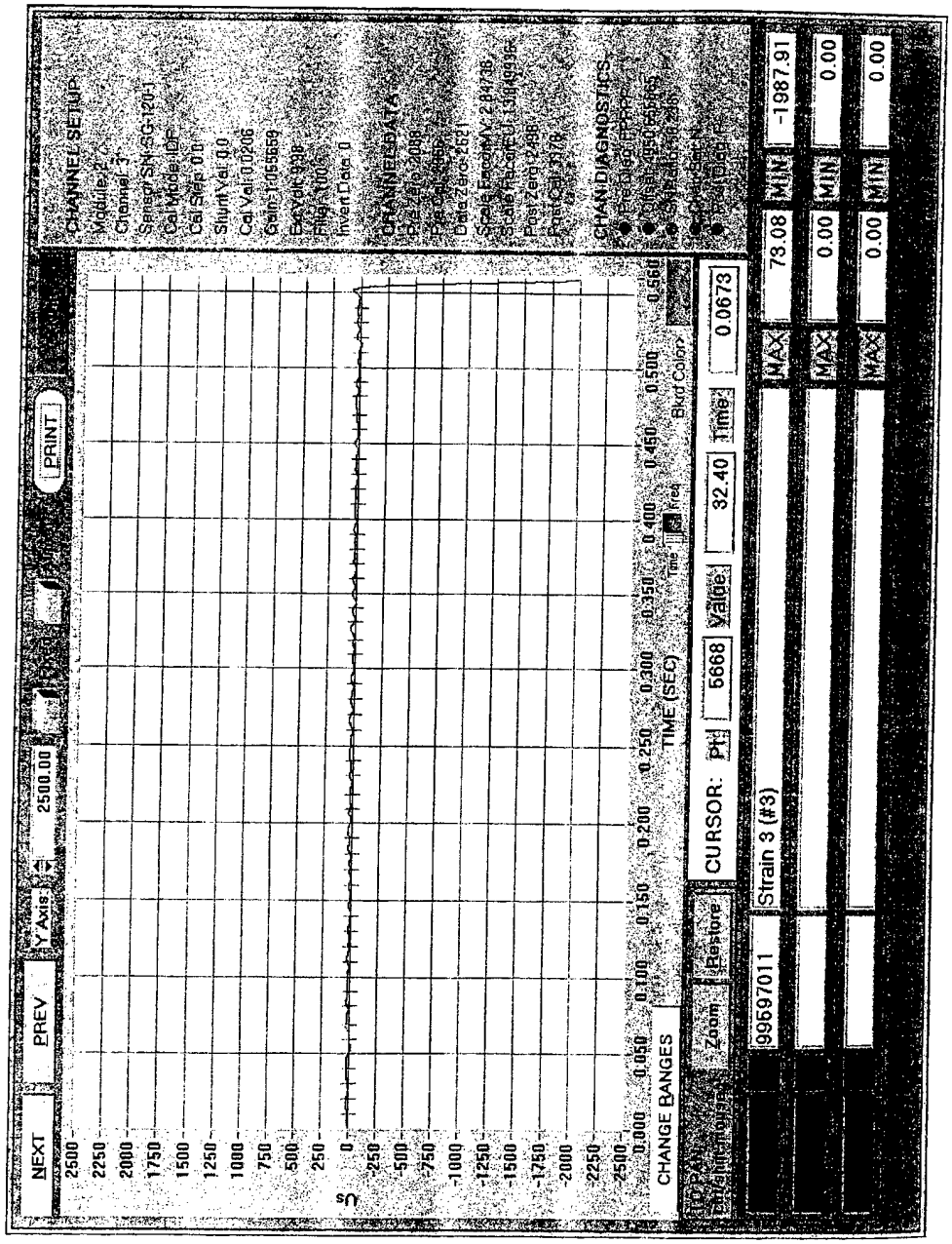
NEXT
PREV
Y Axis
2500.00
PRINT
CHANNEL SETUP
CHANNEL DATA
CHAN DIAGNOSTICS
CHANGE RANGES
Zoom
Restore
CURSOR:
Pt
6668
Value
32.40
Time
0.0673
TIME (SEC)
99697011
Strain 3 (#3)
MAX
73.08
MIN
-1987.91
0.00
0.00

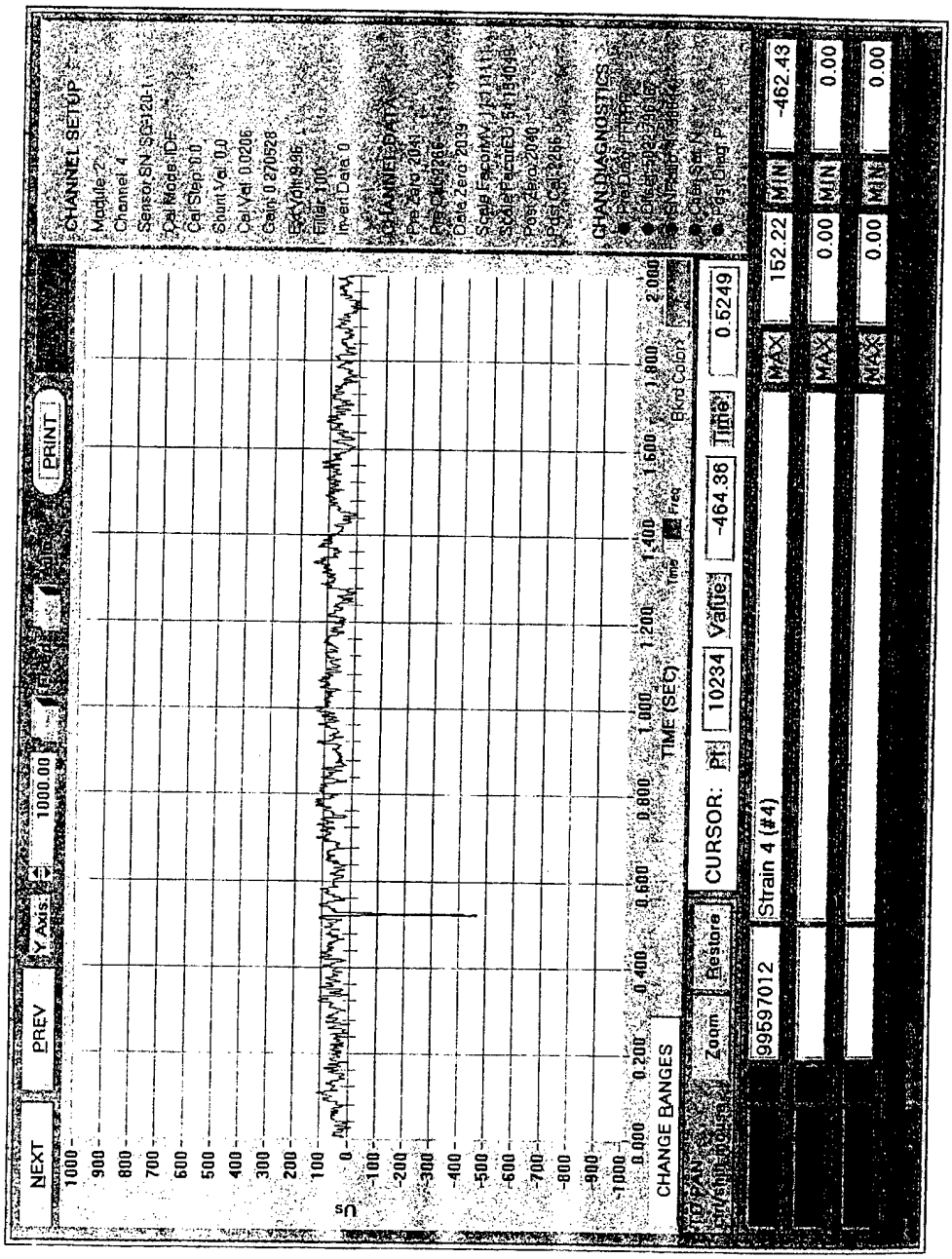
NEXT
PREV
Y Axis:
1000.00
PRINT
CHANNEL SETUP
Module 2
Channel 4
Sensor SN SC-120-1
Cal Mode: DC
Cal Step 0.0
Shunt Val 0.0
Cal Val 0.00206
Gain 0.270528
Filter 100
Invert Data 0
CHANNEL DATA
Date Zero 2039
CHAN DIAGNOSTICS
uS
TIME (SEC)
CHANGE RANGES
Zoom
Restore
CURSOR:
Pt
10234
Value
-464.36
Time
0.5249
Strain 4 (#4)
MAX
152.22
MIN
-462.43
0.00
0.00
0.00
0.00

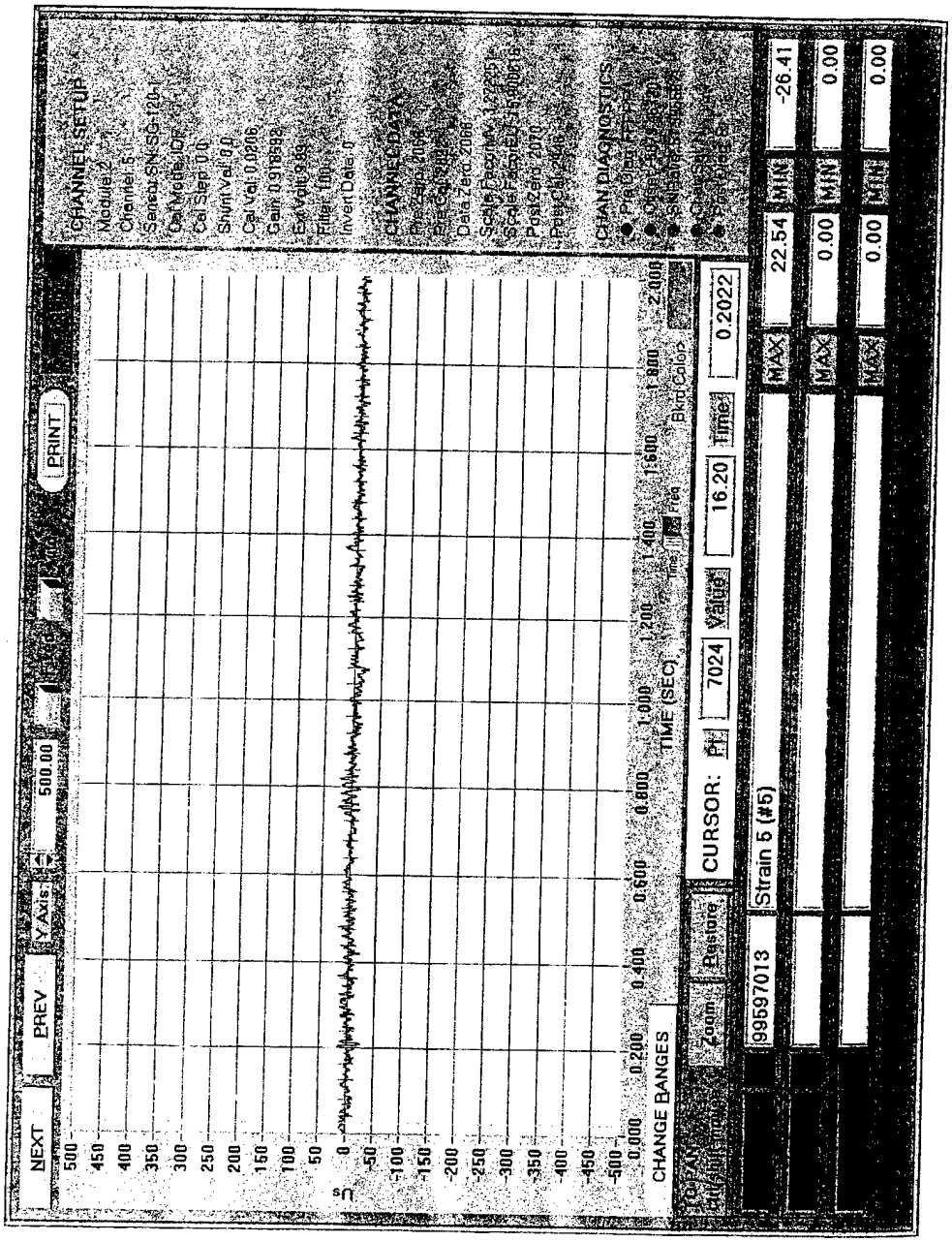
NEXT
PREV
Y Axis:
500.00
PRINT
CHANNEL SETUP
CHANNEL DATA
CHAN DIAGNOSTICS
CHANGE RANGES
Zoom
Restore
CURSOR:
7024
Value
16.20
Time
0.2022
TIME (SEC)
99597013
Strain 5 (#5)
MAX
22.54
MIN
-26.41
MAX
0.00
MIN
0.00
MAX
0.00
MIN
0.00

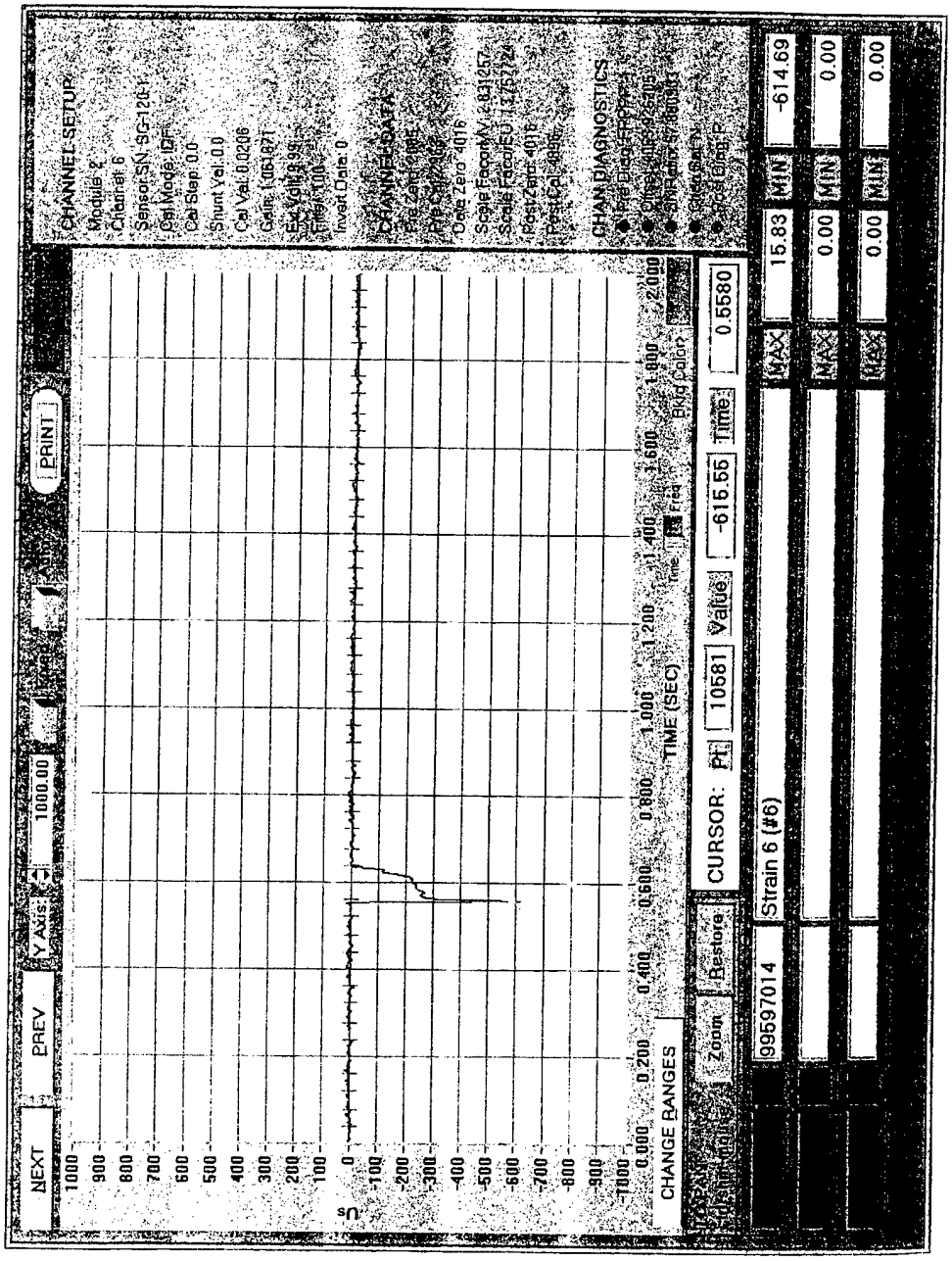
NEXT
PREV
Y Axis:
1000.00
PRINT
CHANNEL SETUP
Module: 2
Channel: 6
Sensor SN: SG-120-1
Cal Mode: IDF
Cal Step: 0.0
Shunt Val: 0.0
Cal Val: 0.0206
Gain: 1.061871
Ex Volt: 9.99
Filter: 100
Invert Data: 0
CHANNEL DATA
Data Zero: 4016
Scale Factor: 2.831257
Scale Factor: 1.3757724
Post Zero: 4016
Post Cal: 4096
CHAN DIAGNOSTICS
Pre Diag: FPPP
Post Diag: P
CHANGE RANGES
Zoom
Restore
TIME (SEC)
CURSOR: Pt 10581 Value -615.55 Time 0.5580
99597014
Strain 6 (#6)
MAX 15.83 MIN -614.69
MAX 0.00 MIN 0.00
MAX 0.00 MIN 0.00

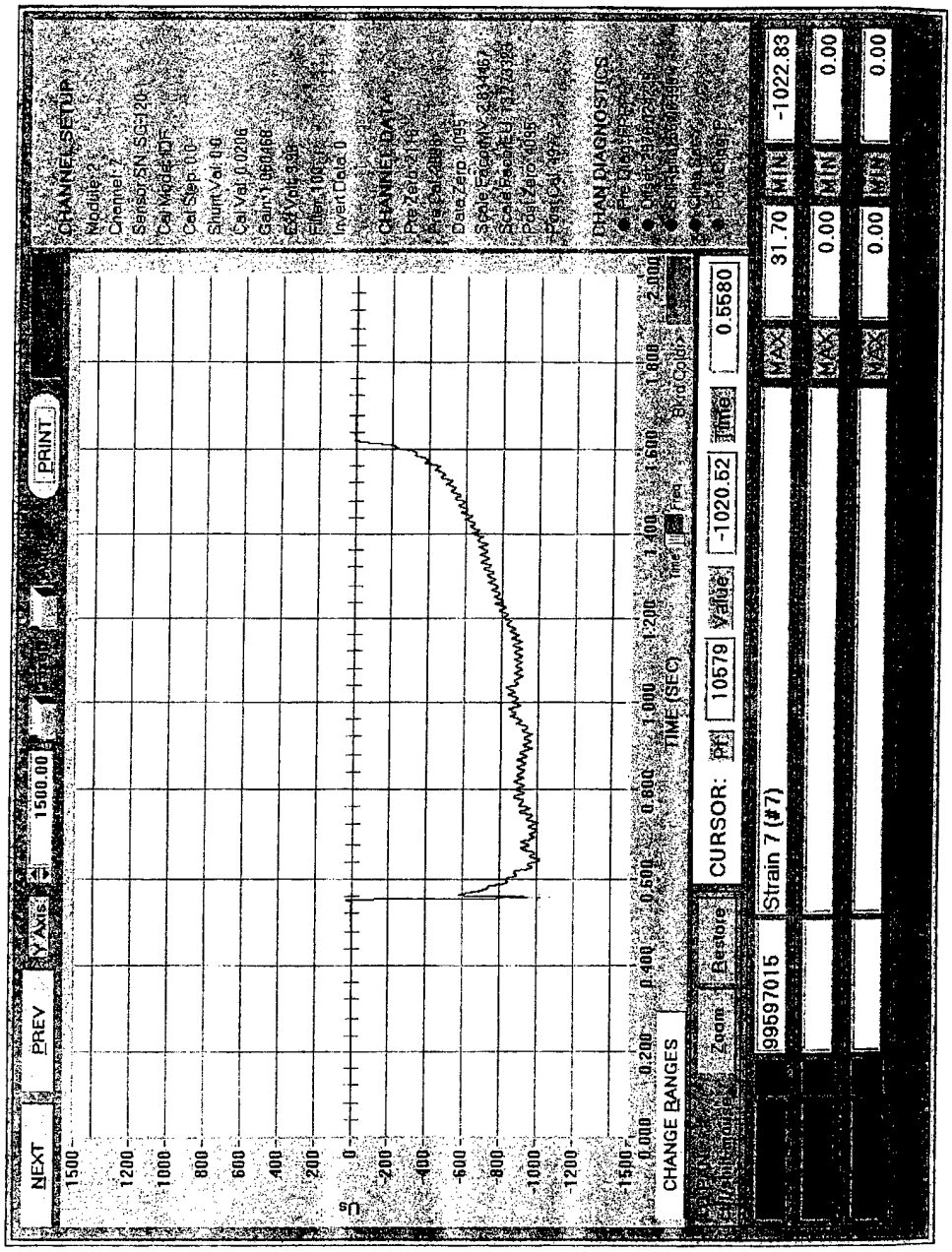
NEXT
PREV
Y Axis
1500.00
PRINT
CHANNEL SETUP
CHANNEL DATA
CHAN DIAGNOSTICS
CHANGE RANGES
Zoom
Restore
CURSOR:
10579
Value
-1020.52
Time
0.5580
TIME (SEC)
99597015
Strain 7 (#7)
MAX
31.70
MIN
-1022.83
MAX
0.00
MIN
0.00
MAX
0.00
MIN
0.00

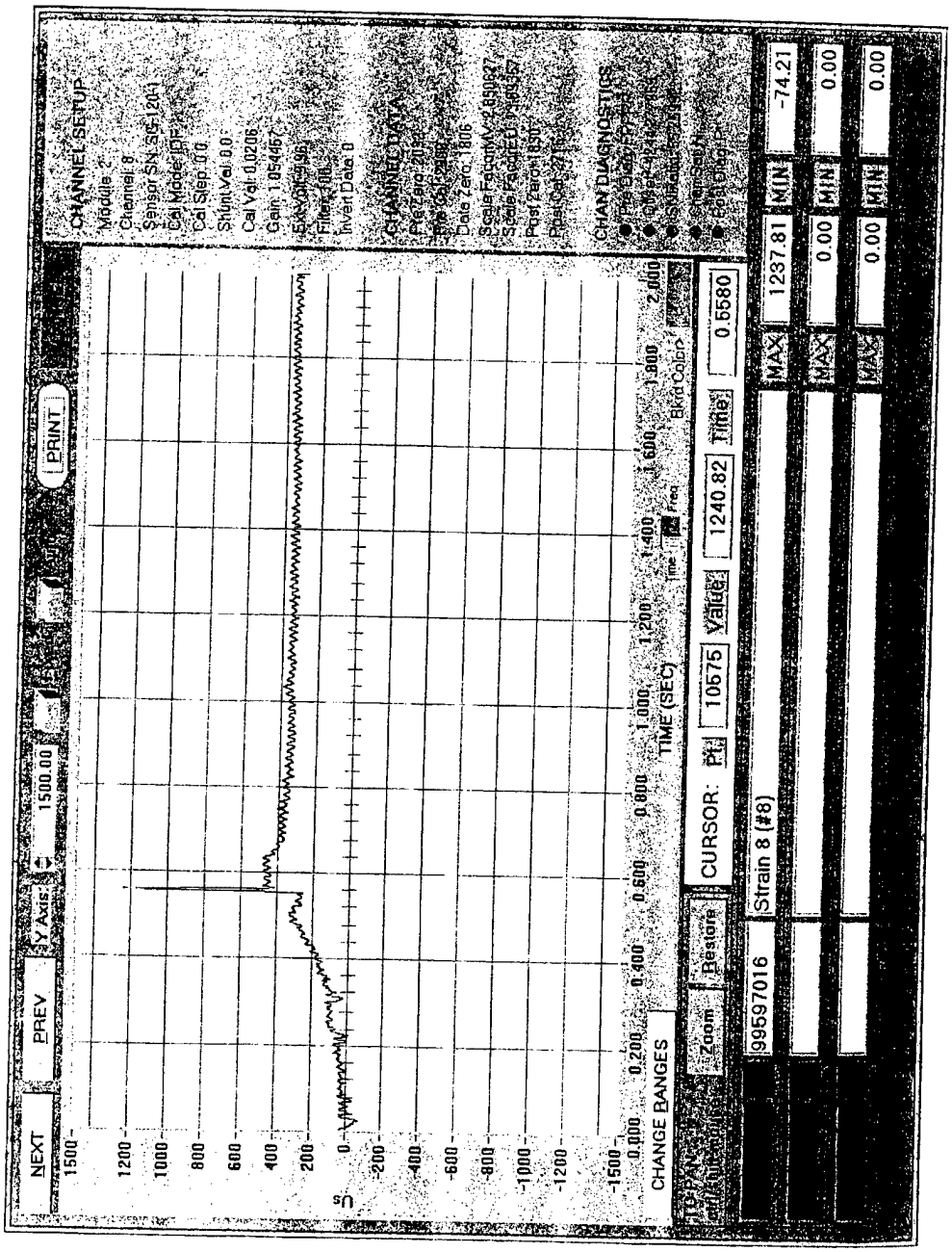
NEXT
PREV
Y Axis:
1500.00
PRINT
CHANNEL SETUP
Module 2
Channel 8
Sensor SN: SG-120-1
Cal Mode: DF
Cal Step: 0.0
Shunt Val: 0.0
Cal Val: 0.0206
Gain: 1.05467
Filter: 100
Invert Data: 0
CHANNEL DATA
Data Zero: 1806
CHAN DIAGNOSTICS
Us
1500
1200
1000
800
600
400
200
0
-200
-400
-600
-800
-1000
-1200
-1500
0.000
0.200
0.400
0.600
0.800
1.000
1.200
1.400
1.600
1.800
2.000
TIME (SEC)
CHANGE RANGES
Zoom
Restore
CURSOR:
Pt
10575
Value
1240.82
Time
0.5580
Bkrd Color
99597016
Strain 8 (#8)
MAX
1237.81
MIN
-74.21
MAX
0.00
MIN
0.00
MAX
0.00
MIN
0.00

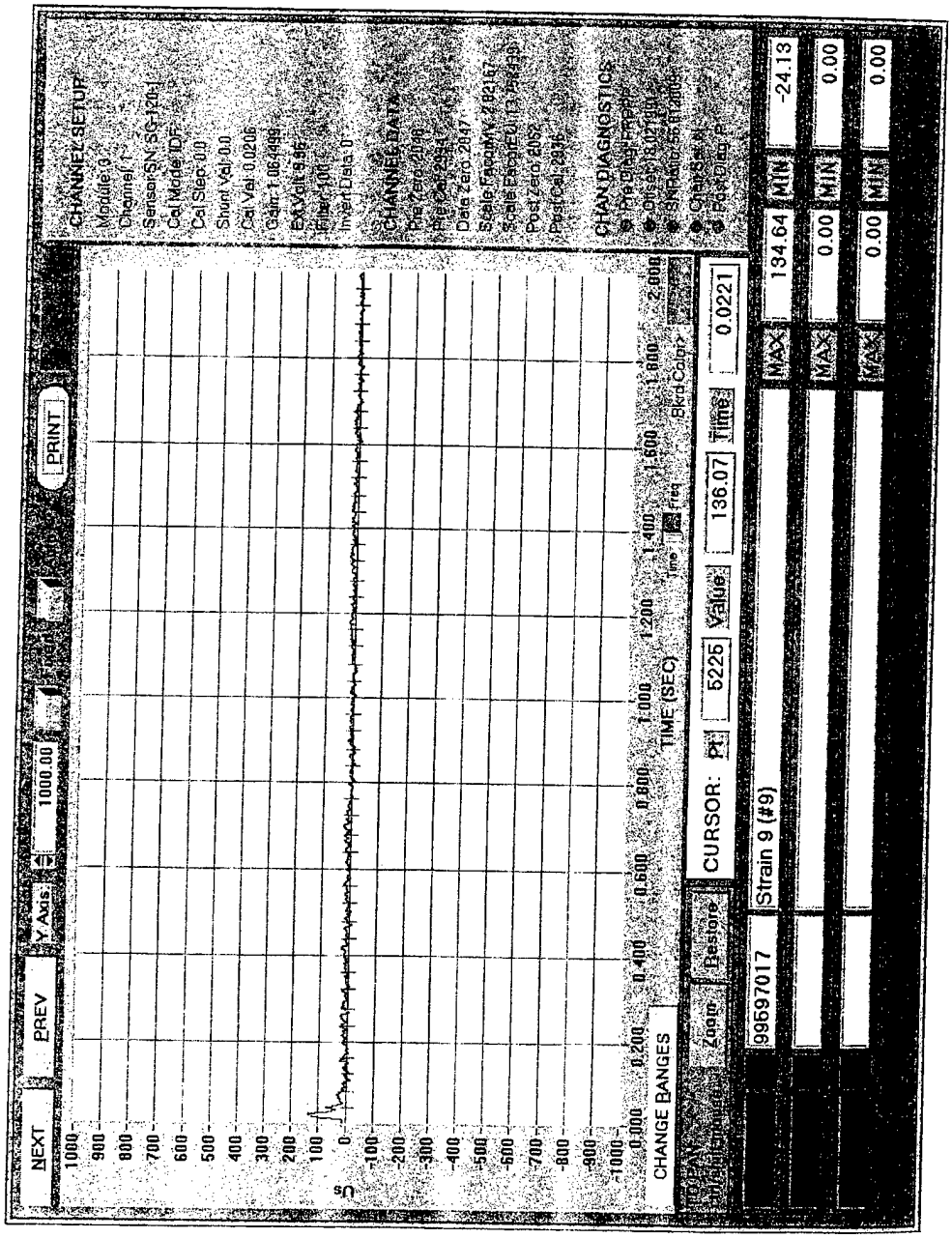
NEXT
PREV
Y Axis
1000.00
PRINT
CHANNEL SETUP
CHANNEL DATA
CHAN DIAGNOSTICS
CHANGE RANGES
TIME (SEC)
CURSOR:
Pt
5225
Value
136.07
Time
0.0221
99597017
Strain 9 (#9)
MAX
134.64
MIN
-24.13
0.00
0.00

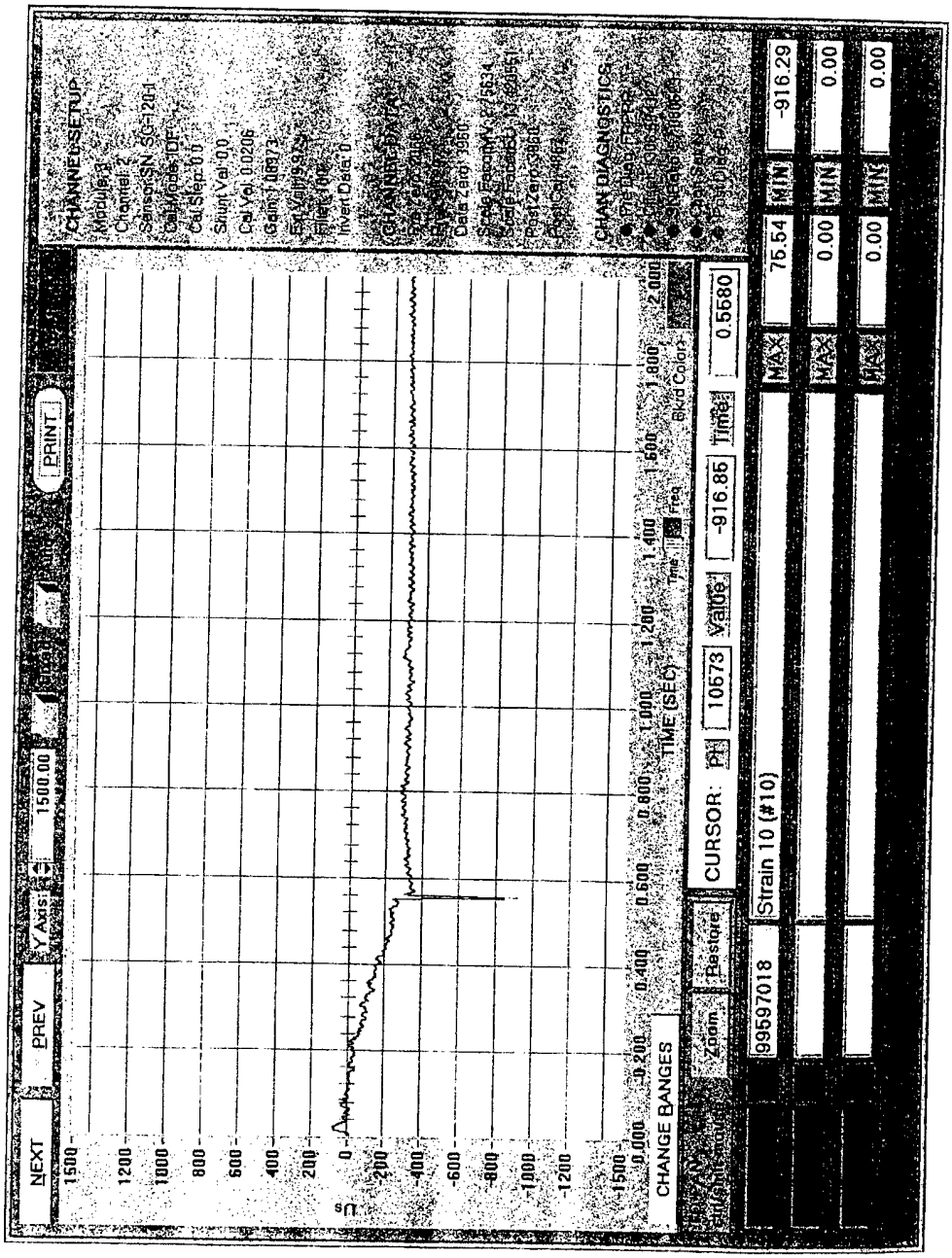
NEXT
PREV
Y Axis
1500.00
PRINT
CHANNEL SETUP
CHANNEL DATA
CHAN DIAGNOSTICS
CHANGE RANGES
Zoom
Restore
CURSOR:
10673
Value
-916.85
Time
0.5580
TIME (SEC)
99597018
Strain 10 (#10)
MAX
MIN
76.54
-916.29
0.00
0.00
0.00
0.00

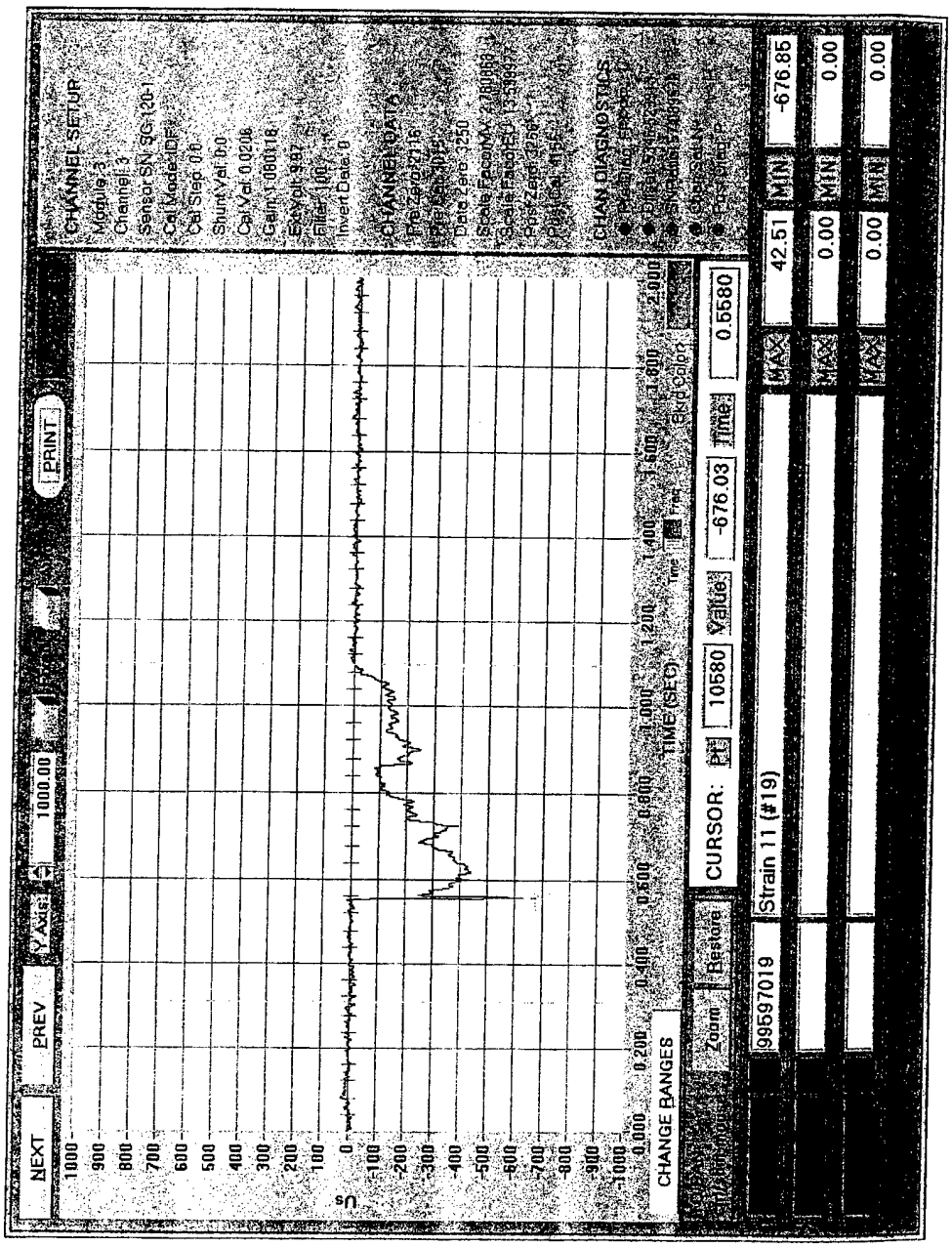
NEXT
PREV
Y Axis
1000.00
PRINT
CHANNEL SETUP
Module:3
Channel:3
Sensor SN:SG-120-1
Cal Mode:IDE
Cal Sig:0.0
Shunt Val:0.0
Cal Val:0.0206
Gain:1.060118
Ex Volt:9.97
Filter:100
Invert Data:0
CHANNEL DATA
CHAN DIAGNOSTICS
uε
TIME (SEC)
CHANGE RANGES
Zoom
Restore
CURSOR:
Pt
10580
Value
-676.03
Time
0.5580
99597019
Strain 11 (#19)
MAX
42.51
MIN
-676.85
MAX
0.00
MIN
0.00
MAX
0.00
MIN
0.00

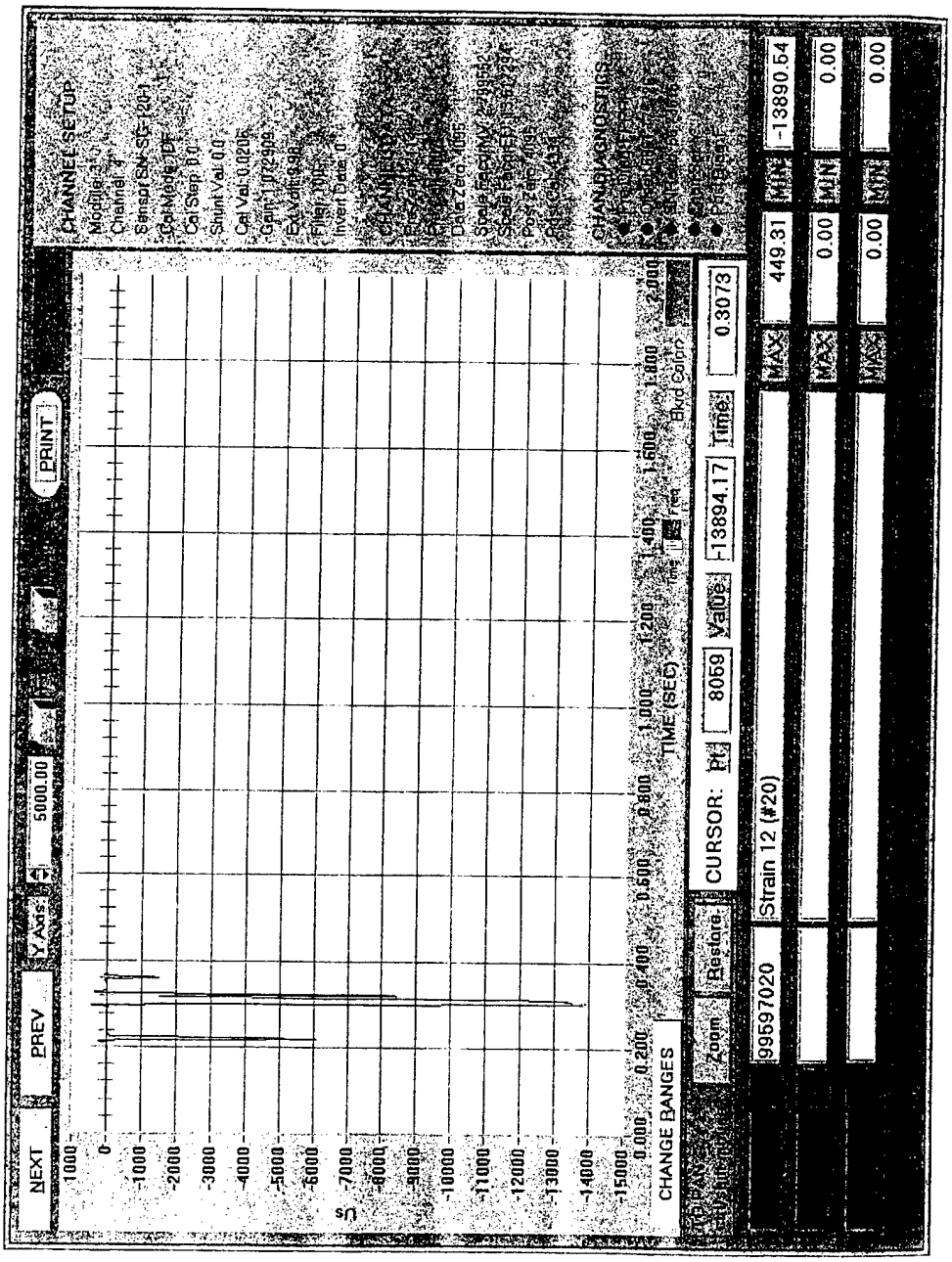
NEXT
PREV
Y Axis
5000.00
PRINT
CHANNEL SETUP
CHANGE RANGES
Zoom
Restore
CURSOR: Pt
8059
Value
-13894.17
Time
0.3073
TIME (SEC)
99597020
Strain 12 (#20)
MAX
449.31
MIN
-13890.54
MAX
0.00
MIN
0.00
MAX
0.00
MIN
0.00

ATTACHMENT I

TEST PHOTOGRAPHS

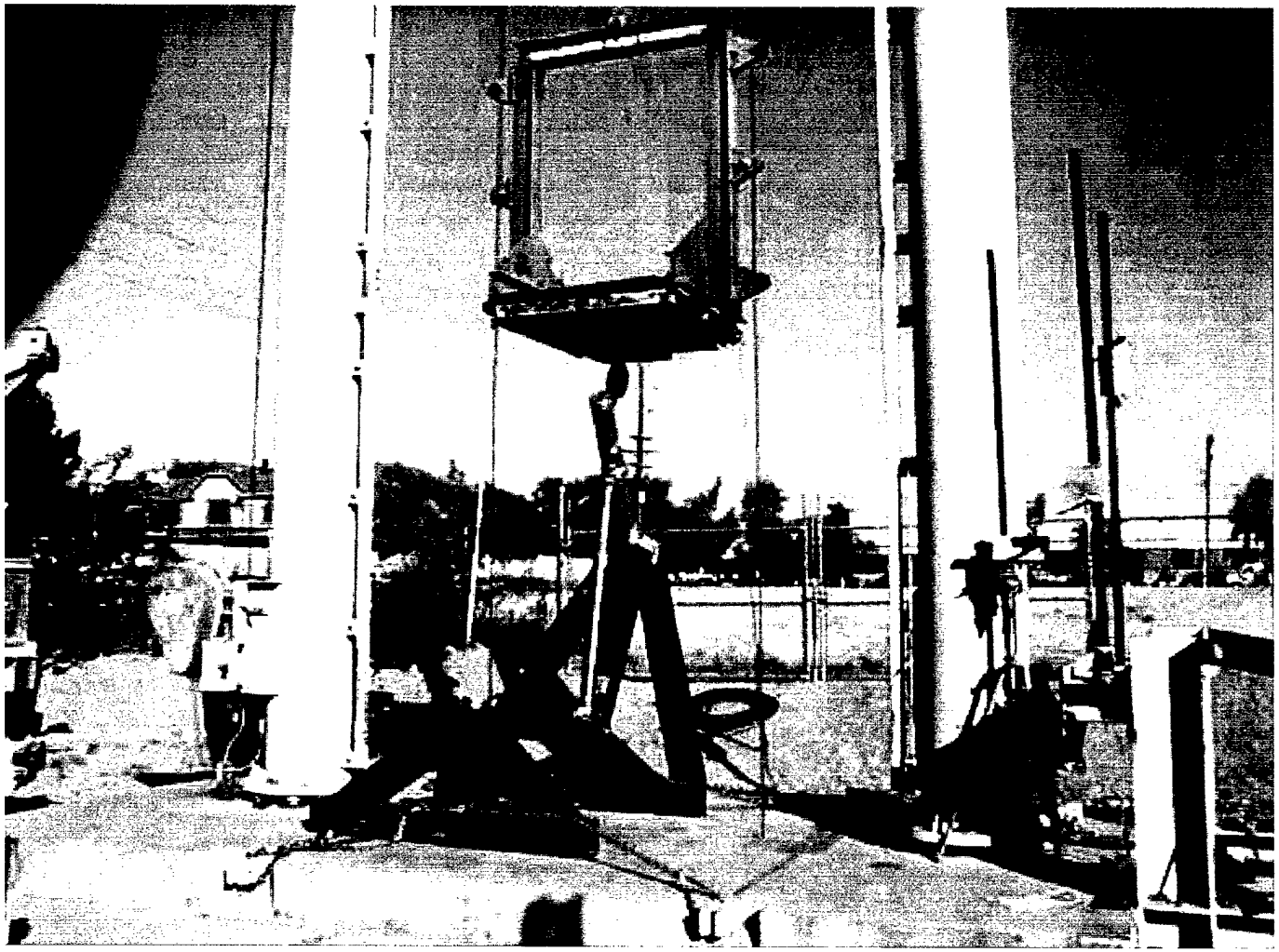

Drop Test Setup

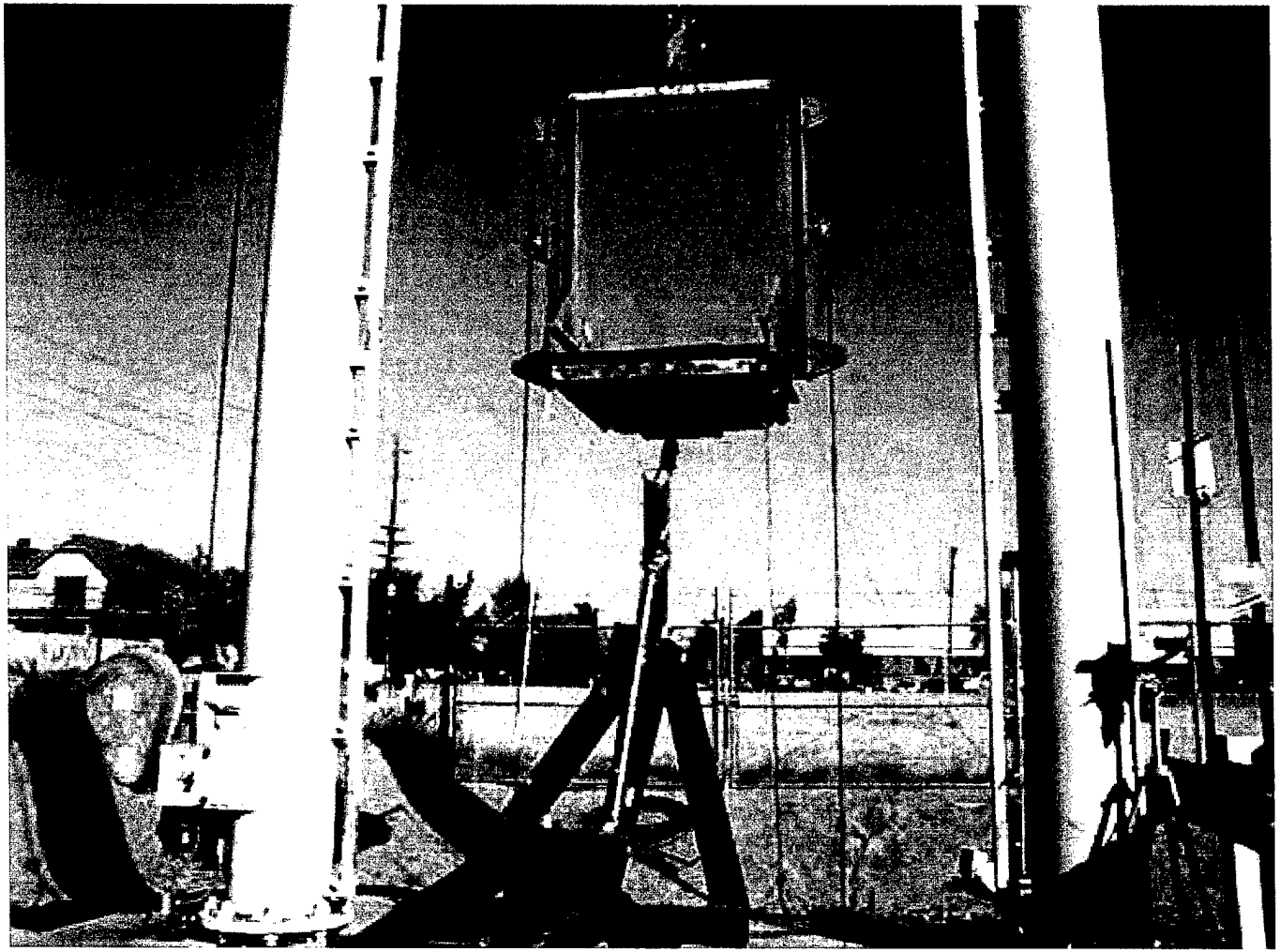

Drop Test Setup

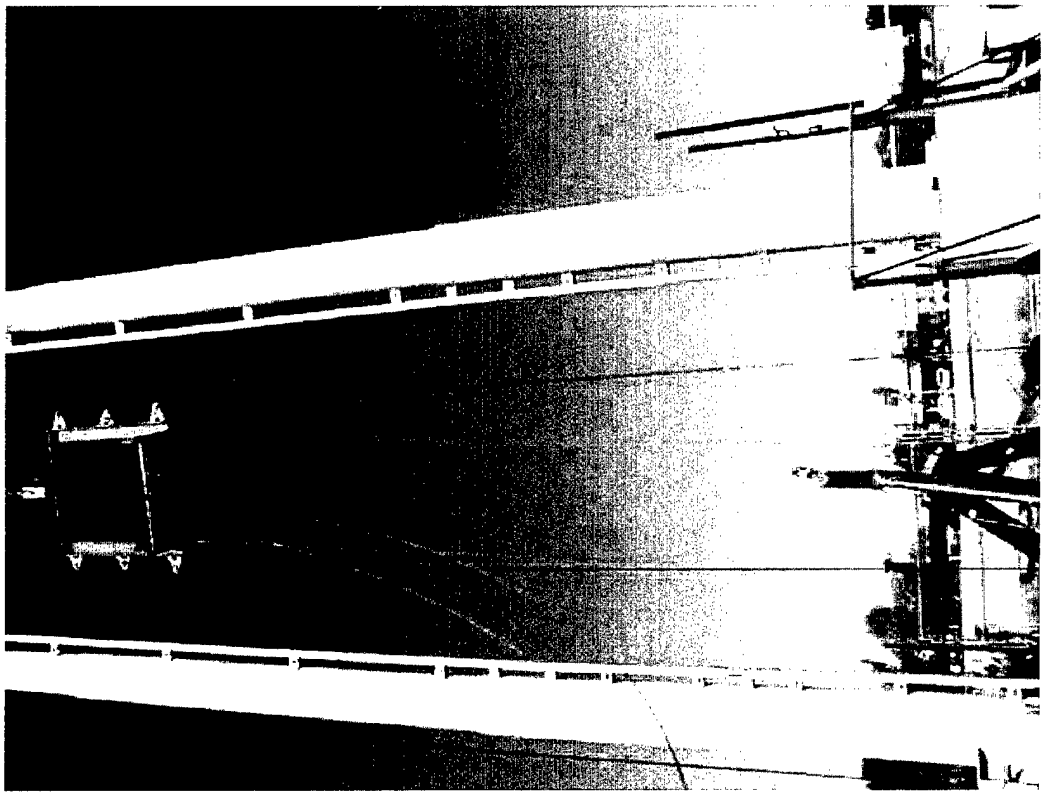

Pre-Impact

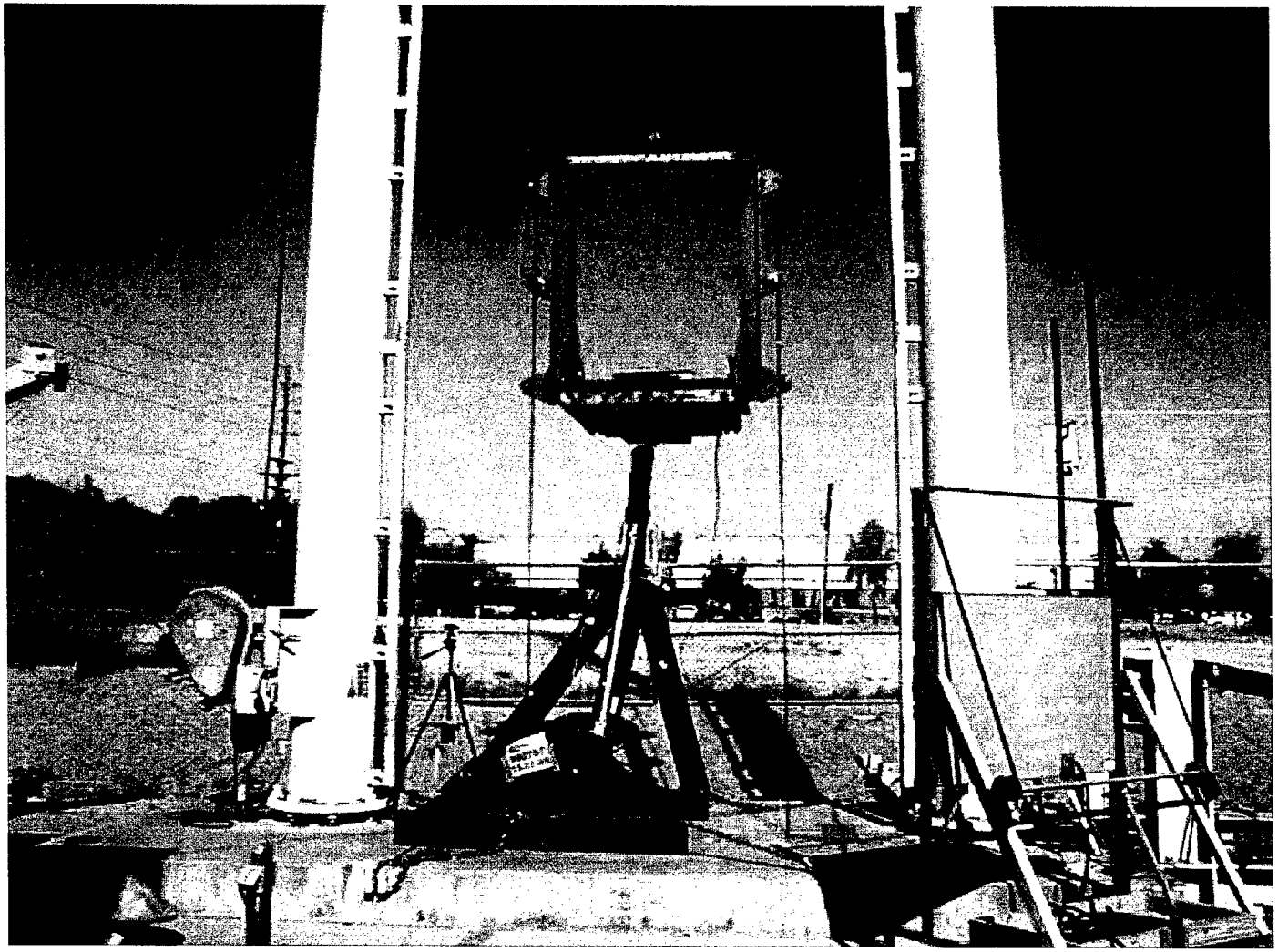

Impact

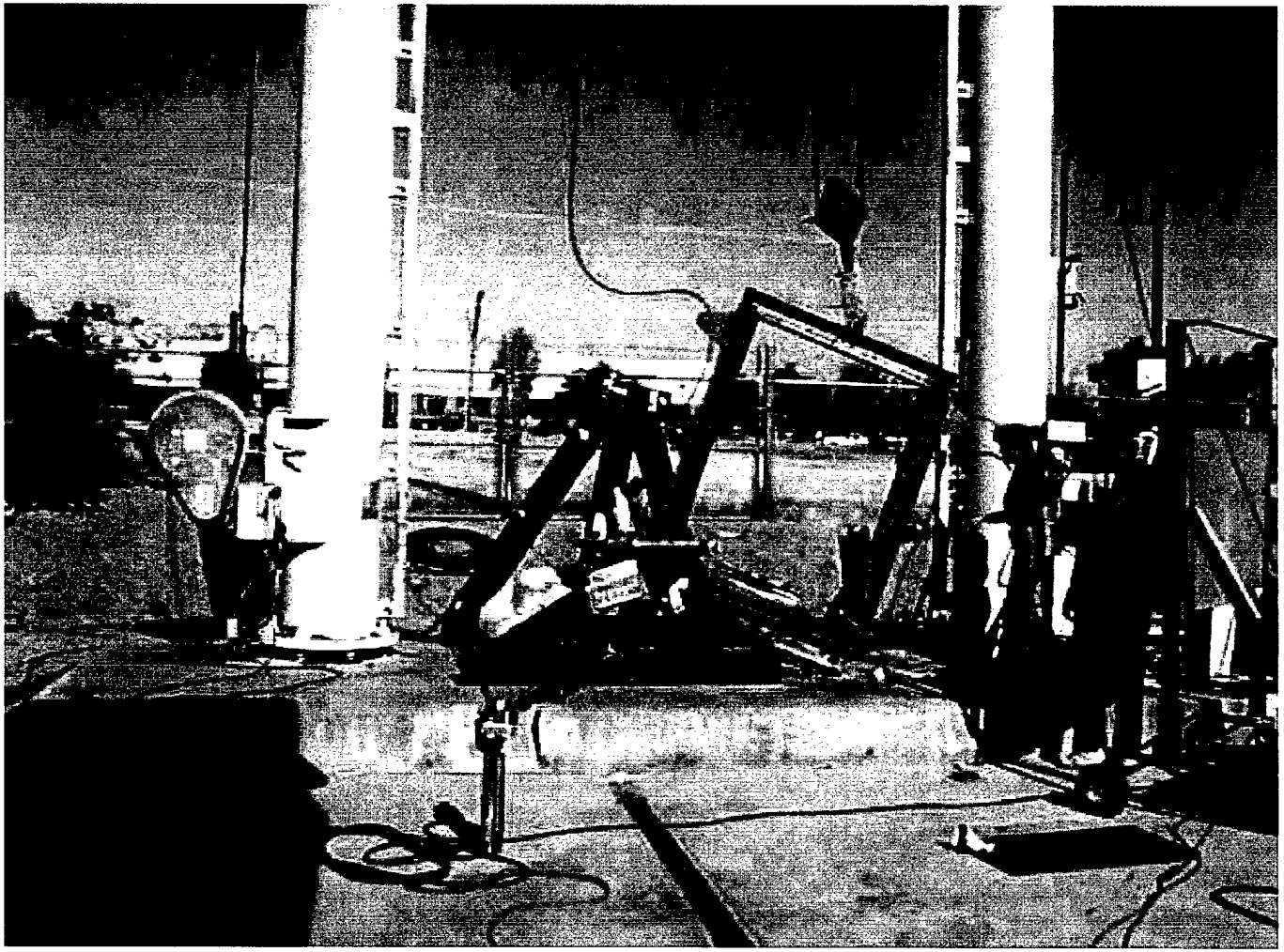

Post-Impact

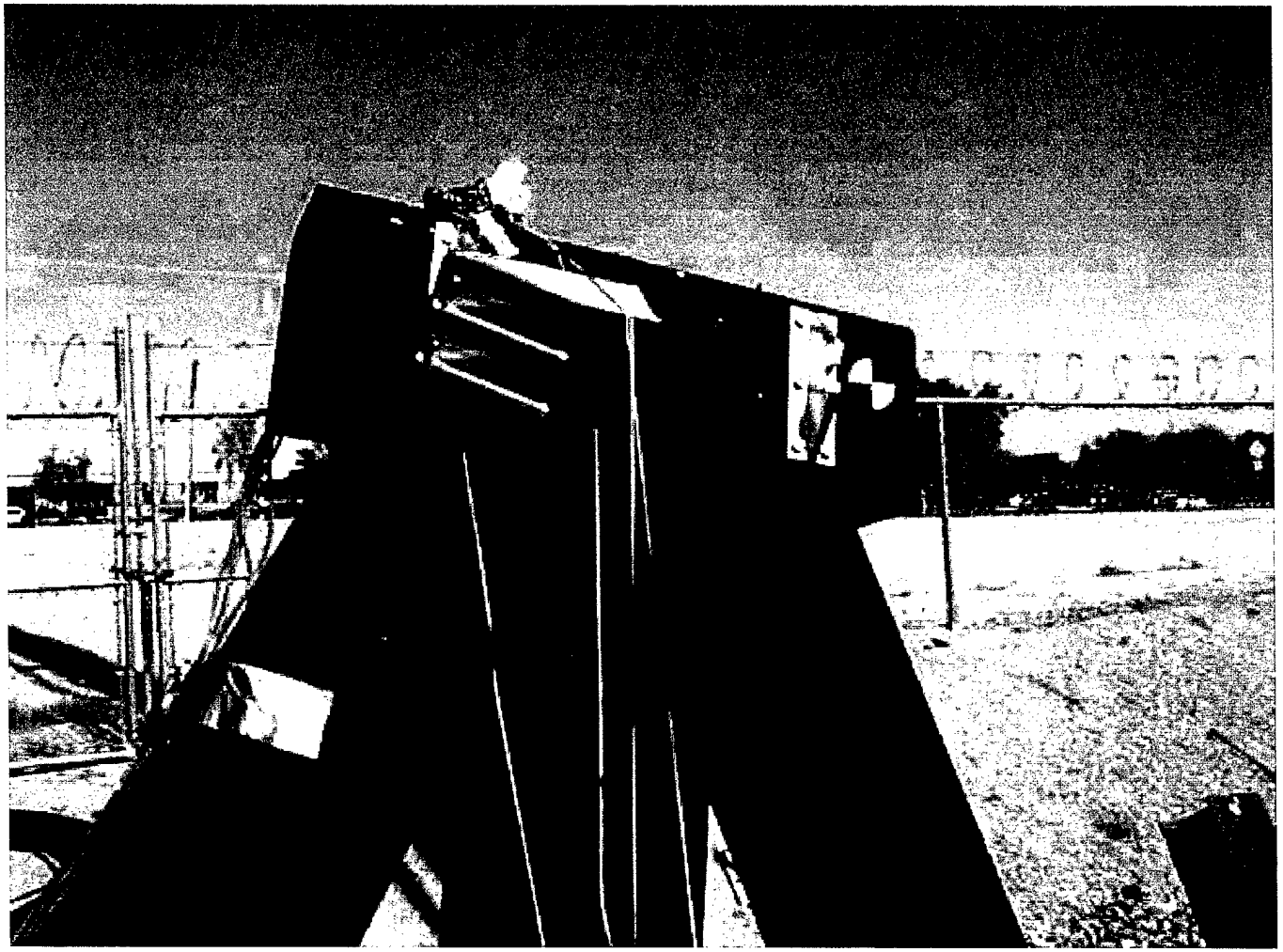

Failed Trailing Arm Support - Primary Failure

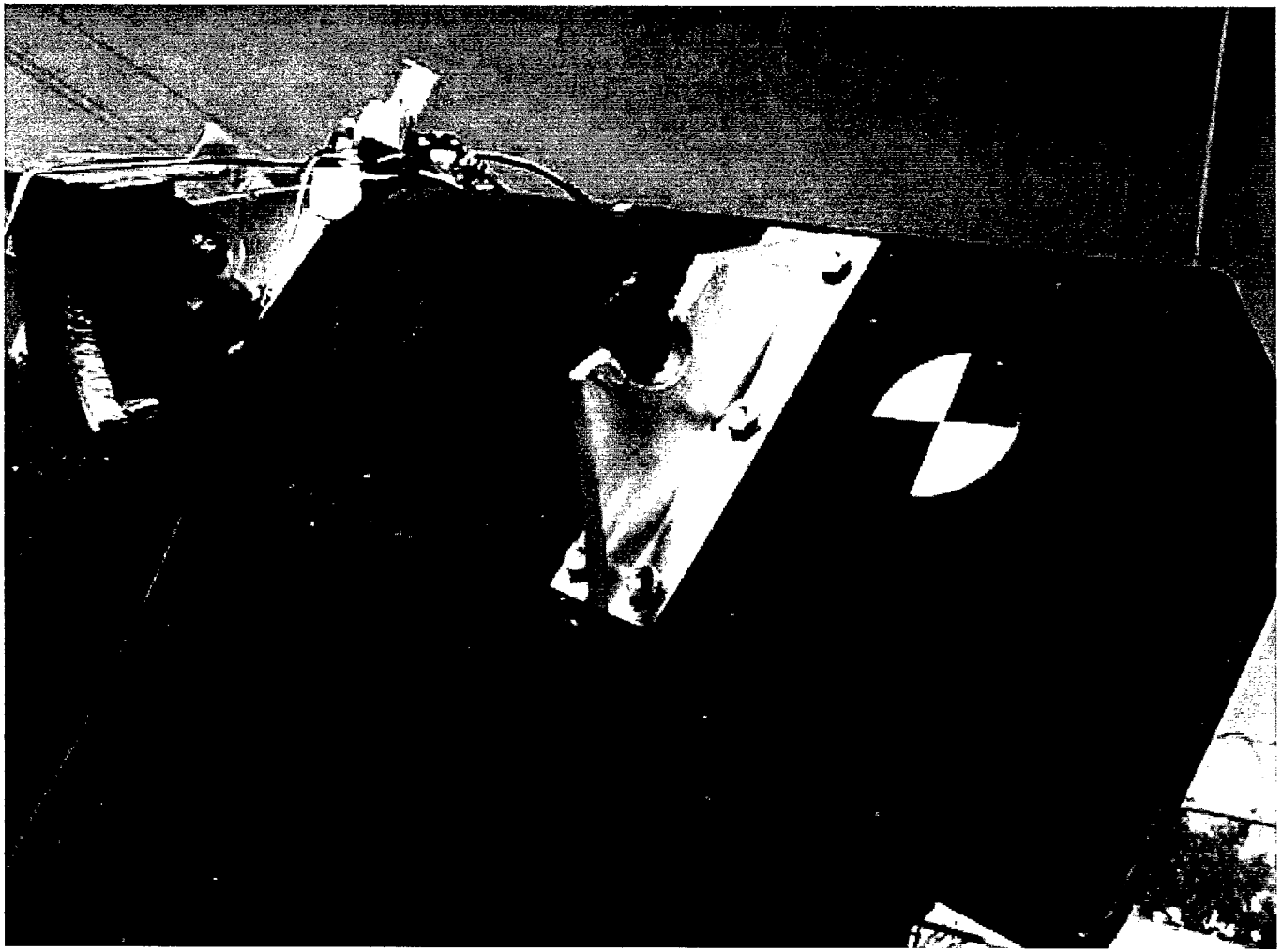

Failed Trailing Arm Support - Primary Failure

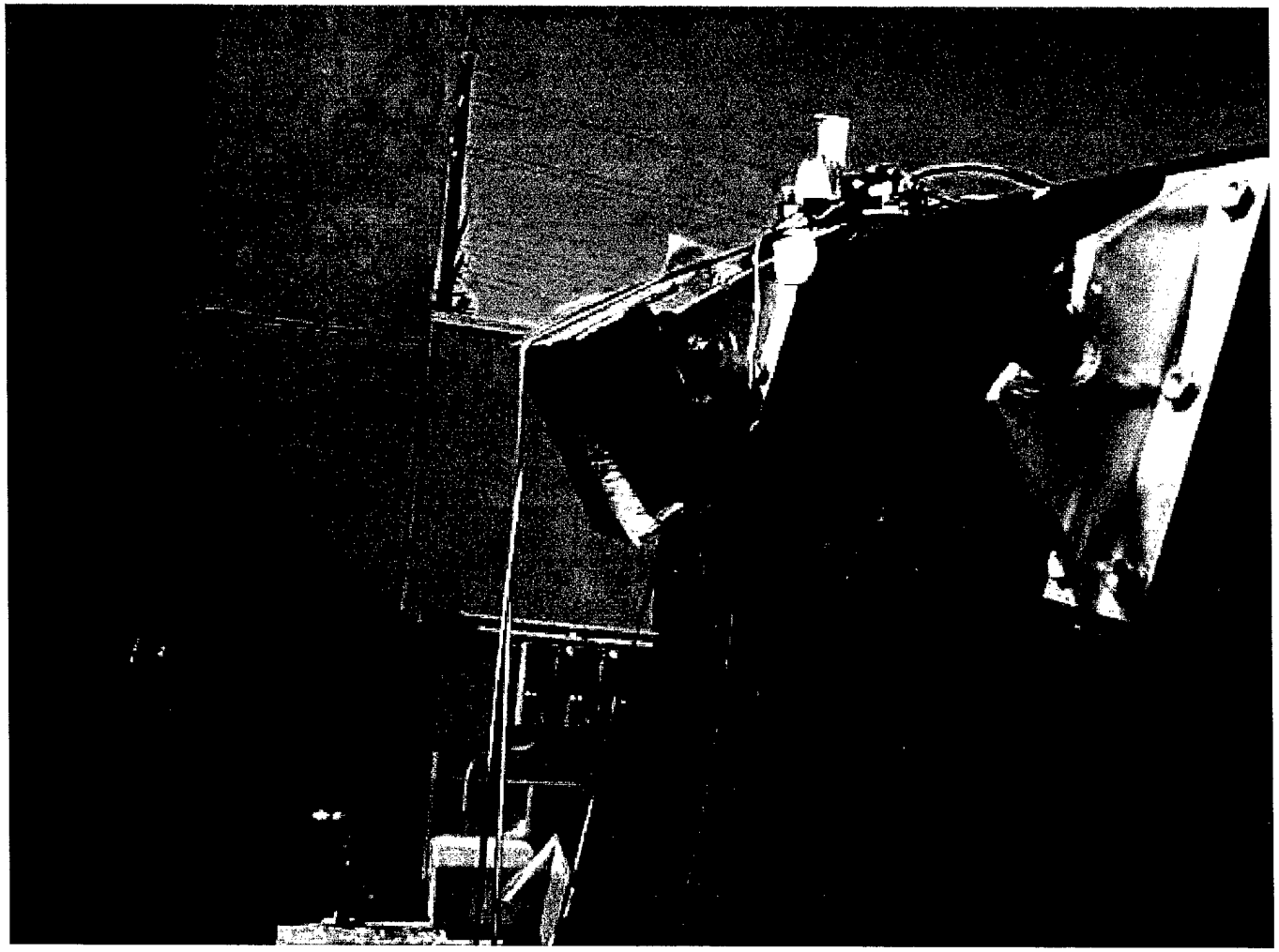

Failed Trailing Arm Support - Primary Failure

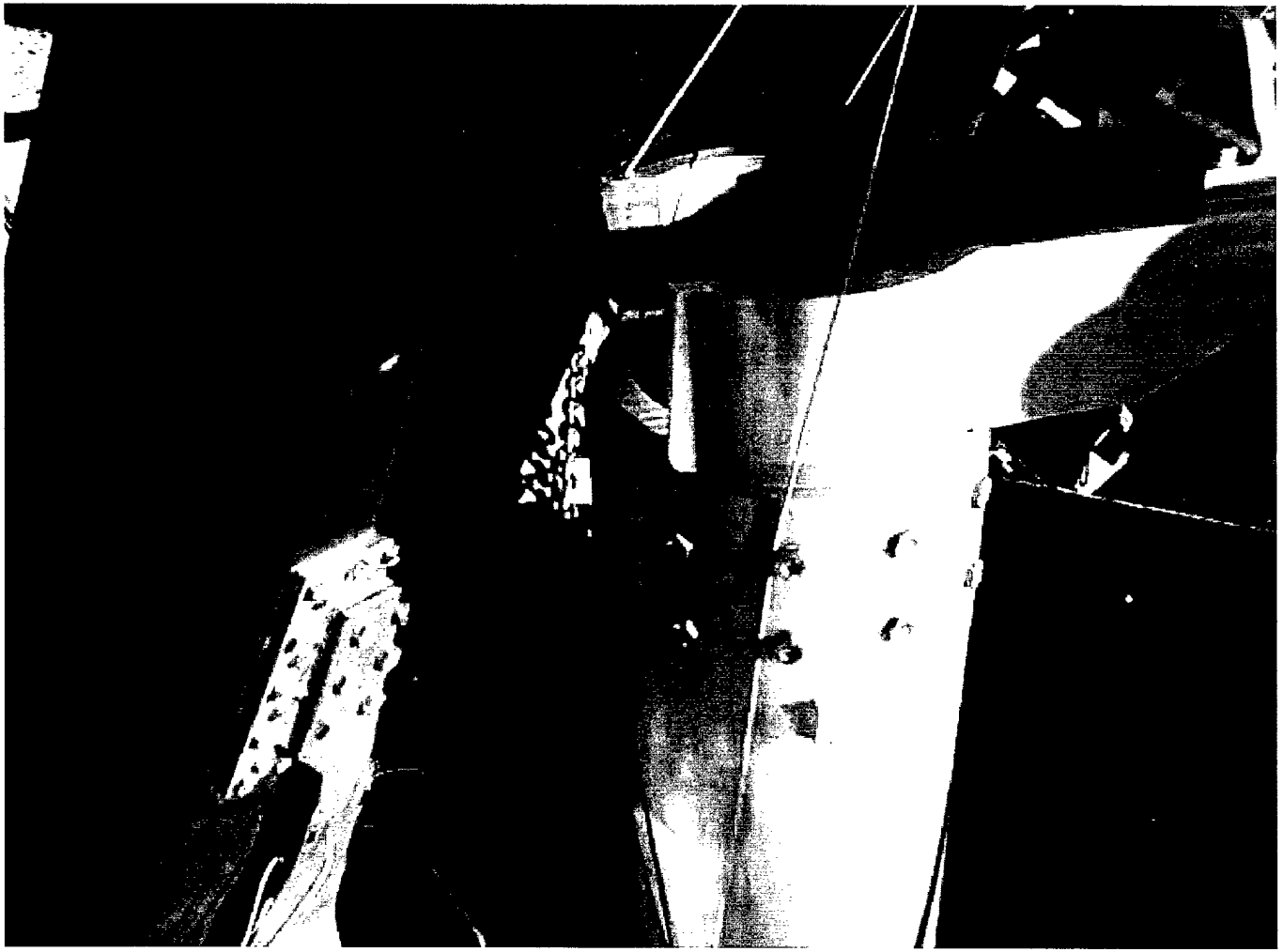

Failed Trailing Arm Support - Primary Failure

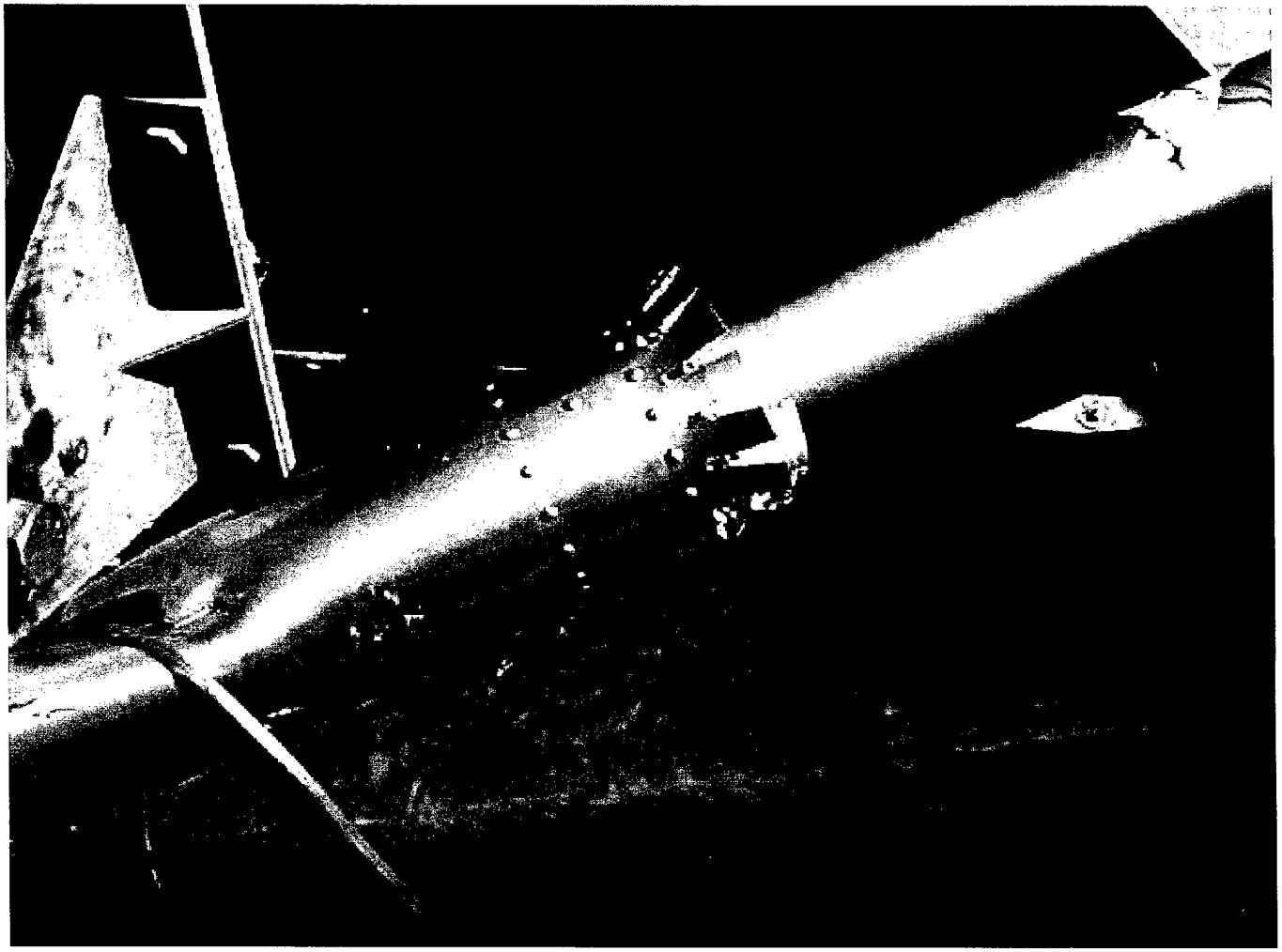

Tube Cutter and Secondary Shock Strut Damage

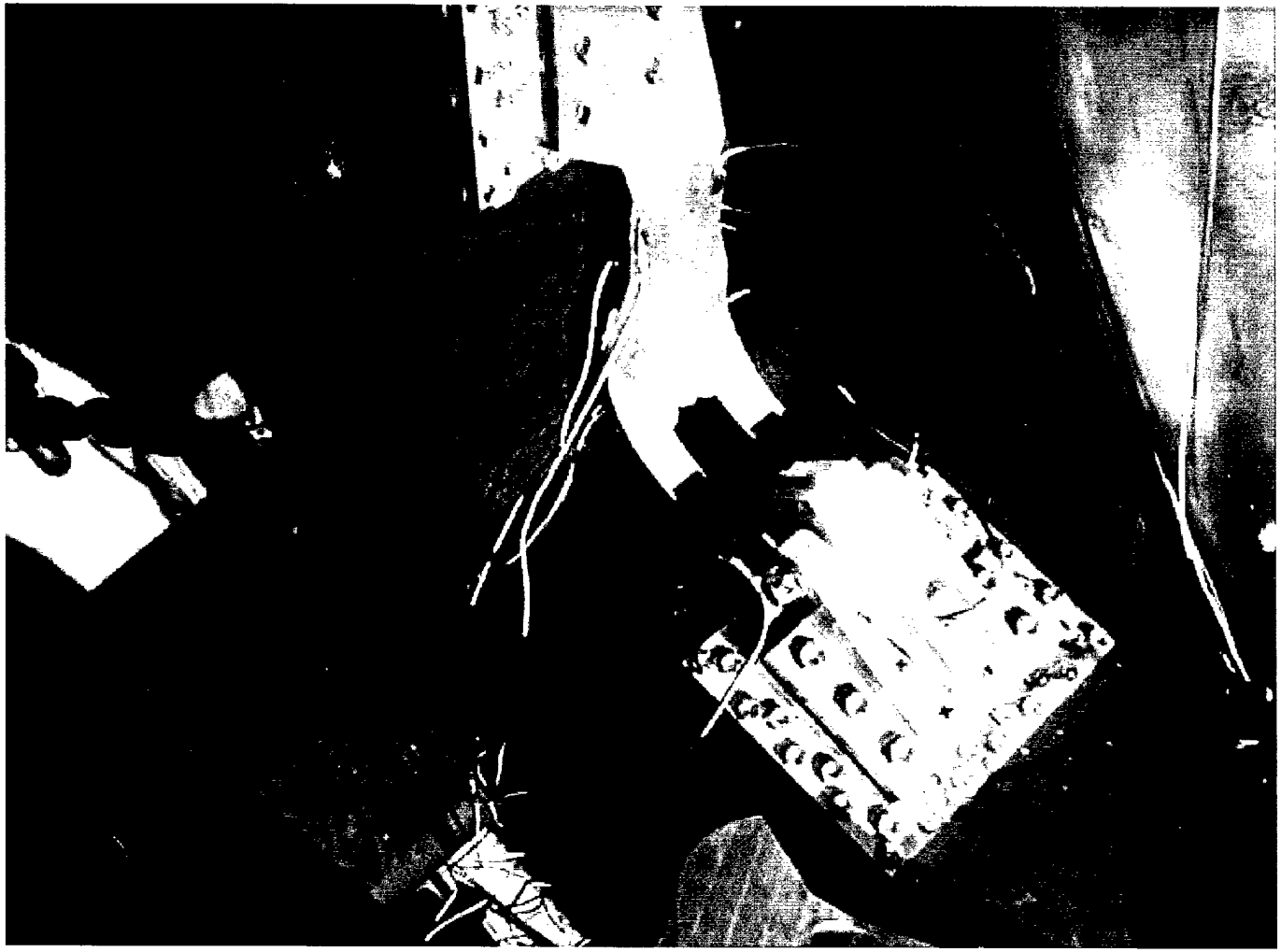

Undamaged Test Fitting with Secondary Link Failure

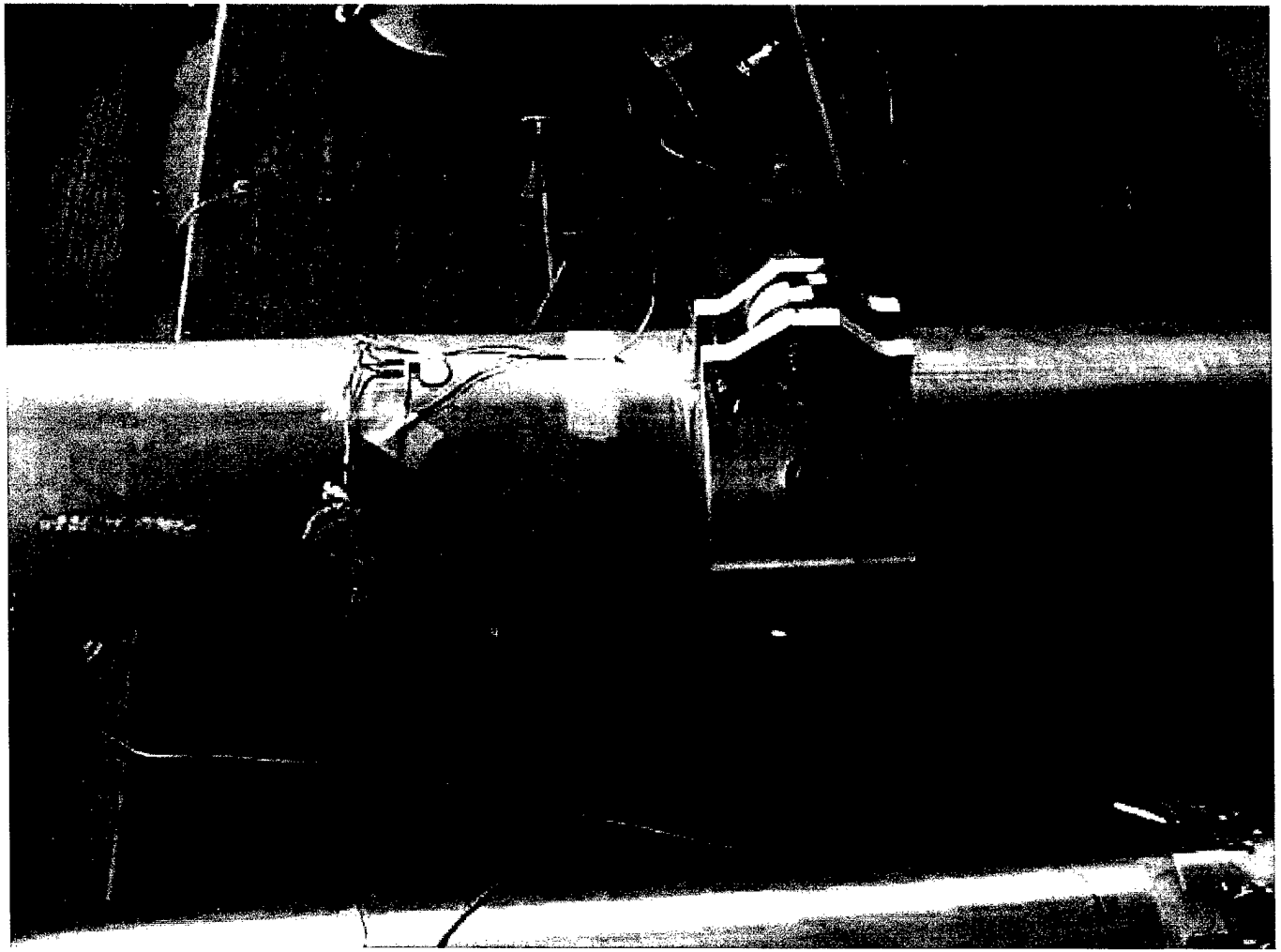

Shock Strut to Trailing Arm Attachment - Secondary Failure

Cracked and Perforated Trailing Arm at Wheel Support - Secondary Failures

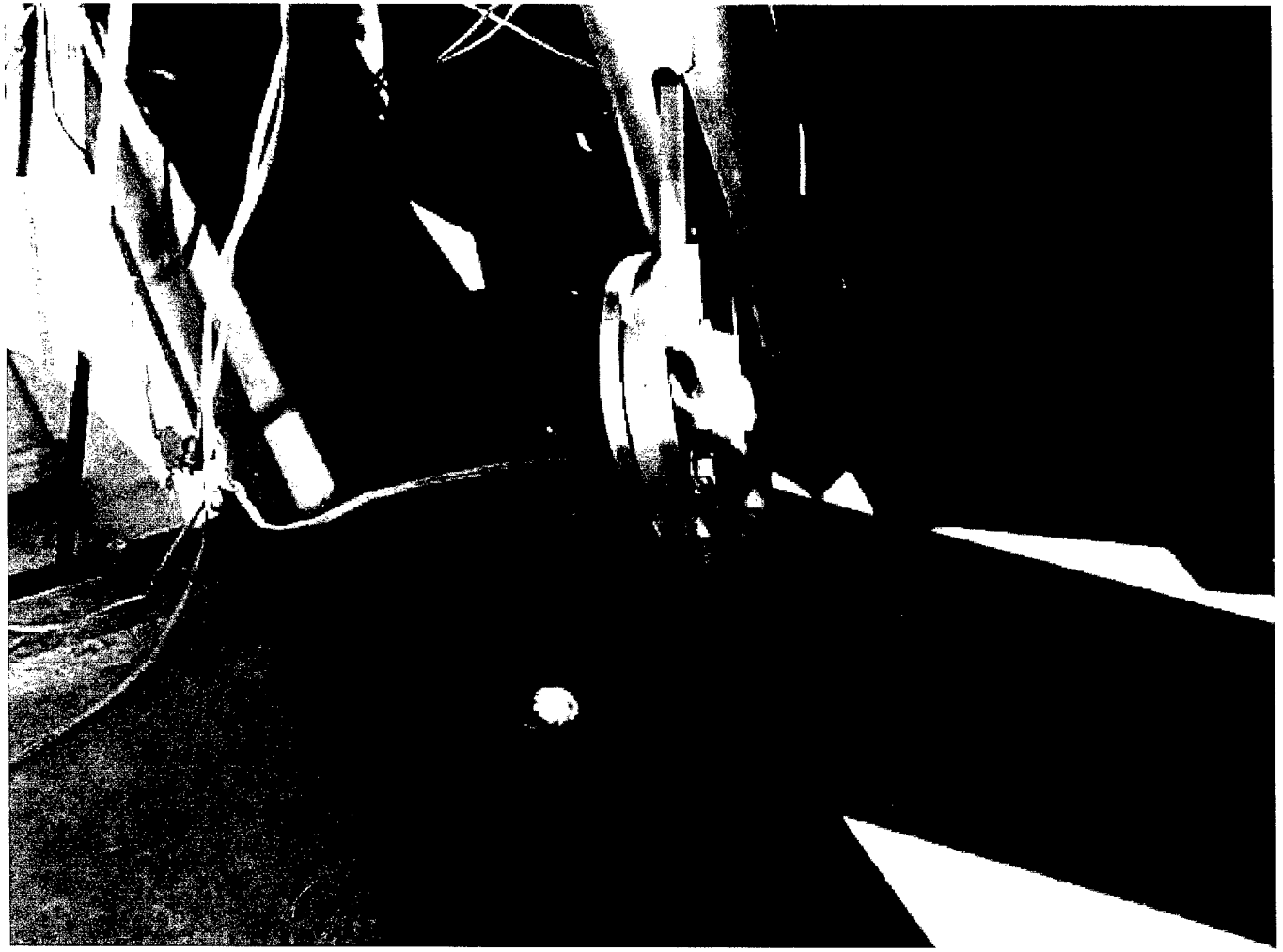

Trailing Arm and Wheel